

Design for demise applied to spacecraft structural panels and experiments for ClearSpace One platform

Présentée le 19 avril 2024

Faculté des sciences et techniques de l'ingénieur
Laboratoire de mise en oeuvre de composites à haute performance
Programme doctoral en science et génie des matériaux

pour l'obtention du grade de Docteur ès Sciences

par

Alexandre Achille LOOTEN

Acceptée sur proposition du jury

Prof. J. Brugger, président du jury
Prof. V. Michaud, directrice de thèse
Dr I. Sakraker Ozmen, rapporteuse
Dr U. Lafont, rapporteur
Prof. A. Vassilopoulos, rapporteur

Dire que nous foulons ce sol de la Lune où jamais la main de l'homme n'a mis le pied !
— Inspecteur Dupond, Les aventures de Tintin, On a marché sur la Lune - 1954, Hergé

To my family, friends and colleagues

Acknowledgements

This work is supported by an EPFL and ESA Network Partnering Initiative (NPI) contract number 4000129740/20/NL/MH/hm in collaboration with Beyond Gravity SA, icotec ag, Bcomp Ltd, Belstead Research Ltd, IRS Stuttgart and ClearSpace SA.

First I would like to express my sincere gratitude to the esteemed and distinguished members of my thesis jury, Prof. Jürgen, Prof. Vassilopoulos, Dr. Sakraker Ozmen and Dr. Lafont, who accepted to take part in the complex evaluation of my research work.

I would like to express my greatest gratitude to Professor Véronique Michaud and Muriel Richard for giving me this amazing PhD opportunity at EPFL in a domain of materials and space engineering that aligns with my personal ideals. Their extraordinary achievements, dedication and great kindness will forever inspire me.

As my thesis director for the second time, extending back to my Master's degree, Véronique has always been extremely reachable and supportive along this adventurous project.

I would like to acknowledge all the LPAC team for their great help and support along those great years, in addition to amazing and memorable moments, especially the Christmas lab parties and winter/summer outings in far-far locations.

I would like to thank especially Raphaël Charvet for all my crazy testing demands and efficient support, Gavin Waddell regarding his help and valuable tips for the manufacturing phases of the project, Valentin Rougier for the beautiful X-ray images, and particularly my dear shared-office colleagues Aigoul Schreier (my PhD twin colleague), Vincent Varanges and Joanne Vaucher who were able to withstand my constant need for chocolate or madeleines, and over-motivation for outdoor activities and sketchy challenges. And sorry again for the Bishorn. I am deeply grateful to Aigoul for her exceptional commitment and SEM expertise in addressing my last-minute analysis request.

Additional acknowledgements go to the ESA Clean Space Office and Concurrent Design Facility teams for their warm welcoming at ESTEC for my 5-month visiting period and their help on my challenging experiments. My gratitude goes particularly to my ESA NPI coordinator and on-site mentor Antonio Caiazzo for his consistent presence and enthusiastic support during these 4 years, in addition to Benoît Bonvoisin and his precious technical advises. A special thanks to my intern office colleagues, Floor Bagchus, Lucia Suriani, Philipp Grüning, Benedetta Cattani, Enrico Tormena, Calum Turner and the fabulous Aurelio Kaluthantrige who assisted greatly in the development of this work and my life quality in the adversely flat environment of the Netherlands.

Acknowledgements

I would like to acknowledge specifically the ideally balanced institution/industry team reunited for 60 monthly meetings under this Network Partnering Initiative project that allowed it to grow from a simple idea to real solutions and critical knowledge improvement toward a safe and sustainable space environment. So thanks to:

Adam Pagan and Professor Georg Herdrich from IRS, for their tremendous knowledge transfer and testing opportunity in their plasma wind tunnel facility. And all the great welcoming of the IRS team I met in Stuttgart.

James Beck from Belstead for his dedicated help and advanced visions regarding testing and modelling works.

Lionel Metrailler from ClearSpace for his support through his great expertise in space systems.

Régis Voillat from BComp for his brilliant expertise and help regarding composite manufacturing and material selection.

Albert Vodermayr from icotec for his precious composite expertise and technical support.

Ralf Usinger and Alessandro Netti from Beyond Gravity for their great support on structural and space aspects.

Je souhaiterais remercier du fond du coeur :

Olivia pour sa patience, son amour, mais surtout pour m'avoir énormément soutenu (supporté) et suivi dans cette folle vie de doctorant. Merci de m'avoir aidé à prendre la décision de commencer ce doctorat. Sans toi je ne serais pas là.

Ma famille : Marit, Pierre, Magne, Sylvie, Audrey, Erik, Fabien, Marie, Christophe et Agathe pour le soutien et les encouragements infaillibles qui ont permis de réaliser ce projet. Merci d'être ma source constante d'inspiration et de force.

Mes très chers Ing. Guillaume et Dr. Blaise pour leurs bienveillance, humour sans pareil et goût prononcé pour des aventures inoubliables.

Mais aussi Indy et Praline pour leur soutien loyal et inconditionnel.

Ainsi que tous mes chers amis.

This work would have never been possible, or at least very much less supportable without you all.

Merci beaucoup! Thank you very much! Vielen Dank! Grazie mille! Hartelijk dank! Tusen Takk!

Ecublens, Station 12, MXH-143, March 29, 2024

A.A.L.

Abstract

With the recent awareness of the space sector on the fragile near-Earth space region and the forecast of the booming number of satellited objects, various mitigation approaches are currently evaluated and start to be implemented to limit the impact of space activities, and achieve a safe and sustainable space environment. Unfortunately, knowledge uncertainties and technology gaps delay our capability to act immediately, especially to apply a design-for-demise (D4D) approach, which aims to modify a spacecraft design and conception process to achieve the safest destructive reentry possible by material substitution, specific geometries, or dedicated subsystems.

As part of a Network Partnering Initiative launched by the Swiss Federal Institute of Technology in Lausanne (EPFL) and the European Space Agency (ESA), this work focuses on the design and experimental evaluations of novel composite components to improve the overall spacecraft demisability. The new system is compared to baseline critical systems, targeting higher altitude break-up while maintaining equivalent mission-relevant properties. The project's main attention landed on a complementary dual strategy with the material substitution of a benchmark system composed of an external sandwich panel and its fasteners. First, a novel short carbon fiber reinforced polyetheretherketone (CF/PEEK) bolted joint design was evaluated to replace critical titanium or steel alloys currently used. And second, a hybrid reinforcement made of carbon and demisable flax fibers is evaluated to replace aluminium panel skins or critical full carbon composite skins. The integration of a thermally conductive and reactive metallic matrix filler composed of aluminium-magnesium alloy micro-powder has also been investigated, as well as the use of discontinuous fiber CF prepregs.

The demisability assessment is performed at material and lab scale component levels. This involves the measurement of material's mechanical properties under static loading at room temperature, and dynamic loading over a temperature range to detect their softening point. Static and dynamic reentry simulation tests are carried out using a laboratory-scale high-temperature creep test developed in this work, and a plasma wind tunnel test to evaluate on one-hand, the thermo-mechanico-physical property change over typical uncontrolled reentry conditions, in particular the material break-up point, and on the other hand, the composite degradation.

Results to date lead to the selection of a promising reinforcement architecture and fastener selection. The study of the joints demonstrates that stainless-steel bolts present no sign of effective demise under testing up to 800°C, whereas the novel short fiber CF/PEEK bolts start to demise before reaching 400°C, while having a superior specific tensile, σ_{UTS}/ρ , and shear strength, τ_{USS}/ρ , within a typical space mission temperature range ($\pm 120^\circ\text{C}$). For the sandwich skin structures, an optimal ply-by-ply carbon-flax hybrid/epoxy shows the best trade-off in terms of demisability and specific mechanical properties for the skin, with respectively a 180% ablation rate improvement starting at a lower temperature as compared to

Abstract

CFRP, while having an equivalent specific bending modulus to the baseline aluminium. The addition of the AlMg filler improved the matrix pyrolysis rate by more than 10% while reducing its onset by 40°C. The preliminary investigation of the use of prepregs with discontinuities in the fiber direction also shows promising results, thanks to the early break-up of the matrix material, liberating the cut plies.

In parallel, a critical analysis of the parameters required to quantify materials degradation in DRAMA, ESA's reentry risk assessment tool, is conducted to allow the integration of newly tested CFRP materials and thus reduce the current casualty risk uncertainties by performing more realistic re-entry simulations. This research project marks a significant milestone in identifying and developing optimal demisable composite structures. The focus on evaluating novel material combinations through dedicated test campaigns underscores the commitment to ensure the readiness of findings for space applications. The direct experiment-to-model approach is particularly noteworthy, as it not only contributes to a better understanding of composite material demise but also effectively reduces uncertainties. The ultimate goal of enhancing the safety of future space debris reentry is clearly articulated, and the research lays an essential foundation for achieving this objective.

Résumé

Avec la prise de conscience récente du secteur spatial sur le risque de saturation de l'écosystème de l'orbite basse terrestre résultant du nombre croissant d'objets qui y sont envoyés, diverses approches de mitigation sont actuellement évaluées et commencent à être mises en œuvre. Celles-ci ont pour but de limiter l'impact des activités spatiales pour préserver un environnement spatial sûr et durable. Malheureusement, les incertitudes en matière de connaissances et les lacunes technologiques retardent notre capacité d'action immédiate. Cette problématique touche particulièrement l'approche de conception pour la désintégration/dématérialisation (D4D), qui vise à modifier le procédé de conception du vaisseau spatial pour intégrer des matériaux ou géométries spécifiques permettant d'obtenir une rentrée atmosphérique la plus destructrice possible.

Dans le cadre d'un projet de partenariat lancé par l'École polytechnique fédérale de Lausanne (EPFL) et l'Agence spatiale européenne (ESA), ce travail se concentre sur la conception et l'évaluation expérimentale de nouvelles solutions composites pour améliorer la désintégration globale des vaisseaux spatiaux. Le nouveau système est comparé à des systèmes critiques de référence, visant une désintégration plus importante, ainsi qu'à des altitudes plus élevées tout en maintenant des propriétés équivalentes pertinentes pour la mission. Le projet s'est porté principalement sur une stratégie en deux parties complémentaires visant la substitution de matériaux d'un système de référence composé d'un panneau sandwich externe et de ses fixations. Tout d'abord, une conception nouvelle de joint boulonné en polyétheréthère renforcé de fibres de carbone courtes (CF/PEEK) est évaluée pour remplacer les alliages en titane ou en acier actuellement utilisés. Ensuite, un renforcement hybride composé de fibres de carbone et de lin est évalué pour remplacer les peaux de panneau en aluminium ou les peaux critiques renforcées exclusivement en fibres de carbone. L'intégration d'une micropoudre métallique réactive et conductrice de chaleur composée d'alliage aluminium-magnésium a également été étudiée, ainsi que l'utilisation de préimprégnés CFRP à fibres discontinues.

L'évaluation de la désintégration a été effectuée au niveau du matériau et du composant dans un environnement de laboratoire. Ceci regroupe la mesure des propriétés mécaniques du matériau sous charge statique à température ambiante, et sous charge dynamique sur une large plage de température, afin de quantifier les caractéristiques spécifiques au comportement de désintégration. Des tests de simulation de rentrée atmosphérique statique et dynamique ont été réalisés à l'aide d'un montage de fluage à haute température développé dans le cadre de ce travail, et d'un essai en soufflerie plasma pour évaluer d'une part le changement des propriétés thermomécaniques-physiques dans des conditions typiques de rentrée non contrôlée, en particulier le point de rupture mécanique du matériau, et d'autre part, le comportement en désintégration du laminé composite.

Les résultats obtenus ont conduit à la sélection d'une architecture de renforcement prometteuse. L'étude

des joints a montré que les boulons en acier inoxydable ne présentent aucun signe de rupture efficace lors des essais jusqu'à 800°C, tandis que les nouveaux boulons CF/PEEK commencent à se désintégrer avant d'atteindre 400°C. Ceci tout en présentant une résistance spécifique à la traction (σ_{UTS}/ρ) et une résistance au cisaillement (τ_{USS}/ρ) supérieures dans une plage de température typique de mission spatiale $\pm 120^\circ\text{C}$). Pour les peaux des structures sandwichs, une disposition optimale hybride de fibres de carbone et de lin avec une matrice époxy présente le meilleur compromis en termes de désintégration et de propriétés mécaniques spécifiques pour les peaux du sandwich, avec respectivement une amélioration de 180% du taux d'ablation à partir d'une température plus basse par rapport au CFRP, tout en ayant un module de flexion spécifique équivalent à l'aluminium de référence. L'ajout de la charge AlMg a amélioré le taux de pyrolyse de la matrice de plus de 10% tout en réduisant son apparition de 40°C. Les travaux préliminaires sur l'utilisation de preimprégnés à fibres discontinues ont aussi montré des résultats encourageant, grâce à la désintégration de la matrice laissant les plis se séparer plus facilement.

Ce projet de recherche marque une étape significative dans l'identification et le développement de structures composites optimisées pour la désintégration. L'accent mis sur l'évaluation de combinaisons de matériaux novateurs à travers des campagnes d'essais dédiées souligne l'engagement à garantir des niveaux de maturité technologiques pour les applications spatiales. Le développement d'une approche directe permettant de lier les expériences aux modèles de simulation présentés dans cette thèse est un point clé pour l'intégration de nouveaux matériaux. Car elle contribue non seulement à une meilleure compréhension de la décomposition des matériaux composites, mais réduit également efficacement les incertitudes de simulation. Ce travail de recherche contribue à l'objectif ultime d'améliorer la sécurité de la rentrée des futurs débris spatiaux futurs, ainsi qu'à l'établissement de bases fondamentales pour atteindre cet objectif.

Contents

Abstract (English/Français)	iii
List of Figures	xi
List of Tables	xvii
1 Introduction & Research motivation	1
1.1 What is the matter with space debris ?	2
1.2 Spacecraft structure challenges imposed by falling debris	5
1.3 Thesis framework	6
2 State of the Art	11
2.1 Atmospheric re-entry environmental conditions	12
2.1.1 Re-entry event observation and in-situ data recording	12
2.1.2 Recovered space debris analysis	14
2.1.3 Experienced re-entry conditions	15
2.1.4 On-ground re-entry condition reproduction	16
2.1.5 Demise criteria - <i>DC</i>	17
2.1.6 Composite materials demise behaviour	19
2.2 D4D applied to external structure	20
2.2.1 Demisable joints	21
2.2.2 Demisable structural materials	22
2.3 Space re-entry modelling	24
2.3.1 Re-entry demise simulation analysis tool	25
2.4 Thesis objectives and methodology	26
2.4.1 Proposed methodology	28
3 Materials & Methods	31
3.1 Materials	32
3.1.1 Bolt joints	32
3.1.2 Sandwich panel facesheet	34
3.1.3 Manufacturing	37
3.1.4 Discontinuous reinforced composite laminate	40
3.2 Structural and physical properties evaluation methods	42
3.2.1 Dynamic mechanical analysis	43
3.2.2 Tensile test	44

3.2.3	Single shear test Bolt joint system	45
3.2.4	Tightening capability cycling test Bolt joint system	46
3.2.5	Outgassing test	46
3.2.6	Vibration test - Space launch loads simulation Sandwich panel	47
3.2.7	4-pt bending test Sandwich panel	49
3.3	Demise evaluation methods	50
3.3.1	Thermogravimetry analysis	50
3.3.2	Thermal conductivity Sandwich panel facesheets	51
3.3.3	Creep Static Re-entry Chamber (SRC)	51
3.3.4	Plasma Wind Tunnel Sandwich panel facesheets	54
4	Advancing spacecraft demisability through a novel composite bolt joint system: a step toward sustainable and safe space environments	59
4.1	Technology of interest - Why composite bolt ?	60
4.2	Mechanical performance comparative evaluation	61
4.2.1	Tensile and shear evaluation	61
4.2.2	Tightening capability	62
4.2.3	DMA	63
4.3	Demise relevant properties' evaluation	64
4.3.1	Static Re-entry Chamber (SRC)	65
4.4	Chapter summary and technology application limitations	67
4.4.1	Perspectives	68
5	Advancing composite demisability: Innovative facesheet materials and reinforcement combinations	69
5.1	Technology of interest - How can we tackle Carbon Fiber Reinforced Polymer (CFRP) demise resistance ?	70
5.2	AlMg micropowder optimal content identification	71
5.3	Structural and physical performances comparative evaluation	72
5.3.1	At laminate level: DMA and tensile test results	72
5.3.2	Space qualification evaluation – Outgassing	76
5.3.3	At sandwich level: 4pt-bending and vibration results	77
5.4	Demise relevant properties' evaluation	84
5.4.1	Thermo-physical analysis: thermal conductivity and thermogravimetry	84
5.4.2	Static Re-entry Chamber (SRC)	88
5.4.3	High fidelity testing through Plasma Wind Tunnel	96
5.5	Chapter summary and technology application limitations	108
5.5.1	Technology application limitation	109
5.5.2	Further work	109
6	Critical evaluation of DRAMA's composite demise model and improved demisability modelling through experiment correlation	111
6.1	SARA composite demise model recovery	112
6.2	Composite demise models comparison	114
6.3	Evaluation of extracted composite material parameters implementation	118
6.3.1	Composite material parameters compatibility process	118

6.3.2	New composite materials' demise parameters extraction	119
6.4	ClearSpace-One end-of-life analysis study case	124
6.5	Summary	128
7	Conclusion	129
7.1	Perspectives	131
A	Appendix	133
A.1	Facesheet material details	134
A.2	Cut-CF (SMC-HP) and continuous-CF (Nappe) samples details	135
A.3	SEM analysis of the aluminium oxide formation from hygro-aging of aluminium sandwich panels	135
A.4	Static reentry chamber video link and temperature profiles reference	137
A.5	Plasma wind tunnel additional data	138
A.5.1	Front temperatures with LP3 pyrometer	138
A.5.2	Front surface temperature monitoring technique comparison	140
A.6	Novel technology assessment and market potential	142
A.7	Modelling spare parts	143
	Bibliography	150
	Curriculum Vitae	151

List of Figures

1.2	(a) Recovered space debris impact locations versus (b) predicted events, based on a November 2016 analysis.[1]	3
1.3	Record stacking of 143 satellites in a Falcon 9 payload bay.[2]	4
1.5	Recovery of a massive space debris in Australia in august 2022, image credits: Mike Mayers [3]. It is mainly composed of CFRP sandwich panels and was identified to be part of the SpaceX Crew-1 dragon module’s trunk highlighted in red in the right image and jettisoned before its re-entry in May 2021, image credit: SpaceX [4]	6
1.6	Highlight of the Design-for-Demise (D4D) approach within CleanSpace Initiative - ESA’s objective Zero Debris by 2030. [5]	7
1.7	DIVE document verification procedure flow chart for the implementation of new systems related to re-entry risk criticality following the recommended D4D approaches. [6]	8
1.8	Illustration of ClearSpace-1 (CS-1) chaser approaching VESPA debris for its capture.[7]	9
2.1	Illustration of an uncontrolled re-entry and the associated key environmental parameters leading to demise process under the destructive conditions [8] [9]. Re-entry illustration credit to ESA-Multimedia [1]	12
2.2	Cygnus OA6 re-entry fragmentation picture taken from the dedicated observation aircraft.[10]. Spacecraft image credit: NASA [11].	13
2.3	Exploded view of the Re-Entry Break-up Recorder (REBR) capsule and the recovered data of different HTV and ATV cargo re-entries.[12]	14
2.4	On the left, a relatively intact carbon fiber/titanium Composite Overwrapped Pressure Vessel (COPV) tank, recovered in Indonesia in 2016. On the right, a Delta II 2nd stage tank recovered in Texas in 1997 (length =1.75m).[1] [13]	15
2.5	Comparative panel of re-entry simulation testing facilities with respect to condition fidelity and setup complexity (in-fine related to the cost).	16
2.6	Tumbling attitude simulator via a rotative sample holder integrated within DLR Plasma Wind Tunnel (PWT) facility. Comparative results on a CFRP cylinder between static and dynamic attitude.[14]	17
2.7	Illustration of the complex interaction factors between ablative materials such as CFRP and an intense heat flux.	19
2.8	Re-entry demisability sensitivity index analysis for D4D approach from the work of Trisolini et al. [15].	20
2.10	Overview of demisable joint technologies and their related demisable rating based on the ranking system developed by Suriani et al. [16]	22

List of Figures

2.11	Bcomp demisable FFRP panel prototype, with a topology optimization windows design made of a thin monolithic laminate rigidified by the characteristic powerRibs TM technology. [17]	22
2.12	DRAMA's five integrated modules for S/C orbital and re-entry risk assessment.	25
2.13	Summary of thesis objectives and key points, based on two interdependent approaches.	27
2.14	Left, artistic view of CS-1 spacecraft capturing VESPA target. And right an exploded-view model with highlighted in green the front and side external panels. The side panels are used a reference for this work and have a dimensions of 1031x747 mm. Credit to ClearSpace.today	28
2.15	Illustration of our benchmark design composed of a sandwich panel and it through-thickness bolted attachment system.	29
3.1	Main testing methods performed through this research work covering specifically structural and demisability evaluation of the various materials and designs selected.	32
3.2	Baseline stainless steel versus our novel CF/PEEK bolts for through-thickness insert fixture to a sandwich panel.	33
3.3	Comparative analysis of continuous (CT) and short (SH) CF/PEEK samples with LPAC XPCi setup from which three type of images can be extracted. The phase scattering image shows rich microstructure information such as fibre distribution homogeneity or voids, which is particularly interesting for composite materials.	33
3.4	Sandwich panel facesheet reinforcement versions selected for this study, with a schematic and microscopic cross-section view of the different fibre types and arrangements	35
3.5	Bulky and angular shaped AlMg particles observed under optical microscope	37
3.6	Temperature and pressure profiles of dual-hold cure cycle used for the autoclave curing of the various composite laminates.	38
3.7	Cross-sections of Flax Fiber Reinforced Polymer (FFRP) filled composite laminate with 1%wt AlMg micropowder, where the some of the largest alloy particles are highlighted by red circles	39
3.8	On the left, the Scholtz autoclave from LPAC loaded with a samples plate. On the upper left, a skin outgassing step to compact the reinforcement or resin plies. On the top right, staking of the aluminium honeycomb on the bottom skin and an adhesive film. And at the bottom, a resulting large sandwich panel used for the vibration and bending tests.	40
3.9	Illustration of the cutting manufacturing process performed by Composites Busch SA for the discontinuous reinforcement composite samples.	41
3.10	Continuous- and cut-CF laminate plates' cutting plan for SRC and DMA samples. Numerical microscope cross-section images in 0° and 90° direction of the laminates.	42
3.11	On the left, DMA 3-pt bending setup. On the right side, comparison of an untested sample (top) with two tested samples with respectively 340°C and 350°C final tested temperatures.	43
3.12	DMA 3pt-bending setup with on the left an untested FFRP+AlMg sample and on the right an installed and charred sample after testing up to 350°C.	44
3.13	Tensile test setup with the video extensometer at the forefront and the red backlight on the left. The sample is placed in between allowing a strong and clear contrast ideal for displacement measures.	44
3.15	Single shear setup to evaluate for M5 bolt shear strength.	46
3.17	Vibration qualification test sequence applied to all three versions.	47
3.20	Thermal conductivity analysis setup schematic on the left and output camera vision on the right with the six measurement points per plate.	51
3.21	The STS-96 (categorised as a highHeating Rate (HR)) and a typical Uncontrolled (UC) (categorised as a low HR) re-entry temperature profiles and heating rates.	53

3.22	Self-designed static re-entry chamber schematic illustration.	53
3.24	PWK4 testing facility at IRS and its schematic view with the different monitoring equipment. Modified monitoring setup configuration presented by Pagan et al. [18].	55
3.26	Superposition of various re-entry S/C trajectory condition and the four IRS plasma wind tunnel (PWK) facilities capabilities. In orange is highlighted a reference condition for a Spacecraft (S/C), with a Ballistic Coefficient (BC)=150 kg/m ² , fo an estimated uncontrolled re-entry trajectory, with a break-up just below 80km and propagation (dashed-orange) following the different fragments' BC. Credits to Pagan [19], IRS-Stuttgart.	57
4.1	CFRP sandwich structure attached via through-thickness bolt joint system.	60
4.3	Ten repetition load cycling results on short-CF/PEEK bolt and nut with final chosen preload of 2.5kN (left), 2kN (middle) and 1.5kN (right)	63
4.4	X-ray Phase Contrast imaging (XPCI) post- cycling tightening test analysis on short CF/PEEK new (left pair) versus tested (right pair) bolt samples. A clear fracture can be observed in the left tested sample after three preloads cycles at 2.5kN, against no visible damages for a recovered 2kN sample (right). The white band on the absorption image corresponds to the PMMA sample holder.	63
4.6	Thermogravimetric Analysis (TGA) (bottom) and Differential Thermogravimetry (DTG) (top) curves of CF/PEEK under air and nitrogen environments.	64
4.8	Left, CF/PEEK sample under static re-entry test. Right, recovered continuous and short CF/PEEK samples from static re-entry test, with a complete fastener separation in the case of the short design.	67
4.9	Illustration of the ideal short CF/PEEK fastener demise within an external sandwich pane	68
5.1	Bcomp Ltd., Beyond Gravity (previously RUAG) and IRS high demisability FFRP sandwich panel prototype, with its skin layup testing in PWT setup on the right and performing vibration testing on the left [17]	70
5.3	Facesheet material Dynamic Mechanical Analysis (DMA) test results. Comparative overlay of their skins' storage modulus.	74
5.4	Facesheet material DMA test results. Comparative overlay of the composite versions' tan δ	74
5.5	Comparative DMA storage modulus trend with temperature of continuous-CF (UD) laminate versus novel cut-CF design (SMC-HP) in the 0° direction.	75
5.7	Comparative 4-pt bending skin stress versus deflection curves of the three sandwich sample versions. The solid lines are for the standard samples and dashed lines for the ones that endured the 95%RH conditioning.	78
5.8	Comparative analysis of the properties of interest for the novel Carbon-Flax Fibers ply-by-ply (CF-FFBP) hybrid against metallic and composite baselines.	79
5.9	Dual camera's view, with respectively (a) the whole sample and (b) a focus view on the left loading pad. (c) Vic2D analysis window where the top and bottom skins strain measurement points are selected.	80
5.10	Comparison of the three different sandwich facesheet materials Frequency Response Function (FRF) graph of all the low-level sine runs.	81
5.11	Sandwich panels out of plane FRF curves from the four corner-placed accelerometers, with the correlated natural vibration modes identified with the COMSOL Finite Element Analysis (FEA) analysis.	82
5.12	Derived damping ratios of the three sandwich panel versions identified by their skin materials (aluminium, CFRP and the novel CF-FF hybrid) at the three optimal vibration modes.	83

List of Figures

5.13	Resulting temperature response transient curves averaged from the 6 measurement points per plate, comparing virgin and AlMg charged FFRP samples.	84
5.14	Experimental data to model correlation for the evaluation of the through-thickness thermal conductivity improvement.	85
5.15	TGA and Differential Thermogravimetry (DTG) comparative analysis of four skin materials under synthetic air.	85
5.16	Comparative evaluation of TGA pyrolysis behaviour of AlMg filler integration in the baseline epoxy and PVB/epoxy blend.	86
5.17	Illustration of pyrolysis reaction kinetic parameters extraction process from TGA data.	87
5.18	Recovered composite samples allowing a complete visual inspection and comparison of the demise state of the four different reinforcement types (CFRP, FFRP, Carbon-Flax Fibers two-by-tow (CF-FFTB), CF-FFPB). On the right picture, a closer view of the ply-by-ply hybrid, with a clear view of the central twill flax ply near a full demise with only carbonated flax fibres left. . .	88
5.20	Reported fracture and demise onsets of the five different panel skin materials evaluated under the uncontrolled re-entry condition.	90
5.22	Reported fracture and demise onsets of the four remaining panel skin materials of interest evaluated under the STS-96 re-entry condition.	91
5.23	AlMg filler effect on surface temperature of FFRP samples under the uncontrolled re-entry conditions.	91
5.25	Effect of composite materials and heating rate (test conditions) on mass loss and mass loss rate under SRC testing.	93
5.26	Comparison between composites materials and the two heating conditions of demise heat alone on the left and related to samples thicknesses on the right.	93
5.27	Cross-comparison of SRC thermo-mechanical curves between the low and high heating rate testing conditions, and UD continuous-CF versus SMC-HP cut-CF. The temperature curves are extracted from the central thermocouple measurement point. The cross at the end of the SMC-HP displacement curves indicates the samples' fracture.	95
5.28	Comparative histogram of SRC fracture and matrix degradation onsets with continuous-CF versus novel cut-CF samples under two reentry-like conditions (UC and STS-96).	95
5.30	Optical vs IR view of the CF-FFPB A sample under Medium Heat Flux (MHF) after 30s.	96
5.31	Complete data overlay comparison under MHF condition with the front temperature data from the thermal camera and the back surface temperature from the MiniPryex.	98
5.32	Complete data overlay comparison under High Heat Flux (MAX-H) condition with the front temperature data from the thermal camera and the back surface temperature from the MiniPryex.	99
5.33	Front surface monitoring method comparison of four samples types, FFRP, FFRP+AlMg, the tow-by-tow hybrid and the thin Carbon Fiber (CF) version A ply-by-ply hybrid.	100
5.34	Front and back surface temperature profiles of both hybrid types under MHF test conditions.	102
5.35	Visual demise behaviour comparison between thin CF (A) and thick (B) ply-by-ply hybrid samples under MHF and MAX-H conditions.	102
5.36	CF thickness influence on temperature curves.	103
5.37	Visual observation of the AlMg integration effects on demise behaviour under MHF.	103
5.38	Front and back surfaces temperature of FFRP and FFRP+AlMg samples under MHF.	104
5.39	Pre-/post-test cross-section micrographs of the various different laminate samples	105
5.40	Pictures of the recovered samples	106
5.41	Resulting ablation heat calculation of the six composite types tested under the two PWT conditions, MHF and MAX-H.	107

6.1	Debris Risk Assessment and Mitigation Analysis (DRAMA) based ablation model parameters flow chart. Where the colors distinguish the processes implemented in the composite ablation model. The arrows' indices are the input parameters. Image credit: Kuch [20]	113
6.2	Cylinder object model and its derived simulated altitude and heat flux profile during a typical uncontrolled re-entry.	114
6.4	Re-entry Survival and Risk Analysis (SARA) module composite material parameter input window with current CFRP baseline material data displayed. The "0" char reaction rate can be observed at the bottom of the central column.	117
6.5	Experimental-to-model method flow chart	118
6.6	SARA material input window with the experimentally extracted parameter for the HTS45/VTC-401 CFRP. Bottom graphs: fitting results of these parameters with PWT Data from our test campaign with 2 test conditions	120
6.7	SARA material input window with the experimentally extracted parameter for the Amplitex TM (AT)5057/VTC-401 CFRP. Bottom graphs: fitting results of these parameters with PWT Data from our test campaign with 2 test conditions.	121
6.8	SARA material input window with the experimentally extracted parameter for the CF-FF ply-by-ply hybrid composed of HTS45 AT5040/VTC-401 with PWT data from IRS with 2 test conditions.	122
6.9	Comparison of the box's surviving mass made with the 2 CFRP versions.	123
6.10	Comparison of the sphere's surviving mass made with the 2 CFRP versions.	124
6.11	Comparison of the cylinder's surviving mass made with the 2 CFRP versions.	124
6.12	DRAMA model of CS-1 core structural element and internal components. The green box represent the external structure and is modelled as a simple box (named Int in the list of object). And at the bottom, an illustration of the 90 elements assembly, initially modelled within the previous box element.	125
6.13	Representations of the S/C and derived fragments re-entry trajectories (altitude versus ground distance/downrange). Top graph illustrates the integration of metallic fasteners, and where the bottom one either short-CF/PEEK fasteners or aluminium external facesheets.	126
6.14	Comparative overview of the D4D specific criteria resulting from the combination of four sandwich facesheets with three fasteners versions.	127
7.1	Illustration of the space safety and space situational awareness importance on our critical infrastructures.	130
7.2	Illustration of a dual assisted break-up concept implementing the low-temperature demise CF/PEEK bolts releasing a potentially demisable sandwich panel.	131
7.3	Credit: Mike Keefe, Denver Post, 2009	132
A.1	Cut-CF (SMC-HP) and continuous-CF (Nappe) DMA samples dimensions and masses before and after test.	135
A.2	Cut-CF (SMC-HP) and continuous-CF (Nappe) . SRC samples dimensions and masses before and after test. The low mass loss of the cut-CF samples comes from the earlier test termination in comparison to the continuous UD ones, which required a longer test duration to fail.	135
A.3	Top, aluminum sandwich panels samples and Zeiss microscope chamber pictures. Bottom, sample cross-section views in a free-edge and an embedded configurations, using the secondary electron detector.	136

List of Figures

A.4	Aluminum facesheet samples cross-section views from the secondary electron detector, complemented by the EDX results highlighting the carbon, chromium and oxygen atoms. With respectively on top, an ambient stored sample and on the bottom, a hygro-aged sample.	136
A.5	Pictures of the Static Re-entry Chamber (SRC) fully assembled setup before and during a test. . .	137
A.6	Complete data overlay of the front temperatures data recorded from the LP3 pyrometer under Max-H (top) and MHF (bottom) conditions.	138
A.7	Comparative overlay of all front temperature data for CFRP sample type under both MHF and Max-H.	139
A.8	Optical video snapshots of the all the PWT tested samples.	141
A.9	Radar plot manual: listing of the integrated parameters within the 5 indexes of the plots.	142
A.10	Radar plot of the SS and short-CF/PEEK fasteners as function of 5 D4D dedicated indexes.	142
A.11	Radar plot of the 4 skins (+ an extended version of cut-CF) as function of five D4D dedicated indexes.	143
A.12	Corrected version of the SARA built-in CFRP material, with highlighted in red parameters from Kuch [20] work, and realistic values such as a adequate structural resin weight fraction corresponding to a $V_f=55\%$	143

List of Tables

2.1	Shallow controlled re-entry parameters in-situ re-entry data from the following re-entry events: averaged REBR (ATV/HTV), STS-96	14
2.2	Materials tested at IRS within their high fidelity PWT facility. With highlighted in green the demisable ones and in red critical ones based on these test results and recovered debris and under a typical UC re-entry scenario. [21][19]	17
3.1	Bolt samples datasheet characteristics. There is no specific data for short CF/PEEK as it was manufactured on request for the project. Values with an asterisk * come from personal communication from icotec ag.	34
3.2	ESAcamp calculated theoretical stiffness comparisons between selected composite facesheet and the aluminum reference in a sandwich panel configuration with all side clamped and respective length and width of 1031x747 mm. The two references are the ClearSpace (CS)-1 side panel with Honeycomb (HC) thickness=30mm and 16.19mm for the new ref. The comparative stiffness parameter is the 1 st vibration Eigenfrequency (EF), denoted f_1 . All the composite versions are assumed to have the VTC-401 epoxy matrix, and where UHM stands for ultra-high modulus, and C and F – T respectively stands for carbon and flax-twill fibers.	36
3.3	Measured physical characteristics of manufactured composite laminates. The FFRP PWT laminates with an asterisk indicate that a different flax grade was used; refer to the materials section 3. For the layup sequence, F-T means flax twill and C carbon.	39
3.4	Measured physical characteristics of reference and manufactured composite sandwich panels. . .	40
3.5	Overview of the test matrix reporting the testing methods and type of materials tested, with CT = continuous-CF and SH = short-CF.	42
3.6	Vibration test levels characteristics	48
3.7	Water intake measurements of the different sandwich panel versions after 18 days week at 20°C and 95%RH.	49
3.8	Selected test conditions detailed parameters	55
4.1	Summarized tensile and shear test results of the two CF/PEEK versions and the Stainless Steel (SS) bolts, with ρ the density.	62
4.2	Summary of the single loading cycle test results on short-CF/PEEK bolt and nuts for Isopropyl Alcohol (IPA) lubrication effect evaluation	62
4.3	Summarized CF/PEEK thermophysical/demise relevant parameters from TGA testing.	65
4.4	SRC demise parameters summary of SS, continuous (CT) and short (SH) CF/PEEK bolts	67
5.1	AlMg reactive metallic micropowder characteristics	71

List of Tables

5.2	Summarized DMA results, with the storage modulus evaluated at 20°C and the derived comparative specific modulus, in addition to the measured the structural properties degradation onset temperature, $T_{degradationonset}$ and the glass transition, T_g	73
5.3	Summarized DMA relevant properties on continuous-CF and Cut-CF reinforcement types with the 3pt bending test configuration.	75
5.4	Standard outgassing acceptance limits from ECSS-Q-ST-70-02C and results from composite skin materials evaluation. With respectively green and red values, compliant and non-compliant values. (*) High TML outgassing is accepted only under certain conditions: equipment $T < 100^\circ\text{C}$, fast water desorption, no high voltage equipment involved and dry gas purging system can control the water re-absorption.	77
5.5	4-pt bending results with calculated stress, facesheets chord modulus and sandwich stiffness from ASTM-D7249-20 based on load cell and Digital Image Correlation (DIC) measurement.	78
5.6	Measured and computed natural frequencies of the three sandwich panels at the selected modes, and the derived damping ratios.	83
5.7	Extracted kinetic from a Coats-Redfern method parameters for virgin and filler matrix system (epoxy vs blend), in addition to the composites CFRP and FFRP.	87
5.8	Physical characteristics of the tested samples under PWT conditions.	106
6.1	Initial orbital parameters of the object to extract the aerothermal load profile for model comparison.	114
6.2	DRAMA parameters' adequate names and units.	116
6.3	List of 1D ablation demise model input parameters related their respective experimental evaluation techniques.	119
6.4	SARA built-in versus experimental CFRP sensitivity analysis results.	123
6.5	Combination evaluation matrix and the selected trigger temperature, based on the lowest of the two combination.	126
A.1	Datasheet sandwich panel facesheet material characteristics, with composite versions integrating the VTC-401 epoxy. The equivalent mechanical properties were computed with ESAcomp. $L T z$ respectively stands for longitudinal, transversal and through-thickness directions. Values indicated with * are not available for confidentiality purposes.	134
A.2	Overview of the D4D specific criteria resulting from the combination of four sandwich facesheets with three fasteners versions. The built-in CFRP is in orange to highlight the danger of using such material resulting in non-conservative criteria as it is poorly described, with unrealistic and missing parameters.	144

Glossary

IRS Institut für Raumfahrtssysteme Stuttgart

LPAC Laboratory for Processing of Advanced Composites

ADR Active Debris Removal

ASAT Anti Satellite

AT AmplitexTM

BC Ballistic Coefficient

CAD Computer-Aided Design

CAS Collision Avoidance System

CF Carbon Fiber

CFRP Carbon Fiber Reinforced Polymer

CF-FFBP Carbon-Flax Fibers ply-by-ply

CF-FFTBT Carbon-Flax Fibers two-by-two

CMA Charring Material Ablating model

COPV Composite Overwrapped Pressure Vessel

COTS Commercial-off-the-shelf

CS ClearSpace

CTE Coefficient of Thermal Expansion

CVCM Collected Volatile Condensable Material

DIC Digital Image Correlation

DIVE Demise Verification Guidelines

D4D Design-for-Demise

DLR Deutsches Zentrum für Luft- und Raumfahrt

DMA Dynamic Mechanical Analysis

DTG Differential Thermogravimetry

DRAMA Debris Risk Assessment and Mitigation Analysis

EDX Energy-dispersive X-ray spectroscopy

EF Eigenfrequency

EOL End-of-Life

EM Electromagnetic

EPFL École Polytechnique Fédérale de Lausanne

ESA European Space Agency

FEA Finite Element Analysis

FF Flax Fiber

FFRP Flax Fiber Reinforced Polymer

List of Tables

FRF Frequency Response Function

FRP Fiber Reinforced Polymer

FPA Flight Path Angle

GEO Geostationary Orbit

HC Honeycomb

HL High Level

HR Heating Rate

ILSS Interlaminar Shear Strength

IPA Isopropyl Alcohol

IRS Institut für Raumfahrtssysteme

LCA Life Cycle Assessment

LEO Low Earth Orbit

LFA Laser Flash Analysis

LL Low Level

MAX-H High Heat Flux

MC Monte-Carlo

MHF Medium Heat Flux

MMOD Micrometeoroids and Orbital Debris

NPI Networking Partnering Initiative

PBP ply-by-ply

PEEK Polyetheretherketone

PVB Polyvinyl-butyril

PWT Plasma Wind Tunnel

QI Quasi-Isotropic

REBR-W Re-Entry Break-up Recorder-Wireless

RML Recovered Mass Loss

S/C Spacecraft

SARA Re-entry Survival and Risk Analysis

SADM Solar Array Drive Mechanism

SEM Scanning Electron Microscopy

SMA Shape Memory Alloy

SRC Static Re-entry Chamber

STS-96 Space Shuttle Mission 96

SS Stainless Steel

TBT tow-by-tow

TC Thermocouple

TGA Thermogravimetric Analysis

TML Total Mass Loss

TP Thermoplastic

TRL Technology Readiness Level

TS Thermoset

UC Uncontrolled

UD Unidirectional

UTM Universal Tensile Machine

UTS Ultimate Tensile Strength

USS Ultimate Shear Strength

WVR Water Vapour Regain

XPCI X-ray Phase Contrast imaging

1 Introduction & Research motivation

1.1 What is the matter with space debris ?

Space can be seen as an infinitely vast and empty environment, and it is the case for most of it, but since few decades the near-Earth orbit region can no longer be identified as such. Today more than 36'500 cataloged elements including operating satellites, rocket bodies, defunct satellites, and mission-related components (covers, adaptors) occupy the large dimensions spectrum in the order of meters to 10 centimetres. An illustration of 22'000 from these tractable objects in mid January 2024 is displayed in figure 1.1. In the lower end of the spectrum, fragmentation debris and surface degradation components are smaller than 10 cm. About one million debris are within the range between 10-1 cm and 130 million between 1 cm to 1 mm. These space debris, representing all human-made non-operative objects orbiting or reentering the Earth's atmosphere, mostly result from Anti Satellite (ASAT) military tests (kinetic killing), on-orbit break-ups (explosion), and collisions. They are principally present in the Low Earth Orbit (LEO) and Geostationary Orbit (GEO) protected regions where most of the operational satellites are located. [22] [23]

Following the actual orbital launch trend, these figures are not declining. Since the beginning of the year 2024 (24 days), already 104 satellites from 14 launches were placed in Earth orbit. Last year an unprecedented average rate of 15 launches and 200 satellites per month was achieved, a **200%** increase since the start of the present work in January 2020! [24]

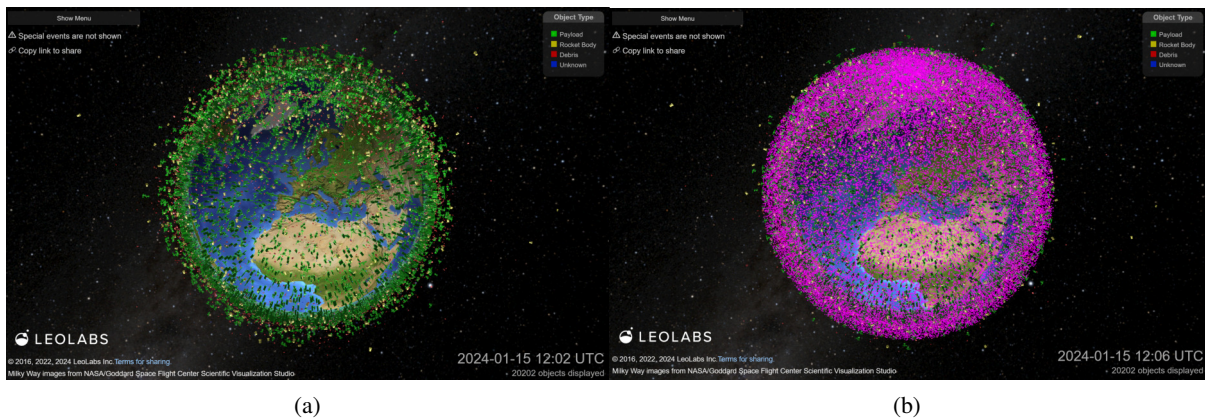


Figure 1.1: Leolabs Low Earth orbit visualization of the ground-tracked orbiting objects size (a) larger than 10cm and (b) ranging between 2-10 cm. [23]

With currently no Active Debris Removal (ADR) operating system, the inoperative satellites representing around 22% out of 11'500 currently functioning ones are therefore acting as flying mines with catastrophic potential on the orbital infrastructure and space sustainability. [25]

And as “what goes up, must come down”, we are imposing on ourselves and the future generations a direct threat. A global ground casualty risk problem arises due to spacecraft components designed to resist re-entry, coupled with a chosen Uncontrolled (UC) post-mission disposal method, or unintentional uncontrolled re-entry.

LEO satellites have a designed functioning life expectancy ranging from 6 months to 10 years and most of them are not equipped with controlled re-entry thrust capabilities; therefore they plan on performing uncontrolled reentries. Such manoeuvre should happen less than 25 or 5 years after orbital mission

1.1 What is the matter with space debris ?

termination, where the second recently updated lifetime limit of 5 years was set as a recommendation (and internal policy) from ESA and several national space agencies, concerning only missions past 2023. This will consequently raise the uncontrolled re-entry events in the coming years, passing from less than one hundred to several hundreds or even thousands per month. Such unsustainable approach will inevitably lead to catastrophic ground impacts if critical parts survive re-entry, due to the past and still current low integration of design for demise concepts, in addition to non-binding regulations [26] [27]. Such an issue is not geographically specific as it can be observed in figure 1.2, where all the continents and seas are impacted in reality (a) and in theory (b).

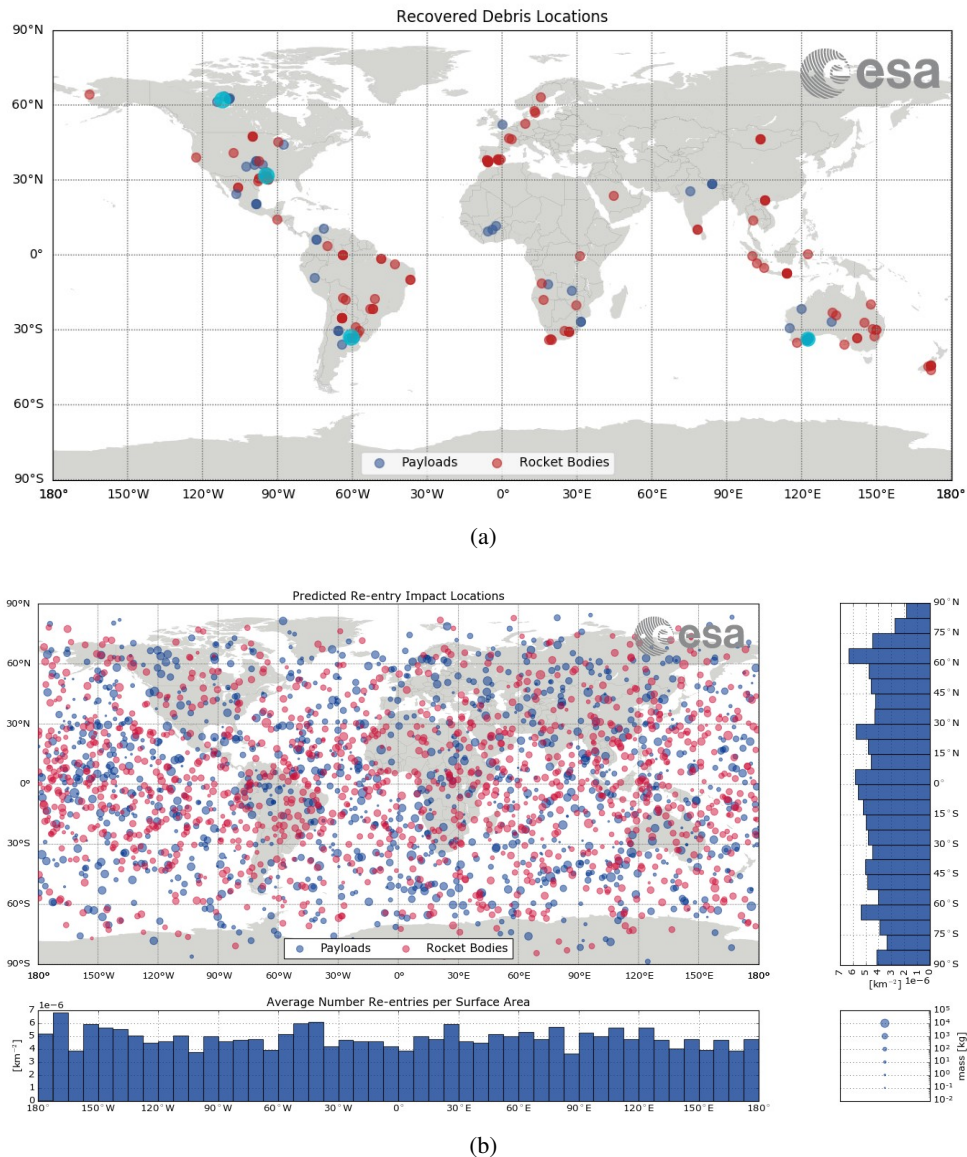


Figure 1.2: (a) Recovered space debris impact locations versus (b) predicted events, based on a November 2016 analysis.[1]

The indirect threat of space debris to several critical infrastructures is real and irremediable in the short term and possibly in the long term with our current space debris mitigation/remediation technologies. The concerned strategical infrastructures are communication, navigation (GNSS), sensitive position monitoring, weather forecast and at larger scale Earth monitoring. With a severe disruption of the space infrastructure, direct and long-term issues could place any country in delicate situations or even in an emergency state

with a drastic reduction of the population safety level. Extreme perturbations in the transport system, shortage in essential imported supplies (such as food and energy), delays in emergency response time, unalerted significant landslides are some examples of effects derived from such events. [28]

Following the recent international space debris focused events (European Space Agency 8th space debris conference [29], the Second International Orbital Debris Conference (IOC II) [30] and EPFL IRGC space debris collision risks governance workshop [27] are some examples), a clear lack of coordination between the scientific institutions and the industry, in addition to a limited political willingness to act, have been identified regarding the update and application of stricter regulations, hard-laws and/or binding instruments. The origins of such inadequacies are multiple, from differences of conception about shared space to low liability risk management, but the insufficient situation awareness of the wide-ranging actors is a key point. This issue is linked to the scarce data on cost evaluation of satellite damage/disruption and space debris population, especially for small-range objects. This situation leads to a general under-evaluation of such risk. It induces slow space debris remediation efforts, in addition to preventing an accurate representation of the overall environmental situation and discrediting the support of stricter regulations/law and their enforceability [31]. In summary, we are aware of space debris populations and their derived risks on operational satellites but we are missing precision on how much, where it is distributed and how it is evolving. Thus, we need direct actions to mitigate the risks at the source, and to acquire more data to analyse the situation and the effectiveness of future measures.

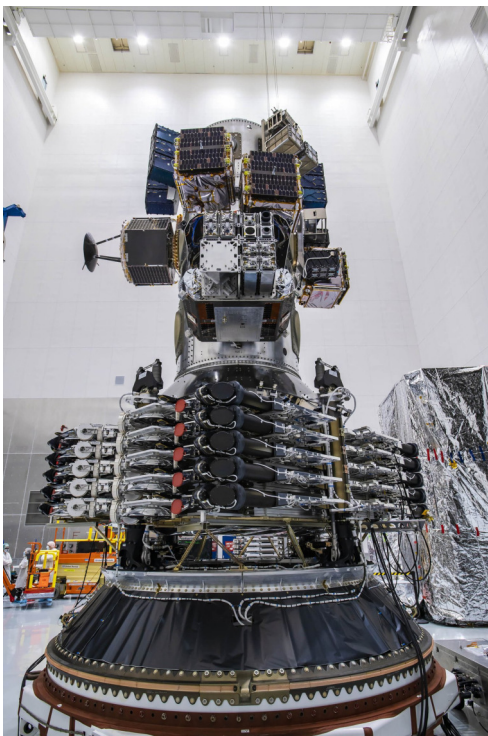


Figure 1.3: Record stacking of 143 satellites in a Falcon 9 payload bay.[2]

are a direct threat and already induced ground casualties. The re-entry event numbers trend is going to follow the current exponential numbers of orbital objects with a delay of a few years (4-8 years) as reported by the ESA's Space Debris Office statistics presented in figure 1.4 [34]. In graph (b) the predicted re-entering objects type are presented, with UI-unidentified elements, PM/RM-respectively payload and

On the positive side, the dynamic Earth atmosphere and solar radiation pressure are helping us by respectively dragging and pushing the debris down in the atmosphere where they can disintegrate in a reasonable time, such as less than the 5 years to comply with recently published ESA space debris mitigation policy and requirements [32][33]. For long orbital lifetime objects, specific requirements were developed to reduce this lifetime or clear them out of the protected LEO and GEO regions. This is achieved by implementation of Collision Avoidance System (CAS), their passivation at their End-of-Life (EOL) and clearance of the protected region either by re- or de-orbiting. In the case of a passive de-orbit (uncontrolled), a casualty risk lower than $1:10^7$ needs to be assured.

This leads us to the ground-impact threat issue. It is the less-known but nonetheless critical second face of the double-head axe of space debris. It is induced by the combination of the current use of re-entry resistant materials for the sake of high durability S/C designs, and an uncontrolled re-entry, leading to a global threat all over the planet. These events are characterized by sky-falling pieces, ranging from a few cm to several meters as illustrated in the figure 1.5, which

1.2 Spacecraft structure challenges imposed by falling debris

rocket elements released intentionally for the mission, PD/RD-respectively payload and rocket debris from accidental release, PF/RF-respectively payload and rocket fragments from explosion/collisions, RB-rocket bodies, PL-payload (satellite, probe).

Thus, with the current exponential launch trend, an inevitable continuous artificial shooting stars show is forecast for the incoming years.

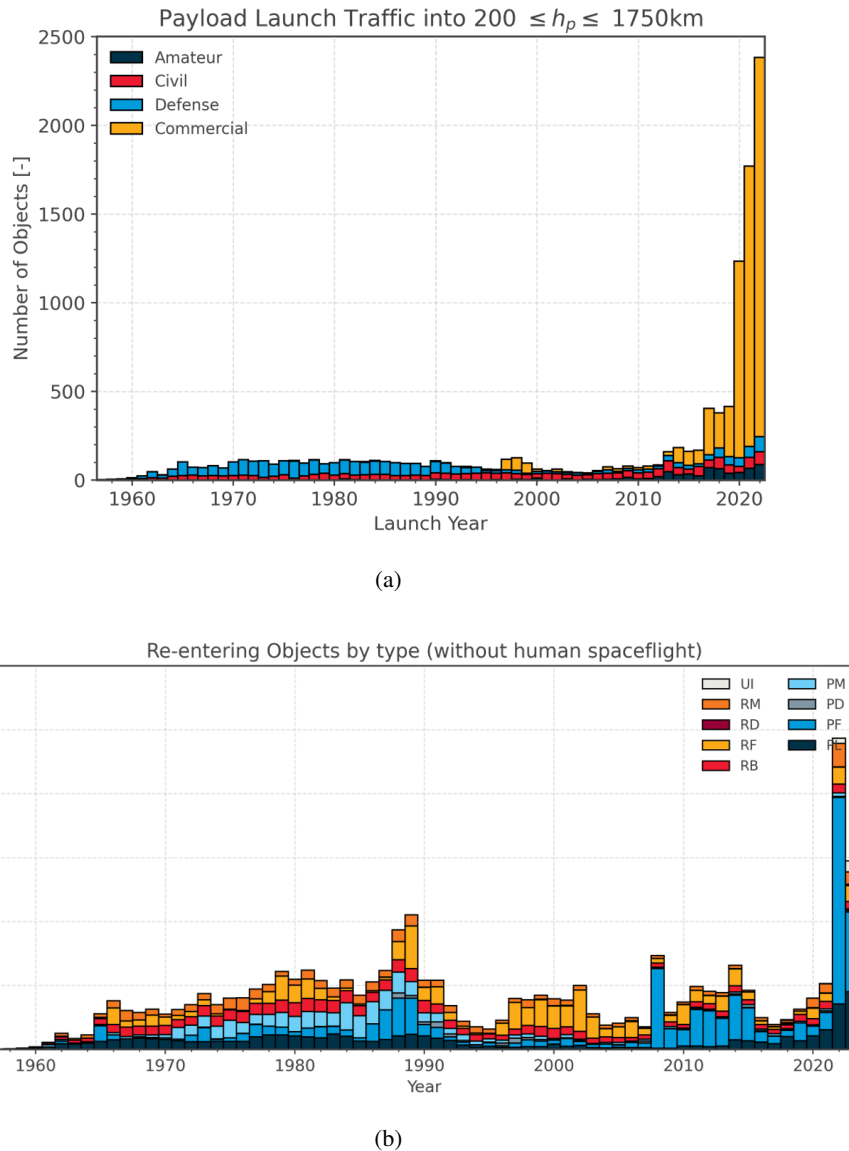


Figure 1.4: Yearly cumulative graph of (a) newly launched objects in LEO and (b) re-entry events. [34]

1.2 Spacecraft structure challenges imposed by falling debris

Spacecraft re-entry is a critical phase in the lifecycle of any space mission. One of the significant challenges derived from this phase is the survival of certain fragments or debris post re-entry. These surviving fragments pose potential threats to both aerial and terrestrial environments. Their survivability is primarily attributed to their material, geometry and location within the spacecraft. Materials with high melting points, such as titanium and stainless steel, are more likely to survive the intense heat and pressure during re-entry. Similarly, larger fragments have a lower surface-to-volume ratio, which allows them to

endure the re-entry environment better. Fragments located at the center of the spacecraft are often shielded from the aerothermal flux by the primary or secondary structural elements, thus increasing their chances of survival.

D4D approaches prioritize the creation of spacecraft structures that aim for a complete demise during re-entry, mitigating the risks associated with surviving fragments. One of the key strategies for implementing D4D is to find ways to ‘open’ the external structure of the spacecraft as early as possible during re-entry. This approach allows the thermal flux to reach the core of the spacecraft quickly. Various techniques, such as using break-up devices or "weak" assembly elements, can be employed to achieve this. This approach requires innovative engineering solutions to balance structural integrity during mission phases with the imperative of ensuring rapid demise during re-entry. Understanding the composition and assembly techniques of spacecraft structures is crucial for implementing D4D effectively.

The main S/C structural components, view as the box walls, often include sandwich panels and monolithic structural support and connection elements. Currently, demisable structural composite materials are not available for the space sector, where only the well-known re-entry-resistant continuous fibre CFRP option is used, for its specific properties, and good resistance in the space environment. In addition, precise material requirements and related testing methods to assess demisability are not yet fully defined due to the multifactorial complex break-up sequences and demise behaviours.

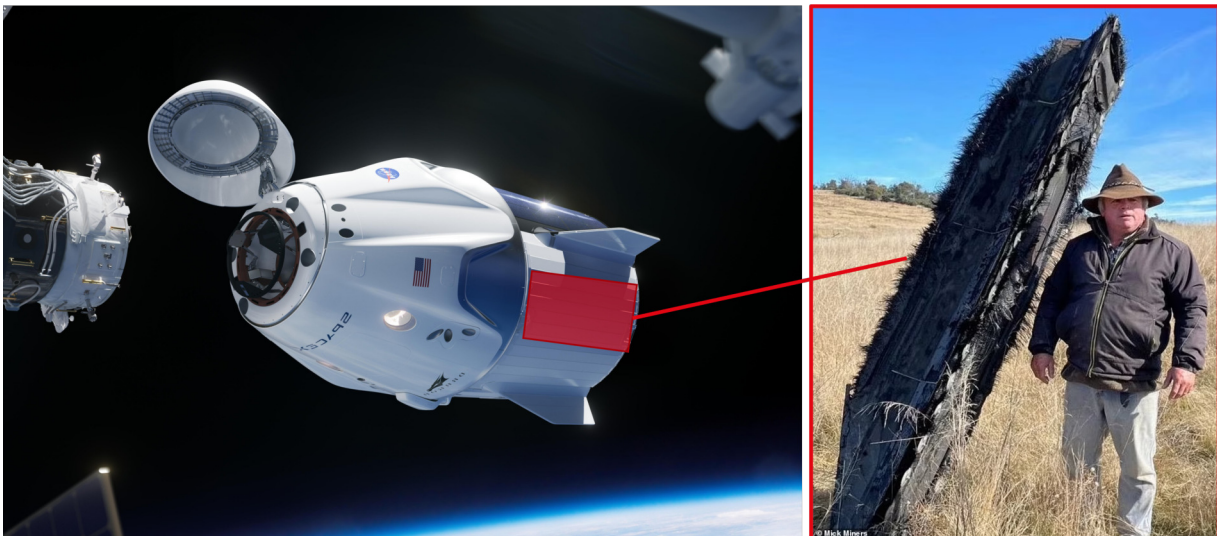


Figure 1.5: Recovery of a massive space debris in Australia in August 2022, image credits: Mike Mayers [3]. It is mainly composed of CFRP sandwich panels and was identified to be part of the SpaceX Crew-1 dragon module's trunk highlighted in red in the right image and jettisoned before its re-entry in May 2021, image credit: SpaceX [4]

1.3 Thesis framework

Existing strategies for mitigating space debris are insufficient to ensure a sustainable space environment. In response to this challenge, the European Space Agency (ESA) has recently introduced its Zero Debris approach, as outlined in Agenda 2025. This initiative is geared towards significantly reducing the generation of debris in Earth and lunar orbits by 2030 across all of ESA's future missions, programs, and activities, in addition to secure technologies towards safe and sustainable End-of-Life (EOL) management. These are core missions of ESA's Clean Space Office, where the work topics are highlighted in the following figure 1.6.

ESA has thus recently updated their Space Debris Mitigation Policy and Requirements applicable to its missions [32] [33]. However, recognizing that space is a globally shared resource, ESA acknowledges that its efforts alone are not adequate. To encourage others to adopt a similar commitment, ESA has facilitated the development of the Zero Debris Charter. It is pushing for a collaborative effort involving over 40 diverse stakeholders from the space sector to collectively aspire to reach a Zero Debris environment.

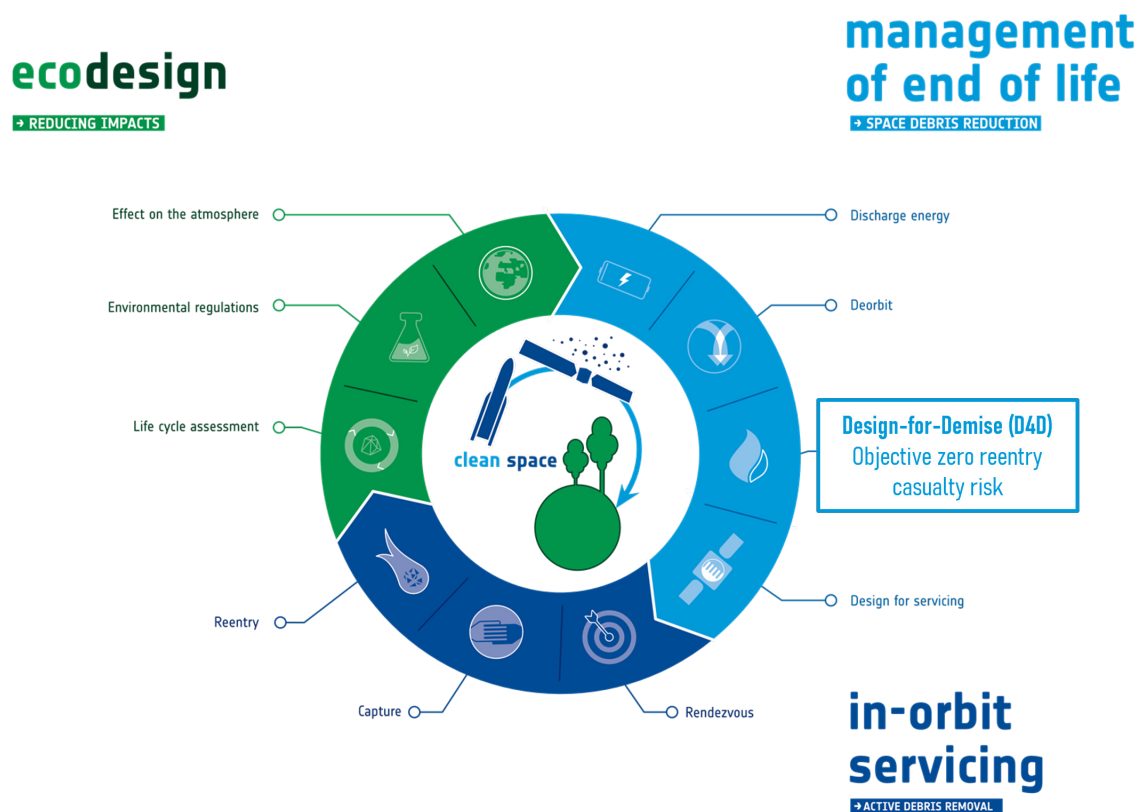


Figure 1.6: Highlight of the D4D approach within CleanSpace Initiative - ESA's objective Zero Debris by 2030. [5]

Achieving complete disintegration during re-entry is possible through the implementation of the Design-for-Demise (D4D) approach in mission conception. This involves early design planning of the spacecraft in a manner that ensures its intentional and as early as possible disintegration upon re-entry into the Earth's atmosphere.

D4D methods can be classified into two categories, depending on whether they affect the entire spacecraft (system level) or focus on specific equipment (equipment level). The evaluation of D4D technologies can be performed through computational tools, on-ground facility testing, and re-entry flight experiments. Computational tools aim to capture the physical processes happening during re-entry, relying heavily on the thermal properties of commonly used materials. On-ground facility tests seek to recreate aerothermomechanical phenomena experienced during re-entry, providing correlation data for the demise models. While these methods complement each other, there still exist significant gaps and approximations that warrant further understanding. Continuous efforts are required to bridge these gaps and enhance the precision of D4D methodologies for more effective spacecraft design and controlled disintegration during re-entry.

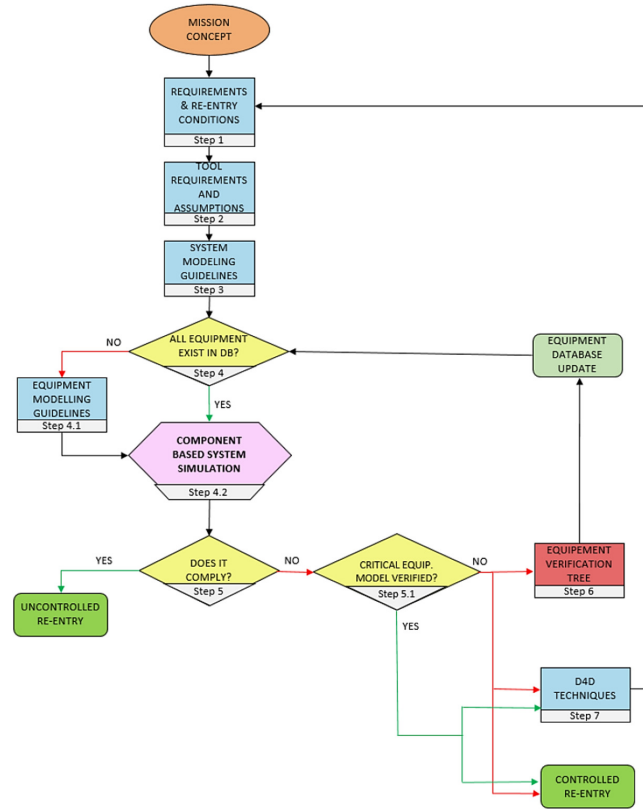


Figure 1.7: DIVE document verification procedure flow chart for the implementation of new systems related to re-entry risk criticality following the recommended D4D approaches. [6]

The Ariadne’s thread of this thesis is thus to identify, test, and model new composite materials combinations that are optimally designed to demise during re-entry while maintaining the typical space mission qualifications such as structural requirements and low outgassing.

A composite sandwich structure, together with its attachment to a space structure was identified as a realistic case for the benchmark design towards S/C demisability improvement, since not only the material should possibly desintegrate upon reentry, but also the attachment so as to allow early detachment of the panels and better disintegration.

From this baseline, the research aims to confront the main question established as:

How can we tackle future space debris and decommissioned Spacecraft (S/C) re-entry casualty risk with the development of highly demisable composite structure panels and fasteners?

The global plan of attack of this research was constructed from two interconnected pillars performed in close collaboration with the project partners. The main one was based on the selection and development of adapted material solutions, together with the development of realistic testing methods that simulate the re-entry condition to be able to screen materials. A second aspect focuses on the improvement of composite materials re-entry response model for demisability, and the derived ground casualty risk analysis.

The overall objective can be articulated as the maximization of the S/C overall disintegration upon Earth orbital re-entry through material substitution applied to the external structural panels. It is achieved by promoting their early opening and/or demise to expose the internal components to the destructive re-entry environment. This approach aims to minimize the external panels aerothermal shielding effects during

re-entry. The ideal objective is a "zero" casualty risk mission, meaning a total ablation of the components down to negligible dimensions/mass during re-entry, which should lead to less than 15 Joules ground impact energy following ESA's space debris requirements. [35]

Such mitigation approach is a core strategy of Design-for-Demise (D4D), which aims to modify a spacecraft material selection and design process to achieve the safest destructive re-entry possible by material substitution, specific geometries, or dedicated subsystems. Unfortunately, this concept is still quite novel and suffers from a lack of in-situ re-entry heat flux profiles and fragmentation data, which are essential to build complete and realistic re-entry models at the equipment and material level, but also to validate the ground testing parameters. The materials response to this environment, especially for composite elements such as Fiber Reinforced Polymer (FRP) skins for sandwich panels, is oversimplified and highly depends on their macro- and micro-structure. These gaps are recognized by the different space agencies, which have launched multiple dedicated projects during these last 5 years, such as *COMP2DEM* from which the first public data were presented last October 2023 at the Clean Space Industry Days. These activities data and methodologies are gathered in databases such as ESTIMATE [1], and additionally lead to more standardized analysis and testing guidelines. ESA's Demise Verification Guidelines (DIVE) document is a good example, where multi-level guidelines allow a complete overview of the demisability objectives. It continuously gathers analysis and testing guidelines for demise studies at system, equipment and material levels.[6]

In the following sections, after a review of the current state of the art, followed by materials and methods, the three main chapters will be exposed, with (I) Demisable CF/PEEK bolt fastening system. (II) Composite reinforcement hybridization and metallic filler mitigation to re-entry demise resistance of S/C external structure, and (III) Critical assessment of DRAMA-SARA tool and experimental correlation method.

In term of research support and collaboration, this project topic was launched by eSpace and Laboratory for Processing of Advanced Composites (LPAC) as a Networking Partnering Initiative (NPI) with European Space Agency (ESA) which aims to support state-of-the-art technologies that are pertinent to future sustainable space operations. Six industrial and institutional partners embarked on this space and material engineering adventure.

This group was composed of ClearSpace SA, Institut für Raumfahrtssysteme (IRS), Belstead Research Ltd., Beyond Gravity (previously RUAG Space SA), icotec ag and Bcomp Ltd. They supported this study to encourage the development of the technologies each contributing their respective expertise. The EPFL spin-off ClearSpace, has received in December 2019 the lead by ESA to build the first active debris removal mission named ClearSpace-1. The IRS has the rare expertise in the re-entry conditions testing with their several Plasma Wind Tunnel (PWT) facilities, Belstead Research is specialized in simulation of these extreme conditions, Beyond Gravity is an international company working on multiple aspects of the space technology industry, icotec ag is a company specialized in complex parts made by composite flow moulding process and Bcomp is a firm working on natural fibre based high performance composites.



Figure 1.8: Illustration of ClearSpace-1 (CS-1) chaser approaching VESPA debris for its capture.[7]

2 State of the Art

This chapter reviews the current status of research in the fields relevant to the thesis background. As a result, a first part will review what is known about the environmental conditions during atmospheric re-entry, so as to identify the thermo-physico-mechanical loads experienced by the material and structure. This leads to the identification of the state of the art on demise criteria and how to measure/quantify these, with particular emphasis on composite materials. The following part reviews the design for demise approach as applied to structures, joints and materials. Modelling activities to predict the break-up and disintegration of structures and materials are then introduced. Finally, the thesis objectives, filling the research gaps identified in the literature, and methodology, close this chapter.

2.1 Atmospheric re-entry environmental conditions

Since the early days of manned space exploration, getting back safely from space has been the top priority. A lot of work has gone into designing space vehicles and probes that can handle re-entry. To do this, we had to understand and replicate the conditions objects face during their return through the atmosphere. This involves gathering data on the re-entry environment based on different flight paths.

Depending on an object's altitude, velocity, shape, and materials combination, the aerothermomechanical loads initiated from the initial kinetic and potential energy lead to various combined effects, with a common basic principle based on the atmospheric composition as a function of altitude, leading to progressive heating of the object, as well as tumbling effects. Basic conditions of an uncontrolled re-entry are summarized in figure 2.1. Studying atmospheric re-entry has been an ongoing effort, evolving from analyzing recovered capsules and space debris on earth to real-time monitoring of re-entering vehicles and in-situ measurement techniques. However, these methods often rely on complex missions, expensive equipment, or rare events. [36][37]

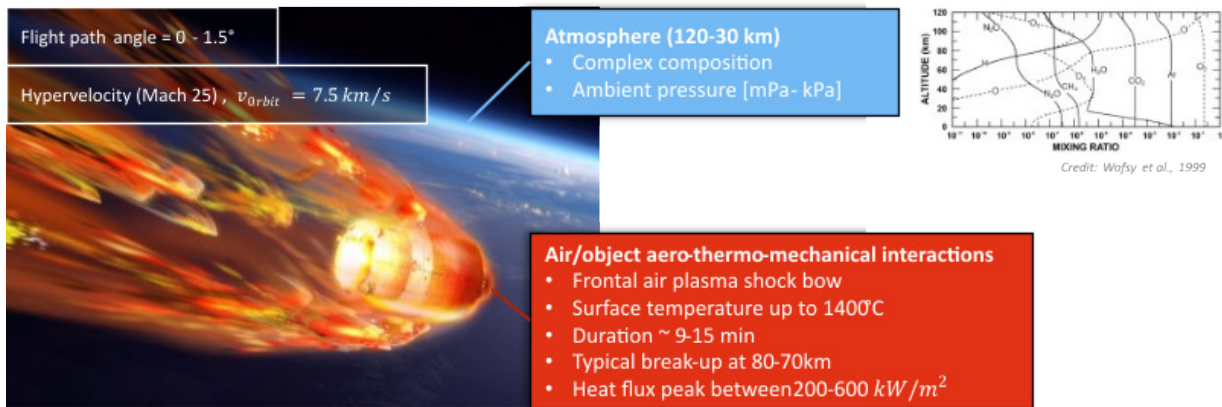


Figure 2.1: Illustration of an uncontrolled re-entry and the associated key environmental parameters leading to demise process under the destructive conditions [8] [9]. Re-entry illustration credit to ESA-Multimedia [1]

2.1.1 Re-entry event observation and in-situ data recording

The comprehensive observation of selected and precisely forecasted re-entry events, whether conducted from the ground or in the air, employs a diverse array of instruments. These instruments encompass RADAR, multispectral high-resolution cameras capable of capturing a broad spectrum from near-infrared to ultraviolet, and sophisticated spectrographs. This multi-instrumental approach serves to enhance our understanding of the intricate processes involved in re-entry, an example of such re-entry fragmentation is provided in figure 2.2. [10][38]

In-situ monitoring techniques stand as the pinnacle of data acquisition capabilities. This advanced approach entails installing dedicated monitoring equipment on a re-entry-capable vehicle, such as the space shuttle, or within a re-entry-resistant capsule. The typical on-board equipment includes Low/High-G accelerometers, gyroscopes, internal pressure sensors, GPS receivers, and temperature sensors (thermocouples). These instruments enable an in-depth study of the breakup sequence, with pressure variations, temperature rises, or significant accelerations serving as key indicators. So far, only a handful of missions have successfully achieved hard data recovery using this method.

A list of such missions include the OREX mission by JAXA in 1994, ESA's ARD experiment in 1998, STS-96 (Space Shuttle Discovery) in 1999, and ATV1-5 re-entries from 2008 to 2015, equipped with REBR capsules illustrated in figure 2.3 [36][37][12]. While most of these missions were embarked on a large spacecraft, monitoring primarily controlled re-entry conditions, some involved a shallow flight path angle trajectory, therefore experiencing conditions closely equivalent to uncontrolled re-entry cases. Table 2.1 provides data for two cases illustrating this scenario.

The Cygnus OA6 destructive shallow re-entry observation campaign in 2016 illustrates one of such shallow re-entry mission. To illustrate the critical need for data in this field, the activity combined airborne observation, depicted in figure 2.2, with an in-situ re-entry monitoring system encapsulated in the Re-Entry Break-up Recorder-Wireless (REBR-W) capsule from Aerospace Corp. Unfortunately, the mission encountered setbacks as no data were transmitted to the Iridium intermediary satellite. This issue was attributed to problems such as battery malfunction, radiation interference, or a critical shock incident involving the capsule [10].

The latest mission on this topic, which unfortunately turned as a failure, was the Von Karman Institute 3U CubeSat demonstrator, QARMAN (QubeSat for Aerothermodynamic Research and Measurements on Ablation). It was injected into LEO from the ISS in January 2020. Its sole mission purpose was to record uncontrolled reentry condition data with a novel cork front heat shield. Unfortunately, the contact was lost during its descent into Earth's atmosphere as it went down much slower than planned due to lower-than-anticipated solar activity, and the predicted orbital lifetime of 4 months ended as a 2 year long free flight [39].

A noteworthy upcoming mission planned to be launched in 2027, DRACO, short for Destructive Re-entry Assessment Container Object, aims to demonstrate D4D technologies. It is planned to have a short orbital lifetime as a dummy satellite, integrating various dedicated recording systems to monitor the demise/break-up process. Further details about this mission are available in the presentation by Elconor-Deimos [40].



Figure 2.2: Cygnus OA6 re-entry fragmentation picture taken from the dedicated observation aircraft.[10]. Spacecraft image credit: NASA [11].

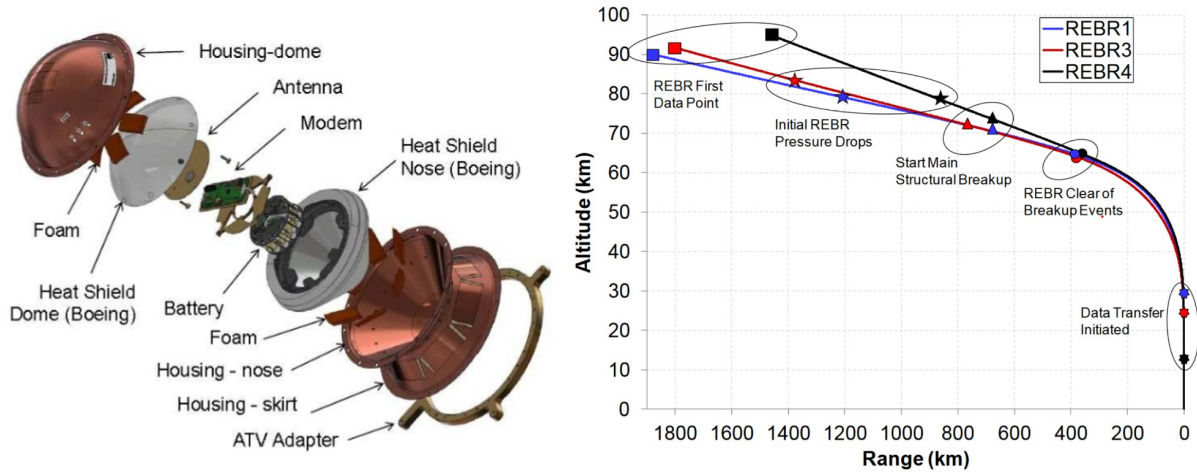


Figure 2.3: Exploded view of the Re-Entry Break-up Recorder (REBR) capsule and the recovered data of different HTV and ATV cargo re-entries.[12]

By analyzing re-entry events, researchers gain valuable insights into the fragmentation phenomenology, heating conditions experienced by the re-entering object, and the ability to identify different components through the analysis of demise reactions emission lines for example. This methodological synergy not only provides a detailed understanding of the re-entry process but also contributes significantly to advancing our knowledge of atmospheric entry dynamics.[36]

Table 2.1: Shallow controlled re-entry parameters in-situ re-entry data from the following re-entry events: averaged REBR (ATV/HTV), STS-96

Re-entry object	ATV/HTV REBR, 1,3,4 [12][41]	STS-96 [42][43][44] [45]
Re-entry initial velocity (Alt>120km) [km/s]	7.6	7.8
Flight-path-angle [°]	-1.5	-1.2
Attitude	Tumbling	Fully controlled
Maximum monitored temperature [°C]	1550	1150
Peak stganation point heat flux [kW/m ²]	850* (*reconstructed)	450

2.1.2 Recovered space debris analysis

The recovery of ground-impacted space debris, as illustrated in figure 2.4, underscores the re-entry resistant nature of certain components. An intriguing example is the retrieval of an "intact" stainless steel tank, weighing approximately 250kg and measuring close to 2 m in length, from a Delta-II second stage rocket found in the Texas desert. This discovery is part of the 166 objects recovered since 1962, with the ESOC branch of ESA establishing a comprehensive database and conducting technical post-flight analysis on these debris [1]. The material characterization of these metallic pieces, including microstructural analysis, crystallography, and composition analysis, provides valuable insights into the experienced conditions by comparing them with their initial states [13]. For instance, an investigation into recovered silica-phenolic composite thrust chambers, stainless steel, and titanium tanks from a Delta-II rocket case study revealed re-entry velocities ranging between 7.4 and 7.9 km/s, shallow flight-path angles (Flight Path Angle (FPA)) between -0.09 and -0.26°, a minimum apogee of 127 km, and a maximum experienced temperature around 1280°C [13][46].

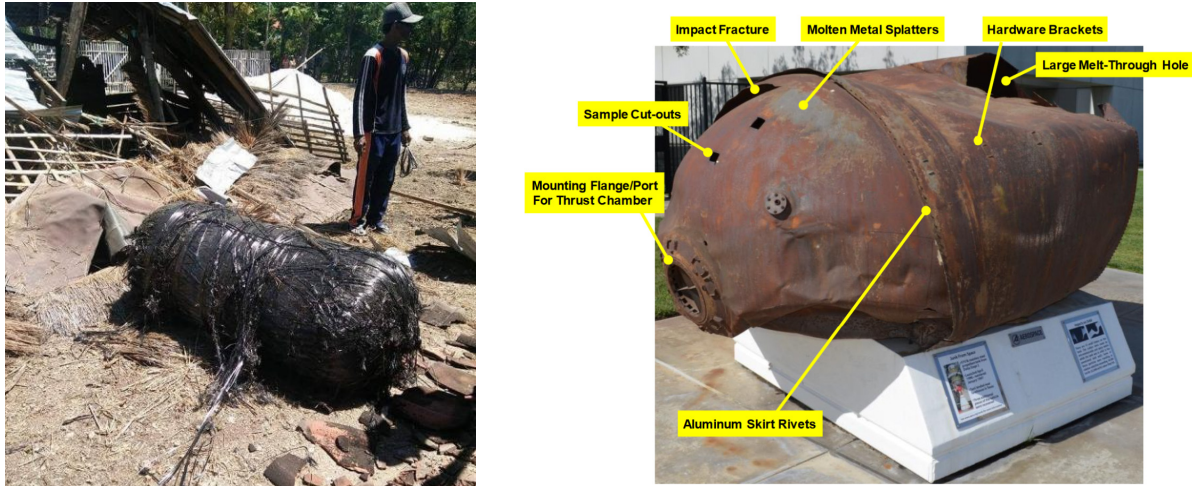


Figure 2.4: On the left, a relatively intact carbon fiber/titanium Composite Overwrapped Pressure Vessel (COPV) tank, recovered in Indonesia in 2016. On the right, a Delta II 2nd stage tank recovered in Texas in 1997 (length =1.75m).[1] [13]

2.1.3 Experienced re-entry conditions

As illustrated in the initial figure of this chapter, 2.1, the demise process occurs in the thermo- and mesosphere between 120km-30 km altitude region where progressive aerothermodynamic interactions are taking place. Main break-ups have been reported to happen around an altitude of 80 km [37][45][6]. The conditions experienced by the reentering object strongly depend on its BC, FPA and attitude (tumbling or fixed). For example, based on work of Beck et al. [9], the relevant heat flux can pass from $2000 \text{ kW}/\text{m}^2$ in the case of a fixed orientation demise, up to $500 \text{ kW}/\text{m}^2$ in the case of a tumbling S/C and even $100 \text{ kW}/\text{m}^2$ during its fragmentation due to the high aerothermal breaking and break-up induced lower BC. The important demise-related re-entry parameters, such as the Flight Path Angle (FPA), aerothermomechanical effect window, S/C attitude and experienced heat flux strongly depend on the type of de-orbiting strategy, uncontrolled, controlled or semi-controlled. This last option, also named assisted-reentry, is a recently validated method from Aeolus spacecraft successful semi-controlled re-entry and demise above the south of the Atlantic Ocean. With a significantly lower impact on the S/C initial conception than controlled, such EOL de-orbiting method involves selectively influencing the descent trajectory directly via low-power thrusters and/or by playing with the atmospheric drag by "simply" orienting the spacecraft along its trajectory. It aims to optimize safety, landing locations, and mission objectives. [47][48]

An uncontrolled re-entry results in a shallow trajectory, prolonging the high interaction flight phase and encouraging heat storage, leading to a larger footprint of ground fragments. Typical parameters in this scenario include a flight-path angle (FPA) shallower than -2° and an interaction window of around 10 minutes, aligning with Soyuz, Gemini, and STS missions that reenter with similar parameters and provide valuable in-situ data and studies. The tumbling averaged heat flux is typically in the range of $100\text{-}520 \text{ kW}/\text{m}^2$ according to the studies of Pagan et al. [49] and Beck et al. [9].

Now during a controlled re-entry, the spacecraft is steeply precipitated into the atmosphere (typically $\text{FPA} > 2^\circ$) to confine all fragments within a selected disposal area. This results in a more aggressive environment with heat fluxes reaching several MW/m^2 , leading to a higher surface temperature but for a shorter time, with interaction windows usually between 5 to 7 minutes [50]. This controlled approach prevents excessive heat soak, as opposed to the shallow (uncontrolled) re-entry where heat has time to

diffuse further inside the spacecraft. Opting for a controlled de-orbit maneuver ensures minimal casualty risk, as it aims to target an unpopulated region of the globe, usually the South Pacific Ocean Uninhabited Area (SPOUA) also named the spacecraft cemetery, and is therefore not of interest in terms of casualty risk and design-for-demise conception approach. But this EOL option critically relies on the main systems to function until its last moments.

2.1.4 On-ground re-entry condition reproduction

The reproduction of re-entry conditions on-ground is extensively complex, as it requires the combination of various pieces of equipment, usually costly and highly demanding in terms of maintenance due to the extreme cyclic running conditions. But they are a necessary step to perform materials screening and demise capability assessment. An illustration of the various testing methods related to the demisability characterization can be observed in figure 2.5. So far, two categories of high-fidelity experiments have been developed, based on either a static or a dynamic heat flow. In the first case, a static re-entry simulation chamber (SRC) is used in which the pressure, temperature loads, and optionally mechanical ones, are set according to the case study. This is used to investigate the thermophysical/-mechanical response of materials under typical atmospheric conditions. It is important for early-stage materials selection as it is usually smaller, easier to operate and less costly equipment than the dynamic environment testing approach. In addition, it presents the valuable advantage of allowing transient environmental conditions within a single test run such as experienced during a real re-entry [22][51]. To date only Aerospace & Advanced Composites GmbH (AAC) in Austria has such facility available to the public. [52]

The dynamic experiment is performed with a PWT setup also named plasmotron, where high enthalpy plasma gas flow is projected onto the sample, simulating the aerothermodynamic loads within preselected testing conditions. The aero-thermodynamic response of a material, an assembly or an equipment can thus be evaluated under high-fidelity steady-state conditions. The demise characterization through this method requires several runs under specifically correlated test conditions to recreate point by point (discretely) the real re-entry trajectory conditions. Today Europe has four center with PWT facilities, IRS in Stuttgart (Germany), VKI in Bruxelles (Belgium), DLR in Cologne (Germany) and CIRA in Caserte (Italy).

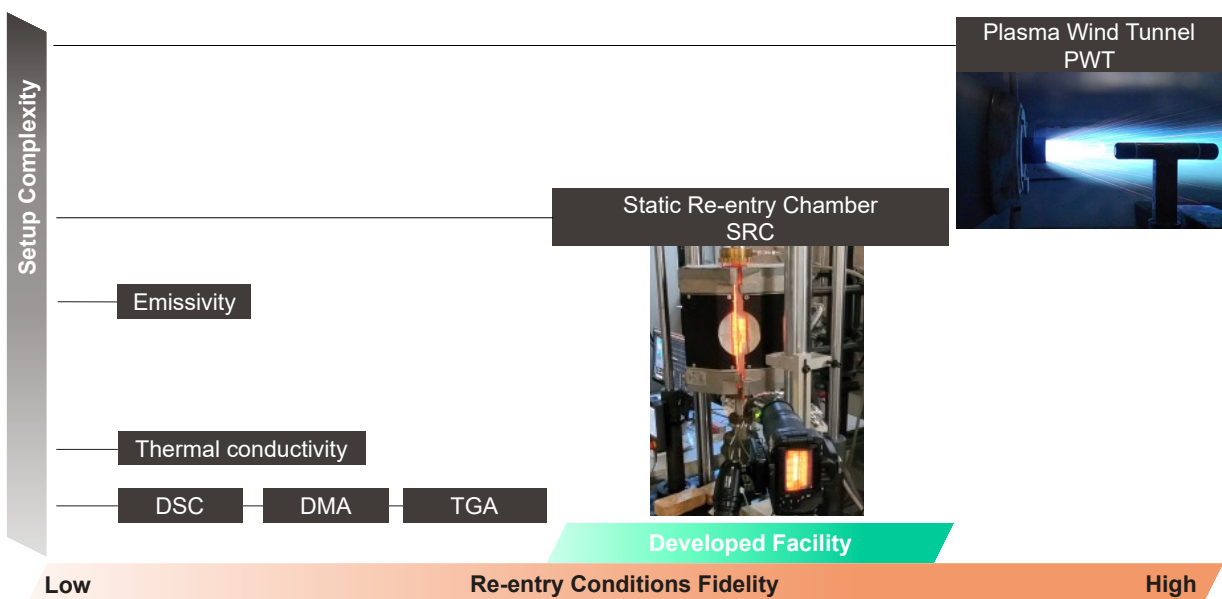


Figure 2.5: Comparative panel of re-entry simulation testing facilities with respect to condition fidelity and setup complexity (in-fine related to the cost).

2.1 Atmospheric re-entry environmental conditions

Table 2.2: Materials tested at IRS within their high fidelity PWT facility. With highlighted in green the demisable ones and in red critical ones based on these test results and recovered debris and under a typical UC re-entry scenario. [21][19]

CFRP/epoxy	JAXA-CFRP
CFRP/cyanate ester	COPV (Ti6AL4V liner+CFRP/epoxy)
CFRP/PEEK	Al 7075 T651
FFRP/epoxy	Al-Li 2099
GLARE (GF+Alu/epoxy)	Sintered SiC
Stainless Steel, AISI 316L	Ti6Al4V

A non-exhaustive list of materials tested in a PWT for demise characterization studies are displayed in table 2.2 displays. ESA's ESTIMATE (European Space maTerIal deMisability dATabasE) webpage gathers data from material and space element dedicated testing campaigns. These scarce and valuable data mainly relate to PWT test activities, such as the *CoDM* (*Characterisation of Demisable Materials*) from IRS and *CHARDEM* (*CHARacterisation of DEMisable Materials*) from Deutsches Zentrum für Luft- und Raumfahrt (DLR). [1]

The testing conditions are based on previously elaborated models and re-entry data from the atmospheric re-entry environmental conditions studies. The resulting experimental data are typically used to characterize material degradation and small assembly fragmentation behaviour. These crucial knowledge allow the demisability categorization of the different material's grade, in parallel to enable demise simulation models refinement and so, improving overall S/C demisability design.

The recent novelty in testing approach with PWT is the integration of a mobile holder such as a rotating cylinder, as presented by Schleutker et al. [14] and illustrated in the following figure 2.6. The concept there is to mimic the re-entry aerodynamically induced tumbling attitude, and validates that a tumbling/spinning re-entering object is expected to a slower demise process.

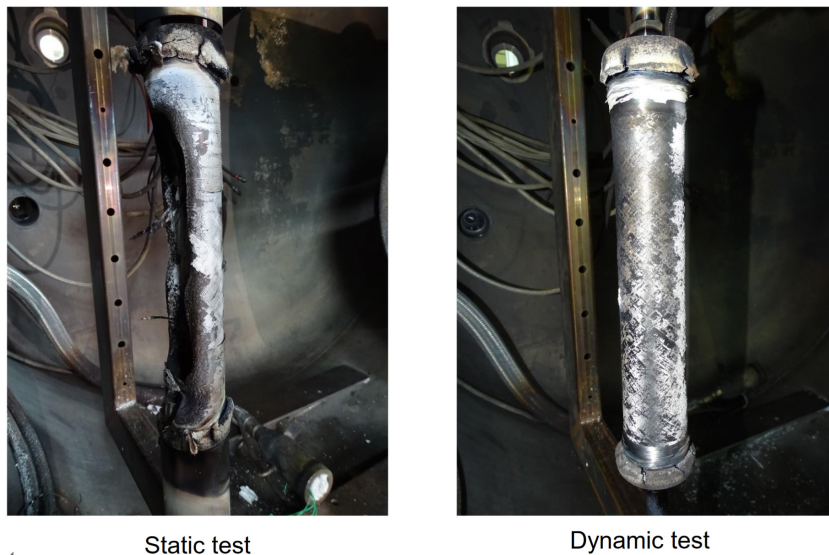


Figure 2.6: Tumbling attitude simulator via a rotative sample holder integrated within DLR PWT facility. Comparative results on a CFRP cylinder between static and dynamic attitude.[14]

2.1.5 Demise criteria - DC

A demise criterion/index of a component defines its capability to lose mass/ablate under the destructive re-entry conditions upon a threshold. It is opposed in a sense to the historical studies on the aerothermo-mechanical properties where the aim was the component survivability to the re-entry environment, but

the physical and material key parameters closely related. BC is the leading parameter in the aerodynamic term of the criteria. It is defined as $BC = m / (C_D * A)$, with m the mass, C_D the drag coefficient (dependant on the geometry) and A the effective area. As a first guess, a low BC could be favourable as it opposes a large resistance to the incoming air flux, thus favouring the demise. However, at hypervelocities, an aerodynamic shock bow is created in front of the object that is distant enough to widely protect its surface from the high enthalpy flux, thus radically reducing the demise capability, whereas in the case a high BC object, the aerothermal ablation flux is maximized with close contact with the high velocity incoming flux [37]. However during the orbital phase, a high BC leads to large orbit lifetime which is unfavorable in term of debris mitigation, so it is preferable to keep this parameter out of the demise criteria to avoid confusion.

From PWT testing, it was found that depending on the type of material, the demise phenomenology is not unique and is driven by different factors, even within similar material classes. Ceramics and high melting temperature metals show a steady state demise resistance behaviour, whereas aluminium, SS or titanium alloys forms a demise resistant oxidation surface layer with a temperature surpassing the melting point upon significant heat flux conditions. For the FRPs, their ablation processes results in characteristic combinations of fiber spallation, ply separation and matrix pyrolysis [21] [53].

In addition, Schleutker [54] experimentally observed that a critical parameter influencing the efficiency of composite ablation processes is the char yield, specified as ϑ_{cy} in our demise criteria. It can be described as the percentage of solid carbonaceous residue that remains after the removal of non-carbon elements during the pyrolysis and carbonization of a polymer. Experimental evaluation of the char yield typically involves analyzing the residual mass using Thermogravimetric Analysis (TGA) with a run conducted at a minimum of 800°C under an inert atmosphere (N₂).[55]

This leaves a demise criteria (DC) mainly based on the object specific thermomechanical/-physical properties, which can be expressed as function of 9 parameters extracted from these few D4D activities focusing on the matter at material level:

$$DC = f[T_m/T_{degrad}, C_p(T), \chi_{cat}(T), \vartheta_{cy}, \varepsilon(T), H_f(T), k(T), E(T), \sigma_{fail}(T)]$$

With melting temperature T_m , and the temperature dependant parameters: specific heat capacity C_p , surface catalycity χ_{cat} , ϑ_{cy} the char yield and emissivity ε , the heat of fusion H_f , thermal conductivity k and mechanical properties E , σ_{fail} . A simpler index based on previous survivability studies was used such as the heat of ablation for example presented by Waswa [56].

The demise index serves as a valuable measure for conducting trade-off analyses with standard spacecraft (S/C) design parameters, including structural properties, in-orbit survivability, radio transparency, toxicity, or cost, facilitating technology comparisons and materials selection.

At the mission level, the orbit type can influence the demisability capability of the S/C. The de-orbit initial velocity from a retrograde orbit, moving against the Earth's rotation, surpasses that from a prograde orbit, enhancing the demise environment. This velocity advantage can be significant, reaching up to 470 m/s in the case of a re-entry event at the equator.

In summary, an optimal material for demisability should exhibit **low** melting temperature, specific heat, heat of fusion, char yield and surface emissivity, coupled with **high** thermal conductivity and surface catalytic activity to facilitate fast heat diffusion and promote mass loss through chemical reaction. Testing results also indicate that additional complex behaviors, such as thermal protection induced by expanded composite layers, can significantly impact demise. Consequently, defining a clear demise criterion remains

challenging. Materials like stainless steel, titanium, beryllium, silicon carbide, and all carbon-based composites (CFRP, CC, CFC), characterized by melting temperatures above 1000°C , are categorized as low-demise capability materials based on recovered debris analysis and ground testing results. This classification aids S/C designers in meeting re-entry casualty risk requirements.

2.1.6 Composite materials demise behaviour

Demisability performance of composite materials such as CFRPs turns out to be opposed to what was originally considered, since these composites a priori have a low degradation temperature matrix. However, even after complete pyrolysis of the matrix, the compact fibers disposition was strong enough to maintain its structural function and turned out to be a very effective thermal shield as illustrated by PWT testing of Beck et al. [9] or recovered debris, figure 2.4.

To work around this issue, exposing the laminate edge or any loss of fiber layup consistency, such as with discontinuous reinforcement, are examples of measures that could facilitate the fiber ply spallation and thus the component demise. Another demisability issue identified later on and illustrated in figure 2.7, is the presence of a convective blockage at the CFRP surface during the high plasma flux interaction and ablation process, where extreme outgassing of the matrix pyrolysis acts as a gaseous thermal shield and prevents the incoming heat flux to reach the material surface [57]. This leads to a component break-up delay.

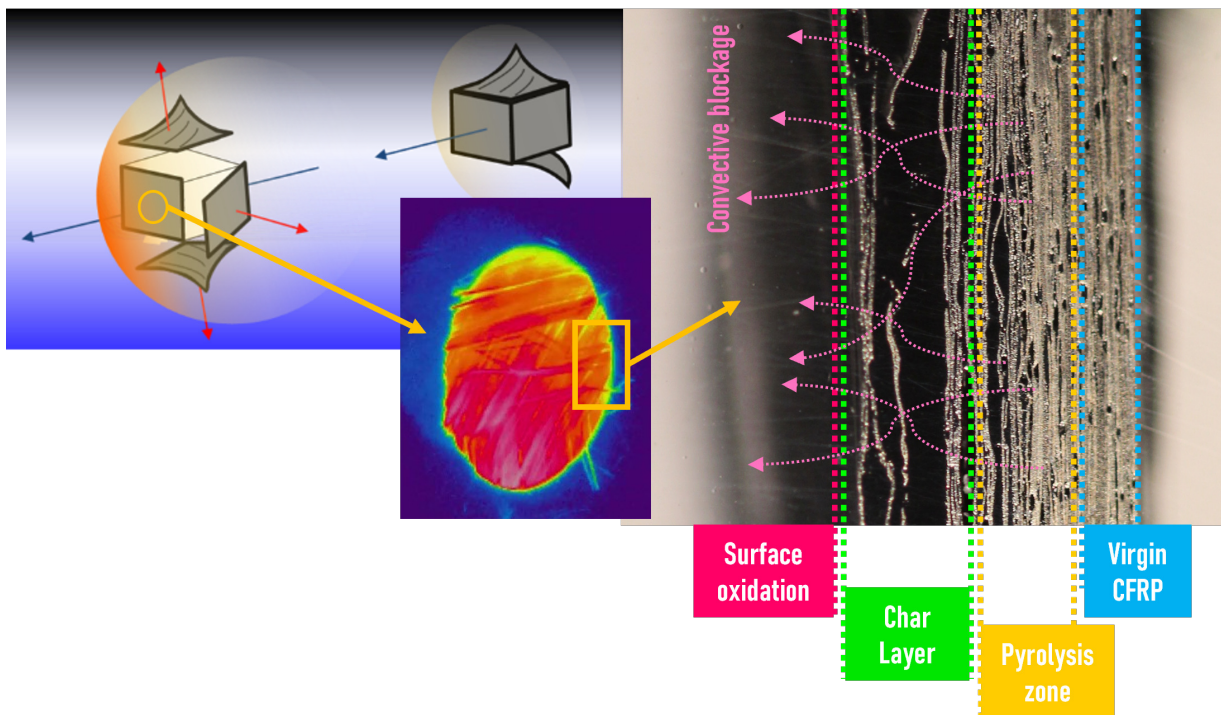


Figure 2.7: Illustration of the complex interaction factors between ablative materials such as CFRP and an intense heat flux.

Improve matrix pyrolysis by fillers

The addition of reactive particles in a FRP matrix can potentially lead to a two-way demisability improvement:

- **Increased trough thickness heat conductivity:** Particles incorporation in the non-conductive matrix work as heat bridges between the reinforcement plies, a property that can play a role to facilitate the composite layer spallation during re-entry.[58]
- **Accelerated pyrolysis:** By incorporating reactive particles in the polymeric component, an acceleration of its pyrolysis degradation reaction is expected, which will facilitate the ablation/spallation of the FRP plies. This filler technique is similarly implemented in solid or hybrid rocket motor propellant for combustion regression rate improvement.[59]

A closely similar approach involving reactive powder was evaluated, utilizing highly exothermic thermite, as reported by Finazzi et al. [60]. In this scenario, reactive powders are enclosed within a dedicated volume of a typical re-entry resistant element (ball-bearing units, Solar Array Drive Mechanism (SADM) for example) or within dedicated capsules strategically placed at selected points on the structure to facilitate early separation at these points during demise.

2.2 D4D applied to external structure

From the gathered data, the heat flux and fragmentation sequence as a function of altitude/time experienced by the S/C re-entry at orbital velocity can be estimated and used to select the adequate demise technology to be implemented. This allows a reduction of the ground casualty risk after re-entry and the selection of an uncontrolled re-entry EOL mission if this risk falls under the 10^{-4} limit. The uncontrolled re-entry is favored as it allows the design of a simpler system, with reduced mass and costs.

To achieve this objective, various paths are possible. Following Trisolini et al. [15] study, sensitivity indexes that have the most significant effect on demise performance were pinpointed, as shown in the subsequent figure 2.8. The crucial factor in the initial condition is a breakup at a high altitude. And where the selection of specific materials plays the highest role in enhancing the tuning effects on a spacecraft’s demisability.

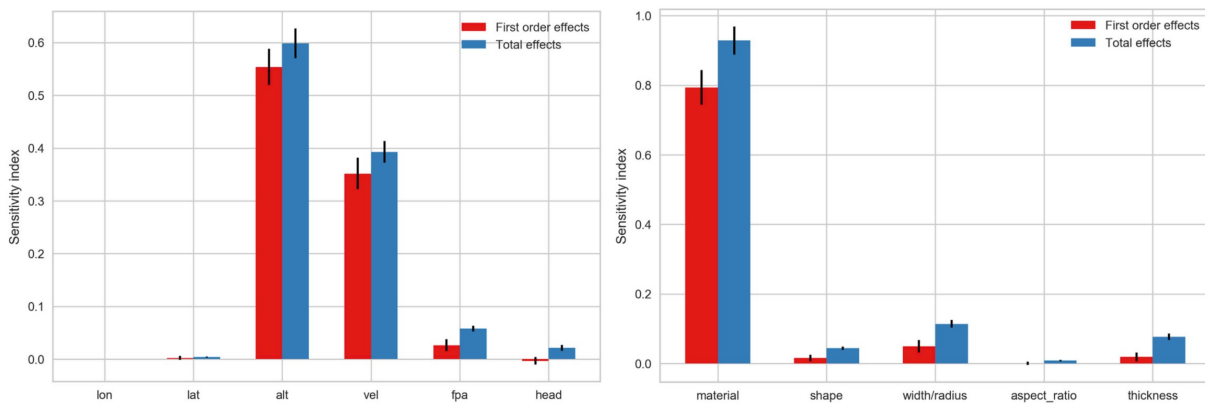


Figure 2.8: Re-entry demisability sensitivity index analysis for D4D approach from the work of Trisolini et al. [15].

Thus, a comprehensive redesign of the spacecraft (S/C), and especially its external structural elements and

assembly, is essential to maximize the encountered heat at equipment level by placing strategic heat paths with high thermal conductivity elements or by integrating reactive exothermic components to accelerate the demise [61][60]. At the material level, an alternative approach involves selecting or tuning materials with lower heat flux requirements, enabling controlled melting or ablation to compromise their functional or mechanical properties.

At the system level, an effective strategy is to expose critical components early in re-entry, employing for example demisable joints or entire structure elements [36].

2.2.1 Demisable joints

The research topic of demisable joining systems has gained attention relatively recently, with initial methods being introduced in 2016. For example, the OHB Designfor-Demise Breadboarding test campaign evaluated four different designs, a two part inserts with solder material, an adhesive bonded cleat, a composite insert, and a shape memory alloy cylinder bolt system [62]. The Shape Memory Alloy (SMA) cylinder bolt technology exhibited the most promising and clear separation at the expected triggering temperature, with only drawback a higher relative mass. However, the composite insert made of carbon fiber-reinforced polyetheretherketone (CF/PEEK) did not show a distinct improvement when compared to a standard aluminum insert, in which joint failure occurred due to honeycomb-insert adhesive potting material degradation. Additional ongoing activities related to this topic include the development of a demisable low melting temperature washer mounted on a modified cleat specific from Thales Alenia Space, made from a zinc-based alloy *EZACTTM* [63]. Furthermore, an innovative concept of demisable joint patches manufactured by additive manufacturing of CF/ PEEK, containing fiber content up to 30%, has been evaluated by a team at DLR Isil Sakraker-Ozmen et al. [64] [65]. Some designs' illustrations can be observed in the following figure 2.9.

Notably, two of these solutions rely on Polyetheretherketone (PEEK) thermoplastic material. This choice is motivated by the numerous advantages of such a polymer type, including its high specific mechanical properties. Particularly relevant to D4D, PEEK presents a melting point much lower than the degradation temperature of thermoset polymers or metallic competitor materials. An extensive exploration and comparison of demisable assembly techniques is provided by Suriani et al. [16], which emphasizes demisable cleats, inserts, and Shape Memory Alloy (SMA) separation systems. A demisability assessment was conducted on these technologies, and the results are illustrated in the table of figure 2.10.

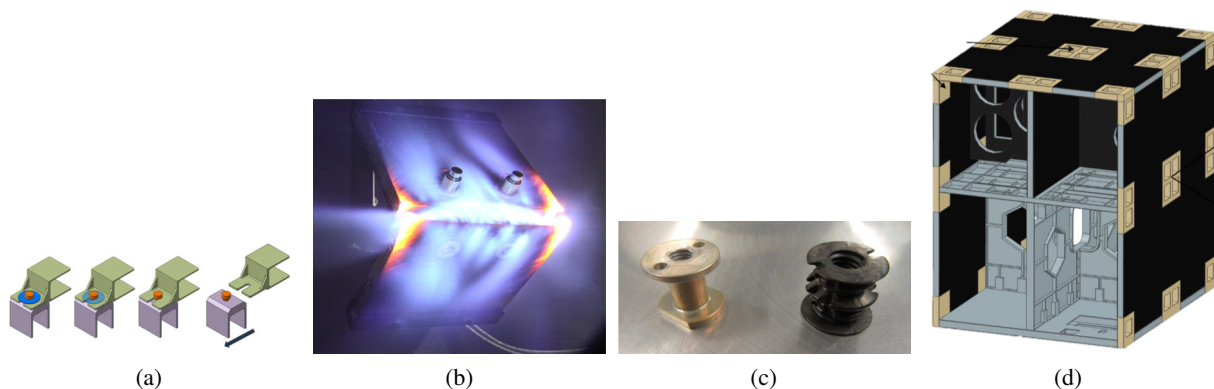


Figure 2.9: (a) Demisable zinc-based washer from Thales Aliena Space [63]. (b) PWT test of SMA actuated cylinder bolts from OHB [62]. (c) CF/PEEK sandwich panel insert from OHB [62]. (d) CF/PEEK patch joint from Patzwald [65].

Concept	Demisability and S/C Break-Up		System Impact				Risk						Costs		Applicability		Rating				
	Break-Up Altitude		Mass Budget		Configuration		Complexity		Uncertainty		Testability		Safety		Recurring Costs			System TRL		Matrix score	
Weight	0.30		0.04		0.10		0.10		0.07		0.08		0.08		0.07		0.07		0.10		
Outside cleat with solder	9	2.70	5	0.19	3	0.29	7	0.69	4	0.26	7	0.58	9	0.74	5	0.35	5	0.35	5	0.50	6.66
SMA concept	9	2.70	3	0.11	4	0.29	6	0.59	8	0.53	7	0.58	7	0.58	4	0.49	7	0.49	8	0.80	7.05
Composite insert	6	1.80	5	0.19	5	0.48	9	0.89	3	0.20	7	0.58	9	0.74	5	0.35	5	0.35	8	0.80	6.38
2-part bonded inserts	6	1.80	5	0.19	5	0.48	7	0.69	4	0.26	7	0.58	9	0.74	5	0.42	6	0.42	8	0.80	6.32
Demisable insert	9	2.70	5	0.19	5	0.48	7	0.69	6	0.40	7	0.58	9	0.74	5	0.42	6	0.42	8	0.80	7.35
Bonded cleats	7	2.70	8	0.30	3	0.29	9	0.89	6	0.40	7	0.58	9	0.74	7	0.56	8	0.56	9	0.80	7.25

Figure 2.10: Overview of demisable joint technologies and their related demisable rating based on the ranking system developed by Suriani et al. [16]

2.2.2 Demisable structural materials

Highly demisable natural fiber

Unconventional material categories, such as organic materials, can find application in these solutions within the space industry. By partially or entirely replacing the CF in a S/C structure by a low degradation temperature fiber such as natural fiber (flax or ramie for example), the demisability is improved while reducing its toxicity and potential residual pollution. Flax fibers used as FFRP have been recently investigated for aerospace technology applications and even S/C structure panels. The current interest in this type of material can be illustrated by the recent investigation of Pagan et al. [18], where a workforce constituted of Bcomp Ltd., Beyond Gravity (RUAG Space at the time) and IRS presented feasibility of using FFRP with a study case based on Copernicus Sentinel-1 satellite lateral panel as shown in figure 2.11 [17]. It was observed that FFRP mass ablation rate is multiplied by 3 to 8 times as compared to that of CFRP and equivalent to 15% of the aluminium one in addition to a much lower demise onset temperature. Identified drawbacks with such fibres are their current additional processing steps methods due to their higher humidity sensitivity and lower fibre compacity requiring an autoclave manufacturing process to obtain high mechanical properties. Another critical point is their reduced stiffness and strength as compared to carbon-reinforced composites. The evaluation of atypical materials for satellite structures structural elements, such as wood, is underway. Recent prime examples are the WISA WOODSAT mission from Finland [66], or LignoSat Space Wood project, launched in 2020 and conducted by Kyoto University and Sumitomo Forestry.[67] [68]. The use of wooden elements allows the integration of lower ecological

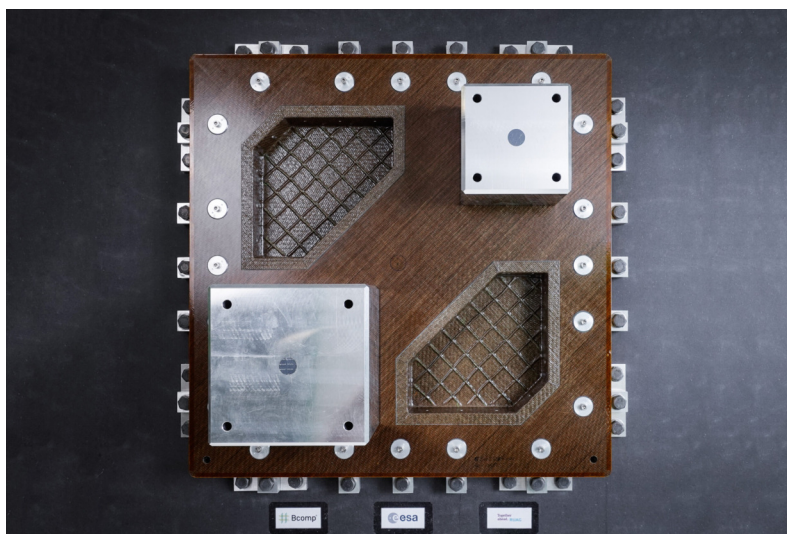


Figure 2.11: Bcomp demisable FFRP panel prototype, with a topology optimization windows design made of a thin monolithic laminate rigidified by the characteristic powerRibsTM technology. [17]

impact material and possibly improving the demisability for thin elements compared to steel, titanium or CFRP.

Topology optimization

An innovative geometric aspect of the D4D strategy involves topology optimization. This approach aims to channel incoming plasma heat flux by employing a specific geometry designed with Computational Fluid Dynamics (CFD) to enhance convective heat flux. Galera et al. [69] research work illustrates this concept, emphasizing the creation of elements with smaller curvature radius to achieve the desired result. When coupled with additive manufacturing, this approach enables a considerably accelerated demise and reduced mass.

Baseline sandwich panel design and requirements

The space industry has reached a mature stage marked by numerous lessons learned and incremental progress. Consequently, any new technology aspiring for space applications must undergo rigorous testing and certification processes before integration into a spacecraft, a procedure that may span several years. This stringent evaluation is no exception for high-performance composite materials used in structural applications.

Historically, steel, aluminum, and titanium alloys were the predominant structural panel materials in the space market. However, with the widespread adoption of sandwich panels in space systems, aluminum alloys and carbon fiber-reinforced polymer (CFRP) have emerged as the two standard choices for the baseline design of spacecraft sandwich structural panels [37][70]. While aluminum exhibits high demisability capability, it comes with reduced specific mechanical properties, being lower by more than a factor of 2 in the case of a flat panel stiffness index $E^{1/3}/\rho$ compared to CFRP. This latter is often preferred for large structures due to its superior specific mechanical properties and high thermal stability granted from its significantly lower Coefficient of Thermal Expansion (CTE). Various honeycomb materials are employed for this application, with aluminum (Al5056) and NOMEX® being among the most common choices.

The typical requirements for such panels can be regrouped under three types of properties:

- **Mechanical:** Highest elastic modulus (bending stiffness), yield strength, fracture toughness and vibration damping
- **Thermo-physical:** Lowest density and coefficient of thermal expansion, largest service temperature range and demisability
- **Mission specific:** Radio-transparency and Electromagnetic (EM) or Micrometeoroids and Orbital Debris (MMOD) shielding

From this analysis, it appears that by partially or entirely replacing the carbon fiber in a S/C structure with a natural fiber such flax or ramie, which has a low degradation temperature, the demisability should be improved while reducing the part's environmental impact. As exposed just above, the application interest of flax based composites for demisable structure was already demonstrated. However, at micro-scale, secondary fibrils separate the main fibre bundles, so there is a lot of unoccupied volume that requires to be compressed to reach high fibre volumetric fraction and thus high specific properties. A hybridization approach with carbon and flax fibers will thus be explored in the present work as a potentially optimal way

to tune the demise and structural performances and to identify promising and realistic solutions for the space industry against current low performance/non-demisable options, such as full aluminium or carbon fibre-reinforced composites.

2.3 Space re-entry modelling

Space re-entry modeling defines methods for simulating and analyzing an object's behavior as it re-enters a planet's atmosphere from space. This involves studying and predicting multi-physics phenomena and interactions as the object penetrates an increasingly dense fluid at hypervelocity ($Mach > 5$). Re-entry modeling relies on key multidisciplinary aspects, including atmospheric physics, flight dynamics, thermodynamics, material science, and structural engineering.

Having answered the 'what,' let's explore the 'why.' Interest in such modeling gained momentum rapidly during the early days of space exploration in the 1960s when satellite missions became a reality, and objectives expanded to include human spaceflights. Addressing the question of how to safely return from orbit required additional knowledge of re-entry conditions and the extensive development of re-entry technologies. Progress in this field was highly motivated by the moon race, involving sophisticated re-entry planning for the return journey to Earth.

Since then, space re-entry modeling has evolved significantly with advancements in computational methods, materials science, and our understanding of aerodynamics and thermodynamics. Beyond designing safe returns for crewed missions and space probes, a new aspect has emerged: optimal destructive re-entry. This aims to ensure ground safety from the growing number of re-entering satellites and space debris, which were not originally designed for demise upon re-entry. The awareness of the global threat posed by uncontrolled re-entering debris has led to significant developments in this aspect of space re-entry modeling and the definition of mission and S/C designs requirements in terms of air and ground casualty risks, as described in the introduction of chapter 1.

This aspect, as detailed in ESA's DIVE guidelines document [6] and the work of Park et al. [71], relies on different atmospheric, aerothermodynamic and material ablation models with an overall large spectrum of maturity. The current lowest in this regard, is the materials one and more specifically non-bulk materials such as composites. The material demise models proposed today are only highly consistent with the bulk class of materials which was validated through space debris recovery and few re-entry data. The highly heterogeneous/anisotropic FRP material class has difficulties to be defined during this complex disintegrating process. In addition to their difficult characterization as their behaviour in PWT testing for example are highly influenced by sample and holder geometries in addition to display a large variety of demise processes depending on their materials combination, as illustrated in the following chapters. This leads to model with high inaccuracies.

Current satellite mission designs relies on destructive re-entry modeling to select the End-of-Life (EoL) strategy following national and international requirements, with three de-orbiting options:

- I. **Controlled** | Costly, complex, safest, required for large S/C
- II. **Assisted** | Highly technical, trade-off between 1 and 2, only proven recently with Aeolus re-entry in July 2023 [48]
- III. **Uncontrolled (UC)** | Simple, safety relies only on probability

Such selection impacts several mission aspects, from structural and propulsion designs, up to the launcher

selection, where for example the case where the S/C necessitates a controlled re-entry requiring a much powerful and heavier propulsion system. To keep in mind that in case of issues regarding flight control or propulsion systems, both 1 and 3 leads to option 2. Therefore critical inaccuracies in simulation results, can induce extremely costly design modifications, but more problematically catastrophic events in the case of significant elements surviving re-entry and potentially inducing casualties.

Considering the increasing implementation of composites in the space industry, the interest in model improvements is extremely large in order to establish optimal S/C design based on precise demisability analysis. This is visible by the creation of dedicated sessions, conferences and workshops on the topic, such as Flight Vehicles, Aerothermodynamics and Re-entry Missions Engineering (FAR) conference or Clean Space Industry Days (CSID) 2023.

2.3.1 Re-entry demise simulation analysis tool

[6]

The first step to assess the ground casualty risk of a reentering object is to precisely simulate its atmospheric re-entry effect prior to the mission definitive design to still allow for hardware modification. The various re-entry assessment tools are classified in two approaches, object or spacecraft oriented, depending on their orbital vehicle modelling complexity.

Regarding the object oriented approach, this vehicle is represented by an assembly of simple geometric objects (box, sphere, cylinder and cones) with a possibility of organising them with parenting links. The fragmentation event and phenomenology is set from the break-up altitude or physics-based dissolution triggers such as temperature, heat flux, dynamic pressure or load factor. The aerodynamic analysis is performed with 3DoF and aerodynamic parameters of the simple object. Similarly for the aerothermal analysis, it is based on each object specific heat transfer properties. With these simplifications, this simulation method is very fast, thus allowing multiple designs comparison. DRAMA/SARA (ESA), DEBRISK (CNES), DAS (NASA), ORSAT (NASA) are software examples using this type of approach.

For the S/C oriented approach, a more realistic object modelling is represented by a panelized geometry model (closely similar to FEM). Thus, the aerothermodynamic analysis is achieved with 6DoF, coefficient and parameters following the real geometry. This allows fragmentation events to be triggered by stress/structural integrity evaluations. Such complex modelling effort comes obviously with high modelling and computing time, but the detailed results are more realistic compared to the object related approach. SCARAB (HTG-ESA) and PAMPERO (CNES) are example of such software category.[37]

For this thesis, the use of European tools (DRAMA) was privileged principally because of the direct contact available from the partnership with ESA. Obtaining easy access to the design of simulation models is essential. Understanding and evaluating the accuracy of the results is necessary, as well as receiving expert feedback. The goal isn't to enhance these models, but to incorporate new material combinations for further use, and assess specific cases.

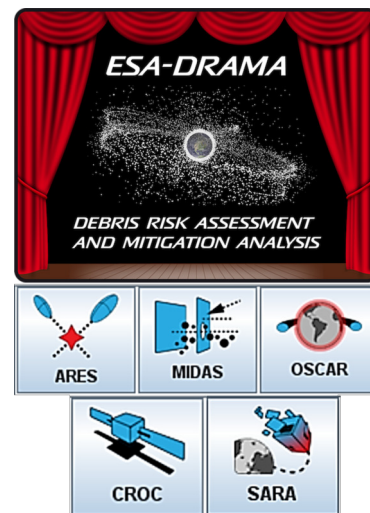


Figure 2.12: DRAMA's five integrated modules for S/C orbital and re-entry risk assessment.

Of the three DRAMA software tools shown in figure 2.12, Re-entry Survival and Risk Analysis (SARA) module integrates on one side aerothermodynamic models from which drag, lift and side forces are calculated (SESAM code), and on the other side the ground risk is calculated from heat transfer and ablation processes which are designed with a lumped-mass model and temperature dependent material properties (SERAM code). The demise is thus represented by the mass loss function linked with the melting rate. The material input properties are density, specific heat, melting temperature, emissivity coefficient and heat conductivity, for eventual oxide formation: surface emissivity, activation temperature, heat of formation and reactivity probability. [37]

This model is adopted and relevant for bulk materials (metals, ceramics, polymers) with isotropic properties. However for FRPs a general model is not yet designed due to the complex and not completely identified demise behaviour. Hence, the current implemented CFRP model is based on a Charring Material Ablating model (CMA), which separates the demise process in two steps, pyrolysis (ruled by Arrhenius law) and surface ablation (ruled by mass transfer and pyrolysis blowing rate) [72]. The component material initially identified as in a virgin state (pre-pyrolysis), progressively transforms into a char state (post-pyrolysis) which surface is then ablated. The input properties for the composite are heat conductivity, emissivity coefficient and fiber ratio; for the resin: density, specific heat, specific heat capacity of the pyrolysis gas, activation temperature, reaction rate, reactive terms, blocking and blowing factor; and finally for the char: density, specific heat, thermal conductivity, heat of formation, activation temperature and reactivity probability.

A major issue leading to over-conservation with such model is the missing ablation term related to spallation or mechanical erosion, which can be a non negligible part for composite materials.

2.4 Thesis objectives and methodology

From the literature review, it thus appears that the design for demise approach has most often been considered from the design/space characteristics point of view, and not often from a materials science point of view, highlighting the need to develop novel material solutions to increase the demisability of composite materials. As a result, the main objectives of the thesis work presented in this document are:

Objective A: Gain a complete knowledge overview of composite material demise process under re-entry-like environments

Having conducted extensive literature reviews and participated in dedicated composites and Design-for-Demise (D4D) workshops and conferences, a broad understanding of the main processes related to the demise of materials in this category was acquired. Additionally, gaps in current research and development were identified, especially in the characterization of the demise behaviour and materials combination. Given the ongoing high levels of interest and dynamic policy changes aimed at achieving a sustainable and Zero-debris space environment, the knowledge surrounding this subject is rapidly evolving, necessitating continuous updates on this matter.

Objective B: Identification and evaluation of composite material substitutes for spacecraft external structure panel assembly to improve overall demisability

To fulfill this objective, several innovative material combinations and designs are proposed, including novel fastening systems based on carbon/PEEK composites. Additionally, three novel sandwich skin

materials and configurations have been introduced: hybrid skins combining flax and carbon fibers, metallic reactive powder incorporated into the composite matrix, and CFRP composites integrating cut-ply. It is important to note that the concept of cut/short fiber composites for early demise was not reported in the literature, and is evaluated in this work for the first time as a potentially elegant solution to the non-demise of carbon based composites.

To validate these solutions, two sets of evaluation methods were employed. The first set focused on confirming their demisability, while the second set assessed their mission-related structural capabilities.

Objective C: Development and evaluation of static re-entry chamber to assess novel material thermomechanical-demise capabilities

To address the characterization gap between standard laboratory equipment (TGA and DMA) and PWT facility for assessing new material demisability, a complete static re-entry chamber was assembled, calibrated and operated. This tool facilitated the identification of key physical and structural loosening aspects on sandwich panel facesheet and fastener samples, consequently enabling an efficient and early S/C break-up.

Objective D: Improve experiment-to-model implementation methods of composite materials for existing re-entry-risk evaluation software

A crucial aspect of material demise evaluation involves the ability to predict and model observations and measurements using numerical modeling. To address this, an experiment-to-model method specifically designed for composite materials is introduced. This approach aims to facilitate the direct integration of experimental material-level properties into ESA’s object-oriented re-entry analysis tool, DRAMA (Version 3.1.0).

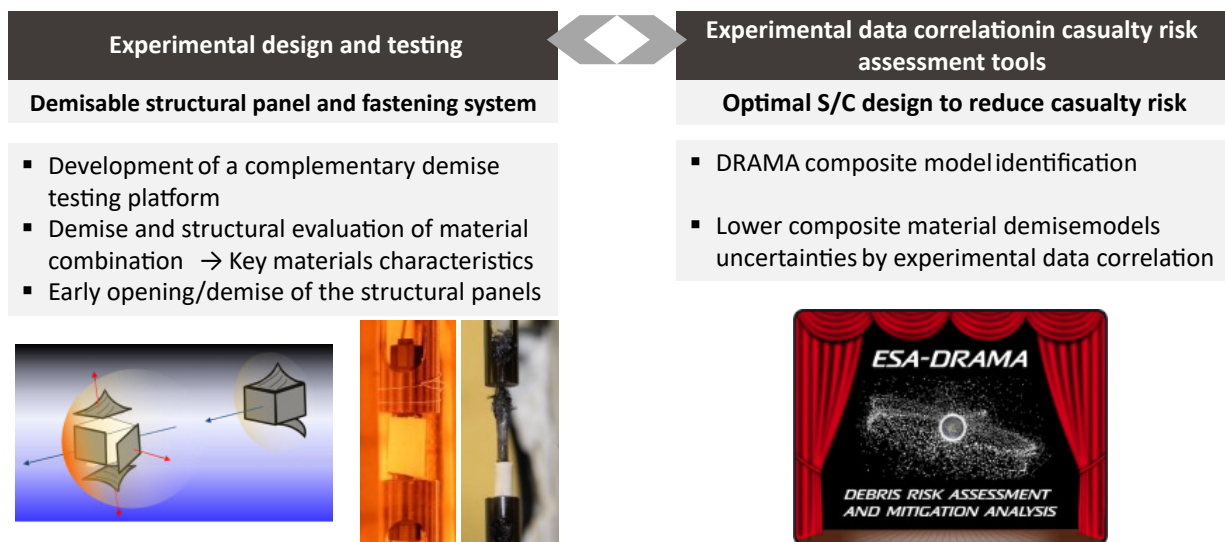


Figure 2.13: Summary of thesis objectives and key points, based on two interdependent approaches.

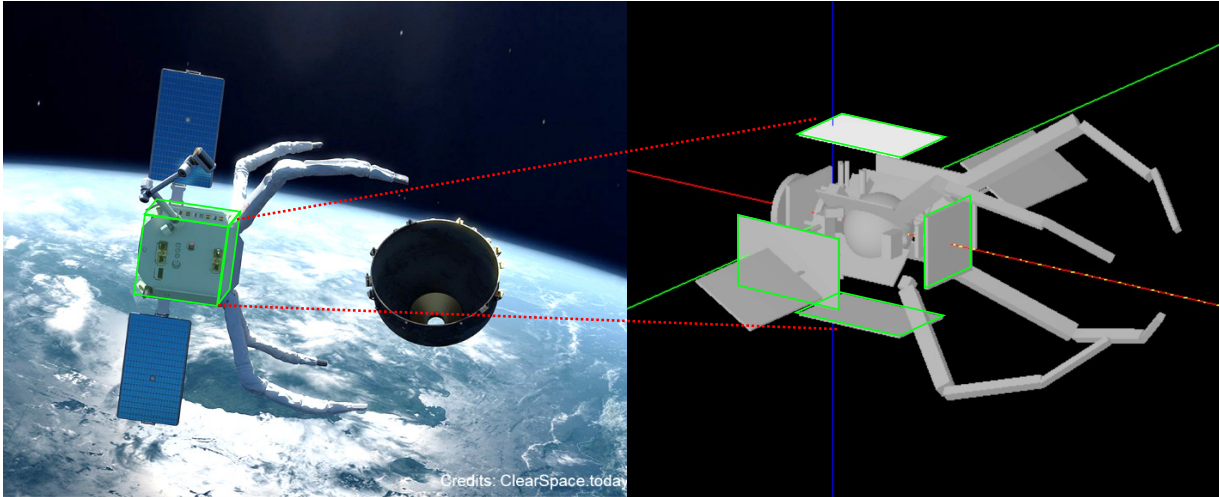


Figure 2.14: Left, artistic view of CS-1 spacecraft capturing VESPA target. And right an exploded-view model with highlighted in green the front and side external panels. The side panels are used as a reference for this work and have a dimensions of 1031x747 mm. Credit to ClearSpace.today

2.4.1 Proposed methodology

To reach these objectives, the following methodology has been followed:

- (i) A case study has been identified, inspired from the needs of ClearSpace to address both composite panel structures but also their assembly, so as to foster early break-up of the structure, displayed in figure 2.15.
- (ii) First, the environmental conditions in terms of heat/time/pressure/composition for a given de-orbit option were identified so that the material demise conditions are evaluated in a relevant manner, and two conditions were selected.
- (iii) Then, sandwich panel materials and a fastening system were selected in view of early and full break-up under such conditions. A dual system approach was thus selected to enable a complementary/redundant and versatile solution; whereas for example in the case of design limitations, only one of the approaches could be implemented and would still allow a much safer re-entry event. A benchmark solution is a full aluminum sandwich panel (Al skins and honeycomb core), assembled with steel bolts, which is in principle demisable but not optimal in terms of weight penalty. The dual system proposed in this work is oriented on specific material substitution for the spacecraft external sandwich panel and fasteners. As exposed in figure 2.15, novel composite materials were implemented to these two elements in order to propose solutions that are beyond the state of the art yet should fulfill the set of requirements for mission and demisability, with specifically produced short-CF/PEEK bolts for the fasteners and a combination of flax-carbon fibers hybridization with a reactive metallic matrix filler for the facesheets. Additionally, an patented cut-CF facehseet material was explored considering its potential to break-up similarly to short fiber composites.
- (iv) The secondary goal was to improve the materials demise model for re-entry simulation by completing the composite disintegration behaviour database.

The achievement of such goals was realized through the research method following space technology development methods with trade-off analysis, analytical and experimental testing of the critical functions

(demisability, active joint release), new systems validation in a laboratory environment and testing in relevant environment (re-entry chamber and Plasma Wind Tunnel (PWT)). After this last step corresponding to Technology Readiness Level (TRL) 5, such technology can be implemented on a S/C, such as CS-1 presented in figure 1.8 which was chosen as the case study.

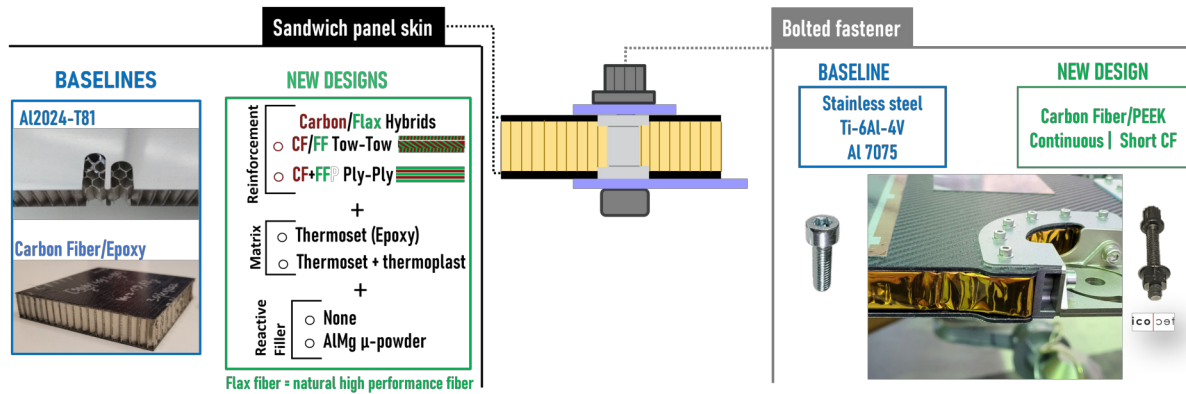


Figure 2.15: Illustration of our benchmark design composed of a sandwich panel and its through-thickness bolted attachment system.

3 Materials & Methods

In the initial section of this chapter, the materials used in this project are presented, first those dedicated to the fastening system, followed by the materials of interest regarding the sandwich panel facesheets. A second section is dedicated to the presentation of the various testing and evaluation methods used or developed throughout this project, which are summarized within the following figure 3.1. The mission operation related aspects are covered through the thermomechanical evaluations and the End-of-Life (EoL) aspects through the demisability ones.






	Bolt fasteners 	Facesheets and sandwich panels 
THERMO-MECHANICAL 	<ul style="list-style-type: none"> ▪ Dynamic Mechanical Analysis– DMA , 3pt bending ASTM D5023 ▪ Tensile ASTM F606 & ASTM D3039 ▪ Single shear ASTM F606 ▪ Torque clamp force (cycling) ISO 16047/ASTM F606 	<ul style="list-style-type: none"> ▪ DMA , 3pt bending ASTM D5023 ▪ Tensile ASTM D3039 ▪ 4-pt Bending sandwich system ASTM D7249 ▪ Vibration – Dynamic loads sandwich system @ESTEC ECSS-E-ST-10-03C 
DEMISABILITY 	<ul style="list-style-type: none"> ▪ Thermogravimetry Analysis– TGA ASTM E1131 & ASTM E1641 ▪ Static reentry chamber @ EPFL Mechanical loosening onset 	<ul style="list-style-type: none"> ▪ TGA ASTM E1131 & ASTM E1641 ▪ Static reentry chamber @ EPFL Mechanical loosening onset ▪ Plasma Wind Tunnel - PWT @ IRS Stuttgart Relevant environment

Figure 3.1: Main testing methods performed through this research work covering specifically structural and demisability evaluation of the various materials and designs selected.

3.1 Materials

3.1.1 Bolt joints

To investigate the demisability capacity of our novel composite proposition for the bolted joints, a stainless steel (SS) A2-70, AISI 304 grade such as shown in 3.2, was selected as the reference benchmark material for bolts. Indeed, it is widely available and used in aerospace applications due to its high corrosion resistance.

The composite equivalent was selected to be made from CF/PEEK material, as it is ideally suitable for aerospace applications through its combination of both high-end mechanical performance carbon fibers and thermoplastic matrix. Indeed, compared to the aerospace-grade Ti6Al4V titanium alloy, the resulting composite with a fiber volume content of at least 55% presents high specific Ultimate Tensile Strength (UTS) defined as UTS over density (respectively around 210 MPa/gcm^3 for Ti alloy versus 180 MPa/gcm^3 for this composite), low thermal expansion coefficient (9 $\mu m/m \cdot ^\circ C$ versus 2.5 $\mu m/m \cdot ^\circ C$) [73], in addition to high vacuum compatibility and high space environment resistance [74]. Regarding D4D applications, its 350°C relatively low melting temperature, as compared to structural metals, is the key point of this selection.

Two types of reinforcement have been selected for the composite fastener, both produced by icotec ag with Hexcel IM7 carbon fiber, the first is composed of continuous Carbon Fiber (CF) and the second with short CF, and both integrated within PEEK from SupremTM. The short fiber design was designed and manufactured on demand to explore the potential of better fastener break-up during demise, as will be demonstrated later. CF/PEEK bolts and nuts are manufactured using Composite Flow Moulding, a patented injection moulding technique. In this process, a simply shaped bulk pre-form of CF/PEEK is heated beyond the polymer's melting point. It is then injected into a dedicated mould to achieve the final shape. This method allows for the creation of products with complex shapes and the integration of both continuous and short reinforcement fibers with an optimal fiber volume fraction $V_f=55\%$. Such manufacturing method induces a non-homogeneous microstructure with preferential longitudinal fiber orientation.

For a preliminary materials analysis, both reinforcement design microstructures have been analyzed by digital microscopy and X-ray Phase Contrast imaging (XPCi) based on experimental parameters from tei [75], with no significant differences observed regarding fiber distribution or porosity, as shown in figure3.3. This latter novel non-destructive evaluation technique principle revolves around an interference pattern generation that undergoes specific alterations when an object is positioned between the X-ray source



Figure 3.2: Baseline stainless steel versus our novel CF/PEEK bolts for through-thickness insert fixture to a sandwich panel.

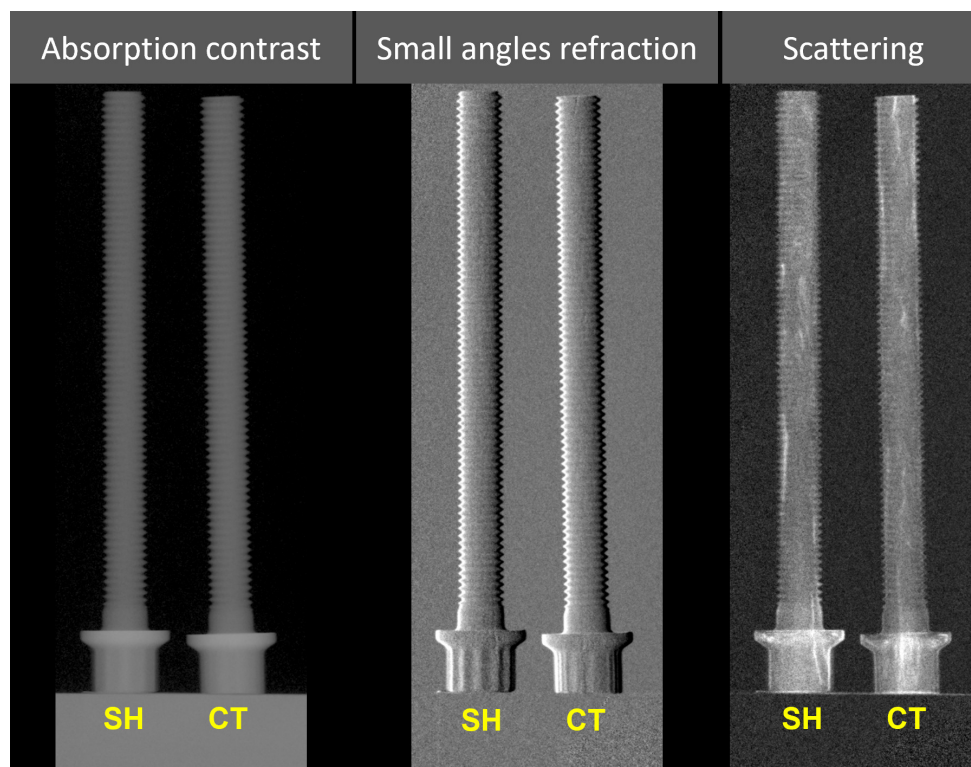


Figure 3.3: Comparative analysis of continuous (CT) and short (SH) CF/PEEK samples with LPAC XPCi setup from which three type of images can be extracted. The phase scattering image shows rich microstructure information such as fibre distribution homogeneity or voids, which is particularly interesting for composite materials.

Materials & Methods

and gratings. Consequently, the phase modulation leads to intensity modulation, and by analyzing such alterations in the intensity pattern with and without the sample, small and ultra-small angle scattering images can be identified. Its high sensitivity to inconsistencies within a sample at a scale smaller than the image resolution makes it ideal for observing materials with comparable absorption and refraction characteristics but distinct microscopic internal structures, which is typically the case for fiber-reinforced polymer composite systems. Bolt sample material and dimensions have been selected according to the manufacturer's stock availability. Their characteristics can be found in table 3.1.

Table 3.1: Bolt samples datasheet characteristics. There is no specific data for short CF/PEEK as it was manufactured on request for the project. Values with an asterisk * come from personal communication from icotec ag.

Material	CF/PEEK- $V_f=55\%$		Stainless steel
Density ρ	1.55 g/cm ³		7.7 g/cm ³
Grade	Continuous-CF	Short-CF	A2-70 AISI 304
Standard	UNJF 10-32		M5
Diameter [mm]	4.7625		5
Length [mm]	50 and 55		55
Elastic Modulus [GPa]	30-50 *	-	190-203 [73]
UTS [MPa]	290 *	-	700 [73]
Ultimate Shear Strength (USS) [MPa]	349 *	-	1490-530 [73]

3.1.2 Sandwich panel facesheet

Three novelties regarding material substitution applied to structural components are evaluated in this research. The first concerns an extensive fibre reinforcement material selection leading up to the identification of a hybrid reinforcement made of carbon and demisable flax fibres to replace aluminium or full carbon composite sandwich panel facesheets. Secondly, the integration of a thermally conductive and reactive metallic matrix filler was studied. An aluminium-magnesium alloy micro-powder was evaluated, aiming to reduce the convective blockage issue inspired from rocket solid propellant studies for solid or hybrid propulsion systems [76], in addition to improving through-thickness thermal conductivity, typically lacking in laminate FRP materials [58]. Finally, the possibility to use CFRP prepregs with initial cuts in the prepreg was investigated, as this material provides the same stiffness and slightly lower strength as a regular CFRP, but the cuts should allow better ply-by-ply demise.

Sandwich panel facesheet versions

For the present study, five skin materials were compared, with their base material characteristics presented in table A.1 of the appendix A. The two first materials are currently used in the space industry: an aluminium 2024-T81 alloy and a CFRP composed of thin-ply TENAX HTS45 unidirectional carbon fibers with an aerial weight of 50 gsm. Apart from its inherent higher structural performance [77][78], the thin ply material was selected to achieve a Quasi-Isotropic (QI) layup and at least equivalent stiffness to the aluminum reference design. Then, for FFRP, three fiber configurations were previously evaluated in terms of processing, demisability and availability, two twills (ATTM5040, ATTM5043) and one UD ATTM5057), and where finally only the ATTM5040 grade was kept. The two last skin materials are carbon-flax fibers hybrid reinforcement designs: A Commercial-off-the-shelf (COTS) intraply hybrid, named Carbon-Flax Fibers two-by-two (CF-FFTB), produced by Bcomp (ATTM 5027) and a self-assembled interply hybrid, Carbon-Flax Fibers ply-by-ply (CF-FFPBP), arrangement as illustrated in figure 3.4. This latter is a combination composed of TENAX carbon fibres, similar to the CRPP ones, and Bcomp ATTM5040 twill

300gsm flax fibres. This flax fiber version in a prepreg format was chosen as it was the only one available prepreg with the similar VTC-401 epoxy resin than the other prepreg used in this work.

Regarding, the matrix material, two types of resin were evaluated. The pre-cited space-qualified VTC-401 epoxy from SHD Composites was selected as a baseline for its excellent compatibility with flax fibres and the relatively low curing temperature required with this type of reinforcement. The second resin is a lab-developed formula of a Thermoplastic (TP)/Thermoset (TS) blend composed of Polyvinyl-butyral (PVB) and epoxy (from confidential grades), it was chosen for its good trade-off between mechanical performance and low melting point. This latter was only evaluated in an unreinforced resin (virgin and AlMg charged) and CFRP format.

In the following sections, these various material combinations were compared regarding their thermo-mechanical characteristics. A wide set of comparative evaluations regarding structural but more importantly demise capabilities were performed to reach the best trade-off while guaranteeing the fulfillment of all the usual LEO region mission requirements, from mechanical and thermal load-bearing.

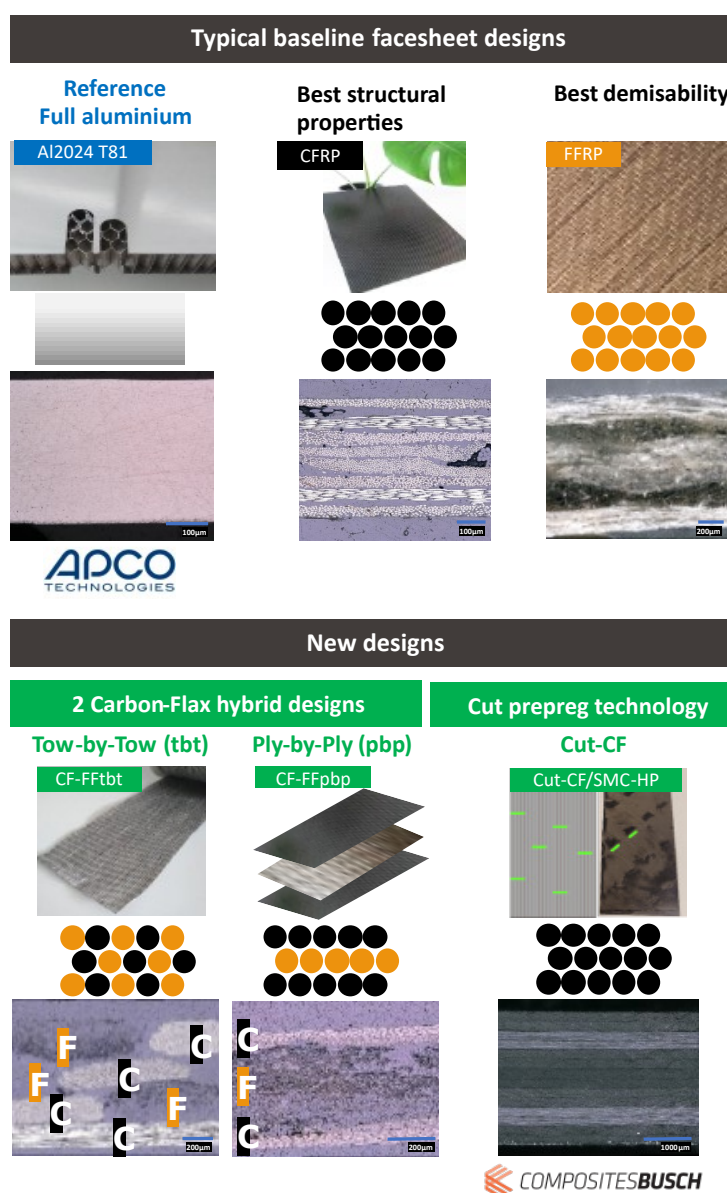


Figure 3.4: Sandwich panel facesheet reinforcement versions selected for this study, with a schematic and microscopic cross-section view of the different fibre types and arrangements

Layup sequence selection

The composite skin laminates sequences and thicknesses were determined according to a structural stiffness analysis for the bending stiffness, using analyses from the ESAComp tool from Altair Engineering Inc. ClearSpace-One aluminium external side sandwich panel design was used as a reference, and datasheets from the suppliers for honeycomb and skin properties. All the layups were set to be Quasi-Isotropic (QI) configurations, as it allows an optimal balance of strength and stiffness in both axial and transverse directions in addition to high shear strength [79]. Another reason for such a choice resides in the thermal loads consideration, which is crucial regarding spacecraft mechanical and operational stability. Following the manufacturers and preliminary manufacturing trial, a minimum fibre volume fraction, V_F of 55% was set as an objective to maximize the mechanical properties.

The aluminium panel reference sample received from ClearSpace for testing was manufactured with a lower HC core thickness, 16.19 mm instead of the 30 mm of the CS-1 study-case side panel. Therefore the composite sandwich panel designs are based on this *new reference* panel and both configurations are detailed in the following table 3.2. The HC space qualified aluminum core material, Hexcel^(R) Al5056 CRIII-3/16-0.0007P (perforated), is the same for all the sandwich samples.

It can be observed that in theory, with the optimal carbon and flax combination (UHM CF and AT5043 for example) a 10 to 30 (37)% panel mass reduction can be achieved while keeping a similar stiffness as the aluminium reference, and even around 3% compared to the CFRP design. For the PWT test campaign, dedicated thicker composite laminate samples were manufactured with layup sequences and thicknesses displayed in table 3.2. For the PWT FFRP and FFRP+AlMg laminates, an Unidirectional (UD) flax prepreg AT5057 was employed in order to be compared to similar material grade previously tested by IRS and Bcomp under additional plasma conditions. In addition, two versions of CF-FFPBP hybrid were manufactured with a different CF layer thickness detailed in table 3.3. This arrangement was chosen to assess the effect of the CF critical layer thickness on the delamination/spallation process.

As notified in the previous section, for this study, only the Tenax HTS45/AT5040 ply-by-ply hybrid combination was tested, even though it presents slightly lower stiffness performance than the aluminium reference. Therefore the mechanical performance can only be superior to what is presented hereafter, by implementing for example a lower gsm flax grade such as 5043 instead of the 5040, and/or higher-performance carbon fibers.

Table 3.2: ESAcomp calculated theoretical stiffness comparisons between selected composite facesheet and the aluminum reference in a sandwich panel configuration with all side clamped and respective length and width of 1031x747 mm. The two references are the CS-1 side panel with HC thickness=30mm and 16.19mm for the new ref. The comparative stiffness parameter is the 1st vibration EF, denoted f_1 . All the composite versions are assumed to have the VTC-401 epoxy matrix, and where *UHM* stands for ultra-high modulus, and *C* and *F – T* respectively stands for carbon and flax-twill fibers.

Facesheet name Composition	Aluminium 2024-T81	CFRP HTS45	FFRP AT5040	CF-FFTB AT5027
Sequence	-	[0/45/90/–45] _S	[0/45/0]	[0/45/90/–45]
Skin thickness [mm]	0.305	0.44	1.2	0.8
CS-1 ref. f_1 [Hz]	445	493	330	403
CS-1 ref. Normalized f_1 /panel mass	1	1.28	0.74	0.8
New ref. f_1 [Hz]	282	320	213	253
New ref. Normalized f_1 /panel mass	1	1.34	0.46	.73

Facesheet name	CF-FFBP		
	HTS45+AT5040	HTS45+AT5043	UHM M55J+AT5043
Composition			
Sequence	[0 _C /90 _C /45 _{F-T} /90 _C /0 _C]		
Skin thickness [mm]	0.62	0.49	0.49
CS-1 ref. f_1 [Hz]	440	444	526
CS-1 ref. Normalized f_1 /panel mass	0.96	1.10	1.30
New ref. f_1 [Hz]	275	280	344
New ref. Normalized f_1 /panel mass	0.95	1.10	1.37

Reactive metallic filler selection

Based on previous studies [76] [80] and material availability, a 50-50 aluminium-magnesium alloy (AlMg) was identified, also known as magnalium and typically used for pyrotechnics and thermal decoy defence system. The powder's micro-level dimension was selected as an optimal trade-off between handling safety and effective reactivity. While these metallic powders can significantly increase the heat of combustion through their highly reactive exothermic oxidation reactions originated from their low ionization energy. This material can also be pyrophoric [81]. Trade-offs between particles material, size, shape and quantity was assessed to keep mechanical properties loss, toxicity hazard and mass as low as possible while maximizing reactivity and thermal conductivity. [82] [58]

A preliminary iterative analysis employing TGA allowed the identification of an optimal powder content within the composite matrix by evaluating the mass loss rate improvement over six different matrix filler contents (0.1%, 0.2%, 0.5%, 1%, 2.5%, and 5% by weight). The thermal conductivity improvement characteristic was not considered as a selective criterion. The objective of this analysis was rather to identify the AlMg content that exhibits the most significant improvement in demise characteristics. This is translated as looking for the lowest: char yield, pyrolysis onset, and maximum mass loss rate temperatures, while aiming for the highest: mass loss rate.

3.1.3 Manufacturing

All the composite-laminates, -skins and -sandwich panels to be tested were manufactured at LPAC-EPFL, except for the specific continuous-CF and cut-CF samples which was manufactured by Composites Busch SA, as detailed in the specific last part of this section. The manufacturing steps were conducted with the support and expertise of Gavin Waddell from LPAC.

Composite laminates

Due to specific material assembly for the hybrid reinforcements and the optimization of the fibre volume fraction, 2 types of composite laminate systems were used. Standard pre-impregnated (prepreg) flax plies (AT5040 or 5043) were used for pure flax composites, a more complex resin film infusion system for the CFRP, CF-FFBTB and a combination of both for the CF-FFBP carbon-flax hybrid version.

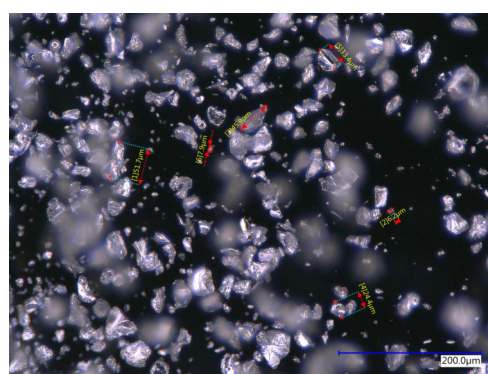


Figure 3.5: Bulky and angular shaped AlMg particles observed under optical microscope

Materials & Methods

All fabrics were oven-dried at 110°C for 10 minutes to prevent moisture entrapment during manufacturing. The resin film and prepreg plies were spiked before the layup step to facilitate air removal during compaction and enhance resin diffusion during the curing process. During the plies stacking phase, the compaction steps were performed every 3 plies or 1000 gsm fibre stacking, using a vacuum bag linked to a primary pump.

Flax fibre composites were cured in a Scholtz autoclave with a two-step cure cycle, which can be observed in figure 3.6. The first stage involved a 1-hour isotherm at 80°C after a 0.6°C/min heating ramp, and was followed by a 0.9°C/min heating ramp to 4-hour isotherm at 120°C. Finally a 0.5°C/min cooling rate was set. The entire process was conducted under an applied pressure of 8 bars. The addition of a second isothermal stage served to lower fiber-matrix and tool-part Coefficient of Thermal Expansion (CTE) mismatch effect, preventing residual stress build-up that could negatively impact the final part's mechanical properties [83]. Post-processing visual and microscopic cross-section inspections of the thin laminates allowed for the detection of defects and assessment of manufacturing quality.

Physical details of the manufactured laminates can be found in the table below (table 3.3).

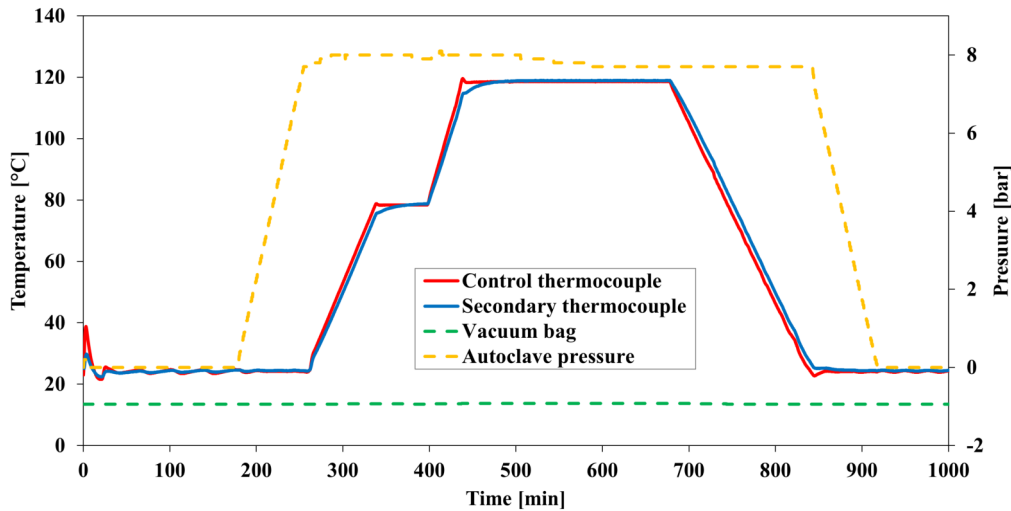


Figure 3.6: Temperature and pressure profiles of dual-hold cure cycle used for the autoclave curing of the various composite laminates.

Metallic micropowder integration

The filler integration procedure is based on a solvent spray deposition method such as presented by Lee et al. [58]. The AlMg powder filler deposition process's main steps for prepregs are summarized as follows:

- Mix the micropowder with pure ethanol, with a respective ratio of 4g for 100ml
- Homogenize the dispersion with a sonicator or lab shaker for a minimum 10min
- Weight the uncoated prepreg plies alone, to later on measure the overall deposited powder quantity
- Calibrate the deposition quantity by modulating the air spray gun pressure and feed volume using a dummy substrate
- Apply the pre-determined layers of dispersion

- Weigh the coated prepreg to obtain the final deposited powder mass

The coated prepreg can then be stacked following the standard laminate composite manufacturing method. The resulting integration can be observed in figure 3.7.

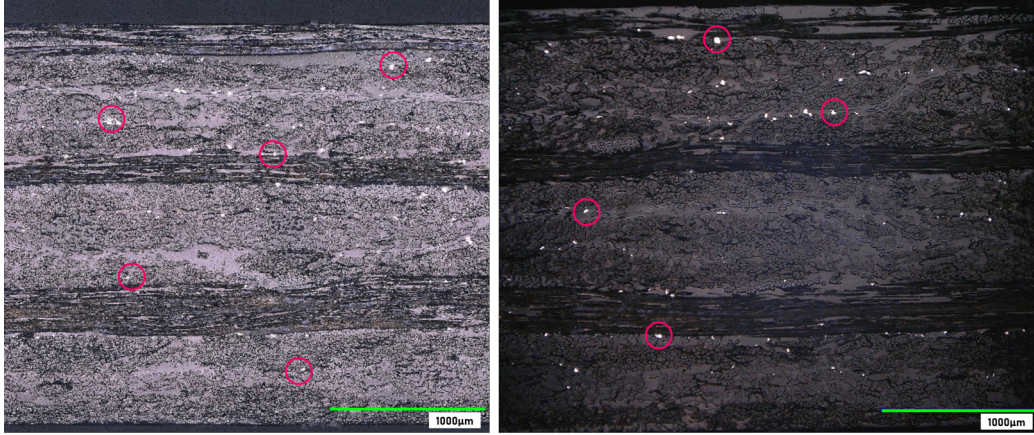


Figure 3.7: Cross-sections of FFRP filled composite laminate with 1%wt AlMg micropowder, where the some of the largest alloy particles are highlighted by red circles

Table 3.3: Measured physical characteristics of manufactured composite laminates. The FFRP PWT laminates with an asterisk indicate that a different flax grade was used; refer to the materials section 3. For the layup sequence, *F-T* means flax twill and *C* carbon.

Facesheet version	CFRP	FFRP	FFRP+AlMg
V_f	60%	58%	55%
Thickness [mm]	0.43	1.19	1.25
Density [kg/m^3]	1587	1340	1352
PWT laminate version	CFRP	FFRP	FFRP+AlMg
Layup sequence	$[(0/45/90/-45)_S]_7$	$[0/45/90/-45]_3$	
Number of plies	56	12	
V_f	55%	52%	51
Thickness [mm]	3.05	2.68	2.72

Hybrid facesheet version	CF-FFTB	CF-FFBP	
V_f	52%	59%	
Thickness [mm]	0.90	0.65	
Density [kg/m^3]	1413	1396	
PWT laminate version	CF-FFTB	Version A	Version B
Layup sequence	$[0/45/90/-45]_4$	$[\{(0_C/90_C)_n/45_{F-T}/(90_C/0_C)_n\}/0_{F-T}]_m$ $n = 1, m = 4$	$n = 3, m = 3$
Number of plies	16	23	39
V_f	52%	54%	52%
Thickness [mm]	3.95	2.99	3.05
CF layers thickness [mm]	-	0.116	0.348

Sandwich panel assembly

The assembly of thin laminate skins and a Honeycomb (HC) core is a crucial step to achieve an optimal lightweight and high-stiffness component. In our case, the manufacturing process involves two steps.

Materials & Methods

First, the skins were cured alone on flat plates in the autoclave as explained earlier. Subsequently, a Gurit SA70 200 gsm epoxy adhesive film was used to assemble the core and the two skins in an oven within a vacuum bag linked to a primary pump. The initial step involved cleaning the aluminum HC in an IPA bath, followed by drying in an oven at 110°C for 15 minutes. The cured composite skins were then prepared on the adhesive-side surface by light sanding with a rotative polisher and P1000 sandpaper. These surfaces were then meticulously cleaned with IPA. Similar to the process for skin manufacturing, the SA70 epoxy adhesive film was spiked before stacking it on the skins and assembling with the HC core. Subsequently, a 6-hour vacuum outgassing step was initiated before a single-hold cure cycle at 110°C.

The physical details of the manufactured sandwiches can be found in the following table 3.4.

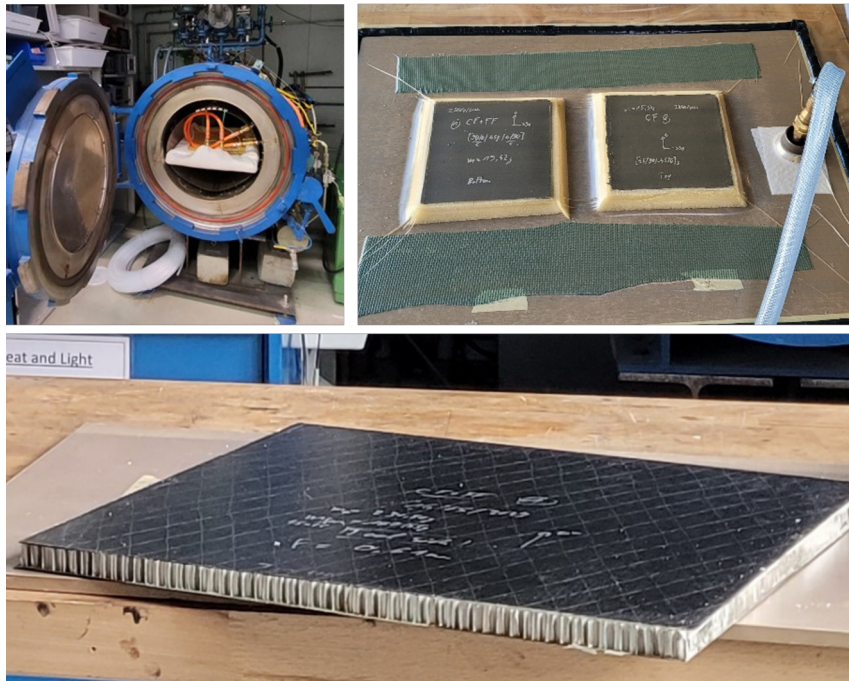


Figure 3.8: On the left, the Scholtz autoclave from LPAC loaded with a samples plate. On the upper left, a skin outgassing step to compact the reinforcement or resin plies. On the top right, staking of the aluminium honeycomb on the bottom skin and an adhesive film. And at the bottom, a resulting large sandwich panel used for the vibration and bending tests.

Table 3.4: Measured physical characteristics of reference and manufactured composite sandwich panels.

Sandwich panels 390x390 mm and HC core 16.19mm			
Facesheet version	Aluminium	CFRP	CF-FFBPP
Skin V_f	-	58%	53%
Skin thickness [mm]	0.305	0.44	0.62
Panel thickness [mm]	16.71	16.98	17.32
Panel density [kg/m ³]	176	146	172

3.1.4 Discontinuous reinforced composite laminate

Continuous Carbon Fiber Reinforced Epoxy Composites usually form a vast part of space structures in use today, but their demisability resistance strongly limits their application. The source of this resistance comes from their capability to maintain integrity upon heating at high temperatures for a significant amount of

time acting as an efficient ablative heat shield. The issue comes from the continuous aspect of the CF implemented, which prevents the material disintegration/breakup after matrix degradation.

So similarly to the short-CF/PEEK bolts presented earlier, a specifically fragmented reinforcement should bypass such demise criticality. Cut-prepregs (named SMC-HP, now commercialised under the name "black shark" produced by Composites Bush SA) were previously investigated by LPAC to improve the drapability in the forming of 3D cornered brackets while preserving the stiffness and strength of the material thanks to an optimized cutting pattern, such as illustrated by figure 3.9. This manufacturing optimization work was performed by Vincent Varanges (LPAC) in collaboration with Composites Busch. Therefore, such SMC-HP material appeared as an ideal candidate for a structural demise optimization approach. The specific discontinuous unidirectional fiber reinforcement placement, which was initially developed to obtain higher drapability while keeping similar mechanical properties compared to continuous unidirectional reinforcement, can be taken advantage of to ensure the disintegration of the material upon atmospheric reentry.

Cut-prepreg technology material

The specifically required CFRP material was manufactured by Composites Busch SA and shipped to LPAC. It was a set of four squared monolithic laminate plates of 250x250 mm, tow made with continuous carbon fibers (named continuous-CF, UD or Nappe) and two with discontinuous carbon fibers (named cut-CF or SMC-HP) composed of AS4 grade fibers and 8551 epoxy. A QI layup was selected with the following sequence in the 0° direction, $[45_2/0_2/-45_2/90_2]_S$. The cut pattern process and shape are protected by a patent from Composites Busch company. The selected and tested pattern is made of small curved cuts of 5mm large and spaced by 50 mm with a 1/3rd length side translation.

The final sample dimensions and mass details can be found in the appendix table A.1 and A.2, and an illustration of the samples, in addition to the laminates' microstructure can be observed in the following figure 3.10.

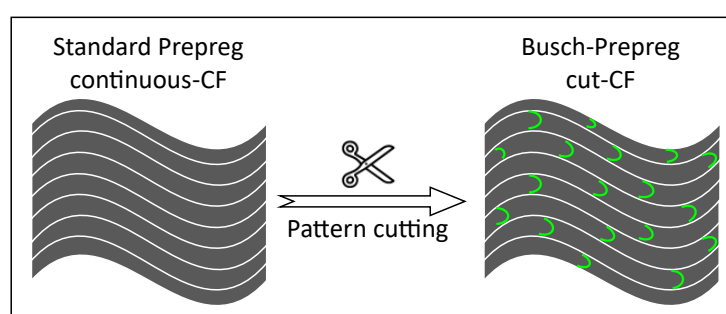


Figure 3.9: Illustration of the cutting manufacturing process performed by Composites Busch SA for the discontinuous reinforcement composite samples.

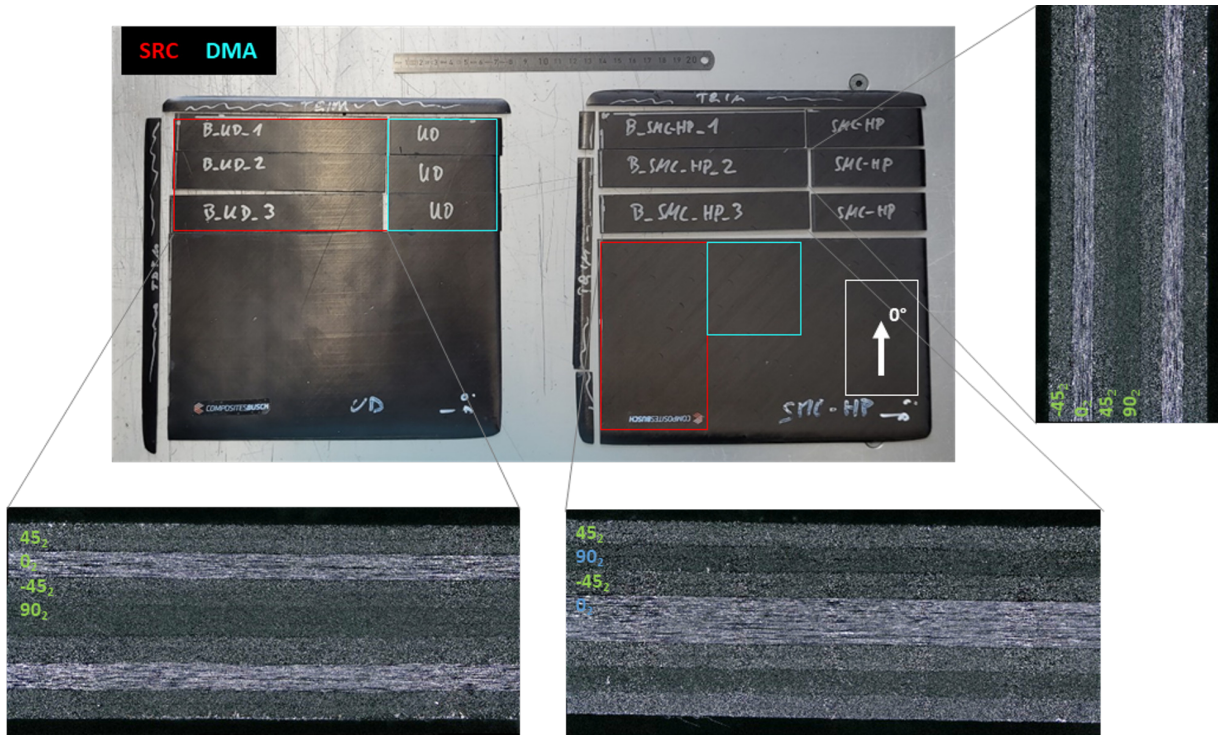


Figure 3.10: Continuous- and cut-CF laminate plates’ cutting plan for SRC and DMA samples. Numerical microscope cross-section images in 0° and 90° direction of the laminates.

3.2 Structural and physical properties evaluation methods

All the testing methods and sample version are summarized in the test matrix presented in table 3.5. Regarding the the bolt joint system, four analysis tools have been employed to evaluate this material grade and specific design. Dynamic Mechanical Analysis (DMA), tensile, shear, and tightening testing techniques were used to assess an adequate material selection based on established study-case requirements. Table 3.5: Overview of the test matrix reporting the testing methods and type of materials tested, with CT = continuous-CF and SH = short-CF.

		Bolt fasteners			Sandwich panel facesheets								
		SS	CF/PEEK CT	SH	Alu	CFRP	FFRP	FFRP+AlMg	CF-FF tbt	CF-FF pbp A B		CFRP-Busch CT	Cut-CF
Structural and physical testing	DMA	x	x	x	x	x	x	x	x	x		x	x
	Tensile	x	x	x		x	x	x		x		x	x
	Shear	x	x	x									
	Tightening test			x									
	Outgassing			x		x	x	x	x	x			
	Vibration Panel 4pt Bending Panel				x	x				x			
Demise testing	TGA		x	x	x	x	x	x	x			x	x
	Thermal conductivity					x	x	x	x				
	SRC	x	x	x		x	x	x	x			x	x
	PWT					x	x	x	x	x	x		

For the sandwich panel facesheets also four structural properties assessment methods were used. A DMA, tensile, vibration and a 4-pt bending testing techniques have been were employed to evaluate new material combinations based on the selected ClearSpace (CS)-1 study-case requirements.

The presented microscopic analyses were performed with a Keyence VHX-5000 digital microscope for the

optical images at LPAC and a Zeiss Gemini 300 scanning electron microscope for the Scanning Electron Microscopy (SEM) and Energy-dispersive X-ray spectroscopy (EDX) analyses at the CIME lab. The samples were prepared after a sequential polishing method. This latter was conducted with the following sandpapers gradings #250/500/1000/2400/4000 under constant water flow, and then a finish step with $1\mu\text{m}$ and $0.3\mu\text{m}$ Alumina powder suspension.

3.2.1 Dynamic mechanical analysis

A TA Q800 analyzer equipped with a 3-point bending fixture, as displayed in figures 3.11 and 3.12, was selected for thermomechanical evaluation in the space mission temperature range. Measurement of the storage modulus in bending as a function of temperature was used to assess the structural properties degradation onset temperature. In parallel, though the loss modulus and the ratio of loss to storage modulus, $\tan\delta$), the damping properties and the glass transition temperature, measured from the $\tan\delta$ peak could be measured. Following ASTM D4065-20 recommendations, the testing parameters were set with a temperature sweep from -150°C to 350°C , a heating rate of $10^{\circ}\text{C}/\text{min}$ and a constant 0.1% strain amplitude oscillating a 1Hz.

Bolt joint system

The CF/PEEK sample's 2 mm thickness was selected to comply with the load cell limitations. Five samples of both continuous- and short-CF were polished to the specified dimensions and tested as displayed in figure 3.11.

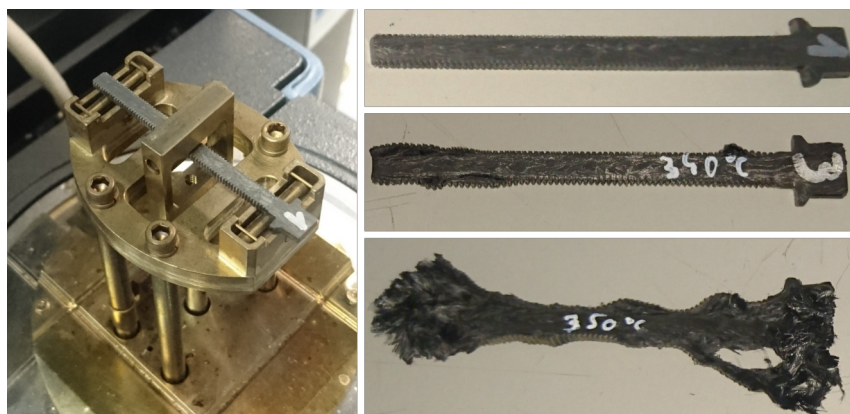


Figure 3.11: On the left, DMA 3-pt bending setup. On the right side, comparison of an untested sample (top) with two tested samples with respectively 340°C and 350°C final tested temperatures.

Facesheets

As depicted in figure 3.12, samples of respectively 60×10 mm length and width were extracted from the reference aluminium alloy sandwich panel and the five different composite laminates manufactured with a diamond disk blade at the EPFL ATMX workshop. These dimensions were selected based on ASTM D7028-07 recommendations, and setup limitations. These laminates characteristics are detailed in table 3.3. Five samples of each skin materials were evaluated.

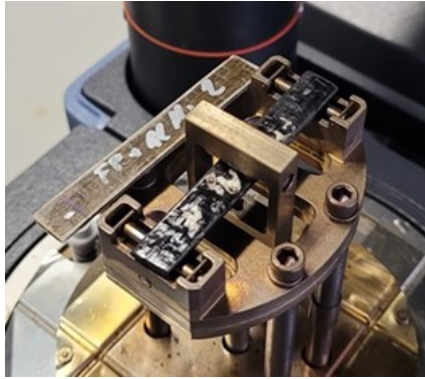


Figure 3.12: DMA 3pt-bending setup with on the left an untested FFRP+AlMg sample and on the right an installed and charred sample after testing up to 350°C.

3.2.2 Tensile test

Bolt joint system

The test procedures follow ASTM D3039 and ASTM E8 to evaluate, respectively, the tensile properties of the composite and the metallic samples. A displacement rate of 2 mm/min was selected. The load is controlled by a 100 kN MFL Universal Tensile Machine (UTM) machine with a self-design M5 bolt holder. The sample displacement is measured by a video extensometer equipped with a bilateral telecentric lens and a red backlight, as exposed in 3.13. The fastener assembly was composed of a CF/PEEK or SS bolt with an SS nut in both cases. The test outputs are the fracture behaviour, the elastic modulus and UTS following ASTM D3039 chord calculation method, where the thread stress area is calculated from the ASTM F606-21. The yield properties were evaluated from the deviation of the linear-elastic behaviour for the CF/PEEK, and based on the 0.2% offset for the SS. Five samples of SS, continuous- and short-CF were tested.

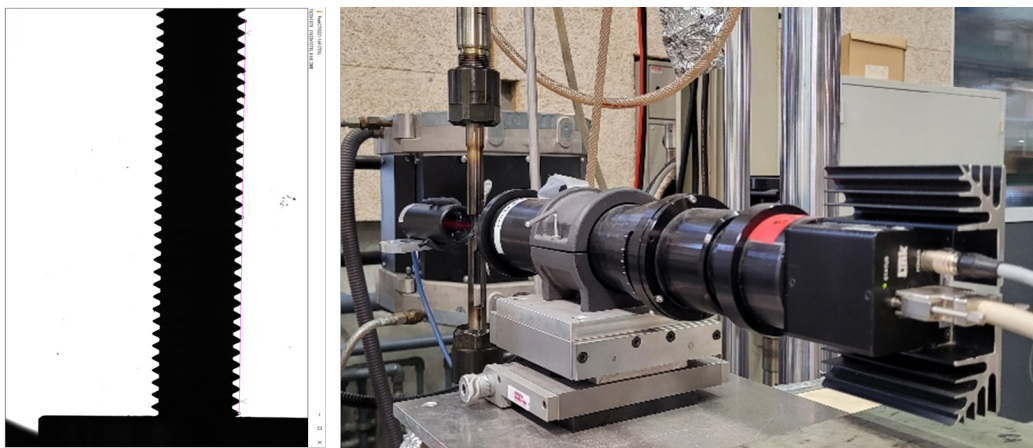


Figure 3.13: Tensile test setup with the video extensometer at the forefront and the red backlight on the left. The sample is placed in between allowing a strong and clear contrast ideal for displacement measures.

Facesheets

The static tensile performance of the composite skins was assessed using coupon samples cut to dimensions of 185x25 mm with a diamond blade on a table saw. These samples included 25x40 mm aluminum tabs fixed with a fast-setting COTS Araldite adhesive, following again the ASTM D3039 standard recommendations. The experimental setup utilized a WalterBai 60kN UTM machine equipped with a double regime extensometer and hydraulic gripping system, as illustrated in figure 3.14, and employed a displacement rate of 2 mm/min.

Only composite skin versions were tested. Four coupon samples were extracted from the remaining manufactured PWT laminates out of the four composite skin versions: CFRP, FFRP, FFRP+AlMg and CF-FFBP. For the ply-by-ply (PBP) samples, only version A was used as it was more representative of the facesheet layup sequence, with less CF reinforcement. The detailed characteristics of the laminates' are presented in table 3.3.

From this test, the fracture behaviour, the elastic modulus, the yield and ultimate strength characteristics can be extracted following ASTM D3039 chord calculation method.

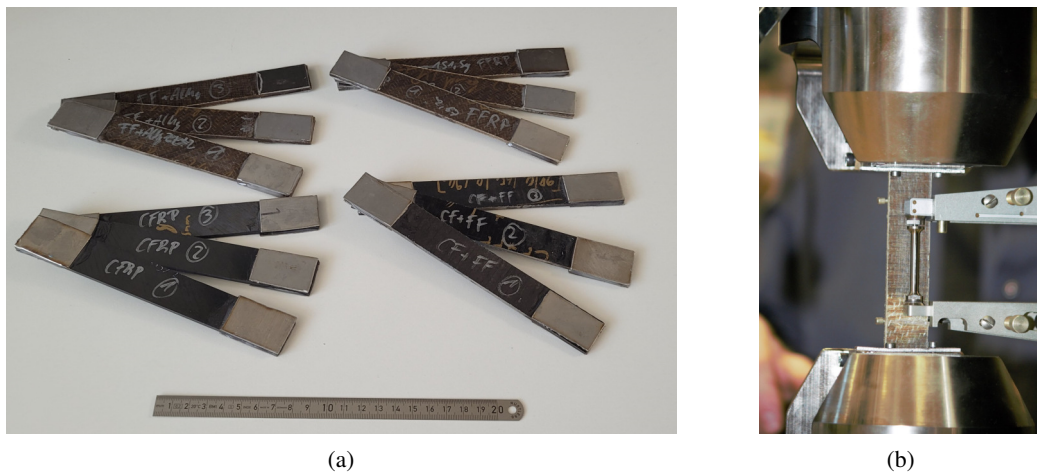


Figure 3.14: Composite facesheets tensile samples (a) and test setup from for laminate testing with the hydraulic clamps and a double extensometer (b).

3.2.3 Single shear test | Bolt joint system

The test procedure is based on ASTM F606/F606M-21 with stainless steel plates holder. The fastener assembly was composed of a CF/PEEK or SS bolt with a SS nut in both cases, and SS washers were placed on each side of the assembly to distribute the stress as illustrated in figure 3.15. A selected preload of 2.5 kN was applied by a respective tightening torque of 2.5 Nm and 5.1 Nm for CF/PEEK and SS samples by using a dynamometric torque-wrench, then the plates were separated at a speed of 2 mm/min. In addition to force and displacement, a camera monitored possible bolt and nut rotation with respect to the holding plates. Five samples of all three materials were tested.

3.2.4 Tightening capability cycling test | Bolt joint system

This test aims to evaluate the cyclic preload capacity and lubrication influence on the novel short-CF/PEEK bolt (same grade as indicated in table 3.1). It was performed by the Construction Laboratory from SFS Groupe Schweiz AG on a dedicated setup. It is composed of a 200Nm drive motor mounted on a vertical drill-mill machine, a 50Nm torque load cell and a 50Nm/25kN preload axial load cell. An AlMgSi grade aluminium head plate was selected to reproduce a baseline sandwich panel aluminium insert.

The test campaign was carried out in two phases, first a single tightening cycle up to a defined preload to assess IPA effect as tightening lubricant against unlubricated samples. Five samples of each batch were tested. Then following the first phase results, a second phase consisted of a tightening cycling test of ten repetitions up to a defined preload, where again five samples each were tested.



Figure 3.15: Single shear setup to evaluate for M5 bolt shear strength.

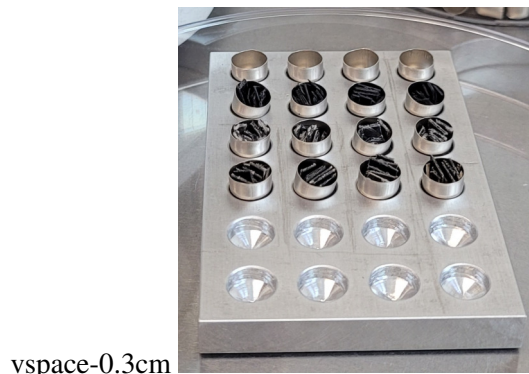
3.2.5 Outgassing test

The initial step to evaluate a material's compatibility for its use in the space environment is its behavior under vacuum and high temperature. This evaluation is performed by an outgassing test, which allows the assessment of the released mass and identification of potential critical components/chemicals under a typical space environment.

To perform such evaluation on our novel materials, the μ -VCM - Screening Outgassing Facility at ESA-ESTEC (Noordwijk, the Netherlands) was employed. Samples, with a mass ranging between 100-300 mg, were prepared in stainless steel crucibles, as depicted in figure 3.16. They were then conditioned in a controlled environment of $22\pm 3^\circ\text{C}$ and $55\pm 10\%$ RH at least 24 hours prior to testing. The testing sequence, based on the ECSS-Q-ST-70-02C standard, starts with the placement of the weighted samples in the test chamber. For 24h, a high vacuum lower than 10^{-5} mbar and a temperature of 125°C are applied. After this, the samples are weighed twice, once right after testing and once again after 24h under the same conditioning as before the test.

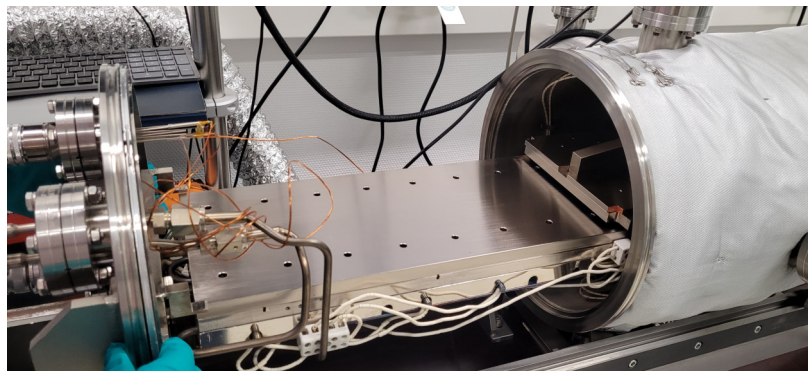
From such tests, four main metrics are extracted. Three are measured with microbalances: the Total Mass Loss (TML), the Collected Volatile Condensable Material (CVCML), and Recovered Mass Loss (RML). The Water Vapour Regain (WVR) is deduced from $\text{WVR} = \text{TML} - \text{RML}$. The outgassing acceptance limits established from the previous standard are displayed later within the results section.

For each materials, a batch of four samples were tested.



vspace-0.3cm

(a)



(b)

Figure 3.16: (a) Dedicated stainless steel crucible with composite laminate sample and (b) interior view of the μ -VCM outgassing chamber.

vspace-0.5cm

3.2.6 Vibration test - Space launch loads simulation | Sandwich panel

This vibration test aims to compare the three sandwich panel versions' stiffness response under through-plane dynamic loads corresponding to a typical payload onboard a VEGA-C launch. The three panel versions are characterized by their different skin materials detailed in table 3.4. The comparative analysis resulting from this test, assess the effect of hybrid fibre reinforcement on dynamic stiffness and damping properties.

To keep the test in a non-destructive range for the samples, a solid mechanics FEA static analysis was performed and controlled by a test engineer from the Mechanical Systems Laboratory (MSL) on COMSOL Multiphysics 6.0. The maximum stresses and strains of our panel samples model are evaluated under two load cases scenario, consisting of a positive (+z) and then a negative (-z) exaggerated vertical 100G acceleration. The results ensured that an under such positive or negative acceleration, the samples are maintained

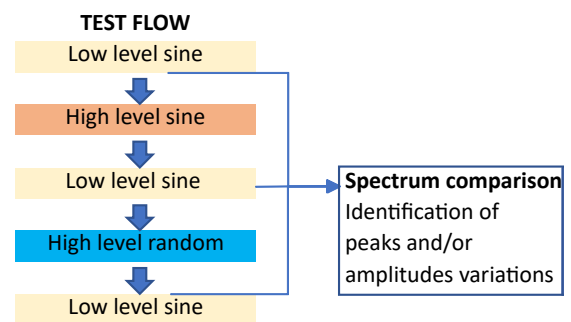


Figure 3.17: Vibration qualification test sequence applied to all three versions.

Materials & Methods

in an elastic regime. This step is used to set an acceleration limit in the vibration table control software.

The test was performed by the TEC-MTV office personnel in the MSL cleanroom of ESA-ESTEC on a LDS 22kN electrodynamic vibration combi-shaker. Standard payload-type Vega-C launch validation conditions were selected based on the MSL Procedure for the execution of Vibration Test of Space Equipment guidelines. These conditions include three test regimes: a low and high level sine (abbreviated Low Level (LL)-sine and High Level (HL)-sine, respectively) and a high level random (HL-random). Such an approach allows the potential assessment of response differences under harmonic versus random regimes. The testing sequence is presented in figure 3.17, and the specific parameters are detailed in Table 3.6. Ambient testing conditions included a temperature range of $(22\pm 3)^\circ\text{C}$ and a relative humidity range of $(50\pm 20)\%$.

The dimensions of the panel samples (390x390mm) were limited by the dimensions of the furnished baseline aluminum panel and the autoclave to produce the facesheet. As for the support system illustrated in figure 3.18, a dedicated aluminum supporting plate and specific bushing for the four central M6 screws were manufactured to allow a representative and balanced test condition. Following ECSS-E-HB-32-20 and using a standard preload calculator, an installation torque of 1Nm was set based on the samples' materials and clamping force-torque, ensuring it stays within the elastic domain of the thin aluminum honeycomb core. For this test a single panel of each version were tested, so a total of 3 panels (aluminium, CFRP and CF-FFpbp).

Vibration control was achieved using two PCB-Piezotronics accelerometers at the center of the assembly: one pilot (P1) and one co-pilot ($CP1_{X/Y/Z}$). The co-pilot was used to check cross-axis excitation and verify the input level. Four accelerometers, glued at each corner using Loctite 454, were employed to monitor the panel's reactions to the vibration inputs. These accelerometers provide FRF curves.

The sample stiffness related to the natural frequencies can be identified from clear peaks of the amplitude corresponding to specific vibration modes. This information can then be used to calculate the damping ratio using the half-power bandwidth method, as detailed by Joshi [84]. This parameter, usually named as ζ , indicates the oscillation decay rate and is calculated as follows: $\zeta = f_N / ((f_b - f_a))$, where f_N is the natural frequency of interest, and $f_{(a,b)}$ are the frequencies corresponding to $Amp_{max} / \sqrt{2}$.

Table 3.6: Vibration test levels characteristics

	Frequency [Hz]	Sweep direction: one up Amplitude [g]	Sweep rate [oct/min]
Low Level Sine	5	0.2	2
	2000	0.2	
	Frequency [Hz]	Sweep direction: one up Displacement/Amplitude	Sweep rate [oct/min]
High Level Sine	5	15mm	4
	11.5	4g	
	100	4g	
	Freq. Bandwidth (20-2000Hz) Duration=1min Frequency [Hz]	PSD [g^2/Hz]	Global Level [gRMS]
High Level Random	20	+6 dB/oct	6.014
	100	0.063	
	350	0.063	
	1000	-6 dB/oct	
	2000	-6 dB/oct	

Such testing also validates the core-skin manufacturing quality and allows for FEA analysis correlations.

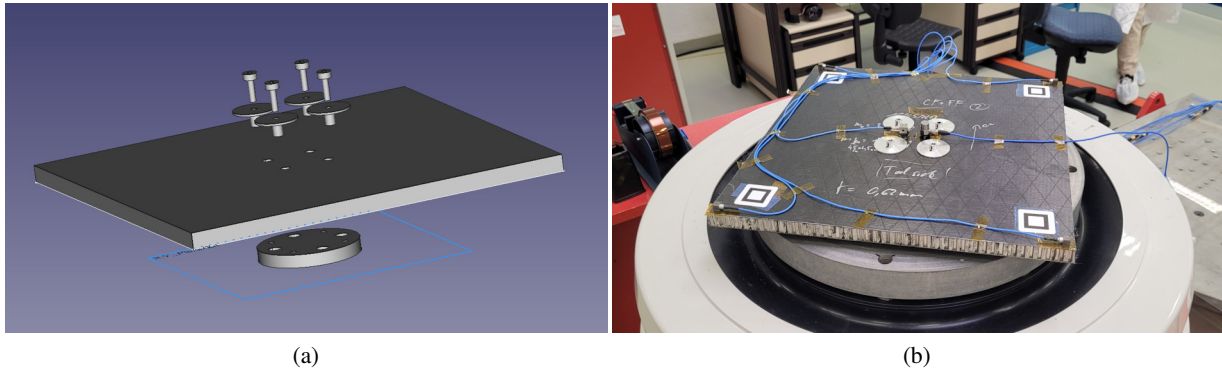


Figure 3.18: Sandwich panel vibration test (a) exploded view of the sandwich panel assembly Computer-Aided Design (CAD) 3D model, and (b) final testing configuration.

Vibration modes

Prior to testing, a FEA analysis was conducted to predict the natural frequencies and vibration modes of the three panels. Performed on COMSOL Multiphysics 6.0 using the dedicated eigenfrequencies analysis tool, the analysis involved setting the designed supporting adaptor plate and four top circular pads in a fixed condition. Each element was assigned the required material engineering constants calculated from ESAcomp laminate analysis tool. For simplifications both facesheets were modelled as a transversely isotropic material, and the core as a bulk element having the properties of the honeycomb structure.

3.2.7 4-pt bending test | Sandwich panel

This destructive static mechanical test method allows the evaluation of the sandwich structure flexural stiffness, the skins compressive/tensile strengths in addition to core-skin bond quality/shear strength in the case of a failure of this region. This test aims to compare the three skin's materials bending performances within a sandwich assembly, and the evaluation of the novel hybrid composite skins versus the aluminium and CFRP baselines. Furthermore, the flax relative mechanical performance degradation highlighted by previous works such as [85] and [86] motivated a hygroscopic sensitivity analysis. Out of the three recovered sandwich panels from vibration test, 6 samples per panels were cut-out. Then half of these samples were placed in a Heraeus HC7015 computer-controlled climatic chamber under a 95% RH and 20°C environment for 18 days. This aging duration was set as a trade-off between the lowest conditioning time and water absorption stabilization based on the moisture diffusion analysis of Beelen [86] and based on ESA TEC-MSP lab recommendations. The resulting water intakes measured immediately after their extraction from the climatic chamber are reported in the following table 3.7. The samples flexural behaviour was then tested within 2 hours after their extraction.

Following ASTM-D7249-20 recommendations, the equipment used for the 4-pt bending consists of a Table 3.7: Water intake measurements of the different sandwich panel versions after 18 days week at 20°C and 95%RH.

Facesheet material	Aluminium	CFRP	CF-FFBPB
Average sample mass [g]	43.70±0.25	38.00±0.33	48.21±0.31
Average intake mass [g]	0.14±0.04	0.16±0.07	0.51±0.04
Intake relative to sample dry mass	0.33%	0.42%	1.06%

Zwick&Roell UTM machine located in the Discovery Learning Lab of EPFL. It was mounted with a respective upper an lower span length of 170 mm and 340 mm. The machine was equipped with a 100kN

Materials & Methods

load cell, paired with a Correlated Solutions DIC monitoring system to extract the region of interest strain and deformation, defined as the section area between the load spans with the core and both skins visible. A cross-head vertical displacement of 6mm/min was set in accordance with ASTM-D7249-20 recommendations. Based on the same standard, the sandwich sample dimensions of 390x45 mm in length and width was selected, with a thickness ranging between 16-18 mm. The monitored reference surfaces of the samples are prepared with a random speckle pattern to facilitate accurate displacement acquisition with the DIC's camera. This is achieved by using a white base coated with a randomly sprayed black pattern, following manufacturer and literature recommendations [87]. The test runs were performed with the support and expertise of Vincent Varanges from LPAC.

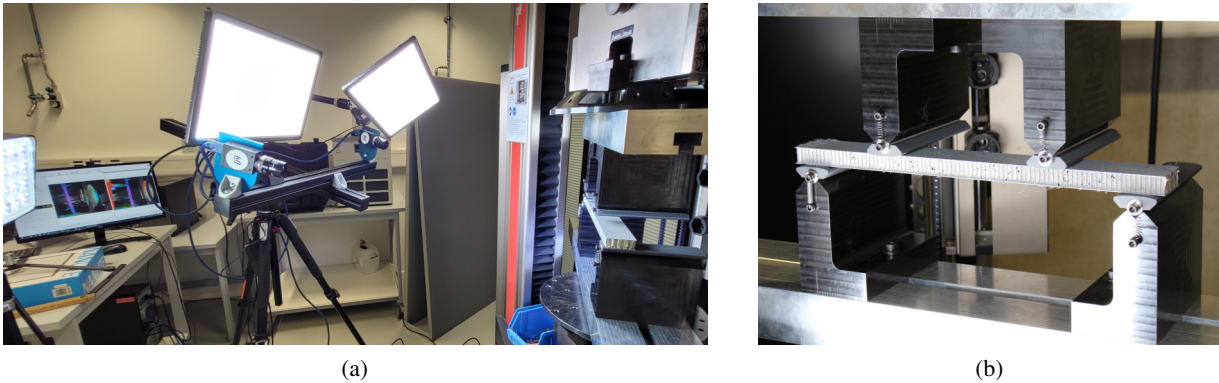


Figure 3.19: (a) Test setup mounted with a DIC monitoring system. (b) Close view of the 4-point bending support bench with dedicated 3D printed flat tabs and a full aluminium sample coated with a random speckle pattern.

3.3 Demise evaluation methods

The quantification of the demise is based on respectively two and four different testing methods for the bolt system and the sandwich panel facesheet, respectively. They both underwent thermogravimetry analysis, and the Static Re-entry Chamber (SRC) developed in this thesis was employed to assess the demise capability under a typical destructive UC re-entry environment. Then, additionally for the sandwich panel skins, a thermal conductivity comparative analysis and a plasma wind tunnel test complete the list of the demise evaluation methods, since a modification of the matrix to ensure faster re-entry was investigated. The evaluation techniques presented in this section allowed the measurement of onset temperatures and timing of mechanical loosening, demise/degradation rate of the samples, in addition to the observation of characteristic physical demise behaviours.

3.3.1 Thermogravimetry analysis

A Perkin&Elmer TGA 4000 equipment was used for thermophysical measurement with machine's limits testing parameters set with a temperature sweep from 30 to 900°C and heating rate of 40°C/min. These settings were chosen to assess thermophysical properties under conditions as closely resembling re-entry as possible. The analysis was performed separately under synthetic air (20%v/v O₂) and nitrogen atmosphere (N₂) with alumina crucibles and initial sample masses ranging between 10 to 15 mg. This method evaluates the mass loss of a small sample along with temperature increase, allowing the identification of the degradation onset temperature, the mass loss rate (DTG) and the residual mass as described by ASTM E1131-20. For each skin materials five samples were evaluated..

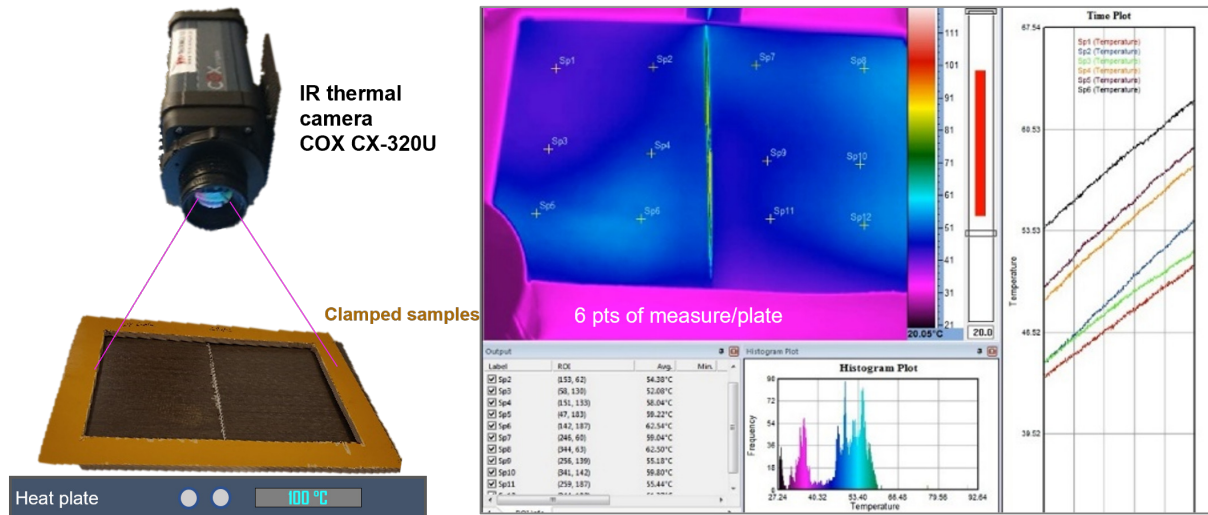


Figure 3.20: Thermal conductivity analysis setup schematic on the left and output camera vision on the right with the six measurement points per plate.

3.3.2 Thermal conductivity | Sandwich panel facesheets

For the thermal conductivity evaluation, a self-assembled setup was used to assess the variations resulting from the integration of a metallic filler in composite laminates. The objective of the test was to assess the influence of a 1%wt resin of AlMg μ -powder filler in FFRP on the through-thickness thermal conductivity. To achieve this, a dedicated setup was assembled, consisting of a COX CX-320U infrared thermal camera, an insulated clamping frame for homogeneous contact, a control thermocouple, and a high-power heating plate support, as illustrated in figure 3.20. Two main calibration steps were performed. In the first step, six surface measurement points per sample were set from the frame and camera field of view. Then, a sample emissivity correction was established with the control thermocouple along different temperature points. The testing procedure started with the heating of the base plate to 100°C. Once complete thermal stability was achieved, recording is set on, and the samples, placed clamped side by side, are rapidly lowered and immediately clamped to the heat plate. The test is terminated once the thermal stability of the whole system is observed.

The remain of the thick PWT laminates manufactured were used as single sample. The CFRP | CF-FFpbp and FFRP | FFRP+AlMg pairs of skin versions were tested comparatively 3 times. As this setup and analysis do not allow a direct quantitative determination of the thermal conductivity, an experimental-to-model correlation step with the COSMOL thermo-physical model was employed to estimate the thermal conductivity improvement by charging the composite matrix with this metallic filler. A 2D transient thermal conduction evolution model with a linear applied surface temperature and ambient surface radiation was used, with specific material properties (density, thermal conductivity, specific heat, emissivity) implemented from previous material tests.

3.3.3 Creep Static Re-entry Chamber (SRC)

A representative re-entry demise capability cannot be directly extrapolated from TGA and DMA testing with their respective 40°C/min and 10°C/min heating rates whereas the realistic conditions are above 150°C/min heating rate. Therefore a novel SRC was proposed and developed throughout this project, with the aim to propose a method that can characterize thermal and structural demise capabilities of various

sample configurations, and perform comparative analysis during material development.

From these objectives, several testing setup requirements were first established. A controlled environment chamber with medium/high vacuum level capability is necessary to closely replicate the space re-entry environmental ambient conditions. Such chamber also needs to be coupled to both a high heating rate heat source and a mechanical testing system. This way, it is possible to pre-load a sample to simulate a realistic loading condition for a given part, then to subject it to a given fast heating rate under a vacuum atmosphere, and record both the temperature, as well as the strain during the test.

The selected testing assembly is thus composed of a hydraulic MFL 100kN UTM machine equipped with a dedicated load cell calibrated for displacement monitoring. Based on the equipment availability, a tensile creep loading was selected to assess the mechanical response. The environmental chamber is composed of a quartz tube allowing optical test monitoring capability connected to a Pfeiffer HiCube dual vacuum pump system, integrating a primary and a turbo- pumps. To prevent massive combustion/pyrolysis byproducts to enter the pump, a cold trap stage was installed on this latter input. A vacuum pressure of 10^{-4} mbar can be achieved with the complete testing setup connected. Regarding the heat source, it is provided by a 12 kW parabolic halogen infrared heater from ChamberIR compatible with the quartz tube. It is assumed to be capable of a $100 \text{ kW}/\text{m}^2$ heat flux. A schema of this setup is illustrated in figure 3.22 and pictures can be found in figure A.5 in the appendix A. The setup assembly and calibration steps were performed with the support and expertise of Raphaël Charvet from LPAC.

Here are displayed the STS-96 and UC re-entry temperature profiles implemented as references to the Static Re-entry Chamber (SRC) temperature control.

The applied heat flux is set to follow two specific predesigned uncontrolled re-entry temperature profiles via Thermocouple (TC) control, these respective temperature profiles are presented in figure 3.21. The first recreates the Space Shuttle Mission 96 (STS-96) external temperature re-entry data [42], with a maximum heating rate of $350^\circ\text{C}/\text{min}$. For the second, the heating rate was reduced by a factor of 3 ($115^\circ\text{C}/\text{min}$) to follow a typically shallow uncontrolled re-entry heating rate, following discussions and recommendations from the group of experts implicated in this project.

Regarding the data acquisition, three Type-K thermocouples were used to allow multilocation temperature measurements (top, center, and bottom of the sample for example), in addition to a Canon 700D high-definition optical camera which monitors the demise behaviour.

The testing procedure is based on the ASTM D7337/D7337M and sample manufacturer recommendations. Therefore this setup provides us with a displacement evolution along specific temperature profiles, the timing of the structural properties loosening onset, and re-entry environment-like demise behaviour. It was used for primary material selection screening prior to the complex and selective PWT testing campaign presented in the next section focusing on novel sandwich panel skin composite materials. The laminate plates were cut with a diamond disk blade at the EPFL ATMX workshop to obtain specific SRC samples with a length and width of 140×25 mm. These dimensions were selected based on ASTM D7337-12 recommendations, and setup limitations. A minimum of 2 samples per skin version and test conditions were evaluated.

Bolt joint system

For bolt sample type a tensile creep preload of 2.9kN was chosen following the manufacturer recommendations, corresponding to a 229 MPa preload stress.

A dedicated sample holder was designed by myself and manufactured by the École Polytechnique Fédérale de Lausanne (EPFL) ATMX workshop. It is made of a 1.4881 grade refractory nickel-alloy steel to prevent

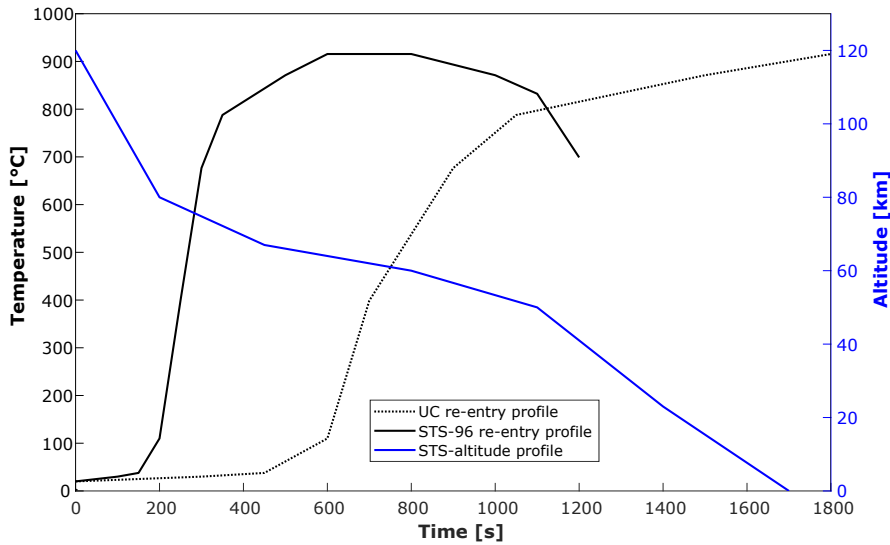


Figure 3.21: The STS-96 (categorised as a highHR) and a typical Uncontrolled (UC) (categorised as a low HR) re-entry temperature profiles and heating rates.

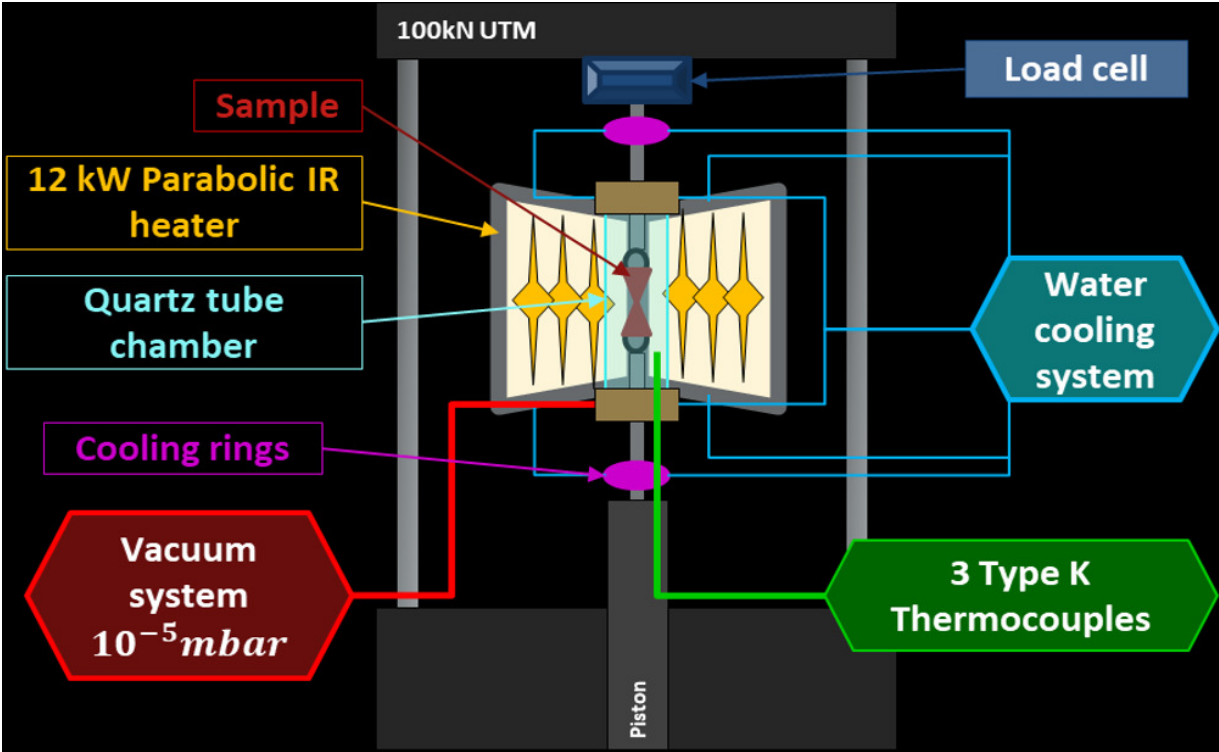


Figure 3.22: Self-designed static re-entry chamber schematic illustration.

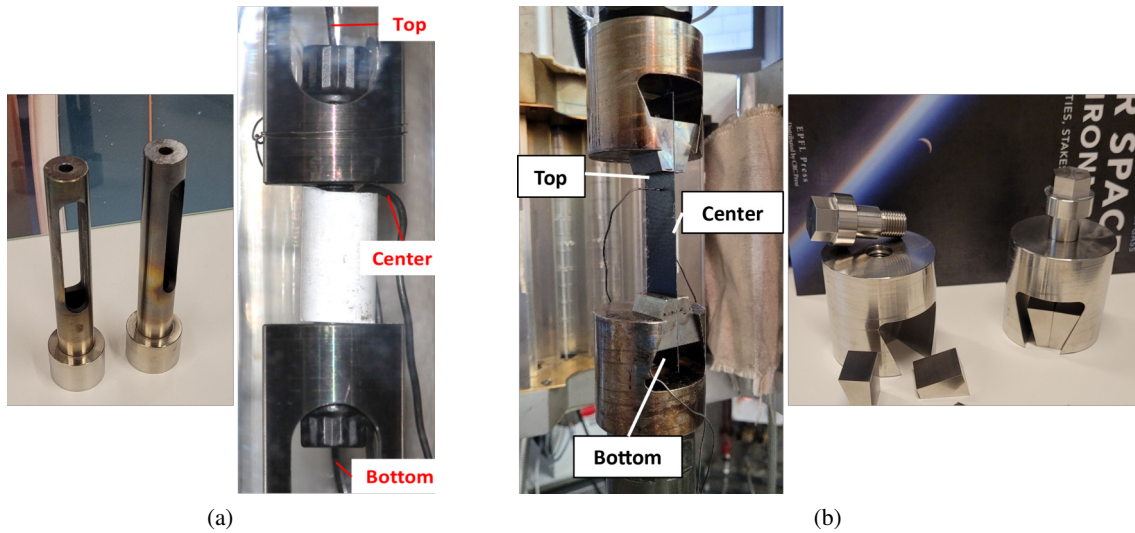


Figure 3.23: Picture of the two tensile creep test sample assembly types with the three thermocouples' positions. (a) The bolt/nut through-thickness joint tensile with alumina cover. (b) The thin-flat laminate sample tensile creep test gripping system.

any distortions during the multiple test runs at relatively elevated temperature. The design and assembly can be observed in figure 3.23. An alumina tube is placed on the bolt sample fitting the holder central spacing to act as a heat shield to simulate the fastener's real configuration where only the head/nut are exposed to the heat flux.

Sandwich panel facesheets

Similarly to the bolt joint system, the demise evaluation at coupon material level of the five sandwich panel facesheet versions (CFRP, FFRP, FFRP+AlMg and the two CF-FFTBT and PBP hybrids) required a specific sample holder. The designed gripping fixture system illustrated in figure 3.23, is composed of 2 threaded adaptors, 4 sliding truncated cones acting as grippers and 2 pins inserted on the top of the previously drilled sample. These latter allow the sliding cones to increase their lateral grip. All these elements are also made of the similar refractory steel.

With samples having different thicknesses, a creep preload of 20 MPa was set for all the samples instead of a force. This value was selected to stay in the elastic regime of all the samples while staying over the load cell minimum range. The testing procedure and parameters have been selected based on ASTM D7337/D7337M, combined with sample and equipment limitations.

3.3.4 Plasma Wind Tunnel | Sandwich panel facesheets

The state-of-the-art ground testing for demisability evaluation of materials or components is the plasma wind tunnel, which can recreate a substantial portion of the extreme aerothermodynamic load conditions encountered during an orbital re-entry. This is achieved through the combination of a vacuum chamber and a plasma generator. Calibration runs, performed with a calorimetric copper heat-flux probe and adjustments to nitrogen and oxygen gas inlet rates, enable the selection of high-fidelity test conditions. However, this complex facility currently presents some limitations, such as sample dimensions limited by the plasma plume to maintain a homogeneous heat flux along the object of study. Furthermore, the testing procedure allows for the establishment of only one steady-state heat flux condition during a test run, thereby preventing the simulation of multiple re-entry trajectory follow-up conditions. This stands in

contrast to a transient heat flux input, such as the static test presented before, which is more representative in terms of the heating profile.

A test campaign opportunity was offered by the IRS through our project partnership in their PWK4 (Plasma Wind Kanal 4) facility to assess, at the material level, the demise performances of our novel hybrids and metallic filler influences. The PWK4, as depicted in figure 3.24, was equipped with the RB3 thermal plasma generator operating in a medium vacuum environment. Further details about the setup can be found in the study conducted by Pagan et al. [88]. The testing range envelope shown in figure 3.26, overlays the test capabilities of the four IRS PWT facilities (PWK1-4) and specific S/C re-entry trajectories. They are displayed in terms of total pressure (plasma flow pressure) and specific enthalpy which allows direct relation to the altitude and heat-flux linked to the Ballistic Coefficient (BC), these parameters are displayed as a background grid. So this envelope graph guided our selection of a testing facility, the PWK4, and two specific test conditions based on a typical UC re-entry case (represented in orange), and a previous FFRP test campaign conducted by IRS and Bcomp. These conditions are a Medium Heat Flux (MHF) and a (High Heat Flux (MAX-H)). Table 3.8 provides the specifications for these conditions.

Based on the test run complexity, a single sample from each of the six selected composite materials were tested. A fix test duration of 60 seconds for all the runs was selected after two initial tests with a CFRP and a FFRP under the highest heat flux conditions, MAX-H. Where The first run with CFRP was terminated after 190 seconds, a duration previously set based on previous test campaigns of the IRS with a similar material. Then the FFRP sample demised completely after 60s and exposed the bare sample holder to the plasma flow, thus setting the test sequence duration. To prevent exposing again the sensitive back pyrometer, the FFRP+AlMg sample was not tested under this high heat flux condition as it was expected to perform a similar or even faster demise. All the test runs were performed by the IRS expert team conducted by Adam Pagan.

Table 3.8: Selected test conditions detailed parameters

Condition name	MHF	Max-H
Reference heat flux [kW/m^2]	520	925
Measured heat flux [kW/m^2]	435	790
Ambient pressure [Pa]	41	27
Reference stagnation pressure with Pitot [Pa]	415	665
Mach number from Pitot [-]	2.92	4.72
Plasma mass specific enthalpy [MJ/kg]	13.7	22.3

Regarding the sample holder and geometry, the IRS well-used coin-shaped sample holder probe was chosen, as such design allows a direct comparison to previously tested materials. Its ring clamping system,

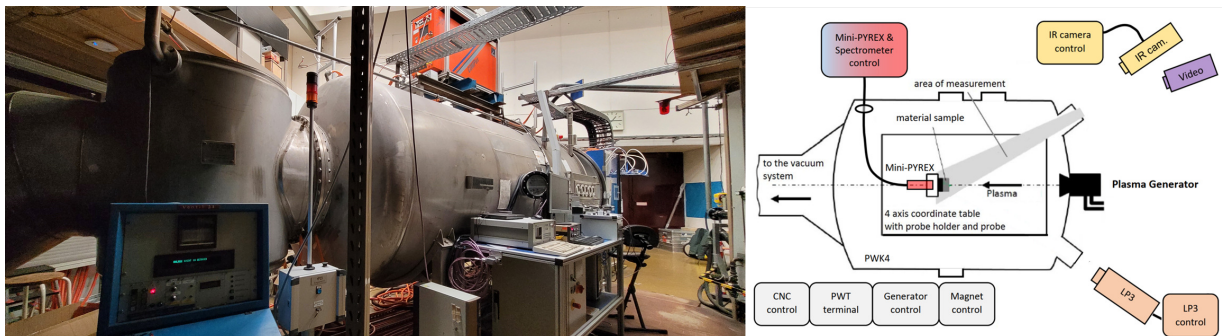


Figure 3.24: PWK4 testing facility at IRS and its schematic view with the different monitoring equipment. Modified monitoring setup configuration presented by Pagan et al. [18].

Materials & Methods

however, results in covered sample edges, preventing fiber or ply edge shear spallation initiated by the plasma pressure flux. The trade-off between these aspects can be further evaluated in the next testing phase at the component level. This design aims to prevent any shear forces or fast delamination to have a complete view of the demise process through the sample thickness, and for example, can be representative of continuous fibres wrapped structure such as a pressurized tank. Therefore, a truncated cone geometry is used with the small surface diameter of 26.5 mm, side angle of 30° and a thickness ranging between 2.5 and 4.5 mm. This shaping was performed with a diamond saw cutting followed by a micro-precision lathe machining of the laminate plate at the EPFL ATMX workshop. The resulting sample shape and holder assembly are illustrated in the following figure 3.25.

As described in the materials section of this chapter, six composite types have been selected based on those tested with the static re-entry chamber. This time, additional plies were added to meet the thickness requirements, along with two versions of the CF-FFPBP hybrid type (A and B), as reported in table 3.3. These 2 variations are differentiated by their successive carbon fiber layer thicknesses, where 0.116 mm and 0.348 mm are the characteristic of respectively the version A and B, aiming to evaluate their influence on the ablation behavior.

Several non-invasive monitoring equipment modules are installed, including an optical Canon 700D camera, a KE technologies linear pyrometer LP3, and a LumaSense MCS640 thermographic imaging camera, acquiring images of the sample's top surface for general demise behavior and temperature. These instruments have a sensitivity limit of 900 K and are calibrated around 960 nm to avoid air plasma irradiation. A Mini-PYREX pyrometer is also installed to monitor the sample's back surface temperature through a dedicated optical fiber mounted in the sample holder, as observed in the detailed figure 4 in the work of Pagan et al. [88].

To describe and identify specific degradation behaviors, images are captured and the mass measured both before and after testing. This is coupled with visual observation and an extensive analysis of the sample surface temperature throughout the test run using the described sensor apparatuses. Given the high temperatures involved, post-test data correction is essential to ensure accurate temperature data obtained from the thermal camera and both pyrometers. This correction relies on a temperature-dependent emissivity, based on previous tests conducted at IRS's emissivity measurement facility.

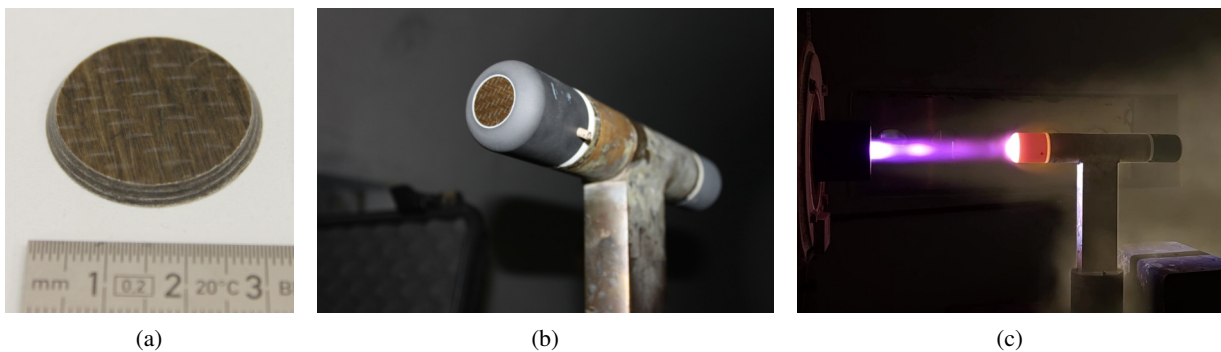


Figure 3.25: (a) An FFRP coin sample prior testing, (b) the sample mounted on the testing probe, and (c) such setup under testing.

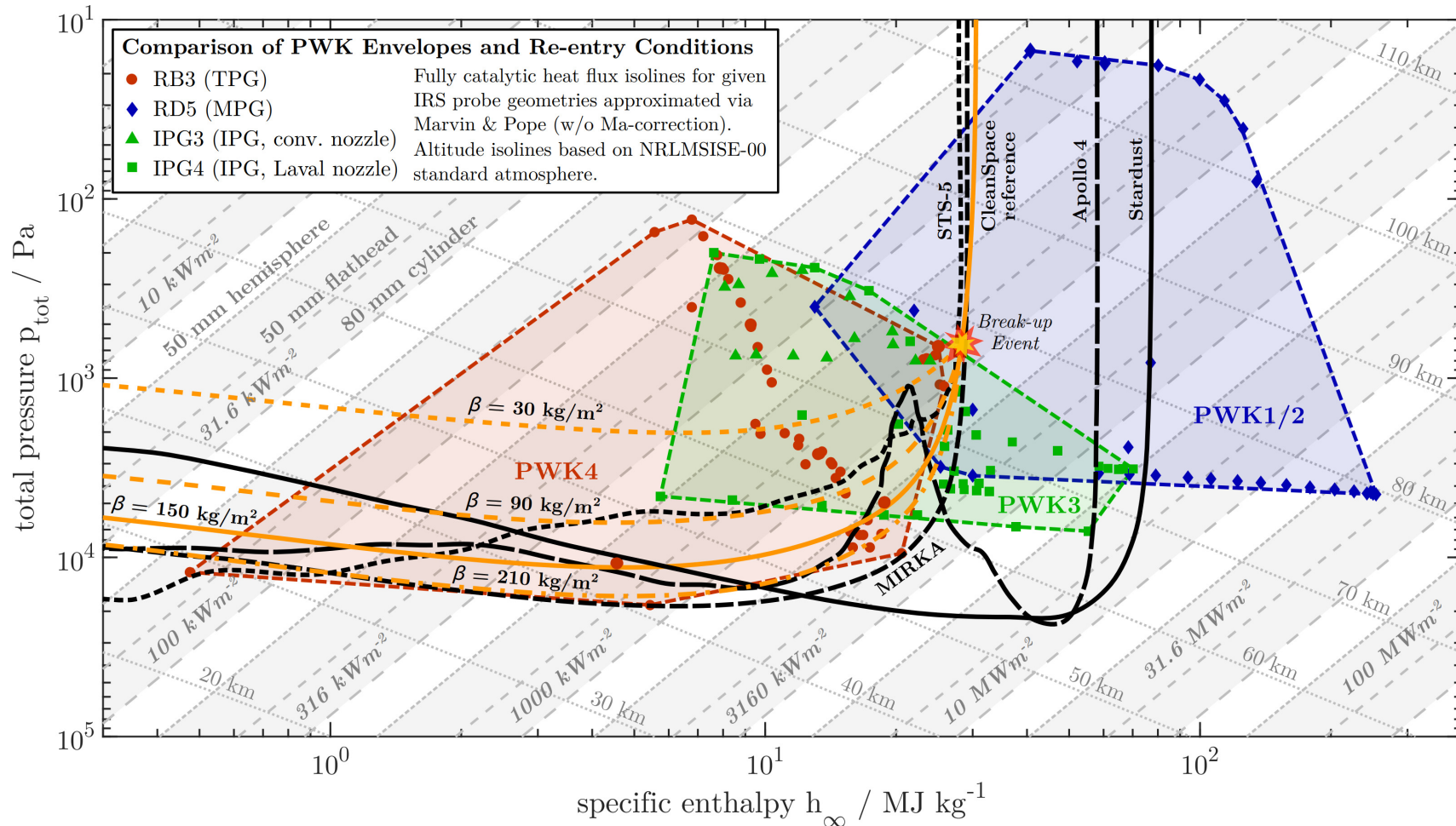


Figure 3.26: Superposition of various re-entry S/C trajectory condition and the four IRS plasma wind tunnel (PWK) facilities capabilities. In orange is highlighted a reference condition for a S/C, with a BC=150 kg/m², for an estimated uncontrolled re-entry trajectory, with a break-up just below 80km and propagation (dashed-orange) following the different fragments' BC. Credits to Pagan [19], IRS-Stuttgart.

4 Advancing spacecraft demisability through a novel composite bolt joint system: a step toward sustainable and safe space environments

This chapter, based on our article published in December 2023 [89], focuses on the evaluation of polymer composite bolts as the main structural satellite panel fastening systems to improve the overall spacecraft demisability during its destructive re-entry into the atmosphere as compared to baseline critical systems, while maintaining equivalent mission-relevant properties. Two carbon fiber-reinforced PEEK (CF/PEEK) designs were compared to a Stainless Steel (SS) baseline in terms of static properties at room temperature, dynamic properties over a temperature range, as well as demise capability by static re-entry simulation testing. The results led us to identify a promising short CF/PEEK composite bolt design.

4.1 Technology of interest - Why composite bolt ?

The present chapter presents the substitution of critical through-thickness bolt and nut materials by a high-performance composite system made of CF/PEEK, figure 4.1 illustrates such typical joining system. As gathered from the state of the art, this replacement should allow a much faster and earlier passive panel release, due to the matrix melting as opposed to degradation and charring in the case of thermoset matrices. The choice of PEEK as a matrix, and a composite, is dictated by the need for the bolt to exhibit mechanical properties that are sufficiently close to those of steel, so as to avoid multiplication of the number of required bolts, as would be the case if pure polymers such as Nylon bolts would be used. This approach differs from the OHB composite embedded insert, as documented in reference [90], as in our case the exposure to the high-enthalpy flow is direct, enabling a dedicated and specific break-up mechanism of the composite part. Such setup is characterized by the rapid initiation of matrix melting, facilitated by the high-enthalpy conditions, and the application of aerodynamic shear forces. Consequently, these factors synergistically encourage the intended separation of the assembly. In a manner similar to DLR's joint patches approach [91], our method also shares similarities, yet with reduced requirements for extensive structural analysis and integration steps due to the utilization of a conventional bolt joint system.

An overall higher spacecraft demisability, synonym of lower casualty risk, is thus expected following our latest results and previous studies, such as presented by Pagan et al. [53] and Patzwald [91]. Such technology should be integrated in combination with demisable panels, preventing critical increase of the casualty area and risk by spreading additional potentially surviving fragments. Such step can be assessed with the Survival and Risk Analysis—SARA dedicated module of the Debris Risk Assessment and Mitigation Analysis—DRAMA tool through the re-entry demise analysis of the panels' separations and the induced risk.

Material level characterizations in addition to mechanical capability and demise evaluation testing have been performed to allow the process of such component integration in a space-qualified structure.

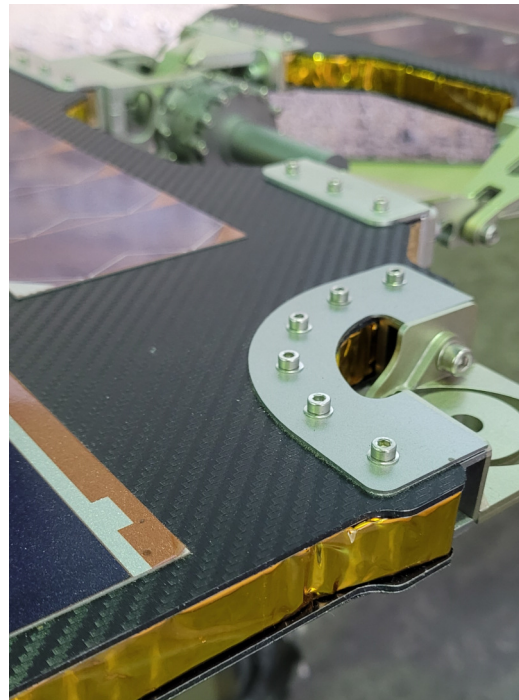


Figure 4.1: CFRP sandwich structure attached via through-thickness bolt joint system.

4.2 Mechanical performance comparative evaluation

4.2.1 Tensile and shear evaluation

Comparative tensile and shear stress–strain curves are provided in figure 4.2, with the material relevant properties reported in table 4.1. The CF bolt design with short fibers exhibits very similar behavior as the long CF one, with less than 5% loss of tensile or shear properties compared to the baseline continuous CF composite. With such small properties' differences, it is difficult to associate the reinforcement type as the major cause, as errors from measurement techniques, such as the displacement evaluation from the video extensometer which is limited by image pixel, and equipment sensibility have been evaluated to be around a 2–4% range each. In addition, the results found for the continuous CF bolt are in good agreement with the datasheet as indicated in Table 3.1.

As a result, 80% and 300% improvement of the specific tensile and shear strength, respectively, can be achieved by replacing stainless steel with CF/PEEK. Both composite fasteners show as expected a brittle fracture behavior. This is illustrated by their sharply ending stress–strain curves in figure 4.2, wherein comparison of SS samples shows a clear ductile fracture behavior with large plateaus and high maximum strain. If we focus more specifically on the shear failure trend, the SS samples showed an expected round ductile failure trend. Where the continuous CF/PEEK samples present sharp small multi-step failure due to the localized displacement of various continuous CF bundles within the geometry section. A behavior that is not observed for the short-reinforced version as these bundles have a finite length that acts as failure initiation points without allowing additional displacement.

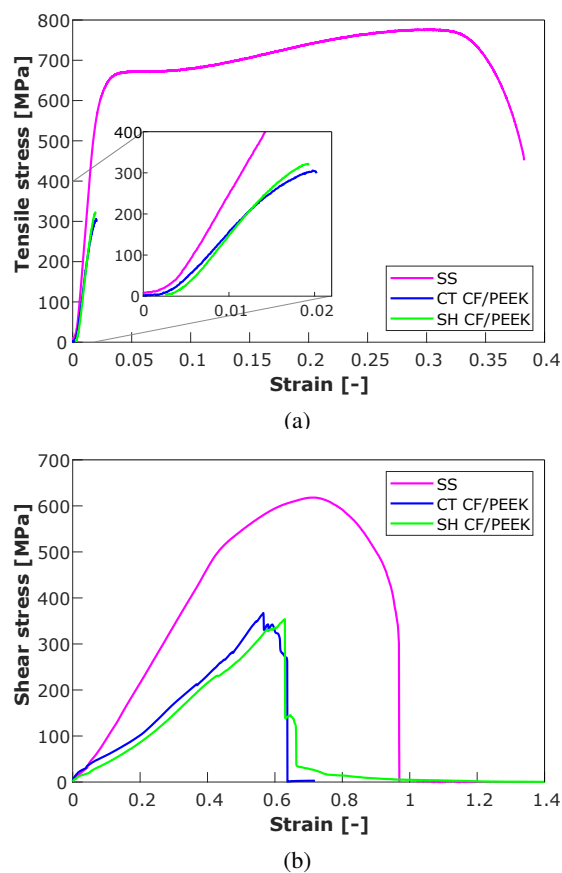


Figure 4.2: Comparative (a) tensile and (b) shear stress-strain curves between SS, continuous and short CF/PEEK samples.

Novel composite bolt joint system

Table 4.1: Summarized tensile and shear test results of the two CF/PEEK versions and the SS bolts, with ρ the density.

Material Reinforcement type	CF/PEEK- $V_f=55\%$		Stainless steel
	Continuous-CF	Short-CF	
TENSILE			
F_{max} [kN]	3.6±0.3	3.5±0.3	11.0±0.1
Yield stress σ_Y [MPa]	239.0±20.6	227.5±15.1	520.9±13.3
Max stress σ_{UTS} [MPa]	285.8±21.1	276.4±26.2	777.3±5.4
Specific strength σ_{UTS}/ρ [MPa/kg m³]	184.4	178.3	101.0
Elastic modulus [GPa]	56.4±3.6	55.2±6.5	189.9±16.5
SHEAR			
F_{max} [kN]	4.6±0.1	4.5±0.4	8.1±0.6
Max stress τ_{USS} [MPa]	364.9±2.3	350.7±32.1	568.5±42.2
Specific strength τ_{USS}/ρ [MPa/kg m³]	235.4	226.3	78.8

4.2.2 Tightening capability

For the clamping performance assessment first phase, conducted at preloads of 2.5 kN and 2 kN, a heterogeneous outcome can be observed from the data presented in table 4.2. It is characterized by closely equivalent average torque values obtained for both lubricated and unlubricated conditions. Alongside this observation, there is a notable measurement variability, particularly pronounced in relation to the loading torque. The most consistently identified lubrication effect manifests in the loading torque plateau, where a smoother and slightly reduced value is apparent as the applied rotation angle increases. From this trend, it has been decided that the second multi-cycling test phase would be performed with lubrication. Due to samples core shear fractures with selected preload of 2.5 kN and 2 kN, a final preload of 1.5 kN allowed the test completion of the ten repetitions for each of the five samples.

Table 4.2: Summary of the single loading cycle test results on short-CF/PEEK bolt and nuts for IPA lubrication effect evaluation

Preload		2.5 kN	2 kN
Applied torque, Ma [Nm]	Unlubricated	4.51±0.50	3.76±0.47
	Lubricated	4.23±0.93	3.87±0.92
	delta %	-6.17%	+2.89%
Loading torque, Me [Nm]	Unlubricated	0.47±0.34	0.22±0.10
	Lubricated	0.27±0.04	0.22±0.04
	delta %	-41.39%	+1.82%

Each cycle/sample application torque can be found in the graphs of figure 4.3. For the 1.5 kN preload, the application torque trend with respect to cycle number shows a clear higher torque level for the first cycle, then it increases slowly up to the fifth cycle and then stabilizes with a plateau up to the last cycle. Therefore, it can be concluded that safe multiple tightening of this specific short CF/PEEK bolt design are limited to a preload of $F_{nmax}=1.5$ kN and an application torque of $Ma = 3.9$ Nm.

Using digital microscopy and phase contrast X-ray imaging analysis techniques in addition to manufacturing quality control, these methods allow post-test damage evaluation such as displayed below in Fig. 10. The tightening fracture damaged area in the second bolt from the right can be clearly identified from the refraction and scattering images; whereas in contrast on the right sample, no critical damage seems to be induced by a lower preload testing, respectively, 2.5 kN vs 2 kN.

4.2 Mechanical performance comparative evaluation

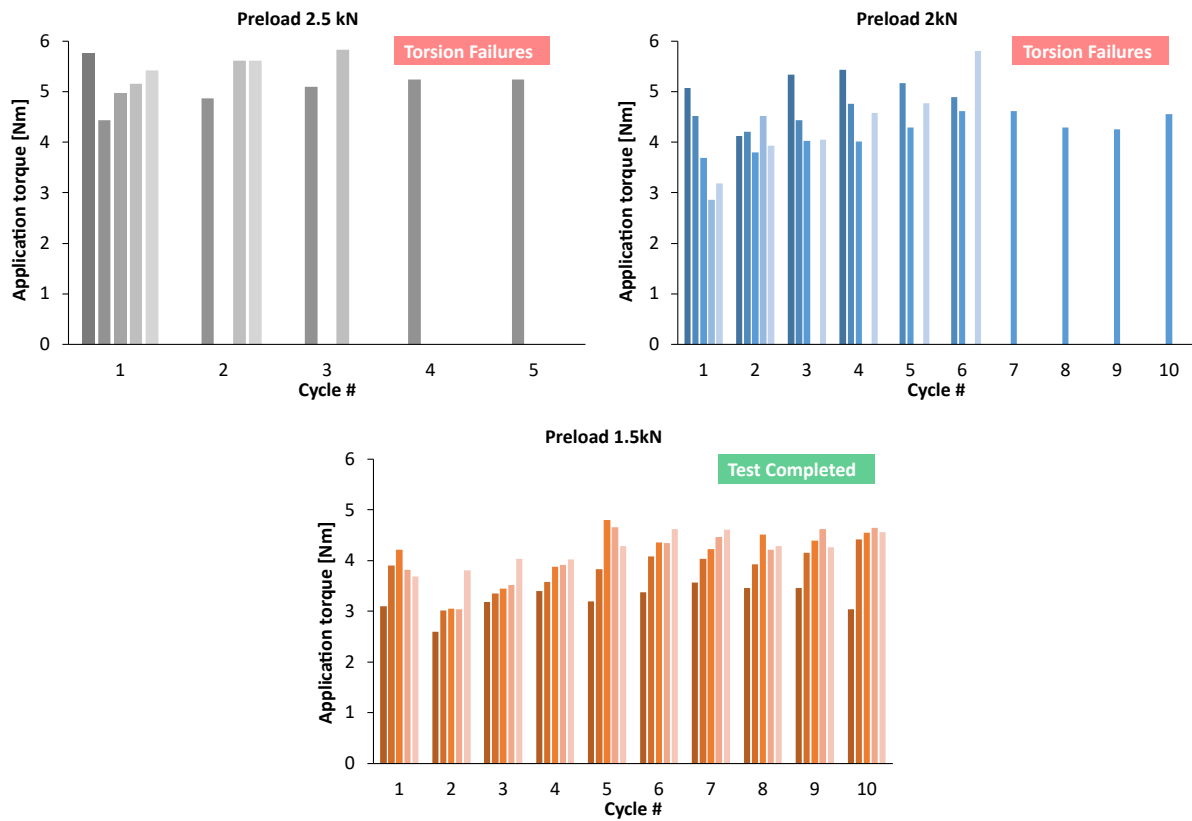


Figure 4.3: Ten repetition load cycling results on short-CF/PEEK bolt and nut with final chosen preload of 2.5kN (left), 2kN (middle) and 1.5kN (right)

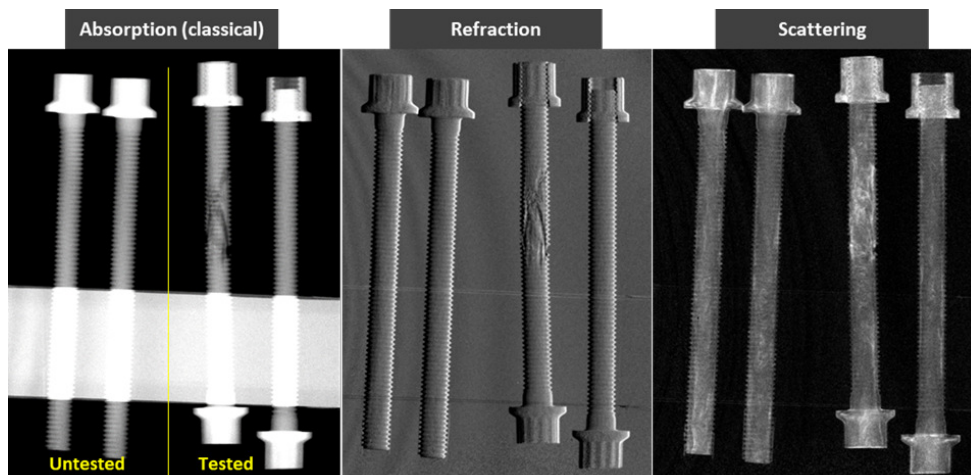


Figure 4.4: XPCI post-cycling tightening test analysis on short CF/PEEK new (left pair) versus tested (right pair) bolt samples. A clear fracture can be observed in the left tested sample after three preloads cycles at 2.5kN, against no visible damages for a recovered 2kN sample (right). The white band on the absorption image corresponds to the PMMA sample holder.

4.2.3 DMA

Storage modulus curves and summarized DMA data, summarized in figure 4.5, confirm that the short CF samples behave very similarly as the continuous ones, with similar glass temperature, melting temperature and storage modulus. Optimal mechanical properties of CF/PEEK bolt can be maintained while operating

between -150°C and 118°C. Melting starts around 335°C, which is significantly advantageous regarding demisability as compared to respectively 1380°C or 1660°C of the SS or Ti6Al4V for a bolt joint system, as it should lose its assembly capability close to this specific point.

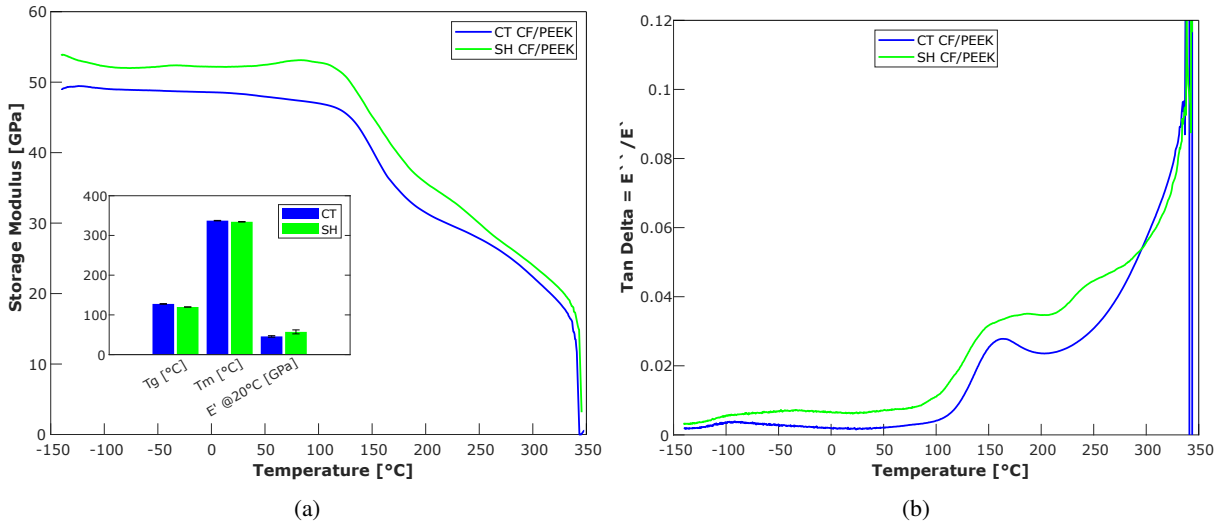


Figure 4.5: DMA curves of (a) the storage modulus E' and (b) $\tan \delta$ evaluation from 150 to 350 °C of continuous versus short CF/PEEK samples. In the bottom left of (a), DMA results summary

4.3 Demise relevant properties' evaluation

The three tests used for this section allow the measurement of onset temperature and timing of mechanical loosening, melting, demise/degradation of the samples, in addition to physical demise behavior observations.

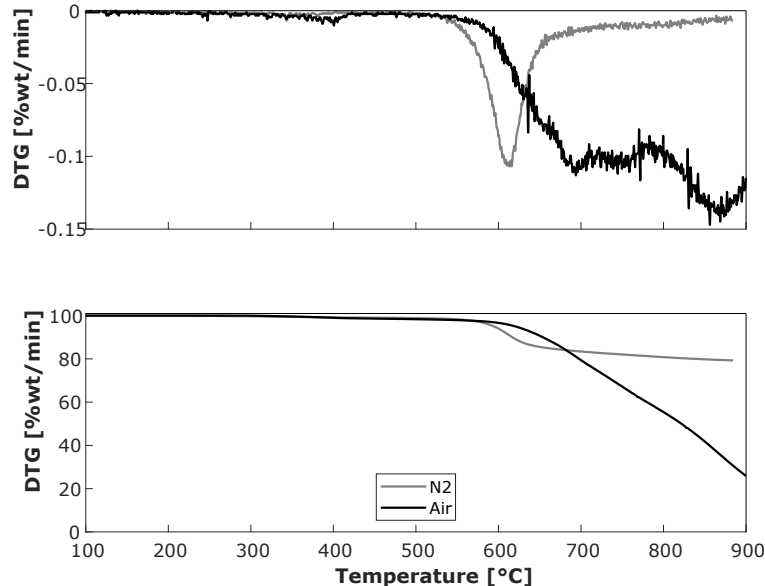


Figure 4.6: TGA (bottom) and DTG (top) curves of CF/PEEK under air and nitrogen environments.

The mass loss curves from figure 4.6 and reported values of table 4.3, indicate that under nitrogen, the CF/PEEK degradation starts earlier in term of temperature (-21°C), but achieves a slightly lower maximum

mass loss rate (-15%) than under air. After 630°C, the demise in air continues at a faster rate with temperature than under nitrogen. It can be noted that even with an identified melting temperature under air of around 335°C from DMA results, the thermal degradation by PEEK matrix pyrolysis starts only around 615°C. This earlier onset under a nitrogen atmosphere is attributed to the use of a high heating rate of 40°C/min to mimic UC re-entry conditions, instead of the standard 5°C/min. So as observed in figures 3 and 13 in the work of Ramgobin et al. [92], a higher heating rate induces a considerably significant larger shift to higher degradation onset temperature under air than under nitrogen (N_2).

In a nitrogen atmosphere, the mass loss rate significantly decreases; while in an air atmosphere, it continues steadily upon 650°C. The oxidation process of the pyrolysed PEEK matrix char and the CF is initiated around that point, with the clear trend difference between DTG measurements under air versus nitrogen, and reaches a near-steady state around 700°C. The multifactorial oxidation kinetics under such conditions, lead to a high selection variability of the maximum mass loss temperature, which can be seen reported in table 4.3. The non-zero mass-loss rate under nitrogen supposedly comes from a second volatilization and dehydrogenation of the residues formed during the initial decomposition stage, as it has been also observed in previous work [93] [94].

Table 4.3: Summarized CF/PEEK thermophysical/demise relevant parameters from TGA testing.

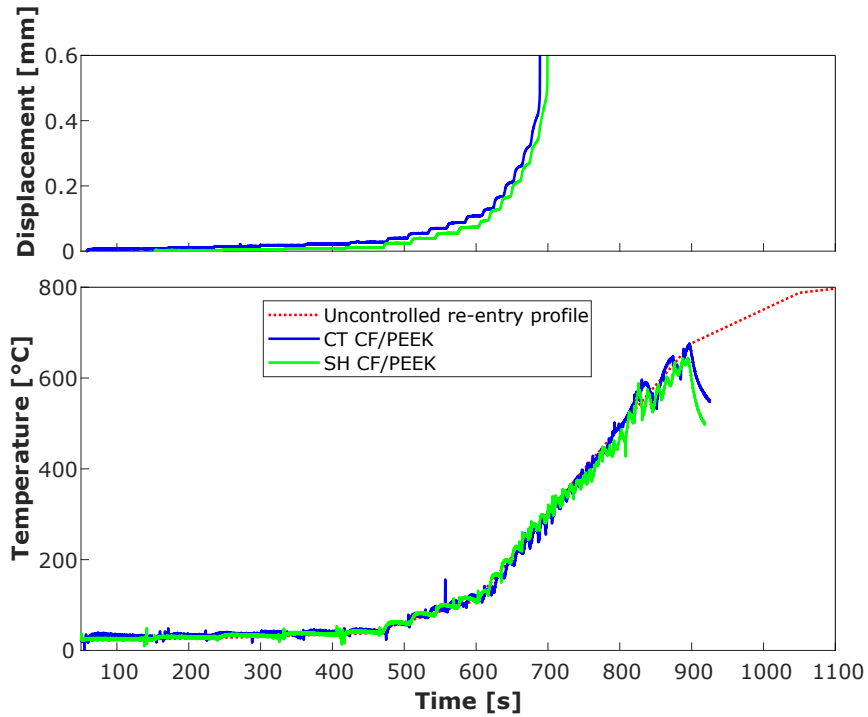
Environment	$T_{\text{pyrolysis onset}} [^{\circ}\text{C}]$	$T_{\text{max weight loss}} [^{\circ}\text{C}]$	Max weight loss rate [%wt/min]
Air	606.7±20.4	683.5±114.0	-13.2±2.4
Nitrogen - N_2	585.9±1.3	614.7±2.4	-11.3±0.8

4.3.1 Static Re-entry Chamber (SRC)

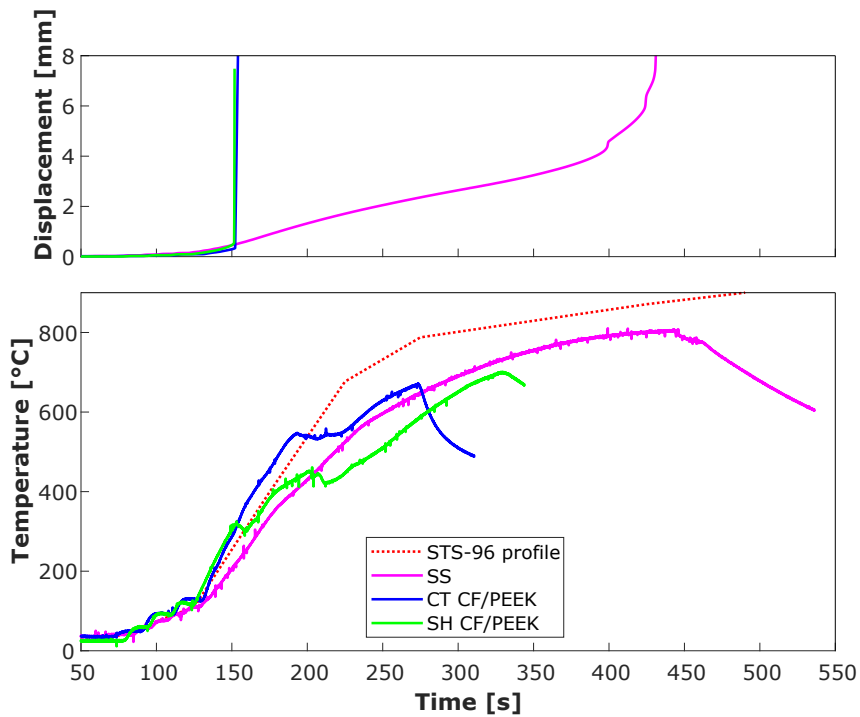
From the third demise-oriented test, CF/PEEK mechanical and demise timing and temperature onsets was characterized under two relevant static re-entry conditions, named UC and STS-96 as presented in figure 4.7, and where the main characteristics points are reported in table 4.4. From the left graph of figure 4.7, it can be observed that axial displacement and the top surface temperature evolutions along the applied UC temperature profile are very similar between the two CF/PEEK samples, although the fracture types and recovered samples present disparities. The continuous CF samples mostly showed a brittle core fracture under both heating rate conditions, where for the short CF ones, the trend was different between the two testing conditions. Under STS-96 (high heating rate), they all presented a thread stripping failure, against a mix of both for the tests under UC (low heating rate) conditions. Concerning the thermomechanical aspect, continuous CF design presents an earlier loosening with lower onsets temperatures, respectively, 40°C and 51°C when compared to the short CF . A trend linked to the short reinforcement samples showing a 45% higher failure strain. Therefore, differences that seems to be directly linked to the specific reinforcement length.

Regarding the heating rate influence, an expected fracture temperature delay under a higher heating rate is verified, with a difference around 24°C for continuous CF and 35°C for the short CF . But an opposite trend is observed in the case of the demise onset temperature, where a respective reduction of -71°C and -8°C from average values is measured with a higher heating rate. The most probable cause from this abnormal trend might come from the setup difficulty to fit exactly the set temperature profile and thus leading in high variability in the high temperature range, in which the demise is happening. In addition, temperature plateaus are observed for both composite sample types before 200 s under STS-96 test conditions, closely aligning with the visual observation of the matrix demise onset. This distinct temperature behavior is not observed during the UC re-entry characterized by a lower heating rate regime.

Hence, it signifies that under such elevated heating rate conditions, the matrix's endothermic pyrolysis reaction and outgassing substantially diminish the incoming heat flux.



(a)



(b)

Figure 4.7: Sample temperature and displacement of continuous and short CF/PEEK samples under the two different re-entry profiles, respectively a UC on the top and b STS-96 on the bottom. In this latter a tested SS sample is additionally displayed

A critical difference of the recovered samples physical performance has been observed and led to the identification of the short CF as an optimal demisable bolt design, this can be observed by the remaining assembly capability after test in 4.8. The observed optimal weak pull-out separation behavior with short CF fasteners, where complete separation of the holder was achieved without additional breakup forces, indicates that above the demise temperature such design allows a complete release of the joining system, such as external sandwich panels for example.

As observed under the STS-96 conditions and displayed in table 4.4, by switching from SS to such CF/PEEK composite alternative, the mechanical loosening onset can be reduced by 500 °C, besides the reduction of at least 380 °C for the demise onset, since no demise behavior was observed for the SS within this testing range. Therefore, a drastically improved potential for the overall spacecraft demise process can be demonstrated by a much earlier break-up.

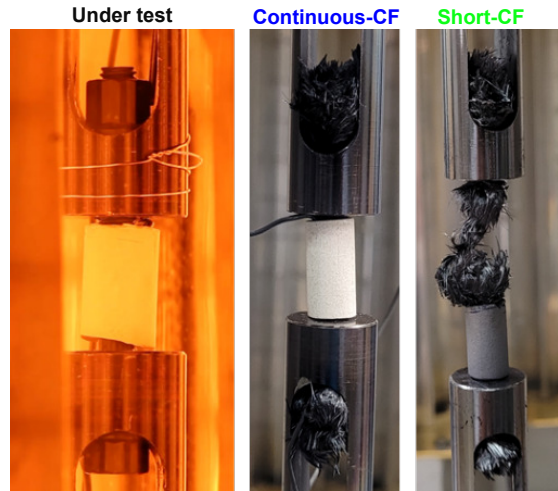


Figure 4.8: Left, CF/PEEK sample under static re-entry test. Right, recovered continuous and short CF/PEEK samples from static re-entry test, with a complete fastener separation in the case of the short design.

Table 4.4: SRC demise parameters summary of SS, continuous (CT) and short (SH) CF/PEEK bolts

Test conditions	UC re-entry			STS-96		
	Material	CF/PEEK		CF/PEEK		SS
		CT	SH	CT	SH	
Fracture onset	Time [s]	635 ±45	666 ±29	154 ±4	160 ±8	432
	T [°C]	212.0 ±38.0	252.5.0 ±37.5	235.8 ±27.0	287.0 ±29.1	802.7
	Strain [%]	0.84 ±0.41%	1.3 ±0.03%	1.06 ±0.14%	1.56 ±0.07%	17.83%
Demise onset	Time [s]	805 ±2	758 ±18	193 ±11	186 ±5	No demise up to 820°C (test termination)
	T [°C]	502.1 ±1.2	401.0 ±19.0	430.8 ±16.1	393 ±11.5	

4.4 Chapter summary and technology application limitations

As part of a general mitigation plan to deal with surviving re-entering space debris threat, the exposed design for demise approach aims to achieve a safe and sustainable space environment by playing with material substitution and spacecraft break-up sequence.

To determine the viability and demise efficiency of a novel fastener material assembly for spacecraft panels, a comparative evaluation has been performed between two CF/PEEK designs and a stainless steel reference. An optimal composite bolt design such as represented in figure 4.9, made of short CF reinforcement in a PEEK matrix, has been characterized and compared to a continuous CF baseline version by microstructure analysis, thermomechanical and tensile testing. The short fiber design does not show any significant loss of mechanical properties at ambient temperature or within the space qualification temperature range of ±120 °C. The demise evaluation by static re-entry chamber under two de-orbit like conditions allowed the identification of heating rate influence on the surface temperature. Where it was observed that the preminent processes governing PEEK demise, pyrolysis and outgassing, exhibited a significant effect on the surface

Novel composite bolt joint system

temperature. Specifically, when subjected to the highest heating rate, these processes yielded a substantial reduction in surface temperature, diverging clearly from the anticipated trend observed at lower heating rate.

This study therefore highlights its ideal complete failure/separation after a short exposure to high heat flux, a point around 10 min along an uncontrolled re-entry-like flight path or with a surface temperature higher than 500 °C. An added advantage of this bolted-joint system lies in its familiarity and extensive utilization as an assembly technique in the space industry sector. This inherent recognition and application should streamline the acceptance and implementation procedures, setting it apart from other existing innovative composite designs. Moreover, composites present a large specific strength improvement as compared to the re-entry resistant stainless steel design, although more bolts will be needed to sustain an equivalent load as compared to stainless steel bolts. And where such technology limitations compared to baseline metallic bolt fasteners, a re-design of insert dimensions such as more attachment points or larger diameter would be required. Although CF and PEEK components have demonstrated flight-proven reliability [70], like any composite system, they might still exhibit higher variability in sample quality compared to baseline materials.

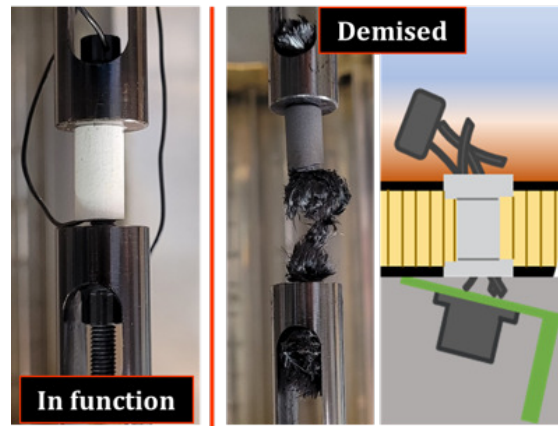


Figure 4.9: Illustration of the ideal short CF/PEEK fastener demise within an external sandwich pane

4.4.1 Perspectives

This technology next phase will be to focus on specific space qualification testing such as thermal cycling creep testing and vibration resistance to achieve the highest TRL possible. In addition to a complete benchmark sandwich panel assembly validation test within a high-fidelity Plasma Wind Tunnel (PWT) facility. Furthermore and aside from the technical points, additional work will be necessary to assess the overall environmental impact of such material substitution and especially the understudied effects on the upper-atmosphere regions. Based on recent studies evaluating the global environmental impact of the space sector, dedicated Life Cycle Assessment (LCA) research highlights the need to address the knowledge gap regarding the environmental effects of objects re-entering Earth's atmosphere. [95] [96] [97].

**5 Advancing composite demisability:
Innovative facesheet materials and rein-
forcement combinations**

5.1 Technology of interest - How can we tackle CFRP demise resistance ?

The critical role of the external structural panel in the demisability of a spacecraft was highlighted in the introduction, and a solution involving novel demisable joints was presented in the previous chapter. However, especially in the realm of space technologies, a single solution is rarely approved, where the keystone to any system is redundancy. Therefore, in parallel with the joint system, a second complementary strategy focusing on the intrinsic composition of the external panel was explored. In the context of a typical sandwich panel structure, the attention was directed toward the material substitution of the panel facesheets.

This chapter illustrates this strategy through the evaluation of three promising approaches to enhance material demisability. The first approach investigates the hybrid reinforcement of carbon and flax fibers, while the second involves the integration of reactive metallic powder into the composite matrix, and the third explores the use of modified prepregs with cut fibers. The novel designs were compared to aluminum and carbon fiber-reinforced polymer baselines in terms of static properties at room temperature, dynamic properties over a temperature range, and demise capability through static and dynamic re-entry simulation testing. The results led our team to identify promising fiber-reinforced polymer composite material combinations.

The objective of this material substitution method was to overcome the critical demise resistance of carbon fiber-reinforced polymer (CFRP), achieve faster disintegration than aluminum, and aim for improved specific structural properties compared to the latter baseline. This method had previously been explored by Bcomp, the IRS Stuttgart, and Beyond Gravity (formerly RUAG Space). They evaluated a full flax-fiber composite skin sandwich panel prototype as a potential solution for this topic, as depicted in figure 5.1 [17]. This design offers the advantage of both complete and faster demisability, along with a lower overall environmental impact compared to CFRP or aluminum designs, although with specific structural properties lower than both baselines. This brings us to the novel design presented here, where hybridization involving a demisable flax fiber and high mechanical properties carbon fiber was identified as an ideal trade-off. In summary, the strategic combination of these materials opens new possibilities for spacecraft design, providing a compromise between demisability and structural performance.

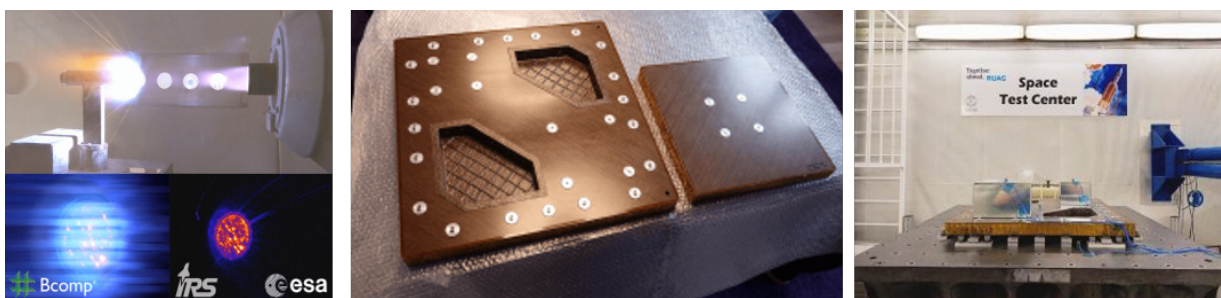


Figure 5.1: Bcomp Ltd., Beyond Gravity (previously RUAG) and IRS high demisability FFRP sandwich panel prototype, with its skin layup testing in PWT setup on the right and performing vibration testing on the left [17]

The study case of this chapter is the structural external side sandwich panel of the ClearSpace-1 spacecraft. A conceptual view can be observed in figure 1.8. This specific element of study, is highlighted in light grey in figure 2.14. Based on the design details and aluminum sandwich panel samples provided by ClearSpace SA, the baseline mission requirements were established and used as a reference throughout the various evaluations presented in this chapter, which will be further detailed and discussed hereafter.

5.2 AlMg micropowder optimal content identification

Figures 5.2 present the results of the TGA and DTG analysis for the pure epoxy, as well as epoxy with increasing powder content. The integration of these particles in the VTC-401 epoxy shows significant pyrolysis improvement compared to the virgin epoxy, 34 | 7% higher respectively under N₂ and air. The selection of the optimal content is based on the trade-off of three demise-related criteria, the lowest degradation onset, maximization of the degradation rate and lowest char yield.

In the following graphs (a) and (b) the difference of onset temperatures is not so distinctive between the different filler contents. But regarding the degradation rate (DTG) exposed in figure (c) and (d) as well as the char yield, a clear step can be observed from 1%wt. This latter additionally shows a relative low char yield compared to the version at higher content. Therefore out of the six filler content evaluated, the optimal 1% resin weight of AlMg content was selected. It exhibits a clear improvement in mass loss rate compared to lower content materials while maintaining a low char yield. Additionally, it lowers characteristic temperatures, with a 15 | 23°C reduction in pyrolysis onset under N₂ and air, and 38 | 50°C for the maximum weight loss. The selected powder characteristics and optimal content are reported in table 5.1. The impact of filler integration on various thermo-mechanical characteristics will be discussed in the subsequent chapters.

An interesting result related to demise, as depicted in the graphs of figures 5.2, is the char yield of the selected VTC-401 epoxy. The remaining mass reaches zero and 8% at 850°C under air and nitrogen, indicating high pyrolysis outgassing and low char formation, favoring demise capability.[54]

Table 5.1: AlMg reactive metallic micropowder characteristics

Powder composition	Aluminium-Magnesium (50-50)
Manufacturer	SFM SA, Switzerland
Purity	99.95 %
Density [kg/m³]	1738
APS [μm]	36.0
Particles shape type	Angular spherical
Optimal filler content/epoxy matrix [% wt]	1.0

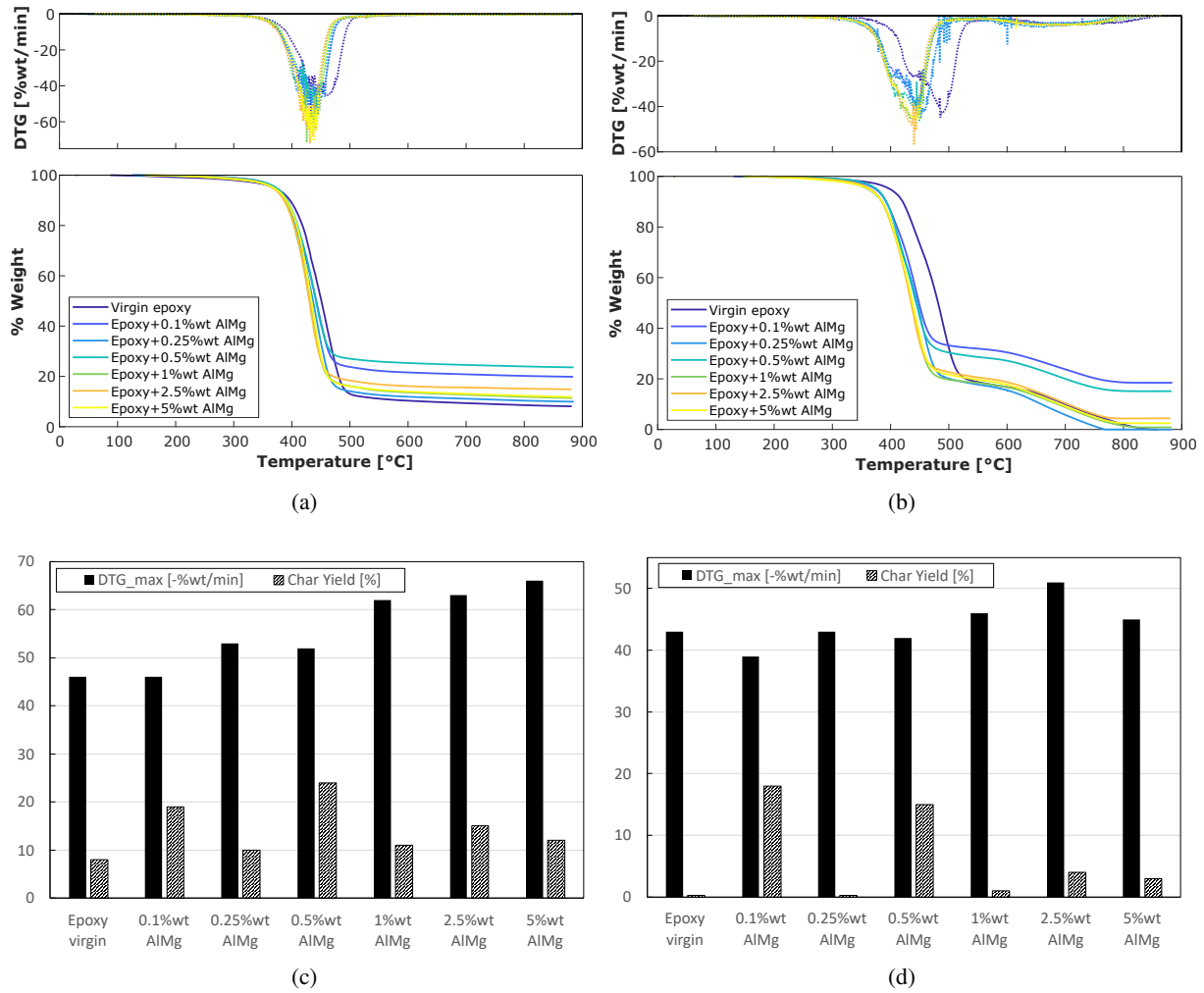


Figure 5.2: TGA and DTG comparative analysis of VTC-401 epoxy filled with six AIMg micropowder contents respectively under (a) nitrogen environment, and (b) synthetic air. (c) and (d) are the respective DTG maximum and char yield with the varying AIMg powder content.

5.3 Structural and physical performances comparative evaluation

5.3.1 At laminate level: DMA and tensile test results

The following figure 5.3 presents the typical DMA mechanical performance versus temperature expressed in storage modulus, where a minimum of 5 samples from each materials were tested. Notable trends emerge in the integration of metallic AIMg micropowder into FFRP composites. This composite type (light green) exhibit a slightly larger bending storage modulus than the virgin FFRP (light blue). This mechanical properties enhancement was expected based on studies precisely looking for such effect, where usually ceramic particles are employed.[98] [99]

A comparison between the blend matrix (PVB/epoxy) (red) and epoxy only (ocean blue) CFRP composites revealed a less consistent storage modulus profile with temperature before degradation onset. This disparity can be attributed to differences in epoxy grades and curing cycles, leading to distinct mechanical performance levels. Consequently, the CF/blend samples exhibited a higher degradation onset temperature than their counterparts.

In evaluating the two hybrid skin versions against the baseline materials, aluminum and CFRP(CF/VTC), it

5.3 Structural and physical performances comparative evaluation

is apparent that the CF-FFTBT samples exhibit non-consistent modulus profile along temperature increase at low temperatures. This phenomenon could stem from their layup and hybrid design, potentially leading to measurement issues caused by thermal distortion. Broadly, the tow-by-tow (TBT) hybrid type displayed a significantly lower modulus compared to references or the PBP hybrid.

In contrast, the PBP hybrid exhibited the most favorable specific bending storage modulus across all samples. This is attributed to its micro-sandwich structure, incorporating a lightweight flax core stack between two stiff CFRP sides. This configuration resulted in a remarkable +46% and +30% improvement in specific bending storage modulus at 20°C compared to the aluminum and CFRP baselines, respectively. Now regarding the extracted thermo-physical properties, which are summarized in table 5.2. The (TP/TS) blend matrix with CFRP exhibits a respective 80°C and 65°C higher T_g and degradation temperature. These differences can be explained by the use of different epoxy grade. This blend approach was not further studied as such combination leads to the opposite of the wanted trend aiming to lower the characteristic temperatures, in addition the manufacturing incompatibility with flax fibers requiring low curing temperatures.

On the other hand, the addition of a AlMg powder to FFRP laminates induces around 20°C lower characteristic temperatures, which is promising

The two hybrids reach closely similar characteristic temperatures to the CFRP samples, with a slightly higher values for the CF-FFPBP.

In terms of damping evaluated from the $\tan \delta$, the use a blended matrix in CFRP resulted in a significant +140% damping improvement. Now when comparing composites with similar matrix material, it is found that as expected the FFRP shows the highest damping properties. Surprisingly, the CF-FFPBP hybrid shows the lowest of all, where it was expected to score in-between FFRP and CFRP, with around 30% higher values than this latter based on Assarar et al. [100] work, where the following relation 5.1 allows to link their damping factor to $\tan \delta$. with Q the damping factor and ζ the damping ratio (a parameter that will be presented later with the vibration test results).

$$\tan \delta = \frac{1}{Q} = 2\zeta \quad (5.1)$$

In conclusion, the findings underscore the complex interplay of material composition, hybrid design, and temperature on the thermo-mechanical/-physical behavior of these composite materials.

Table 5.2: Summarized DMA results, with the storage modulus evaluated at 20°C and the derived comparative specific modulus, in addition to the measured the structural properties degradation onset temperature, $T_{degradationonset}$ and the glass transition, T_g .

Material	Aluminium	CFRP/epoxy	CFRP/Blend	FFRP	FFRP+AlMg
$E_{storage@20^\circ C}$ [GPa]	67.5 ± 0.9	40.2 ± 1.9	46.3 ± 0.4	14.6 ± 0.5	19.2 ± 1.6
Normalized $\frac{E_{storage}}{\rho}$	1	1.08	1.28	0.46	0.6
$\tan \delta$ [-]	-	0.069 ± 0.002	0.170 ± 0.0020	0.114 ± 0.013	0.138 ± 0.006
T_g [°C]	-	125.1 ± 7.9	206.2 ± 1.8	113.1 ± 0.9	94.4 ± 2.3
$T_{degr\ onset}$ [°C]	-	113.2 ± 2.5	178.7 ± 4.7	90.7 ± 1.9	70.1 ± 1.8

Material	CF-FFtBT	CF-FFpBP
$E_{storage} @ 20^{\circ}C$ [GPa]	18.5 ± 0.7	54.4 ± 6.3
Normalized $\frac{E_{storage}}{\rho}$	0.56	1.65
Tan δ [-]	0.140 ± 0.004	0.054 ± 0.001
T_g [$^{\circ}C$]	124.8 ± 3.7	135.8 ± 3.8
$T_{degr\ onset}$ [$^{\circ}C$]	95.7 ± 3.3	104.2 ± 1.2

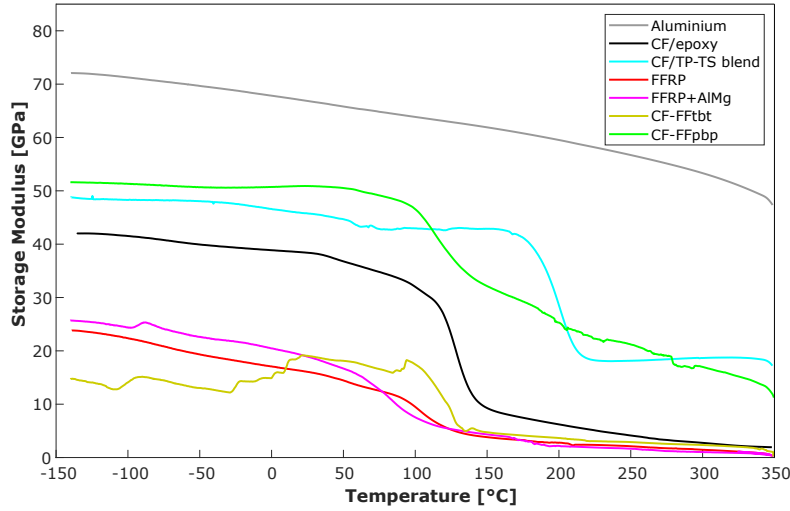


Figure 5.3: Facesheet material DMA test results. Comparative overlay of their skins’ storage modulus.

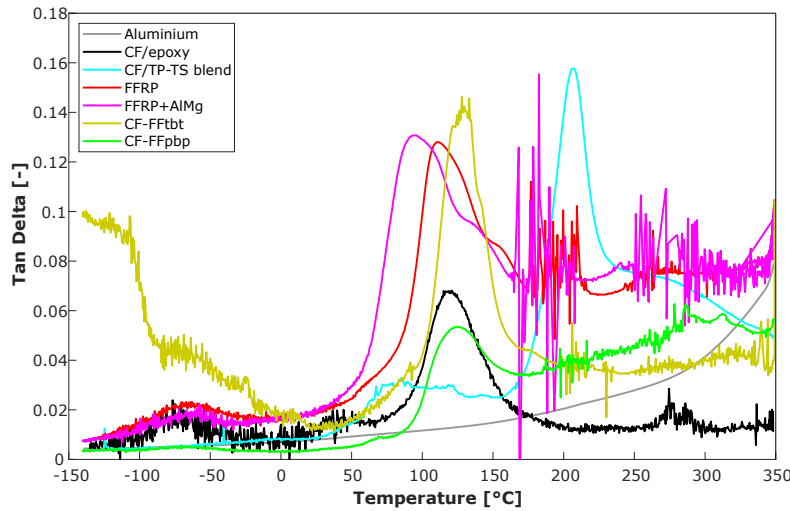


Figure 5.4: Facesheet material DMA test results. Comparative overlay of the composite versions’ tan δ .

Effect of discontinuous CF reinforcement on DMA

Here below in figure 5.5 and table 5.3 are displayed the overall DMA results allowing the assessment of cut-CF design effects on their thermomechanical properties as function of temperature.

The general trend shows no decrease in bending properties of these new cut-CF samples (SMC-HP) compared to continuous-CF/UD laminates as can be observed in figure 5.5. No loss of bending mechanical properties up to 200°C can be observed. A closely similar average elastic flexural storage modulus of 43-47 GPa is obtained at 20°C in the 0° direction for continuous-/cut-CF. However, a higher variability

5.3 Structural and physical performances comparative evaluation

with SMC-HP samples compared to UD is observed. Such observation was expected due to the large specific cut pattern dimensions with respect to the sample dimensions.

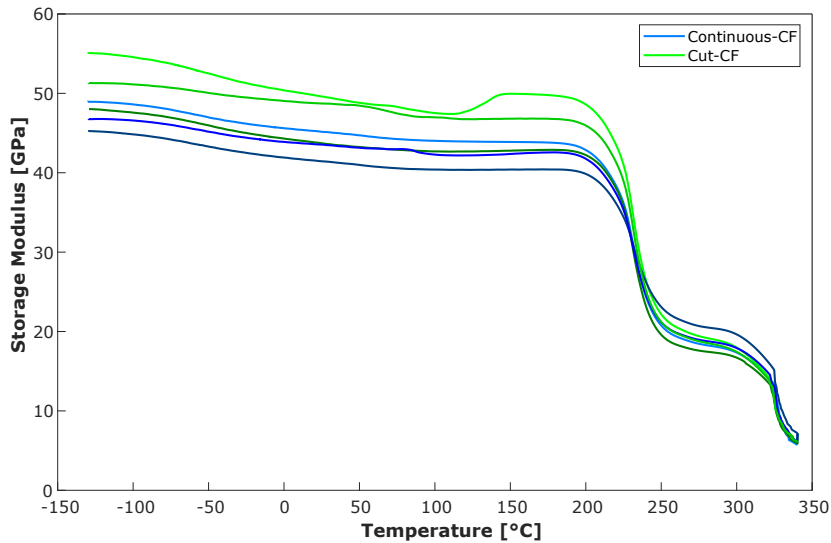


Figure 5.5: Comparative DMA storage modulus trend with temperature of continuous-CF (UD) laminate versus novel cut-CF design (SMC-HP) in the 0° direction.

Table 5.3: Summarized DMA relevant properties on continuous-CF and Cut-CF reinforcement types with the 3pt bending test configuration.

Reinforcement type	Continuous-CF	Cut-CF	Delta Cut vs Continuous
$E_{\text{storage}} @ 20^{\circ}\text{C}$ [GPa]	43.4 ± 1.9	47.4 ± 3.2	-2% ↔ +22%
T_g [°C]	217.2 ± 0.8	219.2 ± 0.2	+0.5% ↔ +1.4%

Assessment of hybridization and metallic filler influence on tensile performances

From the tensile test performed on four composite facesheet materials (CFRP, FFRP, FFRP+AlMg and CF-FFBP), the two main structural engineering properties specific tensile strength, $\frac{\sigma_{UTS}}{\rho}$, and Young's modulus, $\frac{E}{\rho}$, are calculated and displayed in figure 5.6, with ρ the density. The aluminum Al2024-T81 reference material is added for comparison. Its properties' metrics are extracted from Ansys Granta database and an online datasheet from ASM Inc. [101].

The two flax fibre based composites (blue and purple) are well below the baseline performances of the aluminium reference (grey). The ply-by-ply hybrid skin (green) shows a mixed results as it presents a +75% improvement in specific UTS, while a -17% specific modulus compared to the standard aluminum reference. And against the CFRP baseline it exhibits a respective -16% and -14% reduction in specific UTS and modulus performances.

The bottom graph (b), investigates the AlMg integration effect on tensile properties in FFRP. The well-overlapping curves indicates that this metallic powder charge level does not significantly impact the tensile properties of this skin material.

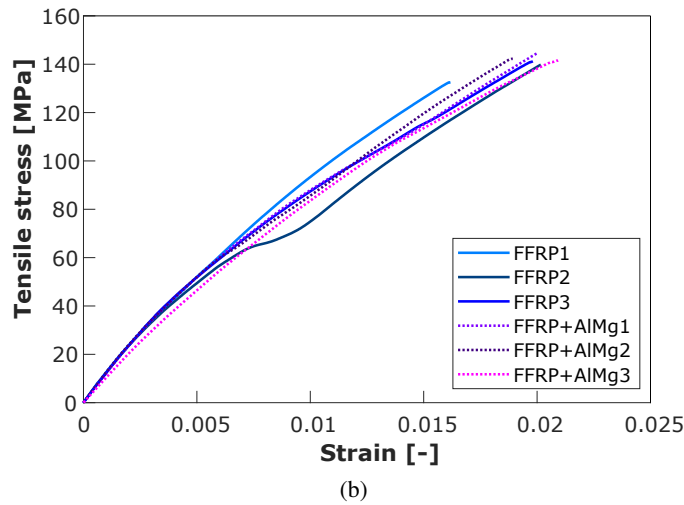
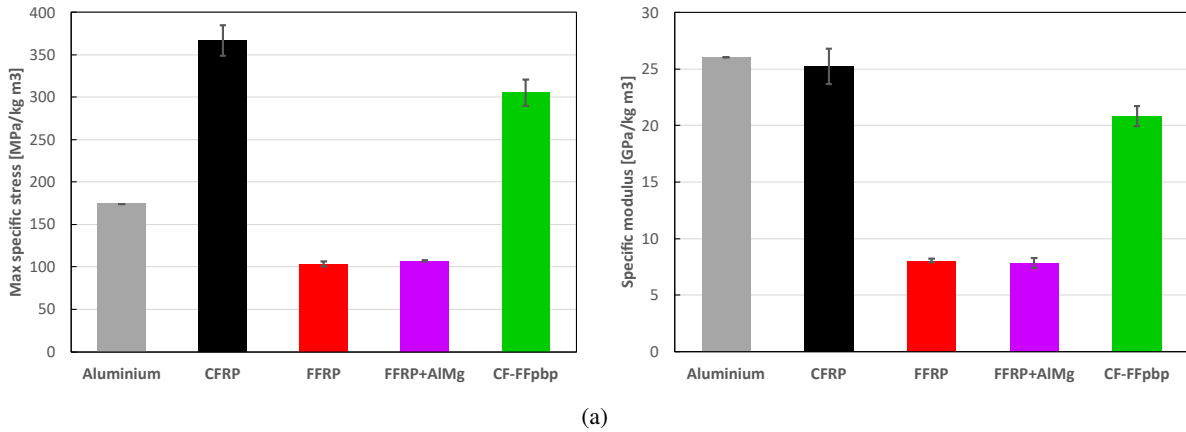


Figure 5.6: Facesheet material tensile test results. (a) Summarized specific UTS stress and modulus for the five tested skin versions. (b) Comparative overlay of the tensile stress-strain curves, assessing the influence of AlMg powder integration in the FFRP composite.

5.3.2 Space qualification evaluation – Outgassing

The outgassing results of the five different composite skin versions are assembled in the following table 5.4 and compared to the acceptance test limits from the space qualification standard ECSS-Q-ST-70-02C. In general, all the samples are compliant to the TML and CVCM criteria. But it can be noted that all the samples containing flax reinforcement showed a slight discrepancy in RML with values >1%. These expected values are in agreement with Bcomp results for samples before they went through a specific bake-out test prior testing [102]. The non-negligible WVR values of the Flax Fiber (FF)-containing samples indicates that such materials require to specify application limitations. Therefore, based on this comparison and ESTEC experts, these non-compliant values can be mitigated for example by a bake-out step of 72h at 130°C, to allow these materials to pass this first space-qualification test.

5.3 Structural and physical performances comparative evaluation

Table 5.4: Standard outgassing acceptance limits from ECSS-Q-ST-70-02C and results from composite skin materials evaluation. With respectively green and red values, compliant and non-compliant values. (*) High TML outgassing is accepted only under certain conditions: equipment T<100°C, fast water desorption, no high voltage equipment involved and dry gas purging system can control the water re-absorption.

Test criteria		TML [%]	CVCM [%]	RML [%]	WVR [%]
Acceptance limits ECSS-Q-ST-70-02C	Mean value	<1 N/A *	< 0.1	< 1	N/A
	Std Dev	< 1/10	< 1/5	< 1/10	N/A
CFRP	Mean value	0.77	0.01	0.49	0.28
	Std Dev	0.06	0.01	0.05	0.11
FFRP	Mean value	5.05	0.00	0.81	4.24
	Std Dev	0.11	0.00	0.00	0.17
FFRP+AlMg	Mean value	4.41	0.00	0.82	3.6
	Std Dev	0.05	0.00	0.06	0.15
CF-FFTBT	Mean value	2.61	0.01	1.2	1.41
	Std Dev	0.06	0.01	0.1	0.16
CF-FFPBP	Mean value	3.03	0.01	1.45	1.58
	Std Dev	0.04	0	0.11	0.15
CF/PEEK	Mean value	0.13	0.00	0.07	0.06
	Std Dev	0.00	0.00	0.00	0.00

5.3.3 At sandwich level: 4pt-bending and vibration results

This section presents the 4-pt bending static mechanical test focusing on the evaluation of flexural stiffness, compressive/tensile strengths of the skins, and the quality of the core-skin bond, including shear strength following the failure scenario. Then in the second part, the vibration test results are displayed, which aim at comparing the stiffness response of three sandwich panel versions undergoing through-plane dynamic loads simulating a VEGA-C launch. The analysis assesses the impact of hybrid fiber reinforcement on dynamic stiffness and damping properties.

Sandwich element bending performances evaluation and effect hygro-aging

The results of the 4-point bending tests are presented in the graphs of figure 5.8 and summarized in Table 5.5. The primary focus was to quantify the mechanical performance of these sandwich panels under ambient and humid environmental conditions, with a specific emphasis on comparing their responses concerning maximum stress and stiffness.

Surprisingly, the findings revealed that the aluminum skin version exhibited superior performance under humid conditions, showcasing higher stiffness measurements. This unexpected observation suggests that aluminum gains flexural performance when exposed to elevated humidity levels. The origin of such property gain was identified by EDX within SEM cross-section analysis of the aluminum sample facesheets embedded within an electrically conductive resin. The SEM manipulation and data analysis were respectively performed and supported by Aigoul Schreier from LPAC.

A 3 times thicker oxide layer on the external facesheet surface can be observed, as displayed in the figure A.4 of the appendix A. This clarifies the 4-pt bending higher modulus, and the 0.33% water intake under high relative humidity conditions of the aluminum panel samples.

Innovative Facesheet Materials and Reinforcement Combinations

Table 5.5: 4-pt bending results with calculated stress, facesheets chord modulus and sandwich stiffness from ASTM-D7249-20 based on load cell and DIC measurement.

	Facesheet material Conditioning	Aluminium		CFRP		CF-FFPBP	
		Ambient	Humid	Ambient	Humid	Ambient	Humid
Load Cell	Max stress, σ_{max} [MPa]	134.41	147.60	106.22	99.90	74.76	67.54
	Std Dev [%]	7.46%	4.15%	1.84%	0.18%	5.68%	1.93%
	Delta humid vs ambient	+9.81%		-5.95%		-9.65%	
	Displacement @ σ_{max} [mm]	3.80	3.69	4.61	4.54	5.17	5.23
	Std Dev [%]	6.23%	4.89%	3.43%	2.96%	2.86%	1.70%
	Delta humid vs ambient	-2.96%		-1.45%		+1.11%	
Digital Image Correlation	Top skin E_{chord} [GPa]	11.5	19.3	10.4	10.9	10.7	3.9
	Std Dev [%]	57.3%	5.0%	31.0%	35.6%	61.6%	44.2%
	Delta humid vs ambient	+68.2%		+4.9%		-63.1%	
	Bottom skin E_{chord} [GPa]	29.5	36.2	18.9	18.5	14.1	13.3
	Std Dev [%]	56.3%	30.9%	32.3%	63.9%	45.4%	62.4%
	Delta humid vs ambient	+22.4%		-2.2%		-6.2%	
	Sandwich flex. stiff. [MN/mm ²]	59.1	68.1	53.6	54.3	63.8	60.9
Std Dev [%]	56.5%	33.0%	32.1%	65.1%	48.5%	61.3%	
	Delta humid vs ambient	+15.2%		+1.2%		-4.6%	

Under high humidity conditions, the CF-FFPBP hybrid configuration exhibited more than twice higher water absorption compared to aluminium and CFRP. This result aligns with expectations, considering the use of flax in the hybrid material. The small fibrillar microstructure of this natural fiber contributes to high capillary intake, resulting in a 60% reduction in maximum stress due to humidity for CF-FFPBP compared to CFRP.

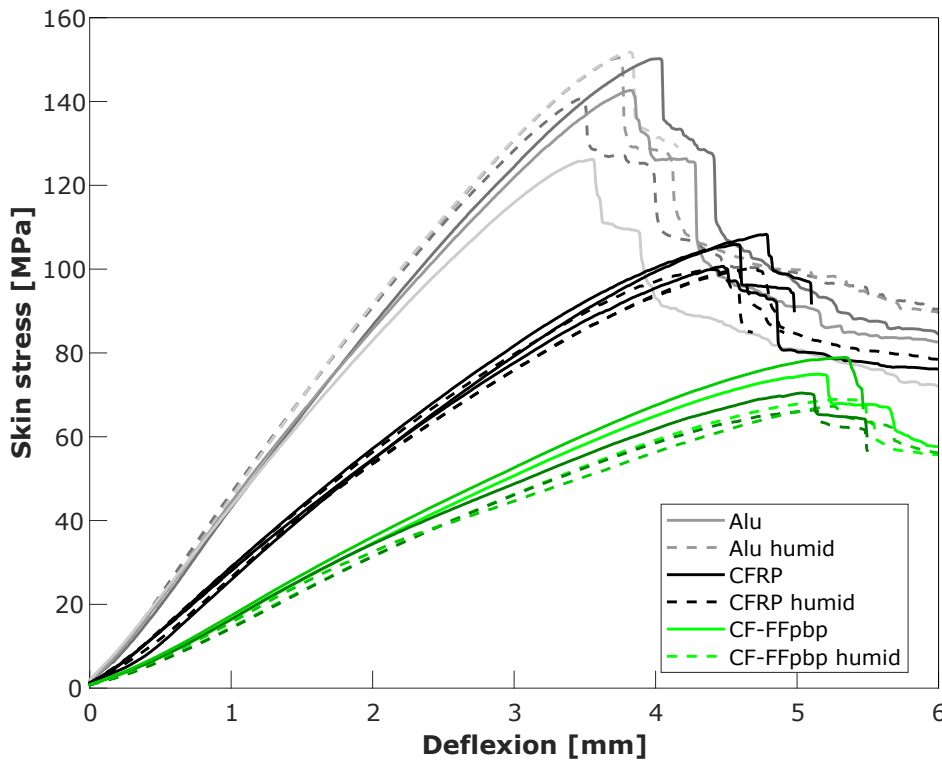


Figure 5.7: Comparative 4-pt bending skin stress versus deflection curves of the three sandwich sample versions. The solid lines are for the standard samples and dashed lines for the ones that endured the 95%RH conditioning.

5.3 Structural and physical performances comparative evaluation

Despite the inherent challenges of high variability in Digital Image Correlation (DIC) data (illustrated by the noisy signal in figure 5.9), a discernible pattern emerges from Table 5.5, indicating that CF-FFPBP panels were notably affected by humid conditioning, leading to overall lower performance. This highlights the sensitivity of the hybrid material to environmental conditions.

Furthermore, the comparative analysis displayed in figure 5.8 reveals that the three sandwich panel types demonstrated similar stiffness-to-mass ratios, with less than a 10% and 20% difference between them under ambient and humid conditions, respectively. However, a substantial variability of 40-50% was observed in these values, emphasizing the need for further investigation into the factors contributing to this variability.

An interesting observation pertains to the bottom facesheet chord modulus (E_{chord}), which consistently exhibited larger values than the top facesheet and showed less sensitivity to humid conditioning. This difference could be attributed to the monitoring system's sensitivity variation between tensile and compressive point displacements or the distinct effects of water presence on tensile/compressive load responses. Clarifying such behavior warrants a dedicated study.

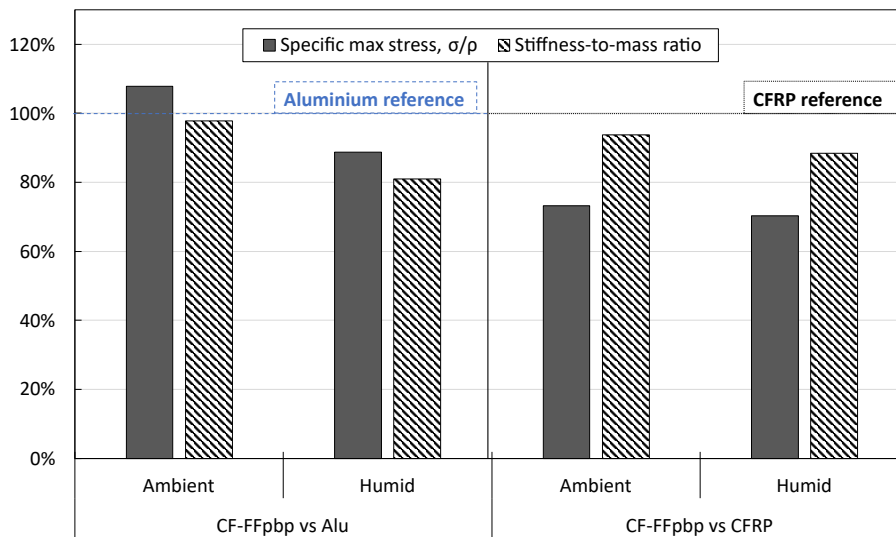


Figure 5.8: Comparative analysis of the properties of interest for the novel CF-FFPBP hybrid against metallic and composite baselines.

In evaluating strain measurements, it was found that DIC strain measurements provided imprecise results due to small edge effects and the sensitivity of the complex setup calibration to sample surface quality. A key takeaway from this aspect of the study is the recommendation for the additional use of strain gauges for sandwich structures to ensure more accurate and reliable strain measurements.

In conclusion, this investigation provides valuable insights into the mechanical behavior of sandwich panels with different skin materials under varying environmental conditions. The findings emphasize the importance of material selection and the need for precise measurement techniques to ensure accurate assessments in similar structural applications.

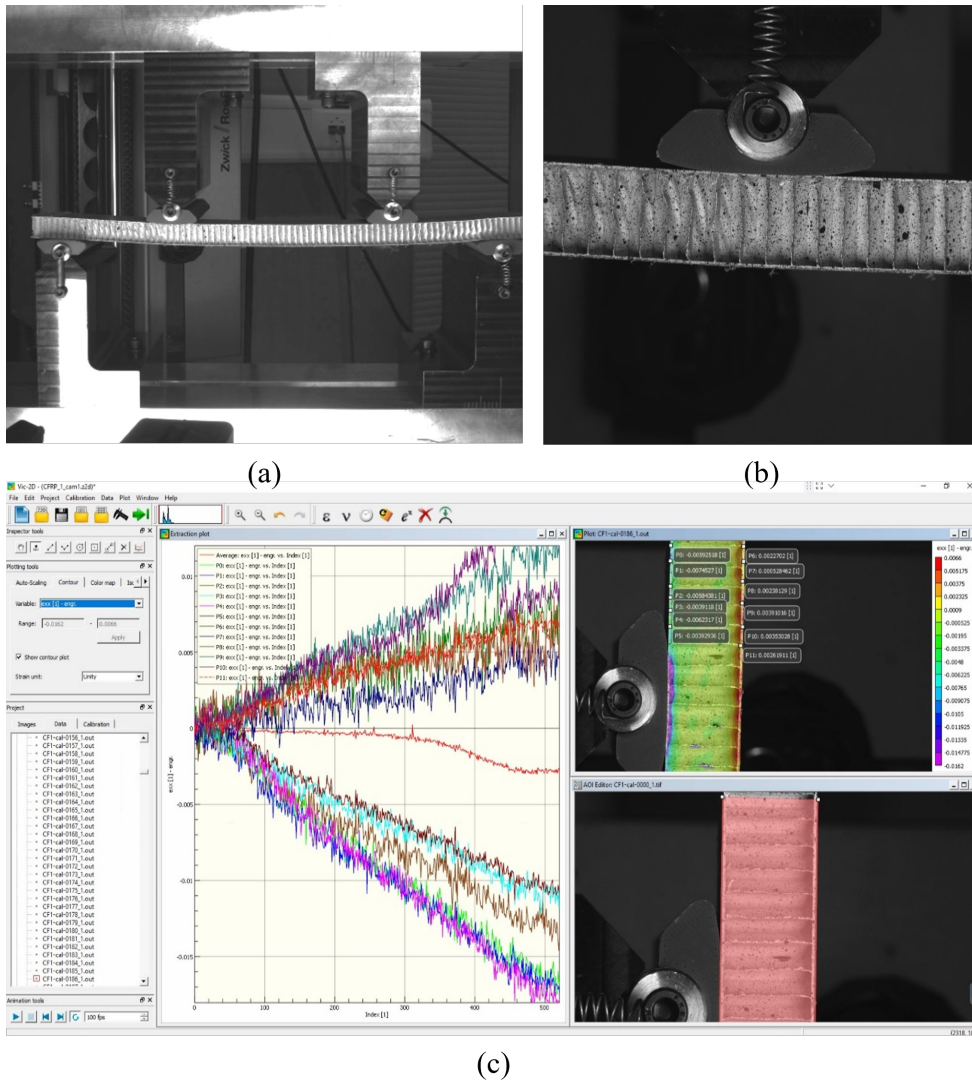


Figure 5.9: Dual camera's view, with respectively (a) the whole sample and (b) a focus view on the left loading pad. (c) Vic2D analysis window where the top and bottom skins strain measurement points are selected.

Comparative evaluation of performance under typical launch vibrations

A comparison of the vibration responses under the LL-sine control runs was analyzed on the monitoring computer right after each HL runs. The FRF profiles exhibited no significant differences, indicating that the 'light' 1 Nm tightening torque effectively maintained the successfully the panels through these load regimes. The absence of bolt rotation, confirmed through visual analysis of paint markings, further supported the effectiveness of the selected torque/preload conditions. In order to use standardized torque/preload conditions, one solution would have been to select smaller bolts, leading to lower preload requirements (the selected design was suggested by the test center team). So in general the three different panels successfully passed the vibration evaluation.

From the FEA analysis presented in the vibration section of chapter 3, seven natural vibration modes were correlated to the accelerometer FRF data from the Z-axis (through-plane) of the three sandwich panel versions. The comparison of the Frequency Response Function (FRF) is illustrated in figure 5.10, while the natural vibration modes correlated to the peaks in natural frequencies are displayed in figure 5.11. Out of the three input levels, only the Low Level (LL) sine was employed for the identification and calculation of dynamic parameters. This choice was made because the high-level sine only goes up to 100Hz, which is less than half the frequency of the first significant amplitude variation, as evident in the graph of figure 5.10. The HL-sine resulted in accelerometer data curves closely following the input reference ones, with no more than 0.5g variations out of the 4g base. Regarding the HL-random level, the data points presented a high noise level, limiting the assessment of the damping ratio. Consequently, only the main natural frequency peaks could be identified, although with low accuracy compared to the LL-sine.

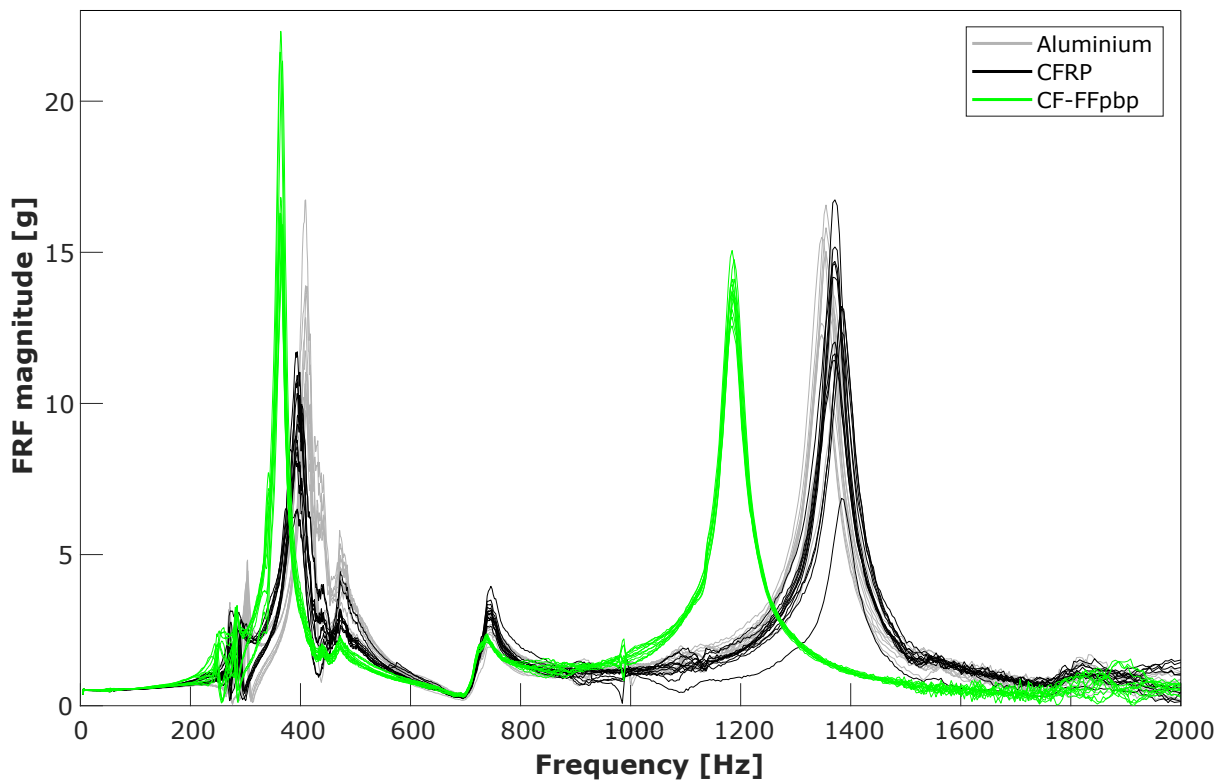


Figure 5.10: Comparison of the three different sandwich facesheet materials FRF graph of all the low-level sine runs.

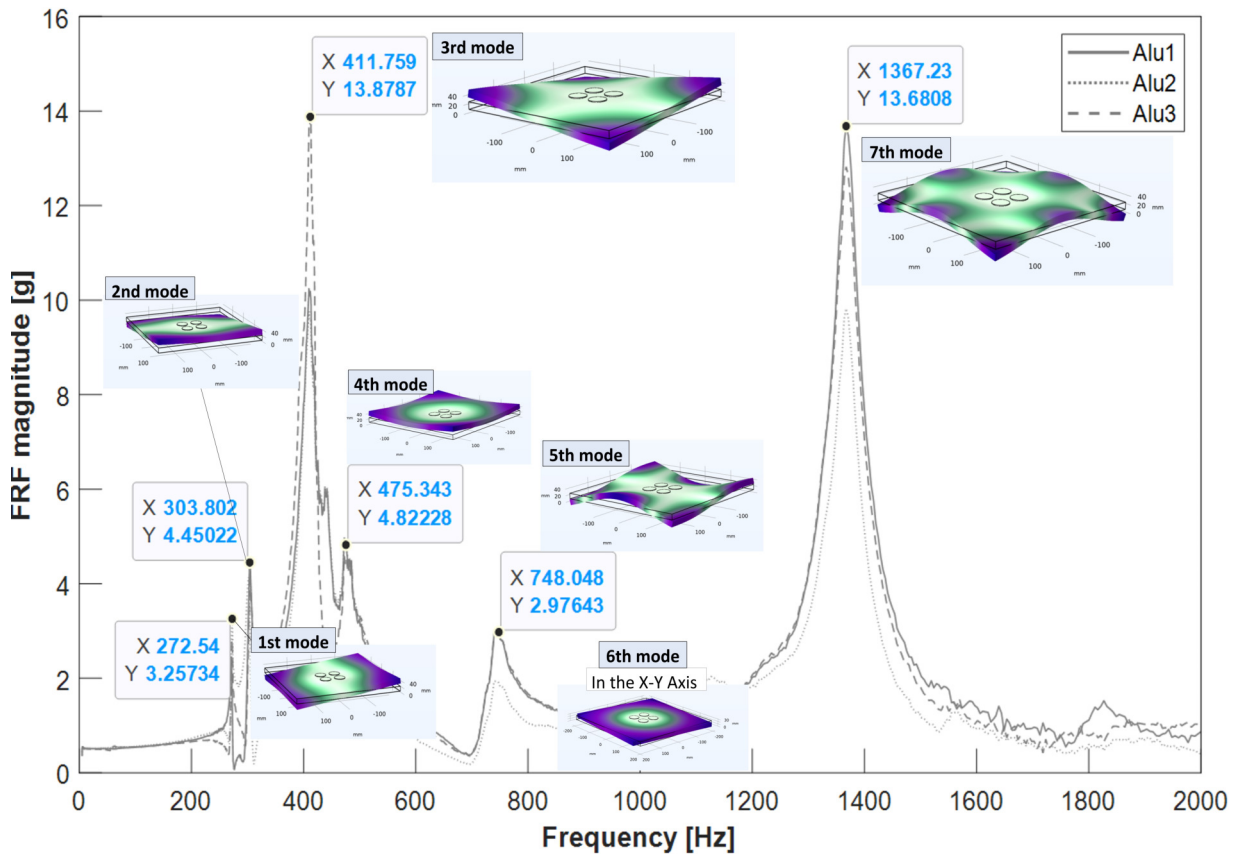


Figure 5.11: Sandwich panels out of plane FRF curves from the four corner-placed accelerometers, with the correlated natural vibration modes identified with the COMSOL FEA analysis.

With the identification of peaks and different vibration modes, comparisons can be made regarding stiffness (related to natural frequency) and damping properties. Among the seven peaks, only the 3rd, 5th, and 7th modes are considered exploitable for extracting quality metrics, given their distinctiveness and homogeneity. The summarized data is presented in table 5.6, extended with theoretical values extracted from COMSOL.

The CF-FFBPB hybrid exhibited the lowest stiffness across all three materials and modes, with the aluminum panel displaying the highest stiffness for the 3rd and 5th modes, while CFRP presented the highest stiffness for the high-frequency mode. The composite panel predictions from COMSOL were approximately 1.5 times worse than the aluminum baseline, indicating a 30% lower stiffness than predicted. This discrepancy may be attributed to modeling simplifications, such as the absence of drilling holes, accelerometer mass on the extremities, and the use of a bulk core element instead of a honeycomb structure, even though equivalent properties were set.

The reason why aluminum is less impacted than composite skins remains unclear.

A relatively small difference in stiffness measurement-prediction between CFRP and the CF-FFBPB hybrid is observed, except for the 5th mode. This could be attributed to higher data noise compared to other peaks. Based on these closely expected theoretical and measured stiffness values, it can be extrapolated that the hybrid design has significant improvement potential by implementing more optimized materials, as detailed in 3.2 in the materials selection section of this chapter.

Concerning the effects on damping properties, the damping ratio trends with natural frequency for our system of study (sandwich panel) do not precisely follow the expected trend as presented by Assarar et al. [100]. The discrepancy might be due to the fact that their study focused on CF-FF hybrid laminates and

5.3 Structural and physical performances comparative evaluation

not sandwich panels.

Significant data deviations are noticeable at the 3rd vibration mode for the aluminium and CFRP panels. Surprisingly, CFRP shows the best damping ratio at this mode, where it was expected to be the lowest across all frequencies. These deviations might be explained by the close presence of the next vibration mode, creating peak superposition. From the 2nd and 3rd vibration modes, the CF-FFBPB hybrid exhibits around a 60% improved damping ratio compared to CFRP. These performances align with expectations based on the work of Assarar et al. [100], where the CF-FFBPB hybrids have a flax fiber content of 32%. Against aluminium, it also shows improvement but with more variability along the natural frequency. At the 2nd natural frequency, the hybrid version outperforms the other samples with a damping ratio improved by more than 5. The strong evolution of the carbon-flax hybrid sample's damping ratio with natural frequency indicates that flax fibers exhibit viscoelastic damping properties, possibly in addition to damping mechanisms sensitive to frequency. Similar behavior was identified in the works of Assarar et al. [100] and Dashatan et al. [103].

Table 5.6: Measured and computed natural frequencies of the three sandwich panels at the selected modes, and the derived damping ratios.

Sandwich panel facesheet material		Aluminium	CFRP	CF-FFBPB	
3rd Mode	Natural frequency, f_N [Hz]	Measured	409.6 ± 1.1	393.5 ± 1.1	364.9 ± 1.9
		COMSOL	516.7	757.5	740.1
	Damping Ratio, ζ [-]	Measured	$5.2\% \pm 1.4\%$	$6.9\% \pm 0.8\%$	$4.0\% \pm 0.3\%$
5th Mode	Natural frequency, f_N [Hz]	Measured	744.7 ± 2.4	743.8 ± 3.2	738.7 ± 1.1
		COMSOL	1282.5	1706.4	1618.1
	Damping Ratio, ζ [-]	Measured	$5.4\% \pm 0.6\%$	$4.0\% \pm 0.1\%$	$6.3\% \pm 0.7\%$
7th Mode	Natural frequency, f_N [Hz]	Measured	1356.5 ± 8.6	1375.1 ± 6.3	1202.1 ± 0.1
		COMSOL	1673.4	2130.7	1989.6
	Damping Ratio, ζ [-]	Measured	$3.3\% \pm 0.2\%$	$3.1\% \pm 0.4\%$	$4.9\% \pm 0.4\%$

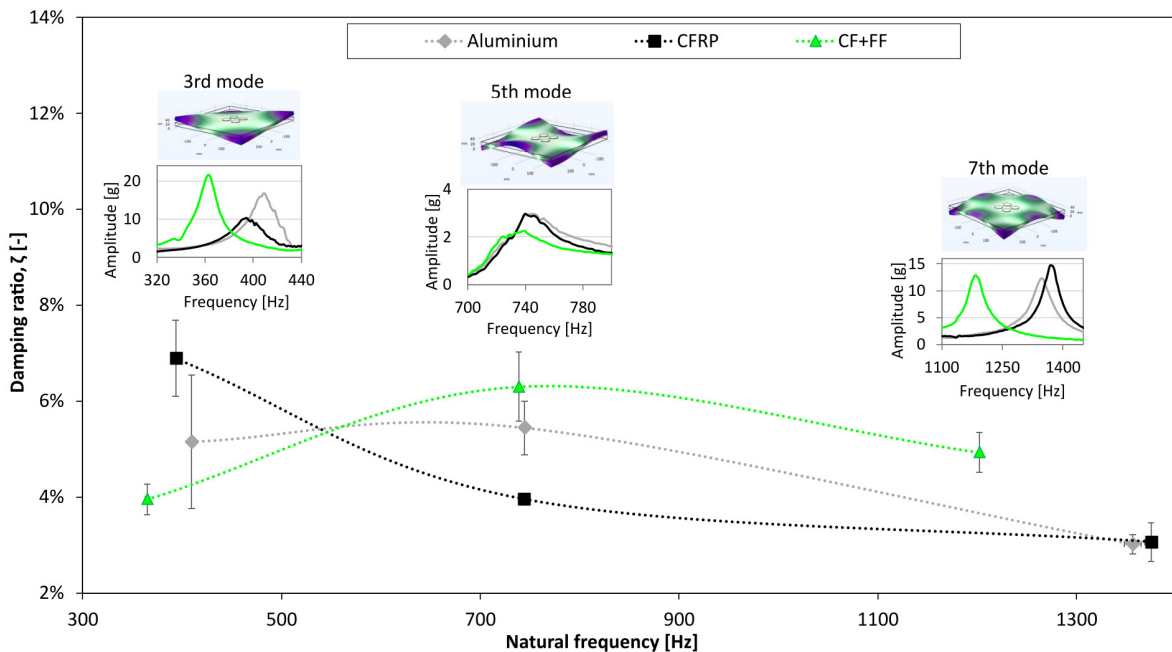


Figure 5.12: Derived damping ratios of the three sandwich panel versions identified by their skin materials (aluminium, CFRP and the novel CF-FF hybrid) at the three optimal vibration modes.

5.4 Demise relevant properties' evaluation

5.4.1 Thermo-physical analysis: thermal conductivity and thermogravimetry

Effect of AlMg micropowder on thermal conductivity

Figure 5.13 presents the temperature profile versus time on the plate surfaces when the bottom is subjected to a 100°C hotplate, where are compared the averaged top temperatures of respectively in red and purple, the virgin and the AlMg-filled FFRP. Overall, a higher temperature increase is found for the AlMg-filled FFRP (in purple) compared to the virgin ones (in red). Since this setup and analysis do not permit a direct quantitative determination of thermal conductivity improvement, an experimental-to-model correlation step using COMSOL Multiphysics 6.0 thermo-physical model was implemented to estimate the thermal conductivity enhancement resulting from the addition of metallic AlMg micropowder to the composite matrix.

A 2D transient thermal conduction evolution model, employing a linear applied surface temperature, was utilized with specific material properties implemented from previous Bcomp datasheets. Following an iteration fitting process with parametric study, the resulting curves are displayed in the graph of figure 5.14. The assessment of thermal conductivity improvement is carried out in the 'linear' region between 40°C and 70°C, revealing a 12±2% increase in through-thickness thermal conductivity with just a 1% resin weight integration of metallic AlMg micropowder.

A quantitative test campaign had been planned to comprehensively evaluate the AlMg filler's effect on thermal conductivity, combining laser flash analysis and HotDisc setups. Unfortunately, due to equipment issues encountered during the visiting period at ESTEC, no data could be acquired during the time frame of the thesis.

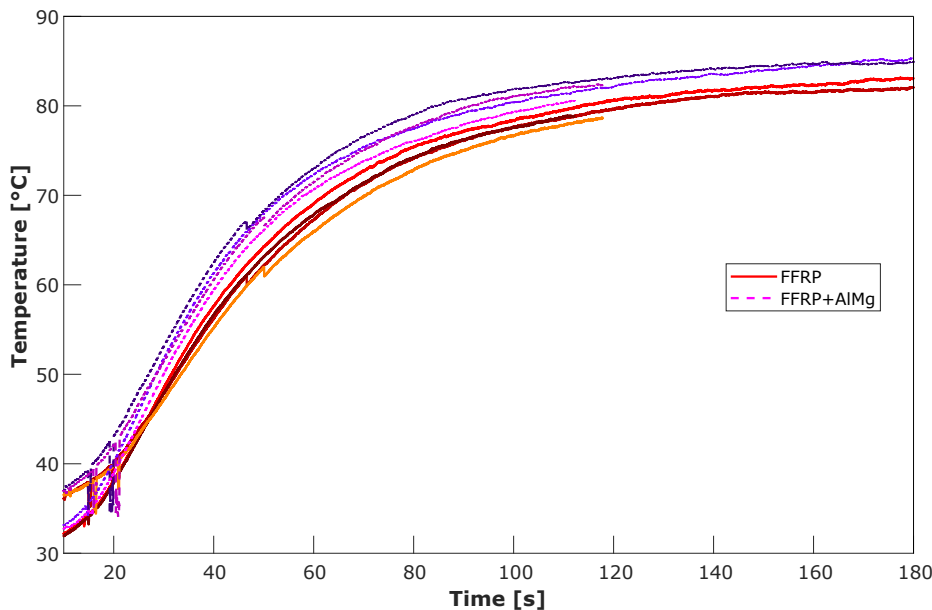


Figure 5.13: Resulting temperature response transient curves averaged from the 6 measurement points per plate, comparing virgin and AlMg charged FFRP samples.

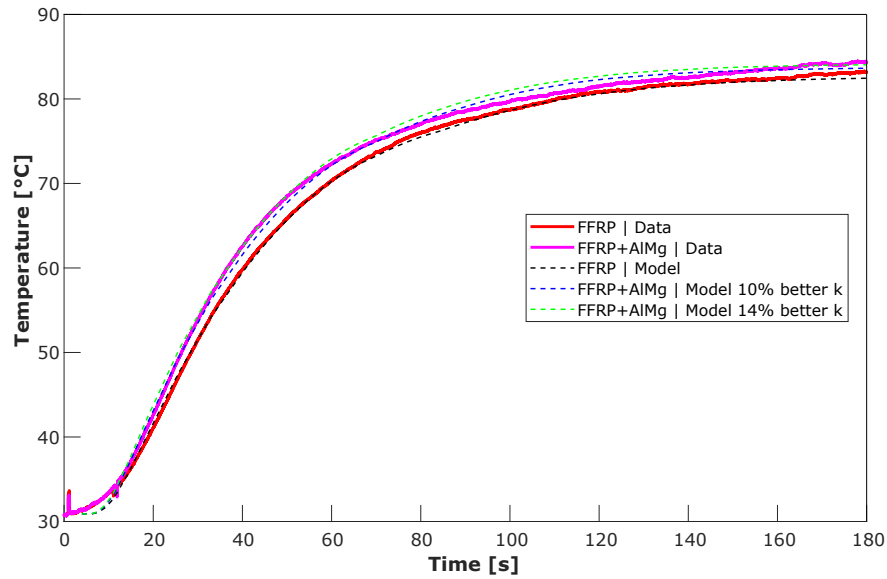


Figure 5.14: Experimental data to model correlation for the evaluation of the through-thickness thermal conductivity improvement.

Thermogravimetry overview analysis of the facesheets

The Thermogravimetric Analysis (TGA) involved a comprehensive comparison of key parameters, including mass loss degradation onset temperature, mass loss rate (DTG), and residual mass, across aluminum and three distinct composite systems. Furthermore, the examination extended to the two matrix materials detailed in the materials section of this chapter, each reinforced with carbon fibers. A comprehensive overview of the diverse degradation behaviors is provided in figure 5.15. Where as a first observation, the presence of water in the FFRP is clear, with a typical few percentage drop after 100°C.

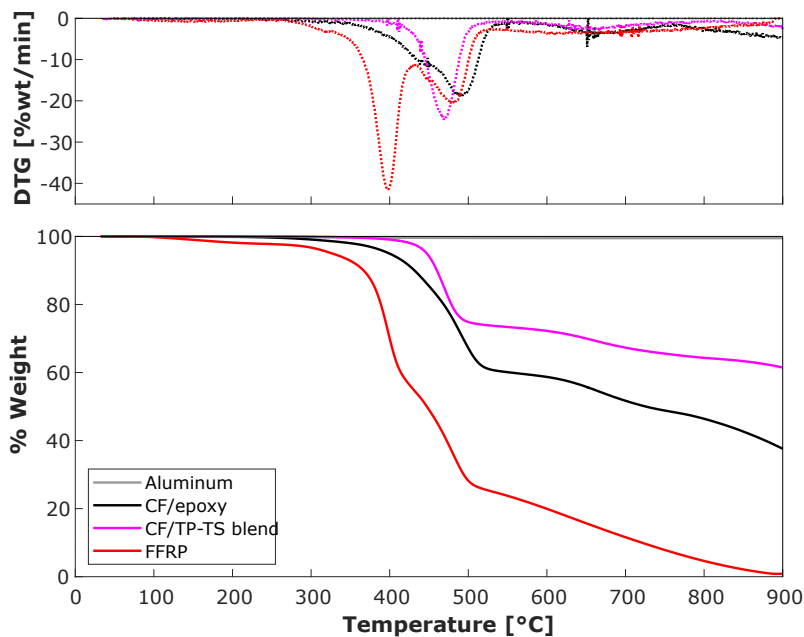


Figure 5.15: TGA and Differential Thermogravimetry (DTG) comparative analysis of four skin materials under synthetic air.

Focusing on the influence of the metallic filler, as depicted in figure 5.16, varying trends were observed between the two matrix types, indicated by the green arrows. While the addition of AlMg to VTC-401 epoxy primarily resulted in a shift toward lower degradation onset and maximum loss temperatures, the PVB/epoxy blend displayed an enhancement in degradation rate and minimal leftward shifts.

In general, the inclusion of the filler resulted in a decrease in degradation onset temperature ranging from -10°C to -45°C, coupled with an improvement in degradation rate ranging from 10% to 50%. When considering these outcomes in conjunction with the earlier Dynamic Mechanical Analysis (DMA) findings, the utilization of a blended matrix appears promising for overall enhanced performance. The complexities of its processing currently prevents further development in combination with flax, but future studies in this direction may prove worthwhile.

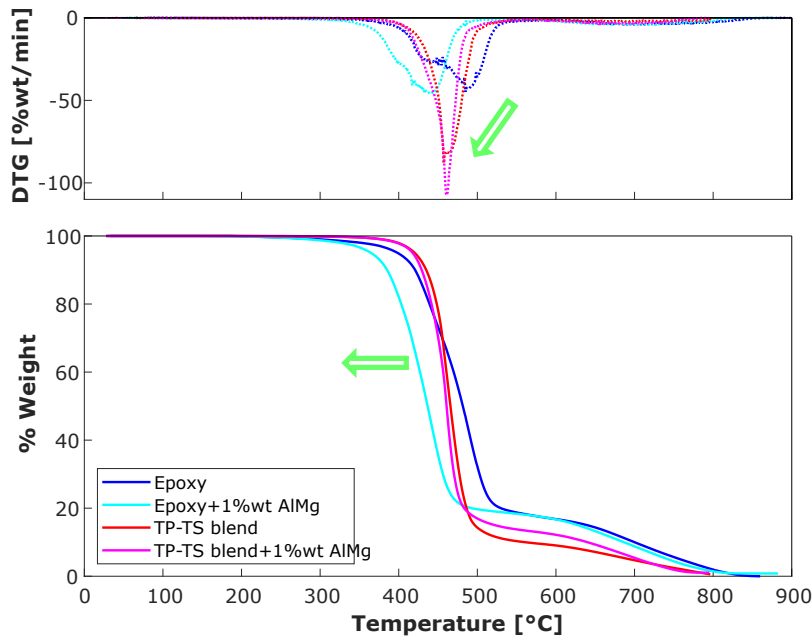


Figure 5.16: Comparative evaluation of TGA pyrolysis behaviour of AlMg filler integration in the baseline epoxy and PVB/epoxy blend.

Moving to the second phase of the TGA evaluation, the determination of pyrolysis degradation reaction kinetics parameters was undertaken. These parameters of interest for the demise modelling of these different material encompass the reaction order, activation energy, and frequency frequency factor. The analysis extended to primary composite systems, including CFRP and FFRP datasets, as well as both virgin and AlMg-filled VTC-401 epoxy. This aligns with methodologies established by Deng et al. [104] and Patidar et al. [105]. Consequently, utilizing an Arrhenius law equation applied with a Coats-Redfern method, the resulting kinetic equation model can be summarized as Equation 5.2.

$$\frac{d\alpha}{dT} = \frac{A}{\beta} \cdot e^{-\frac{E}{RT}} \cdot (1 - \alpha)^n \quad (5.2)$$

So once this equation is integrated and reduced with the logarithms it gives two expressions following the reaction order, n .

$$\Rightarrow n = 1, \quad \ln \left[\frac{1 - (1 - \alpha)^{1-n}}{T^2(1-n)} \right] = \ln \left[\frac{AR}{\beta E} \left(1 - \frac{2RT}{E} \right) \right] - \frac{E}{RT} \quad (5.3)$$

$$\Rightarrow n \neq 1, \quad \ln \left[\frac{1 - (1 - \alpha)}{T^2(1 - n)} \right] = \ln \left[\frac{AR}{\beta E} \left(1 - \frac{2RT}{E} \right) \right] - \frac{E}{RT} \quad (5.4)$$

Here, α denotes the degree of conversion, representing the transformation from the virgin polymer to char, derived from TGA data and expressed as $\alpha = \frac{W_0 - W}{W_0 - W_\infty}$. The parameter β signifies the heating rate. Upon integration and logarithmic transformation, the data are plotted as the second part of Equation 5.3 versus $1/T$. In this plot, the linear segment associated with the predominant decomposition reaction is identified. Iterative processes are then applied to determine the reaction order, n , that results in the highest linearity. Through this analysis, the activation energy is obtained from the slope of the linear trend line, while the frequency factor is determined by its intersection with the vertical axis. This procedure is visually represented in figure 5.17 and the extracted parameters can be found in the following table 5.7.

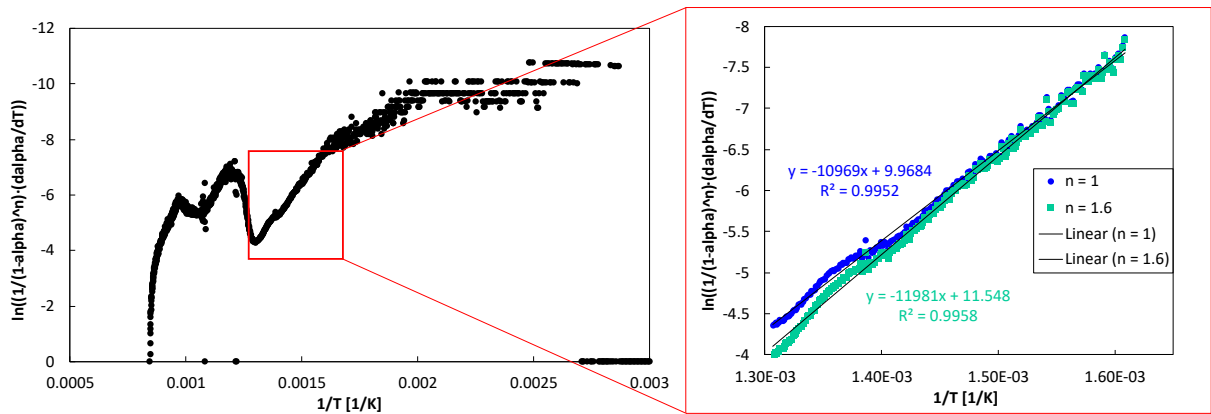


Figure 5.17: Illustration of pyrolysis reaction kinetic parameters extraction process from TGA data.

Table 5.7: Extracted kinetic from a Coats-Redfern method parameters for virgin and filler matrix system (epoxy vs blend), in addition to the composites CFRP and FFRP.

Material	Epoxy VTC-401	Epoxy+AlMg	TP/TS blend PVB/epoxy	TP/TS blend+AlMg
Reaction order, n	1	1.4	0.5	0.5
Activation energy, E_a [kJ/mol]	150.5	152.6	72.6	73.1
Frequency factor, A [s^{-1}]	$3.26 \cdot 10^{10}$	$2.23 \cdot 10^{11}$	$1.76 \cdot 10^{10}$	$2.30 \cdot 10^{10}$

Material	CFRP	FFRP
Reaction order, n	1.6	0.6
Activation energy, E_a [kJ/mol]	99.6	172.4
Frequency factor, A [s^{-1}]	$8.61 \cdot 10^5$	$1.29 \cdot 10^6$

5.4.2 Static Re-entry Chamber (SRC)

Before diving into the quantitative data analysis, preliminary observations based on visual analyses of the test videos available this [link](#) and the recovered samples after the tests, as presented in figure 5.18, allow for comparisons and the identification of potential issues related to the use of various skin versions under the specified clamped configuration.

As anticipated, in all cases where flax fibers were present (FFRP, FFRP+AlMg, and the two hybrids), these fibers left either minimal or no visible carbonated remnants. In contrast, carbon fibers were consistently recovered with no apparent damage and devoid of epoxy, resembling a composite recycling step aimed at extracting the carbon fibers (CF). Additionally, these undemised fibers played a crucial role in maintaining the structural integrity of the entire assembly, suggesting minimal impact on their structural capacity.

No noticeable differences were observed between the virgin and AlMg-charged FFRP samples during and after the test. Comparing the two hybrids, both tow-by-tow and ply-by-ply, the first appears more promising, exhibiting see-through holes resulting from the demised FF. On the other hand, the second hybrid, depicted in the right images of figure 5.18, shows fewer test effects, with intact dry CF plies on each side and a barely existent central twill flax ply.

The effectiveness of the TBT hybrid in terms of demise, especially under the dynamic test conditions of the PWT, will be further explored and discussed in subsequent sections.

Figures 5.19 and 5.21 illustrate the samples surface temperature measured upon the imposition of a defined heating conditions represented as the dashed red line. In the (b), the corresponding strain versus time under the 20MPa constant creep load. In general the strain remains low in the first stages of the test, then increases as the material softens in response to the increasing temperature, until a sudden fracture clearly identified by vertical lines. Figures 5.20 and 5.22 report the time and temperature at the fracture onset, taken at the point where strain increases sharply. In addition to the degradation onset, identified as the instant where the first visual demise behaviour is detected on the video, typically a surface delamination "pop" or surface resin bubbles. For the results under UC re-entry conditions presented in figure 5.19 and 5.20, CFRP emerges as highly temperature-resistant compared to the other four skin versions, exhibiting no fracture until the termination of the test, even at temperatures exceeding 700°C for more than 100 seconds.

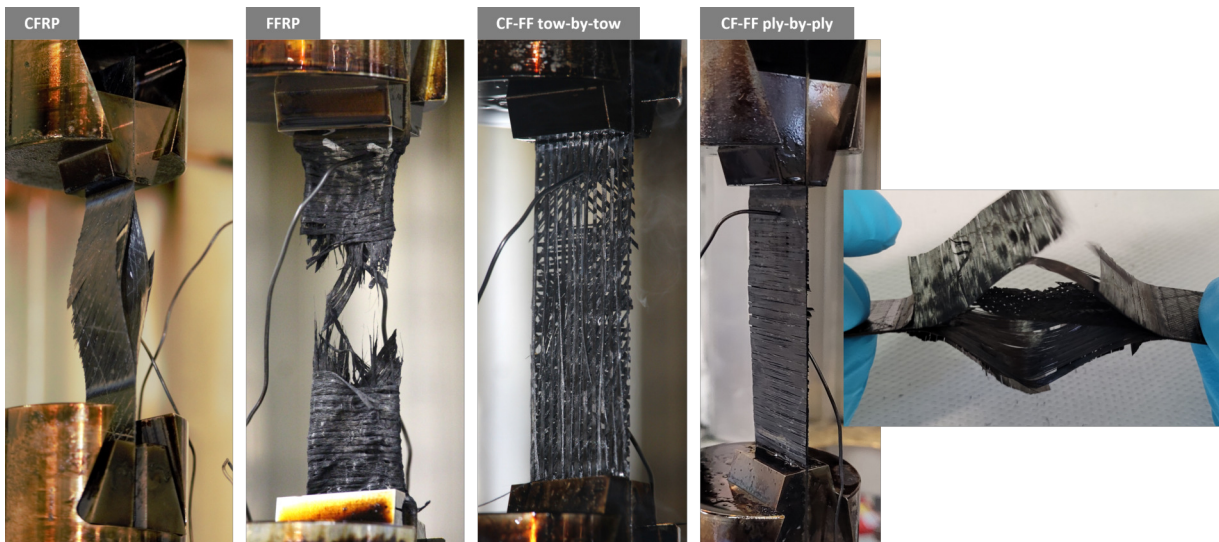


Figure 5.18: Recovered composite samples allowing a complete visual inspection and comparison of the demise state of the four different reinforcement types (CFRP, FFRP, CF-FFTBT, CF-FFPBP). On the right picture, a closer view of the ply-by-ply hybrid, with a clear view of the central twill flax ply near a full demise with only carbonated flax fibres left.

In contrast, the CF-FFPBP hybrid sample, while promising, experienced failure before reaching 580°C. In terms of demisability, the CF-FFPBP hybrid exhibited an earlier and lower temperature fracture compared to the CF-FFTBT version, with reductions of approximately 150 seconds and 160°C, respectively. Despite a similar fracture strain with the two FFRP-based skins, the failure behavior of the CF-FFTBT hybrid appears to be influenced by its flax component.

Upon fracture analysis of the recovered samples, it was observed that skin versions with carbon fibers exhibited a slip failure, with the pin holding system pulling through. On the other hand, full flax samples failed at the center, where the temperature is highest. Examining the reported values in figures 5.20 and 5.22, showing similar test results but for the High Flux, STS-96 re-entry condition, it becomes evident that matrix degradation leading to demise initiates well before mechanical failure. This onset of degradation is determined by visually detecting matrix bubbles and/or surface delamination. No distinct differences or specific trends were observed between the different skin versions. On average, matrix outgassing commenced at a surface temperature of 171°C, occurring after approximately 627 seconds and 214 seconds under UC and STS-96 re-entry conditions, respectively. All versions exhibited extensive pyrolysis outgassing, typically indicated by a plateau in the temperature graphs, visibly apparent after around 860 seconds for the CF and CF-FFTBT samples in figure 5.19.

UC re-entry/Low-HR condition

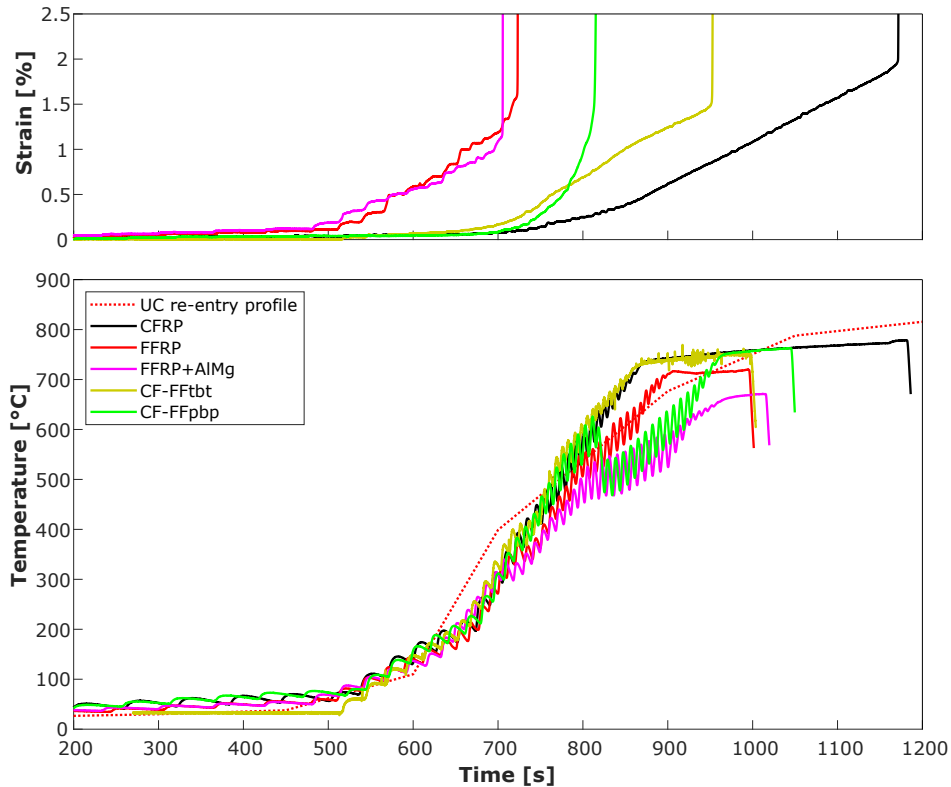


Figure 5.19: Comparative strains and temperature profiles of the five different panel skin materials evaluated under the uncontrolled re-entry condition.

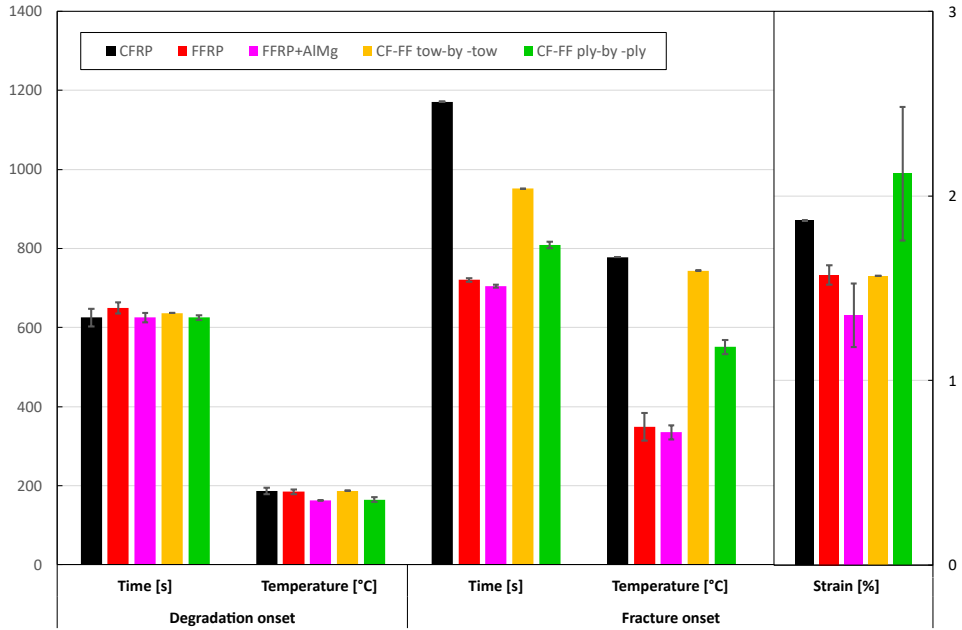


Figure 5.20: Reported fracture and demise onsets of the five different panel skin materials evaluated under the uncontrolled re-entry condition.

STS-96 re-entry/High-HR condition

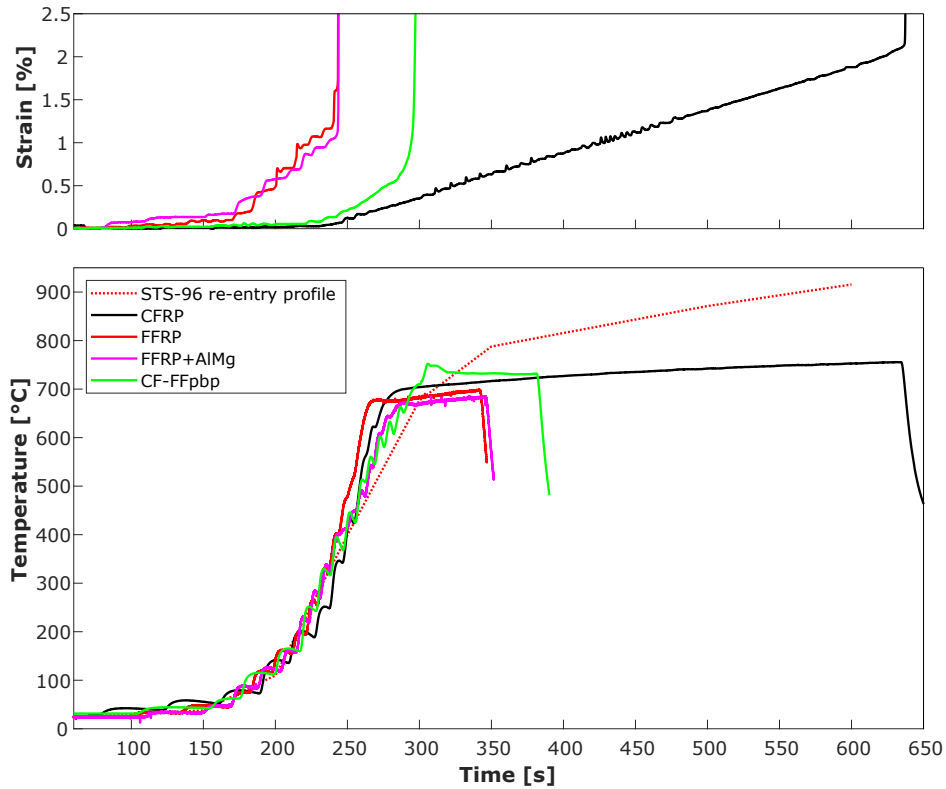


Figure 5.21: Comparative strains and temperature profiles of the four remaining panel skin materials of interest evaluated under the STS-96 re-entry condition.

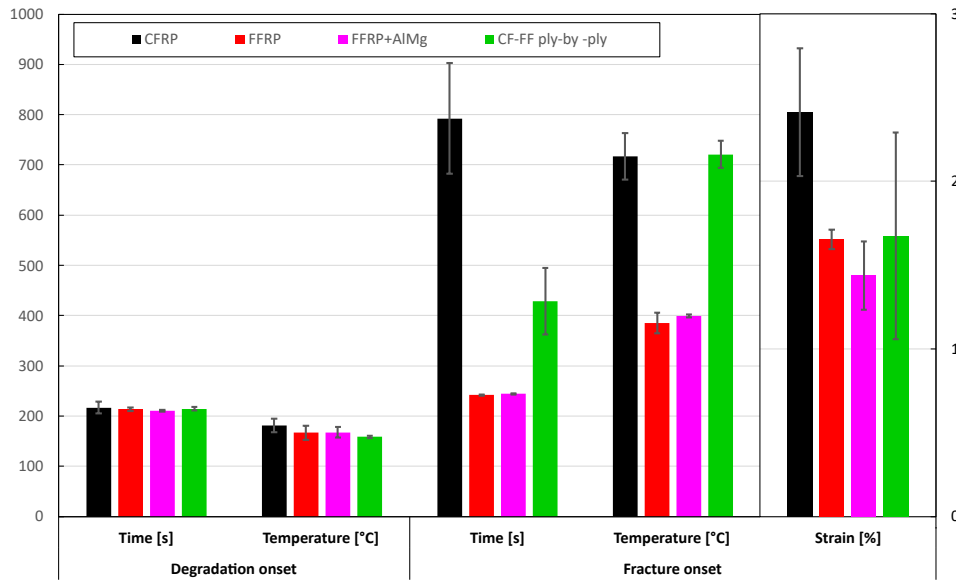


Figure 5.22: Reported fracture and demise onsets of the four remaining panel skin materials of interest evaluated under the STS-96 re-entry condition.

Influence of AlMg integration of SRC

In terms of the influence of AlMg micropowder, subtle differences in fracture behavior are discernible between the virgin and AlMg-charged FFRP, as illustrated in figures 5.23 and 5.24. The observed trend aligns with expectations, indicating an earlier failure and higher temperature at the failure point for the AlMg-charged sample, with respective differences of approximately -11 seconds and +22°C. A comprehensive analysis of the temperature curves in figures 5.23, 5.24 and the accompanying videos reveals a notably higher temperature at the top TC. For the center and bottom TC data, a drop is observed at 720 seconds, with the charged sample displaying a generally lower trend after this point. This drop is attributed to the sample's fracture, causing it to slide down the holder and the attached TC to a colder region, slightly above the surface. Overall, the integration of AlMg appears to have improved the thermal distribution through the samples, as evidenced by the pink and red curves compared to the light and dark blue ones before the drop.

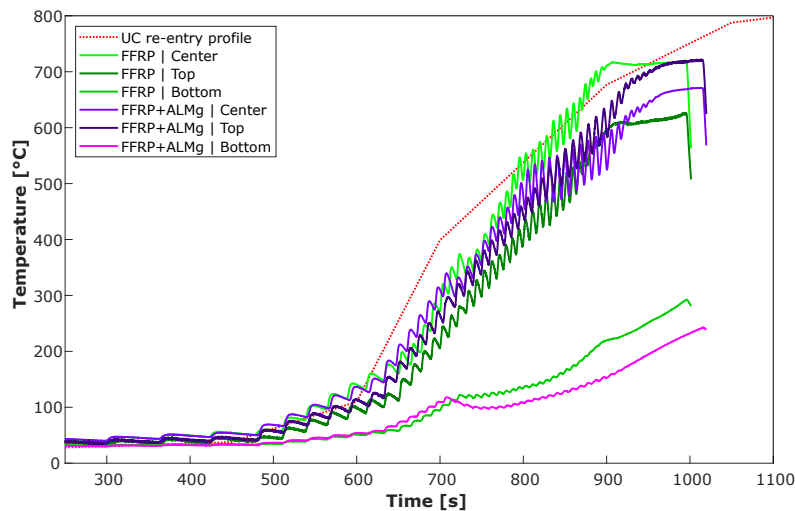


Figure 5.23: AlMg filler effect on surface temperature of FFRP samples under the uncontrolled re-entry conditions.

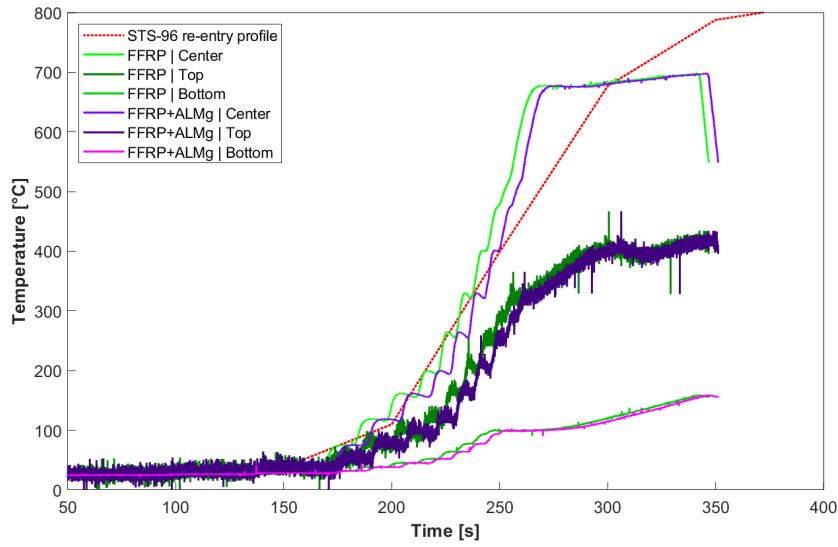


Figure 5.24: ALMg filler effect on surface temperature of FFRP samples under the STS-96 test conditions.

Mass loss analysis

The final dataset extracted from this test campaign relates to mass loss, used to determine the demise heat. It is defined as a combination of the heat of matrix pyrolysis and fiber degradation, encompassing processes like phase transformations, outgassing shielding, carbonization and oxidation. Calculation of demise heat, as displayed by equation 5.5, employs an integrated heat based on surface measurements. It was computed using fitting and integral functions. The mass loss $m(t)$ was integrated following a linear trend over time.

$$Q_{Demise} = \frac{Q}{\Delta m} \quad (5.5)$$

$$\text{with } Q = \int_{t_0}^{t_1} m(T) \cdot c_p(T) \cdot \frac{dT}{dt} dt$$

With Q the heat [J] and c_p the specific heat [J/kg°C].

It can be observed that lower heating rate or heat flux induces a higher heat of demise, with the exception of CF-FFPBP, where high data variability might contribute to the observed phenomenon.

Concerning the comparative evaluation of metallic filler integration into an FFRP laminate, a distinct demise improvement is evident, with nearly 25% lower heat needed, reaching close to 40% when heat is reported relative to sample thicknesses. However, in terms of hybridization effects, the anticipated improvement is not observed. The CF-FFPBP exhibits higher values, with an increase of +54.4% and +147.7% under low and high heating rate conditions, respectively. This discrepancy can be attributed to substantial differences in sample thickness, with CF samples being over 30% thinner. Therefore, by looking at the comparative right histogram of figure 5.26 where the demise heat is reported relative to sample thicknesses, this partially adjusted method still indicates higher demise heat for hybridization compared to CF, with increases of +4.5% and +67.5% under the respective test conditions.

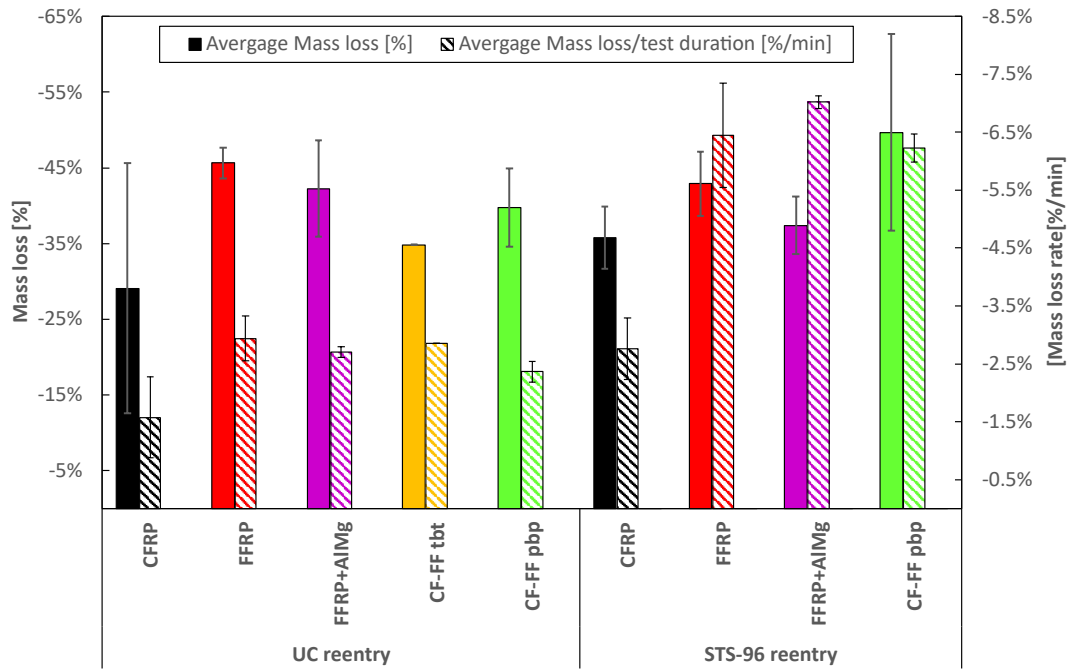


Figure 5.25: Effect of composite materials and heating rate (test conditions) on mass loss and mass loss rate under SRC testing.

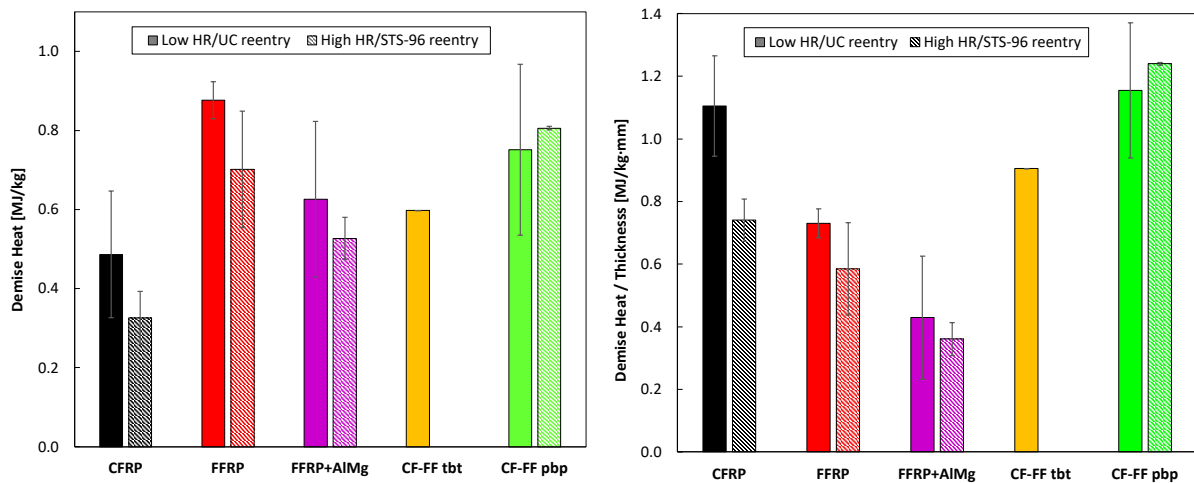


Figure 5.26: Comparison between composites materials and the two heating conditions of demise heat alone on the left and related to samples thicknesses on the right.

Effect of discontinuous CF reinforcement under re-entry-like conditions

The temperature curves are displayed in figure 5.27. A temperature overshoot is observed for all the samples before a plateau compared to the set applied temperature profiles (red lines). This behaviour can be explained by the selection of the top thermocouple as machine controller, as displayed in figure 3.21, inducing a higher heat input to the central part of the samples from where these curves are extracted.

In a second time, it can be observed that in every case the samples surface temperature achieves a plateau around 700°C. Based on the videos, such trend seems to be due to the pyrolysis reaction outgassing cooling effect and by-products covering the chamber tube inner surface resulting in a decrease of the incoming radiative heat.

Innovative Facesheet Materials and Reinforcement Combinations

The introduction of the discontinuous CF reinforcement pattern (SMC-HP) induced a clear earlier and non-uniform failure identified by abrupt drop of stopped lines.

Several remarks and observations can be made from this evaluation results:

- It appears clearly that the demise (matrix degradation) is initiated before the mechanical failure, an expected with such sample thickness and relatively “low” preload.
- The cut-CF design clearly allows an earlier and lower temperature fracture onset under both UC/STS-96 reentry conditions with respectively -201s/-295s and -29°C/-98°C. This can be related to the cut-CF design which seems to induce a lower strain at fracture at this temperature, since the matrix is more sollicitated (more than 50% lower).
- The degradation timing and temperature onsets are similar between the two-reinforcement design as this is set from the matrix demise. The matrix degradation temperature onset is observed between 341-408°C around 660s (UC reentry condition) and 210s (STS-96 condition).
- The crucial demise behaviour difference stands in the type of failure which can be clearly seen on the recovered samples illustrated in the following figure 5.29. The UD/continuous-CF samples showed late slipping failures happening by slow thermal degradation in the holder region. Whereas in the case of the cut-CF (SMC-HP), brittle failures happen at center with cut ply opening clearly observed with the sharp circular cut profiles of fracture interface. So these latter showed a complete monolithic failure and separation, where the continuous ones failed only at the holder drill hole weakened point leaving a quite structurally intact center piece with full CF integrity.
- A post-test separation loading step at room temperature on the cut-CF samples shows an average remaining strength of 600N (8.4 MPa) after the initial fracture. This corresponds to the fracturing of the remaining cut-CF plies in directions other than 0°.
- Regarding the heating rate influence on fracture and matrix degradation onset temperature, an inverse behaviour is observed as compared to the literature. As expected, under a low heating rate (UC profile), the demise happens at lower temperatures. But the trend is the opposite in the case of the fracture with a higher onset temperature under low heating conditions again as can be observed in figure 5.28.

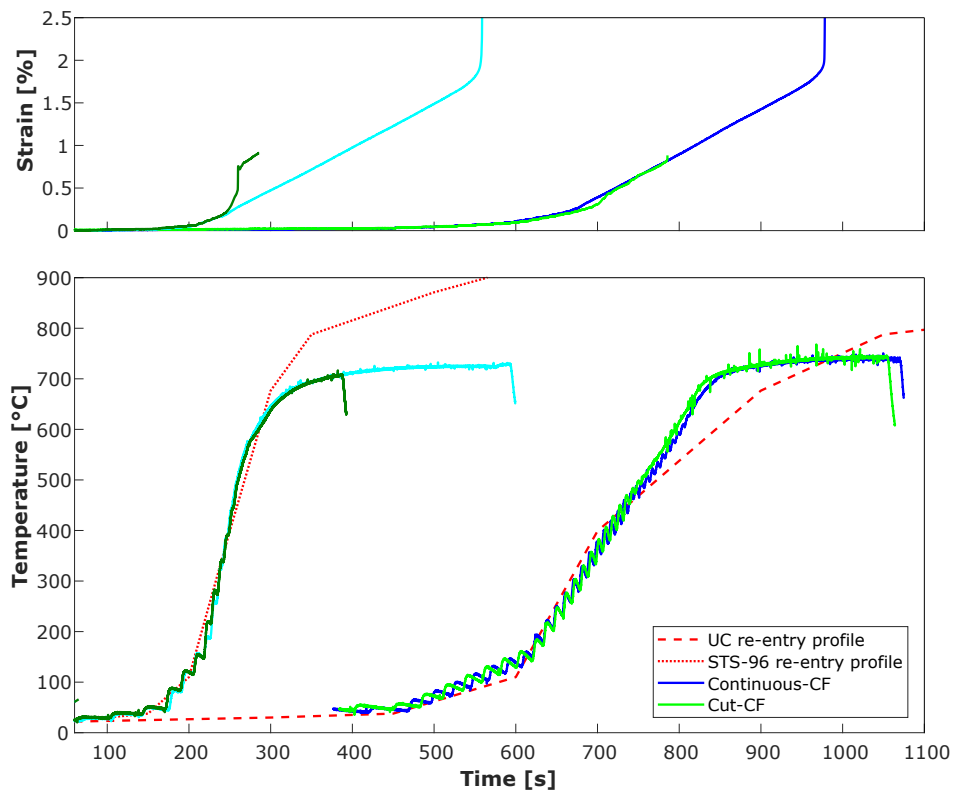


Figure 5.27: Cross-comparison of SRC thermo-mechanical curves between the low and high heating rate testing conditions, and UD continuous-CF versus SMC-HP cut-CF. The temperature curves are extracted from the central thermocouple measurement point. The cross at the end of the SMC-HP displacement curves indicates the samples' fracture.

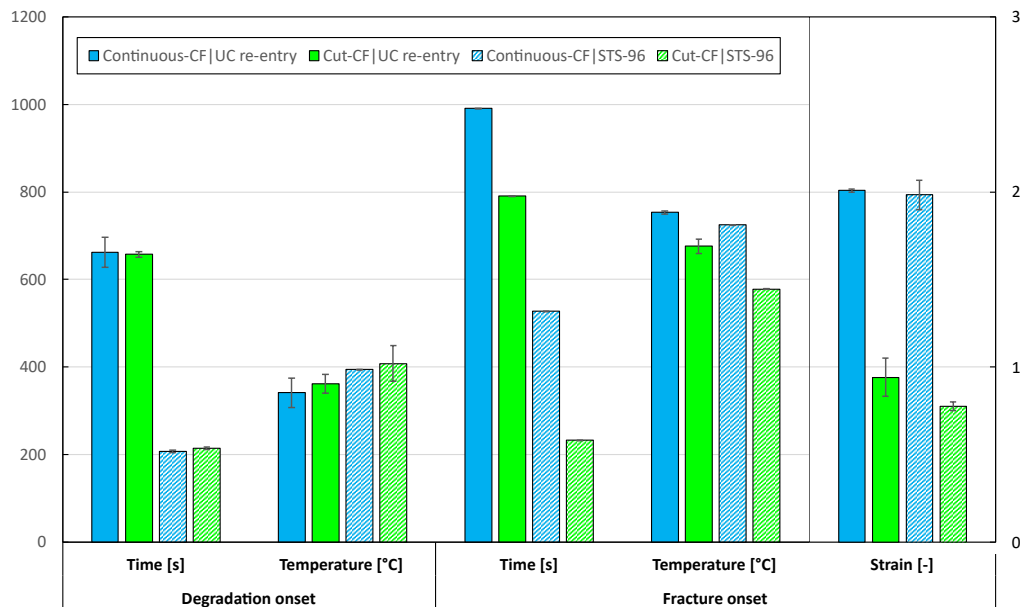


Figure 5.28: Comparative histogram of SRC fracture and matrix degradation onsets with continuous-CF versus novel cut-CF samples under two reentry-like conditions (UC and STS-96).

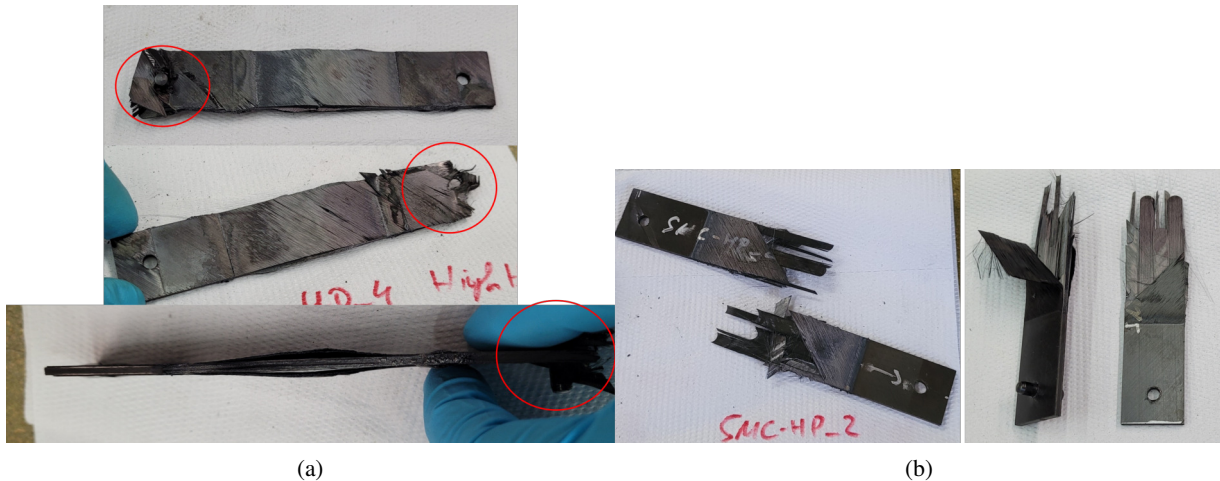


Figure 5.29: Pictures of the recovered samples, allowing the characterization of the failure modes and location. (a) Continuous UD samples, with top pin slipping fracture (highlighted red regions). (b) cut-CF/SMC-HP samples, with clear central part fracture.

5.4.3 High fidelity testing through Plasma Wind Tunnel

With this high fidelity demise testing method, eleven composite samples have been tested under two different hypersonic conditions, which were previously detailed in table 3.8.

The four different sensors, illustrated in figure 3.24, acquired video in the optical and Infrared (IR) ranges, from which the full recordings can be observed with from this [link](#) and snapshots of all the samples can be found in figure A.8. The back and front surface temperatures measured by the mean of pyrometers are displayed in the following graphs of figures 5.31 and 5.32. As multiple monitoring methods and sample types were evaluated, five separate comparative evaluations were performed and are detailed hereafter. It is important to note that all these temperature data were corrected to take into account the emissivity of the sample, a necessary step when using these non-invasive monitoring methods. This temperature-dependent parameter was based on previous total and spectral emissivity measurements performed by IRS on CFRP with their dedicated facility (EMF) [106].

During the CFRP and FFRP first runs under MAX-H, both samples experienced an unexpected dislodgment (pop-out) from the pre-stressed sample holder but they managed to stay in place until test termination. This was due to a faster materials softening than experienced in previous tests at IRS, as a remediation, weaker constraining springs were integrated to clamp the samples.

Several data acquisition issues were found during data compilation following the test campaign. Due to unfortunate thermal camera and front pyrometer calibration errors between the switching of test conditions, the CF-FFTB sample data under MAX-H are unreliable. Also, in the case of the pyrometer measurements, all the hybrid versions data under MAX-H were out of range above 1100°C. As a lesson learned, a set of thermocouples for the back surface temperature monitoring in addition to the pyrometer (MiniPyrex) would have allowed a valuable redundancy and more consistent data. Finally, an optical emissivity spectrometer

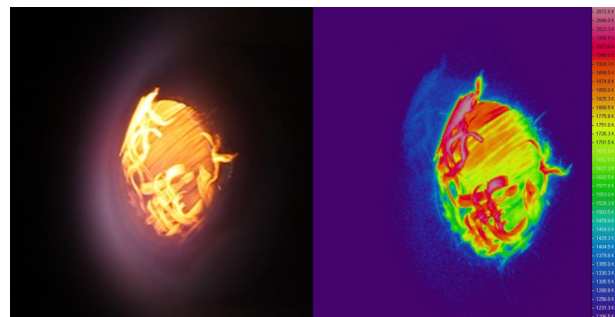


Figure 5.30: Optical vs IR view of the CF-FFPBP A sample under MHF after 30s.

setup was installed but no exploitable data could be acquired from this setup.

The identification and evaluation of key material demise phenomena and parameters to be used for composite demise modelling were achieved by the completion of data collection by pre/post-testing samples' physical characterization. The parameters of interest from this test campaign were:

- Specific demise behaviour (such as pyrolysis, spallation, oxidation, swelling, delamination)
- Temperature profile of the front and back surface
- Surface recession rate
- Mass loss rate
- Ablation heat

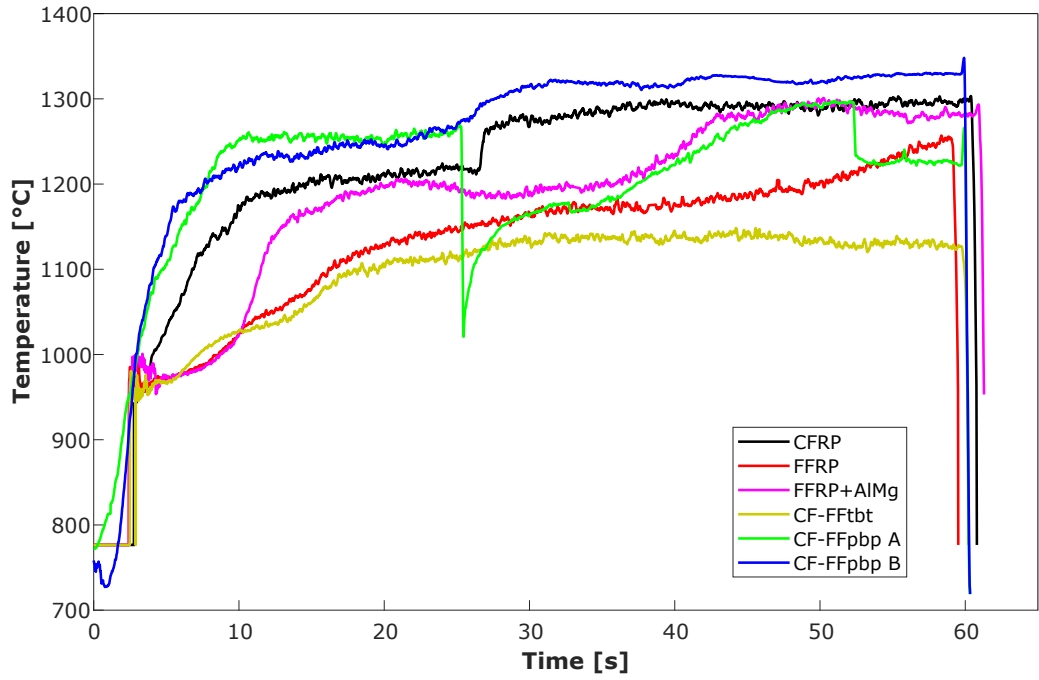
The following graphs summarize the front and back temperature of all the run samples respectively under the Medium Heat Flux (MHF) conditions in figure 5.31 and under the maximum ones (MAX-H) in figure 5.32.

Before focusing on comparative studies, general points can be highlighted. First, regarding characteristic demise behaviours, all the samples displayed different and interesting demise-driven processes, from dynamic carbonization (FFRP based samples), slow and constant fiber by fiber spallation (CFRP), static combustion (CF-FFTBT) to multi-ply separation (CF-FFPBP).

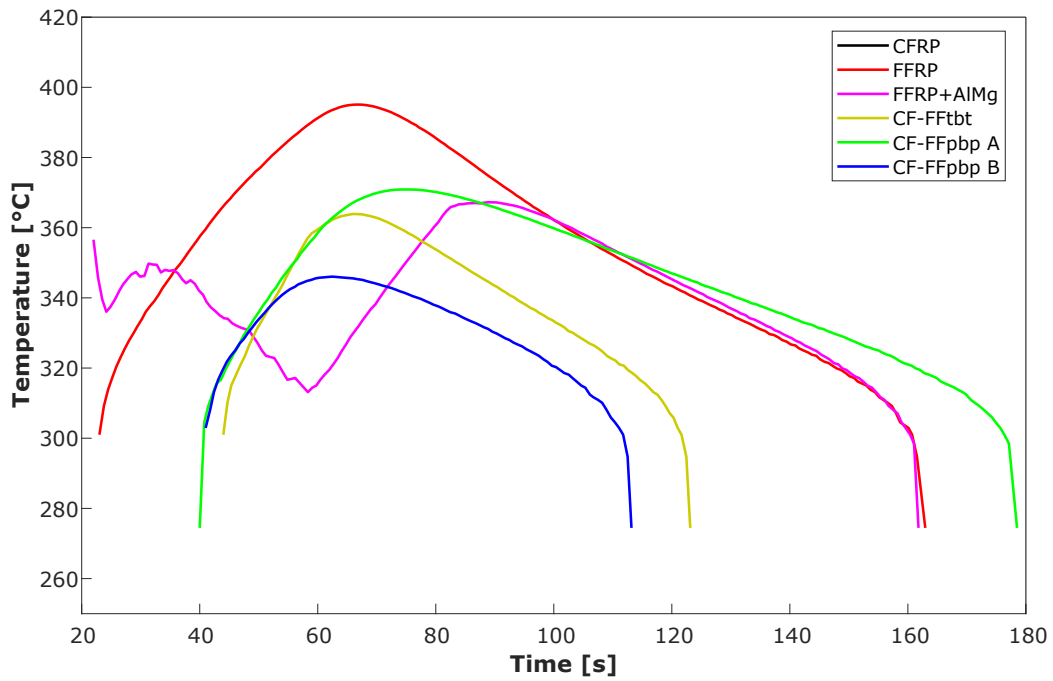
Regarding the front temperature data, the lowest temperature was always observed for the full flax samples, and the highest was observed for the CFRP. In general, the observations for the CFRP and FFRP are highly consistent with what was observed from previous test campaigns with identical or similar material under lower and similar conditions at IRS. [53][18]

Distinguishable sharp drops of temperature are observed for the CF-FFPBP hybrid *A* and *B* in front temperature graphs, and significantly more in the MAX-H one. Using the video recordings to validate if these are artefacts or real physical effects, they actually represent a specific behaviour where the full surface of the ply falls of the sample. A similar temperature drop is observed for the FFRP under MAX-H, but in this case the drop is due to the sample accidental extraction from the sample holder as specified earlier. Under the same condition, the similar encountered issue with the first CFRP run is less distinguishable, with a light bump before a slightly decreasing plateau.

Now regarding back surface temperatures, the trends are not consistent between the test conditions. For example under MHF, the CF-FFPBP version *B* lowest temperature would suggest a low thermal conductivity or some blockage phenomenon, but under MAX-H it shows the highest temperature of the 60 seconds tested samples (apart the artificially high temperature for FFRP from its dislodgment issue). Regarding the CF-FFTBT, the change to a higher heat flux inexplicably induced a lower back temperature (monitoring issue/undetected characteristic demise process). Another outlier is the FFRP+AlMg profile under MHF, where some hypotheses on the cause are detailed in the following AlMg integration effect section.

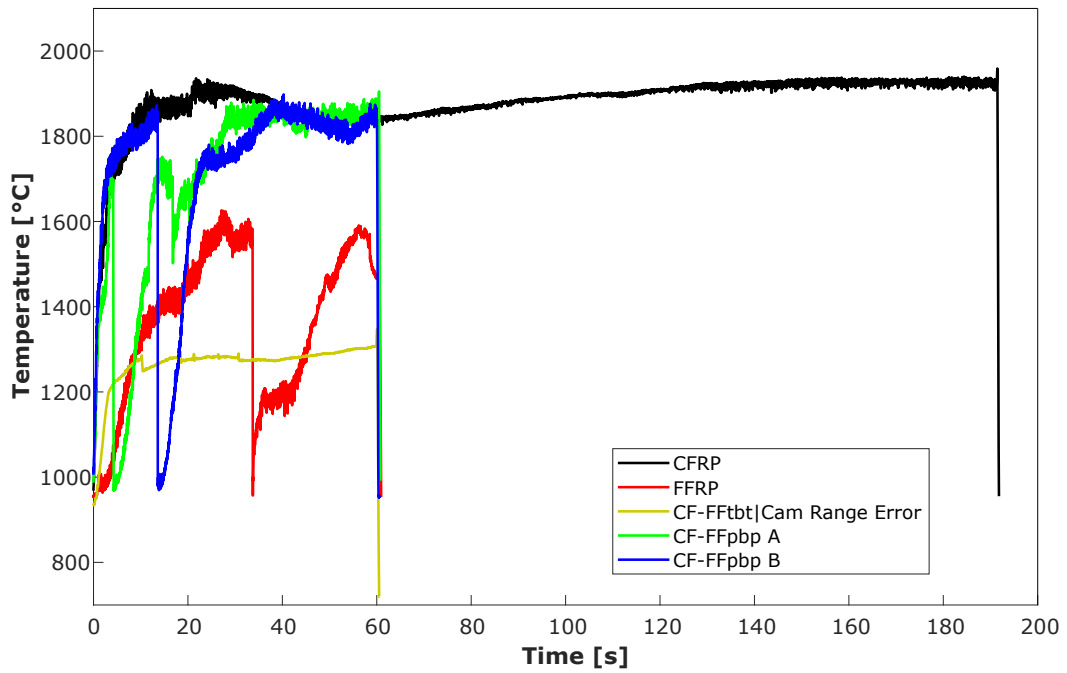


(a)

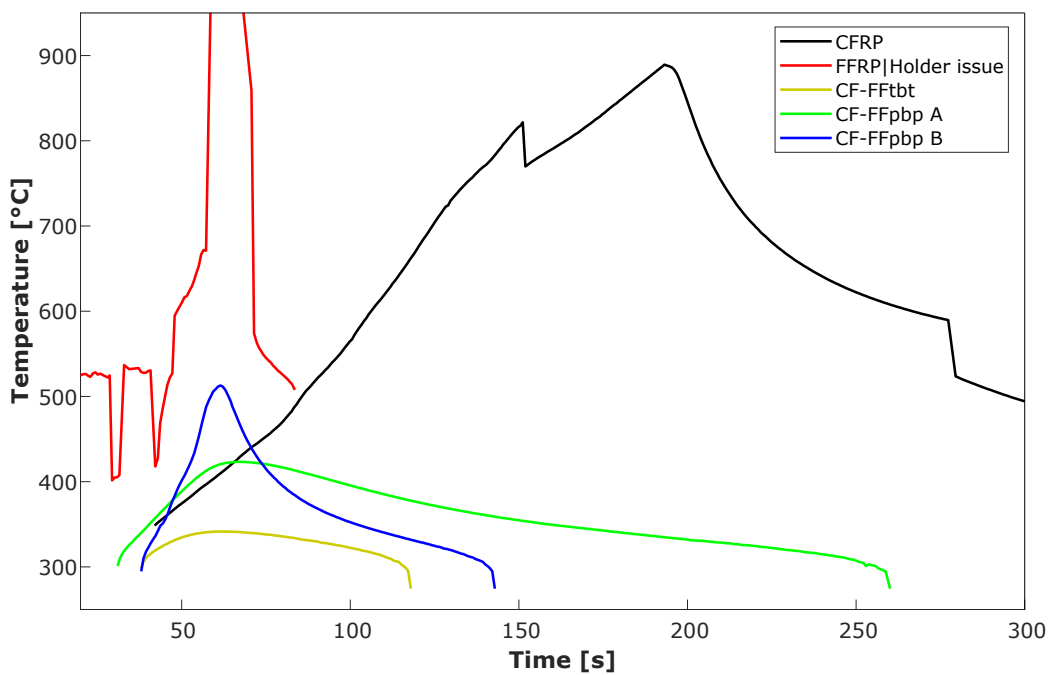


(b)

Figure 5.31: Complete data overlay comparison under MHF condition with the front temperature data from the thermal camera and the back surface temperature from the MiniPryex.



(a)



(b)

Figure 5.32: Complete data overlay comparison under MAX-H condition with the front temperature data from the thermal camera and the back surface temperature from the MiniPryex.

Front temperature measurement method comparison - Thermal camera versus pyrometer

Let's start with the comparative analysis of the two front temperature monitoring methods, where simultaneously an IR thermal camera and a pyrometer recorded respectively a predefined central area of interest and the center point on the sample. The temperature profiles for four different sample types obtained through these techniques are depicted in figure 5.33. However, it is noteworthy that these profiles (dark blue and orange) do not exhibit a consistent overlay across test duration for several sample types. Differences up to 200°C can be observed.

For the CF-FFTBT and before the first vertical drop of temperature of the PBP A hybrid, the data points from both methods align well, a trend also observed with CFRP under the MHF condition (refer to figure A.7 in the appendix A). In contrast, a low degree of overlay is observed for both FFRP-based samples, as well as in the second part of CF-FFPBP A and CFRP under the MAX-H condition. These significant variations may originate from differences in material emissivity and/or surface states. Notably, a pyrometer, being a single-point measurement system, is highly sensitive to such parameters. The differences of demising surfaces can be observed in figure A.8 and what such surfaces looks like after testing in figure 5.40.

Based on this hypothesis, the high variability of CFRP under MAX-H and the ply-by-ply hybrid can respectively be attributed to the sample dislodgment and the ply separation. Both events induced a tilt and uneven surface. The complete dataset recorded by the pyrometer under both test conditions is available in figure A.6 in the appendix A.

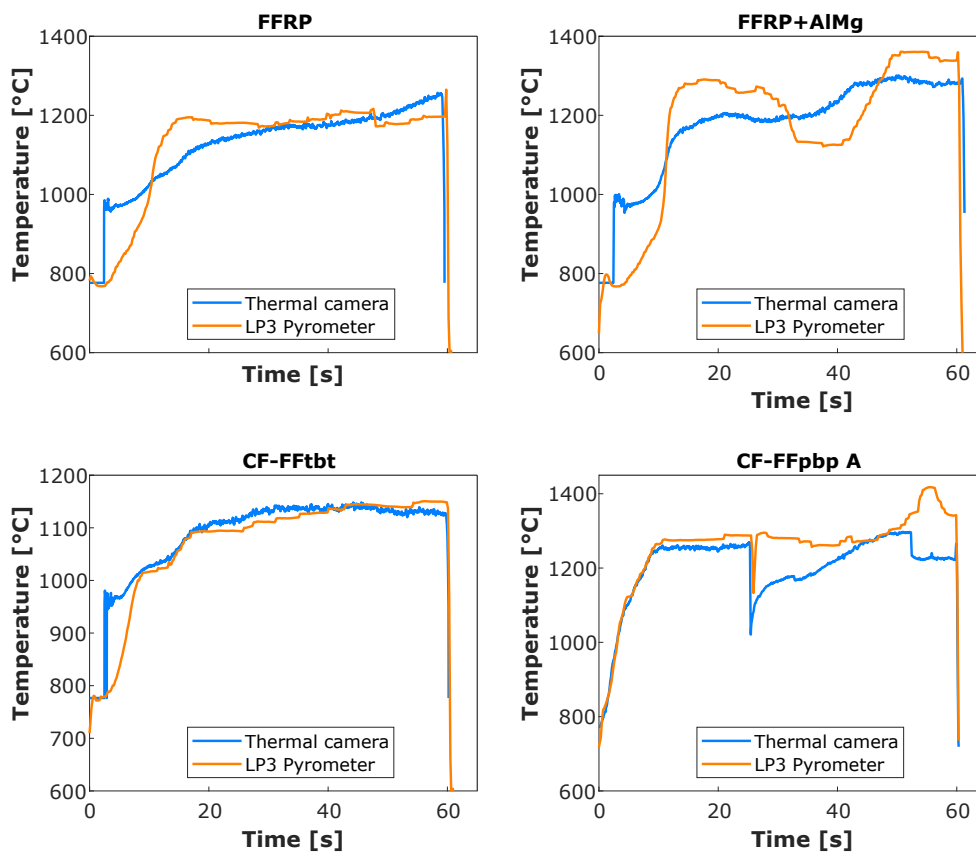


Figure 5.33: Front surface monitoring method comparison of four samples types, FFRP, FFRP+AlMg, the tow-by-tow hybrid and the thin CF version A ply-by-ply hybrid.

Test condition influence - MHF versus MAX-H

As a first observation it can be noticed from figures A.8 in the appendix A and 5.39 that the CFRP samples display a similar and expected demise resistance with an extremely low surface recession process displayed during testing, both under MHF and MAX-H conditions. Once the steady state is achieved and the matrix of the first plies is vaporized, fiber bundles are one-by-one being spallated from the surface from the dynamic plasma blow. So apart from a noticeably faster spallation rate, the increase in heat flux does not lead to the full demise of the CFRP.

For all the other sample types, this heat flux rise induces a clear difference in demise behaviour. For the FFRP under MHF, the carbonizing flax fiber/matrix system turns in a 3D fibrous structure with a continuous radial destructive "blooming" movement of the plies. Such process is clearly accelerated by switching to MAX-H conditions, which can be partially be observed in snapshots of figure 5.37. The FFRP+AlMg samples show a similar trend.

Regarding the hybrids, the tow-by-tow displays a surprising static demise of the flax tows under MHF condition with no visible tow or plies delamination/spallation, and where CF tows spallation only appears under MAX-H. For the PBP hybrid A and B versions, the test conditions altered differently the back surface temperatures but also their characteristic front ply delamination process timing. The details regarding this hybrid type conditions influence can be found below in the dedicated comparative analysis.

Hybridization effect

The tow-by-tow (TBT) and ply-by-ply (PBP) hybrids behave quite distinctly under MHF when looking at their front and back temperature profiles overlay displayed in the next figure 5.34. The TBT (yellow) presents a much lower surface temperature, around -200°C once stabilized. Such cool surface is explained by the presence of flax fiber in the front plies, where this similar temperature trend can be observed along FFRP and FFRP+AlMg samples in figure 5.31. This might be due to the combination of the flax tow carbonization process and the creation of a flux absorbing CF hollow structure due to the complete demise of the flax tows. Such interesting characteristic state can be observed from the videos and snapshots, where clear CF tows stay surprisingly in position. This hollow structure falls apart once the samples are recovered from the holder.

This demise process contrast clearly to the PBP hybrid, for which the surface state is overly active, with short duration carbon fiber or bundles spallation happening before complete ply separations. Along this 60s runs, this separation occurred twice for the version A and not once for the thick CF version B. For this latter it can be noticed from the video that the fist top layer (CF+FF) was moving, and completely fell-off during sample recovery.

This highlights that under similar conditions but with free-edges holder, both these ply separations, for this PBP hybrid, and the tow spallation, for the TBT hybrid, would happen much faster and most probably allow an overall faster demise by preventing the current shading effect from their constrained edges.

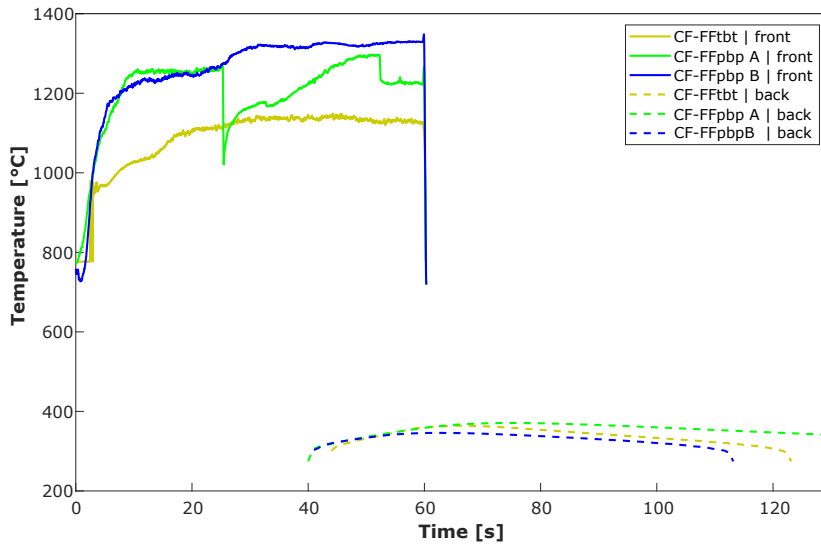


Figure 5.34: Front and back surface temperature profiles of both hybrid types under MHF test conditions.

Carbon fiber layer thickness influence

From the videos, from which illustrative snapshots can be observed in figure 5.35, the flax ply implementation within the ply-by-ply hybrid version A (thin CF layers) shows a fast top CF ply delamination and separation, with two events within the 60 s under both test conditions. Such separation events characterized by a vertical fall of the front temperature can be verified in figure 5.36. In comparison, the version B which integrates 3x thicker CF layers, only shows a single full-ply separation under MAX-H. This is again can be verified by the single drop of the temperature curve (dark blue) in figure 5.36. Thin CF layers thus present a beneficial behaviour towards a fast and efficient composite demise compared to the CFRP tested here or previously reported by Pagan [106], where his parametric study suggested that methods should be found to facilitate the delamination.

The significant front temperature drop during ply separation clearly demonstrates the shielding/insulator

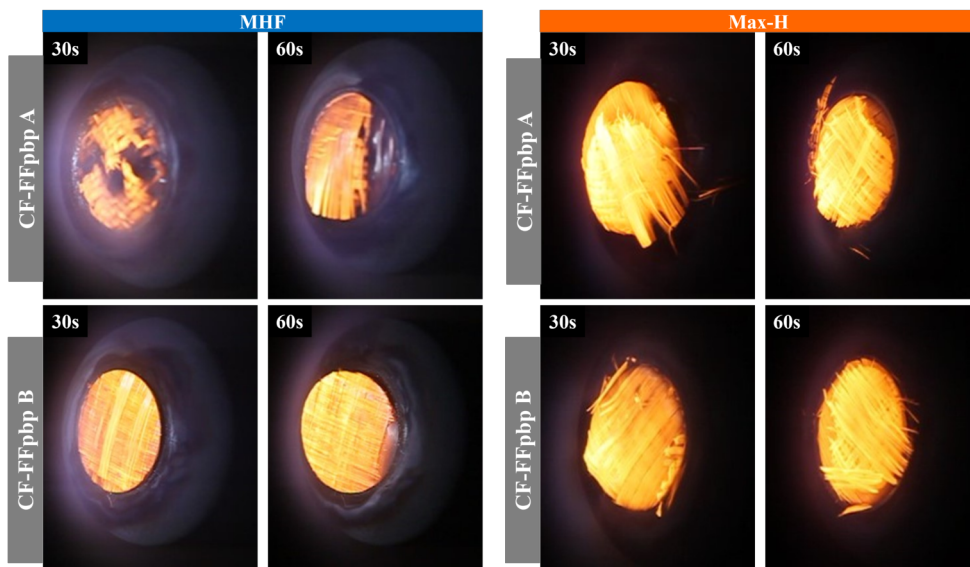


Figure 5.35: Visual demise behaviour comparison between thin CF (A) and thick (B) ply-by-ply hybrid samples under MHF and MAX-H conditions.

effect from the undemisable CF, where even a 0.116 mm layer induces a drop of more than 700°C. This highlights the importance of such separation process.

By comparing the recovery temperature right after these drops, it can be noticed that they are extremely similar whatever the CF thickness (version A or B) or test condition (MHF or MAX-H). This indicates that the heat transfer is quickly stopped by the charred/carbonized flax ply acting as an insulator before allowing the front CF layer separation.

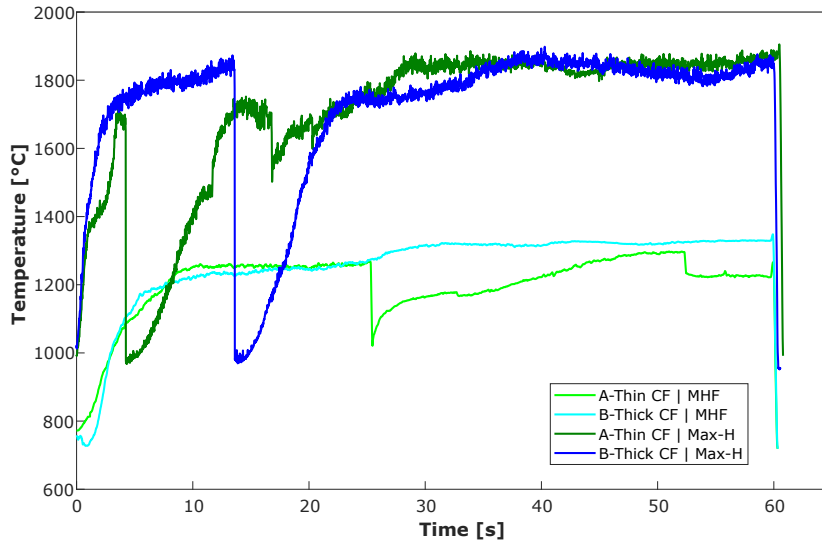


Figure 5.36: CF thickness influence on temperature curves.

AlMg micropowder effect in FFRP under MHF

Based on the optical video recordings, where some snapshots are displayed in the following figure 5.37, both the virgin FFRP and the AlMg filled FFRP composites exhibit a specific demise process, transforming the carbonizing flax fiber/matrix system into a 3D fibrous structure with a continuous and destructive "blooming" movement of the plies. The only difference is that the FFRP+AlMg sample displays faster plies moving towards the center and composite carbonization/pyrolysis. This suggests a noticeable improvement in the demise rate and front surface temperature compared to the virgin FFRP

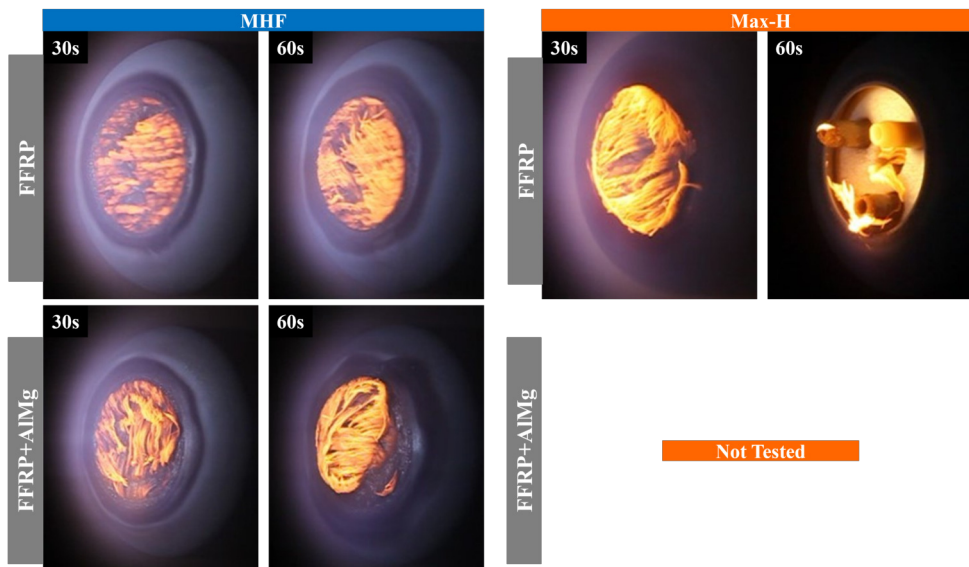


Figure 5.37: Visual observation of the AlMg integration effects on demise behaviour under MHF.

sample, a trend supported by the graph in figure 5.38. This aligns with the findings from TGA, and SRC results presented earlier.

Regarding the back surface temperature, the integration of the metallic powder reveals a surprising hollow profile (purple dashed line) as previously highlighted in the general description of the results. Such depression appears where a maximum and higher values than the virgin FFRP was expected based on the thermal conductivity evaluation. Explaining this trend is challenging with a single dataset; potential factors include acquisition issues, insulation effects due to strong outgassing, or the pronounced fibrous demise process.

The cross-sections of both the virgin and tested samples are shown in figure 5.39. Degradation depths in terms of demised and separated plies were analyzed and are reported in table 5.8.

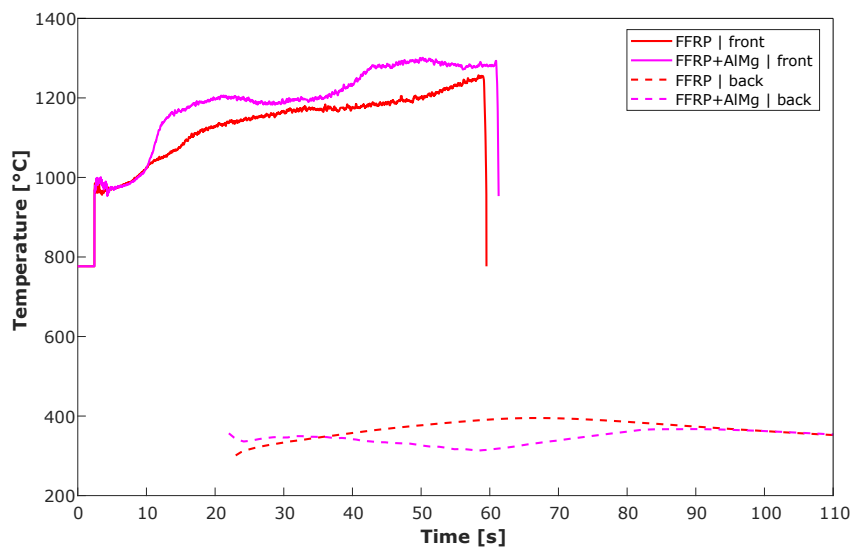


Figure 5.38: Front and back surfaces temperature of FFRP and FFRP+AlMg samples under MHF.

Pre-/Post-test physical properties

The coin test setup imposed an edge clamping, so the real/final demise states can only be observed once the samples are extracted from it. Some specific demised states can be observed from the recovered sample, in figures 5.40 and 5.39. The CFRP plies are as expected from the temperature curves, holding together with just few fibre bundles falling. The virgin and filled FFRP both present a significant thickness increase with rough brittle carbonized flax fibers. The tow-by-tow hybrid, even though looking quite rigid during the test, exhibits several dry CF tows, with a large number separating without effort.

The following table 5.8 reports the number of demised or completely separated plies assessed from the videos and the recovered samples (figure 5.40, in addition to the mass loss and thickness recession rates evaluated from pre-/post-test physical properties. It is important to note that the thickness recession measurements are less reliable than mass loss measurement, due to the uneven recovered sample states (swelling, fibrous and plies separation) and therefore not discussed further.

From these results, several trends and comments can be drawn. Let's start with the extremes, where the CFRP, as expected, presents the overall lowest demise properties, where on the opposite, the FFRP+AlMg under MHF and FFRP under MAX-H display the highest values.

5.4 Demise relevant properties' evaluation

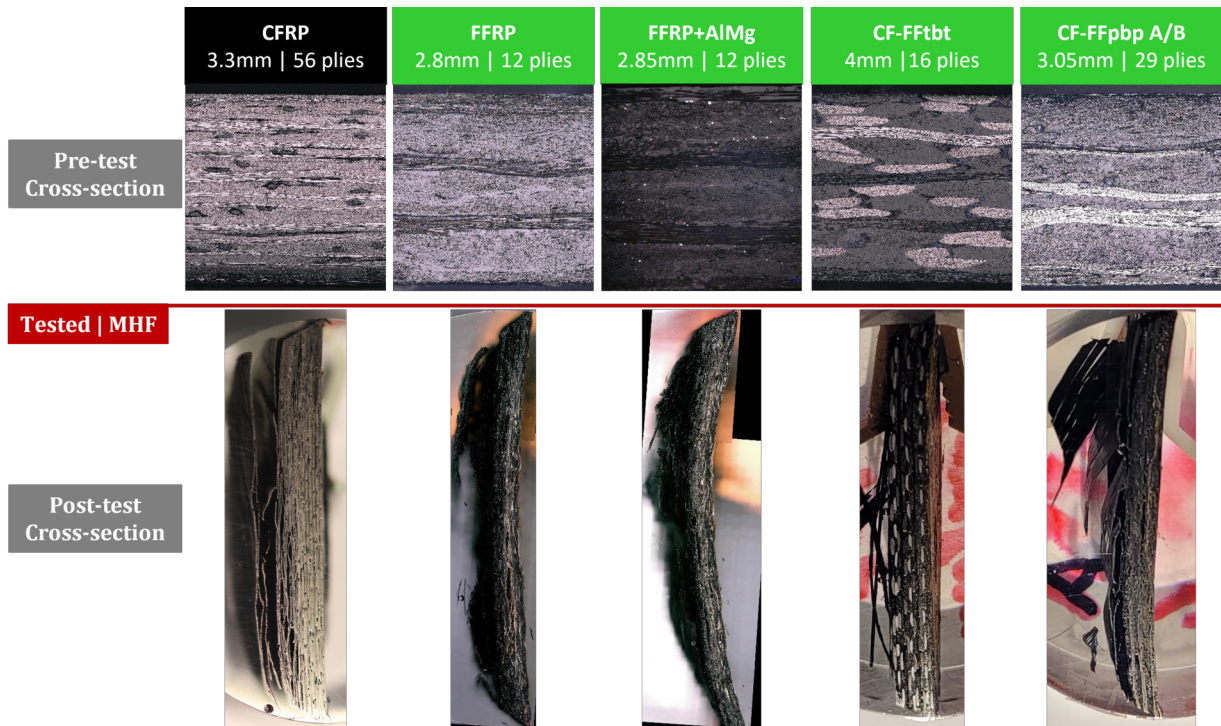


Figure 5.39: Pre-/post-test cross-section micrographs of the various different laminate samples

Compared to the CFRP, the hybrids (TBT and PBP) improve greatly the demise with respectively more than 60% and 200% higher ablation rates under MHF and MAX-H. Then between the two PBP versions, the A clearly stands out with improved properties ranging between 10-20% compared to version B. Then, between the TBT and the PBP version A hybrid, even-though ablation rate differences lower than 5% are observed, the proportion of demised/separated plies is clearly in favour of the ply-by-ply hybrid with an improvement of respectively a 15% and 37% under MHF and MAX-H.

The AlMg integration in FFRP allows a slight 4% improved ablation rate and a 17% higher proportion of demised plies.

These values can be compared to results from previous test campaigns presented by from IRS-Stuttgart, where a different CFRP grade and a similar FFRP were evaluated under wider test conditions as respectively presented in the works of A. Pagan [19] and [18]. For the CFRP, a M55J/EX-1515 (UD-CF/cyanate ester) combination was evaluated and resulted in lower ablation rate than our HTS45/VTC-401 system under closely similar test conditions, with a respective -242% and -38% under medium and MAX-H heat fluxes. Such differences are sensitive to interpretation from a single data point, but the matrix material choice was reported to play a crucial role in demise [107]. Another explanation point can be attributed to the use of thin ply CF in our case, which theoretically should fasten the fibre bundle spallation simply due to their lower amount of single fibers per bundle.

For the similar FFRP material, an ablation rate difference of just 6% is observed compared to the MHF only equivalent test conditions performed, thus validating the interest in such natural material implementation for improved demisability.

Innovative Facesheet Materials and Reinforcement Combinations

Table 5.8: Physical characteristics of the tested samples under PWT conditions.

Sample type	CFRP	FFRP	FFRP+AlMg	CF-FFtBT	CF-FFpBP A	CF-FFpBP B
Medium Heat Flux (MHF)						
Thickness recession rate [$\mu\text{m/s}$]	0.2	10.9	11.4	16.5	8.2	5.8
Ablation rate [$\text{g/m}^2\text{s}$]	20.5	36.3	37.8	34.7	33.0	28.5
% Demised/separated plies	8.9%	12.5%	29.2%	12.5%	27.6%	6.9%
High Heat Flux (MAX-H)						
Thickness recession rate [$\mu\text{m/s}$]	8.6	48.1	-	34.5	31.9	25.6
Ablation rate [$\text{g/m}^2\text{s}$]	21.6	72.4	-	71.8	69.9	62.6
% Demised/separated plies	26.8%	100%	-	28.1%	65.5%	55.2%

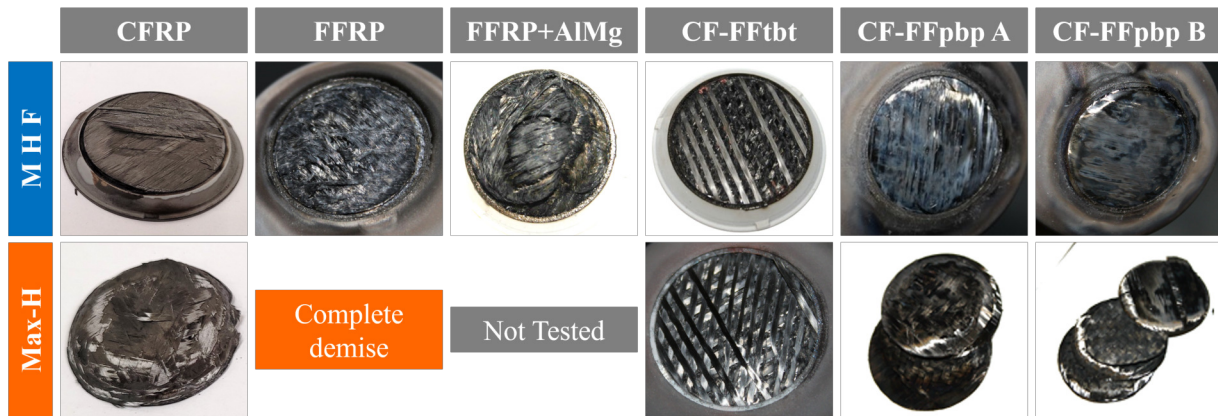


Figure 5.40: Pictures of the recovered samples

Ablation heat

The ablation heat can be defined as the combination of sensible, diffusive, matrix pyrolysis and fiber degradation heats. They are taking into account several dynamic processes such as spallation, phase transformations, outgassing shielding, carbonization and oxidation.[108][109]

The ablation heat calculation method employed here is based on the top-to-bottom approach, which is typically employed with PWT testing as a calibrated and constant heat flux value is available. This relatively simple approach, illustrated by its equation 5.6, allows to encompass all the heat terms and demise processes of composite materials, and thus provides a comprehensive metric for an effective materials' demise performance comparison. Its simplicity significantly reduces the uncertainties induced by the integration of specific material properties such as emissivity, char/oxidation reaction kinetics, and thermal conductivities, which cannot be easily related to the experienced conditions. Such an approach is related to the holistic approach presented by Pagan and Herdrich [21].

$$Q_{\text{Ablation}} \approx \frac{A \cdot Q_{\text{net}}}{\Delta m} \quad (5.6)$$

$$\text{With } Q_{\text{net}} = \dot{q}_{\text{cw}} \cdot \Delta t$$

With \dot{q}_{cw} the input plasma heat flux compared to a cold wall reference [W/m^2], A the exposed surface area, Δm measured total mass variation over the test run and Δt the test run duration.

As observed in figure 5.41 and with the exception of CFRP, all materials tested under MAX-H conditions experience a lower ablation heat. This is expected, as higher heat flux induces faster matrix degradation and

therefore faster composite material ablation/spallation. A similar trend was found with the SRC demise heat results presented in figure 5.26. The CFRP opposite trend here is explained by the significantly longer MAX-H run duration, 190s instead of the 60s for the others.

As expected, CFRP has the highest ablation heat, where the gap compared to the other material is strongly pronounced for the MHF conditions. The 1%wt integration of AlMg allowed only a small reduction in ablation heat in FFRP (-4.0%). The best hybrid version with the lowest heat of ablation is the CF-FFtBT with an ablation heat of 15 MJ/kg slightly above the FFRP. Also relatively closer stands the CF-FFpBP version A, with just 5.0% | 2.6% higher ablation heat under respectively MHF and MAX-H. This latter compared to its version B incorporation 3x thicker CF, shows a respective -13.6% | 10.5% heat reduction. And again this version A against the CFRP reference, displays significantly (-37.9% | -82.6%) reduced ablation heat.

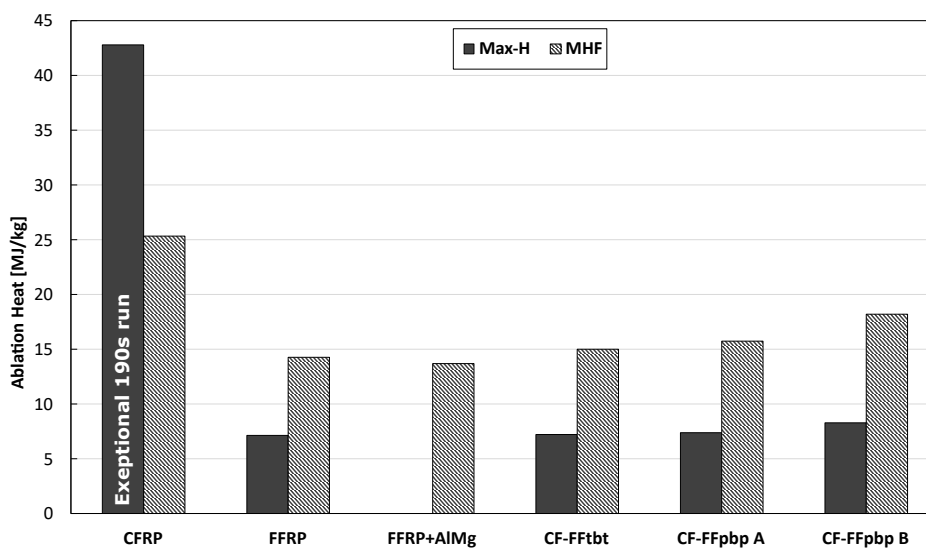


Figure 5.41: Resulting ablation heat calculation of the six composite types tested under the two PWT conditions, MHF and MAX-H.

PWT test summary

Out of all these comparative evaluations under dynamic re-entry environments, the ply-by-ply hybrid with the thin-CF layers and the AlMg integration concepts end up as the winners in terms of optimal combination for demisable sandwich panel composite skins, as they allow an efficient and fast ply separation demise behaviour compared to the CFRP baseline. The ablation improvement from the combination of high demisability flax fiber with critical CF is plainly displayed here with the example of the ablation heat reduction ranging between 40-80%, and therefore gives high hope with regard to the development of a demisable structural composite material alternative for the space actors.

It is also of interest to compare composite solutions to the aluminium baseline; as such material was already evaluated in previous PWT test campaigns, it was not included in this one. Al7075 and Al2099 alloys were tested at IRS, in a similar coin sample configuration under various heat flux conditions. These alloys demise through a typical melting behaviour, where in both cases the melting flow was delayed by the presence of a rigid surface oxide layer. But even when experiencing such surface issue, these materials showed a complete demise under 50 seconds though a 435 kW/m^2 heat flux [53][18]. Therefore,

under PWT test steady state conditions they display a much efficient demise compared to the presented composites materials. Although these are not the same alloy as the case study baseline (Al2024-T81) and as was reported by Schleutker et al. [110], changes in demise are observed based on the alloy composition, in comparison to the composite properties these differences can be assumed as negligible. Notably, due to their lower matrix temperature degradation onset compared to aluminum, these composites may exhibit increased demise effectiveness under significantly lower heat fluxes — a step to be further studied.

The PWT facility and the sensitive monitoring equipment are extremely complex to operate and require high experimental expertise, but they provide unique and highly valuable demise parameters and identification of specific behaviours. These data are currently impossible to replicate by any other means and are necessary to develop high fidelity material demise models. This point is detailed in the next chapter 6.

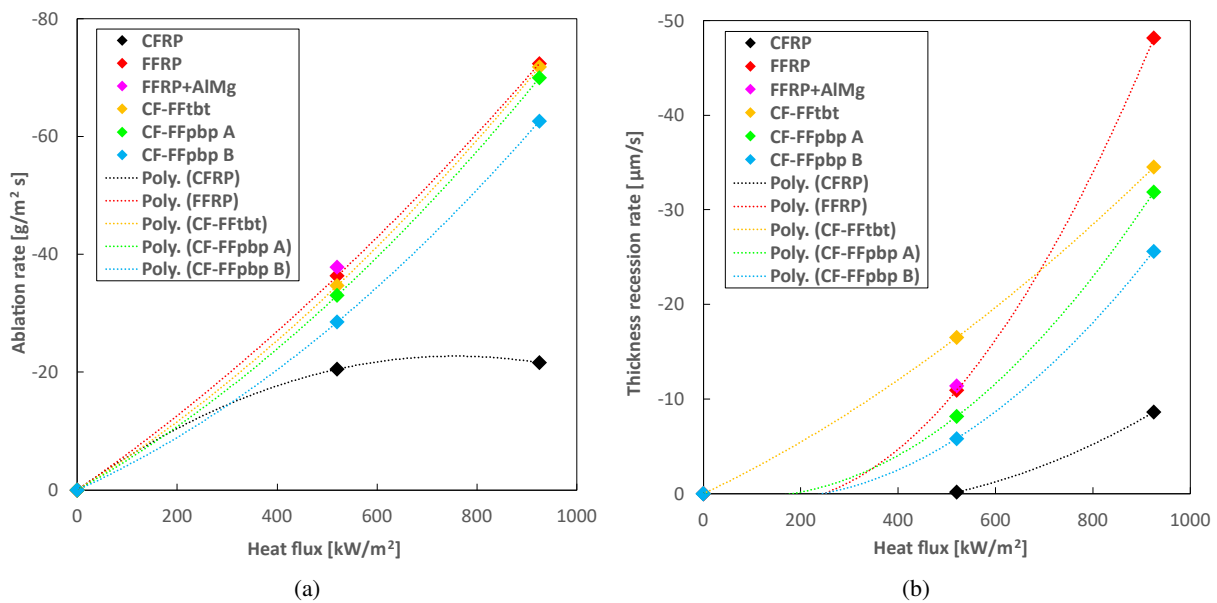


Figure 5.42: Composite samples physical demise characteristics trends in relation to the plasma heat flux with (a) the ablation rate and (b) the thickness recession rate (less reliable)

5.5 Chapter summary and technology application limitations

In the pursuit of a comprehensive mitigation plan addressing the re-entry surviving space debris threat, this chapter placed a central focus on material substitution strategies through the innovative hybridization of reinforcements and the integration of a reactive filler in a Design-for-Demise (D4D) approach. To assess the technological implications of these strategies, comparative analyses were made upon the external sandwich panel design of the CS-1 spacecraft.

The evaluations revealed significant enhancement in demise performance through a strategic material selection. Specifically, a hybrid composition combining flax and carbon fibers, as well as the incorporation of a reactive and conductive filler, demonstrated clear improvements compared to a full carbon reinforcement CFRP baseline design. The CF-FFPBP hybrid composite version emerged as an optimal trade-off between demisable and structural properties based on extensive analyses resulting of a specific static and dynamic thermo-mechanical test campaigns.

The advantages of hybridization were clear in several key aspects. Under the various test conditions evaluated, the hybrid composite showed a remarkable ablation rate improvement ranging from 60-200% compared to the traditional CFRP. The characteristic full ply separation should consequently enable a

faster demise and an earlier structural break-up. Although it did not display a faster demise than aluminium under PWT test, the first CF layer fell-off after just 27 seconds under the medium heat flux conditions. Structurally-wise, this hybrid design demonstrated a 60% superior damping properties at high frequencies, while delivering equivalent mechanical specific performances as the aluminium baseline and around 10% lower than CFRP.

The introduction of a low density reactive metallic filler further optimized the FFRP, with the study identifying an optimal filler proportion of 1% by weight relative to the epoxy mass. This powder presence did not show any mechanical properties drawback, while increasing the through-thickness thermal conductivity by more than 10%.

Now regarding the cut-CF technology, the conducted thermo-mechanical tests have provided crucial insights into the demise performance of the novel discontinuous carbon fibers (cut-CF) CFRP material by the mean of a comparative evaluation method between this latter and a standard continuous-CF reinforcement design. This study validates the interest of using discontinuous carbon fiber to obtain a demisable and high mechanical performance composite system.

The greatest potential advantage of applying this novel technology compared to the hybridization comes from its integration into any existing space-qualified composite material system, in addition to present a limited mechanical properties loss. A relatively small time/cost impact can be expected from the simple additional prepreg manufacturing processing step needed, which is the pattern cutting. And potentially some layup sequence adaptations in order to guarantee the required mission thermo-mechanical performances.

5.5.1 Technology application limitation

However, it is crucial to acknowledge certain limitations and considerations associated with the novel ply-by-ply hybrid reinforcement design. The presented hybrid materials showed lower specific tensile mechanical properties than CFRP and a lower specific tensile modulus than aluminum. These aspects can theoretically easily be solved, through a more optimized ply-thickness selection and the integration of higher modulus CF fibers.

Moreover, the flax hybridization imposes a maximum service temperature limit to 140°C, and exhibits sensitivity to humidity, with non-negligible mechanical property losses at elevated relative humidity. With additional necessary manufacturing steps, including AlMg integration and an autoclave step for optimal flax compaction, a slightly higher overall costs can be expected, primarily attributed to labor-intensive manufacturing steps.

In light of these findings, the chapter not only advances our understanding of composite materials demise but also highlights the trade-offs and considerations associated with the implementation of novel hybrid or discontinuous materials in a spacecraft structure, while aiming to mitigate the re-entry surviving space debris threat.

5.5.2 Further work

Building on the well-defined demise capabilities of the CF-FF hybrid material established in this work, the logical progression involves optimizing the CF and FF ply thickness to enhance specific mechanical properties. This step necessitates a dedicated mechanical test campaign, employing additional evaluation methods such as Interlaminar Shear Strength (ILSS) and sandwich facesheet shear properties. Implement-

ing this optimization, along with further space qualification tests, will facilitate an efficient strategy for implementation in the space industry.

In parallel, a quantitative analysis of thermal properties through techniques like Laser Flash Analysis (LFA) and hot-disc should validate the through-plane thermal conductivity effects induced by the AlMg metallic filler integration.

Regarding the cut-CF technology, some recommendations can be made:

- A next step could implement thinner laminates (thin-ply technology) to be compatible with sandwich panel skins application, typically requiring submillimeter layup.
- Such evolution could also implement space-qualified grade composite fiber-resin systems, as well as alternative cutting patterns to specifically optimize the overall strength retention of the part versus demisability.
- Ideally perform a complex but important demise validation test campaign at material level with the Plasma Wind Tunnel facility at the IRS in Stuttgart for example.
- And finally, evaluate possible combinations with additional demise improvement methods, such as integration of reactive filler in the resin.

With a clear understanding of the demise behavior and specific structural properties of various composite systems, the next steps to reach the S/C integration step (TRL 6) involve validating a component-level demise testing of a full benchmark sandwich panel within a PWT. With such test performed under both low and medium heat fluxes the potential demise improvement against aluminium baselines might be observed.

Subsequently, an in-situ demonstration mission becomes imperative to prove the technological impact, reaching the highest grade TRL 9. Several missions are under study for this purpose, and currently, the most advanced is ESA's DRACO mission (Destructive Re-entry Assessment Container Object) detailed in the state of art (chapter 2).

6 Critical evaluation of DRAMA's composite demise model and improved demisability modelling through experiment correlation

Today several types of re-entry safety assessment software exist, running on recent and optimized demise models, both in terms of results, experimental-to-model correlation accuracy and user interface, as presented in the dedicated section of the state of the art in chapter 2. In the present work, ESA's re-entry risk assessment module, Re-entry Survival and Risk Analysis (SARA) within the DRAMA tool, was selected as it is currently the recommended software to perform the analysis for re-entry risk assessment on European missions. Its adoption is crucial, as it aligns with the stringent standards and requirements set by the space industry for mission validation by the European Space Agency (ESA).

In this chapter, an approach is proposed to implement, as directly as possible, the experimental composite material properties acquired in this project into the existing DRAMA-CFRP demise model. This procedure could enable the integration of newly tested materials into this re-entry analysis tool, and thus reduce current casualty risk uncertainties by performing more realistic re-entry simulations.

This path was motivated by several issues encountered while attempting to implement different composite material grades and our newly tested composite materials within DRAMA to assess their impact on re-entry casualty risk. Due to the unclearly expressed composite material model input parameters' names and their nonexistent descriptions in the User's Manual, it was impossible to obtain meaningful results when trying to directly implement the new material parameters.

Therefore, the first big step was to identify the current ablation/demise model built-in SARA through a combination of knowledge and data recovery and sensitivity analyses. Then an evaluation of the selected tuning parameters was performed to fit the highest-fidelity experimental data (SRC and PWT) with the verified model. Finally, an assessment of this experiment-to-model correlation method's robustness was carried out by implementing additional PWT data with different material compositions and test conditions. Additionally, the first step led to the identification of several flaws in the material input parameters window interface in comparison to the related model parameters of SARA in the current DRAMA version 3.1.0. Details regarding the inconsistencies are exposed in the following demise model comparison section.

6.1 SARA composite demise model recovery

The complete SARA's CFRP-like ablation demise model has never been published in the open literature, and only a few equations and physics details were exposed, as presented by Fritsche [111], which states that the model is based on a non-distributed document, *M.Kuch, Master Thesis, TU Braunschweig, 2011* [20]. This means that only a guess-and-try technique was possible to improve material demise representativity and mitigate results' uncertainties without modification of the built-in CFRP-like model. So after a material parameters sensitivity analysis and trials by model reconstruction with COMSOL multiphysics computing tool, no satisfactory fitting results were achieved. The only solution left was then to retrieve this 2011 thesis from M.Kuch.

After several emails and phone exchanges with the Technische Universität Braunschweig data and archive department, the original 107 pages German paper thesis version was found, scanned and sent to me. It contains a full 1D ablation model Matlab code and all the CFRP-like material parameters currently used for the current CFRP material model of DRAMA. In addition, it contains a PWT experimental comparative evaluation to validate the modeling approach.

The 1D transient heat equation implemented in that work is displayed in equation 6.1, where the pyrolysis reaction and gas blow effects are represented with the two last right-side terms. Parameters are defined as c_p for the specific heat and k the thermal conductivity of the composite material (separated in 2 states,

virgin | charred), and h_{pyr} the resin-only heat of pyrolysis. Regarding the heat balance of this equation, two heating terms are concerned: the plasma radiative heat flow and the surface oxidation. On the other side, five cooling terms are represented: material heat dissipation, pyrolysis reaction, surface re-radiation, pyrolysis gas blowing factor and its cold flow through the char. For the mass loss aspect, three terms are considered in the model: matrix pyrolysis transformation, fiber spallation (from gas blowing effect) and char/fiber oxidation.

$$\rho \dot{c}_p \frac{\partial T}{\partial t} = \frac{\partial}{\partial x} \left(k \frac{\partial T}{\partial x} \right) + h_{pyr} \frac{\partial \rho}{\partial t} + \dot{m}_{gas} \dot{c}_{p, gas} \frac{\partial T}{\partial x} \quad (6.1)$$

In terms of ablation processes (heat and mass transfers), the recovered Matlab model takes 5 of them into account. Their detailed definition can be found in Kuch [20] document and where their derived parameters' flow chart is illustrated in figure 6.1. These processes are:

- Thermal conduction (pink)
- Pyrolysis decomposition (grey)
- Pyrolysis gas blowing (yellow)
- CF and char oxidation (blue)
- Adaptive time steps from heat conductance (green)

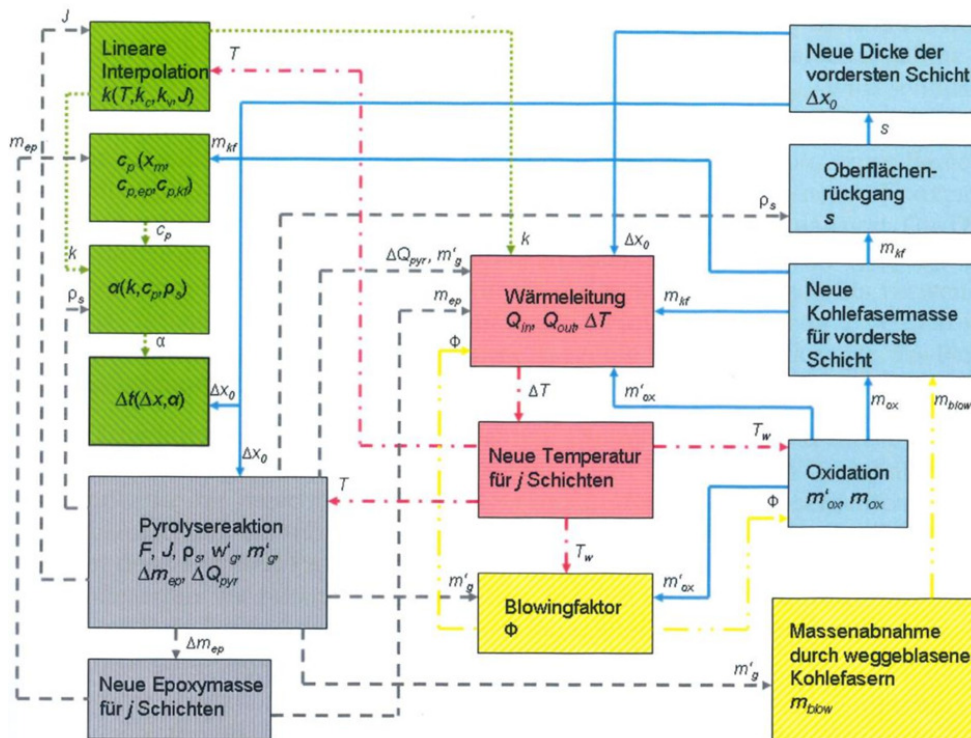


Figure 6.1: DRAMA based ablation model parameters flow chart. Where the colors distinguish the processes implemented in the composite ablation model. The arrows' indices are the input parameters. Image credit: Kuch [20]

6.2 Composite demise models comparison

After a translation work and the Matlab script update, the first step was to validate that the recovered code remained consistent with the code currently implemented in SARA, with no core modifications made since 2011/2012.

This validation process involved firstly, specific models parameters selection to ensure similar initial conditions, and secondly iterative comparisons between the updated recovered Matlab code and SARA's outputs.

To test the parameters, a simple bulk cylinder model of 10 cm radius and 2 cm thickness was created in SARA, established with an uncontrolled re-entry trajectory parameters from an initial orbital state detailed in table 6.1. A fixed attitude was set for the object, leading to a peak heat flux of 800 kW/m², as illustrated in figure 6.2. This latter and the object geometry simplicity are necessary to be compared to the Matlab 1D demise model, to which the atmospheric model integrated in DRAMA (NRLMSIS, [112]) was added. A preliminary run of SARA with these parameters allowed the calculation of the object's tumbling cross-section and experienced heat flux profile as a function of time for this case study. These outputs were then integrated as initial parameters in the Matlab model.

Table 6.1: Initial orbital parameters of the object to extract the aerothermal load profile for model comparison.

Orbital parameters	
Semi-major axis [km]	6375
Eccentricity [-]	0.0511
Inclination [deg]	98.78
RAAN [deg]	310.79
Argument of perigee [deg]	212.99
True anomaly [deg]	180

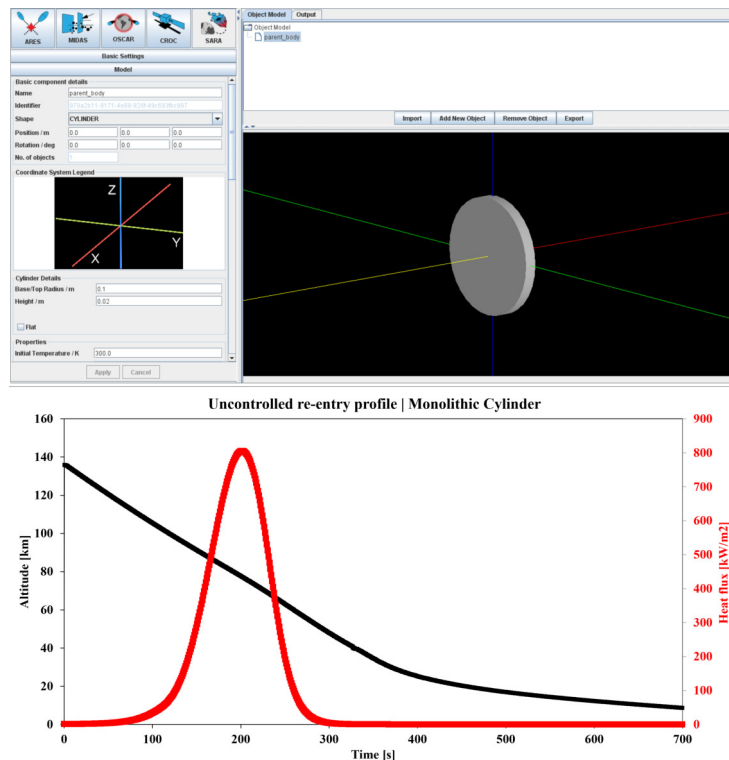


Figure 6.2: Cylinder object model and its derived simulated altitude and heat flux profile during a typical uncontrolled re-entry.

Iterative comparisons were then performed on this simple geometry, to compare both code's outputs. The char reaction rate, and the 3 reaction terms pyrolysis process, as defined in the thesis following the Arrhenius formula of equation 6.2, were selected as the two fitting parameters based on their discordance between SARA's values and those reported in the thesis (with either different values or linked to another material property with inconsistent units). F represents the pyrolysis reaction rate, expressed as a function of A_i the i-order frequency factor and E_i the activation energy, T the temperature and finally R the molar gas constant. The object surface temperature and remaining mass profiles over re-entry time were used as comparative factors.

$$F = \sum_{i=1}^3 A_i \cdot e^{\frac{-E_i}{RT}} \quad (6.2)$$

Figure 6.3 presents a comparison of the temperature profiles (top) and the total mass (bottom) of the object versus time during re-entry, obtained using DRAMA (red) and using the recovered and modified Matlab code (blue). Panel A displays the first iterative step where the Matlab model integrates all the functions and parameters from the recovered thesis, specifically the pyrolysis reaction with 3 terms and a char oxidation reaction rate frequency factor of 0.63. A clear mismatch can be observed between both the temperature and the total mass curves. This led us to the second iteration, panel B, based on the fact that no parameter inputs are available for multiple pyrolysis reaction terms in SARA. Thus a single-term Arrhenius formula is implemented while keeping the char oxidation parameter to 0.63. As a result, a clear fit of the temperatures is observed in the top figure, while the mass trend is still misaligned. The final iterations presented in panel C and D led to the quasi-perfect model's concordance, where the difference from the previous iterations is a char reaction rate frequency factor set to zero following SARA baseline CFRP value (named Char rect.rate [1/s]), figure 6.4. The difference between panel C and D stands in the tumbling sample's cross-section area which is fixed in the Matlab model and dynamic in DRAMA. So panel D represents the results with the smallest cross-section, showing a nicer fit to the temperature peak. These results' concordance indicates that the recovered code is the same as the one integrated into DRAMA with minor changes (mainly simplifications).

From these results and the extensive use of SARA module though these years, several observations were made:

1. First, the Software User Manual of DRAMA does not have any detailed documentation on this model and even on input parameters' definition. This is quite critical for the space Studies/industries in order to evaluate their S/C re-entry ground casualty risk in a relevant manner when integrating new composite components.
2. The vaguely named "*Comp. ratio*" parameter founds out to be the composite **resin** weight fraction and not the standardly used fiber volume fraction. A simple parametric sweep analysis of this parameter from 0.01 - 0.99, can validate this critical issue.
3. The current DRAMA CFRP-like model uses a simplified pyrolysis reaction with a single term Arrhenius formula parameter, $F = A_1 \cdot e^{\frac{-E_1}{RT}}$, instead of the three terms formula (equation (6.2) as displayed in the reference thesis.
4. Probable wrong parameter name, order of magnitude and unit of "char heat of formation" parameter of SARA is given as "30'300 [J/K]", where in the thesis the only similar number is defined as "specific heat of oxidation" with a value of "30.3e6 [J/kg]" (from page 20-21 of M.Kuch Thesis

[20]).

5. The standard CFRP material presented as a baseline in DRAMA does not take into account char/fibre oxidation as the char reaction rate is set to "0", whereas the thesis model indicates an oxidation rate frequency factor of 0.63.
6. In addition this char reaction rate cannot be saved in the material file and is always reset to "0" at every opening of DRAMA (including the reopening of another DRAMA window). So the char reaction rate needs to be checked and filled accordingly.
7. A hard thickness limit of minimum 1mm seems to be set for CFRP-like material, which is problematic as most of the CFRP-sandwich panels have sub-millimetre skin thicknesses. In these cases, it is currently impossible to perform demisability evaluations with this tool.
8. Another issue, which was reported already in 2020, concerns the "child-release" trigger, which allows to create a hierarchy to the objects, for example a casing and elements inside. The issue is that the parent box/higher element first disappears, even if is not demised, liberating the objects inside. This leads to the impossibility of creating a representative sandwich panel assembly with such tool, as some parts would disappear and not be fully accounted for.

In the following table 6.2, the five confusingly and/or wrongly displayed model parameters' names in the "CFRPs" input window are summarized, and illustrated in figure 6.4. These significant divergences from the original thesis model imply that either they were not implemented well, or that the implementation of the built-in model lacks clarity.

Table 6.2: DRAMA parameters' adequate names and units.

DRAMA-CFRP model parameter name	"Real" ablation model parameter name
Comp. Ratio [-]	Matrix weight fraction [-]
Char reaction rate [s^{-1}]	Char oxidation reaction frequency factor [-]
Epoxy activation Temperature [K]	Epoxy pyrolysis activation energy [J/mol]
Epoxy reaction rate [s^{-1}]	Epoxy pyrolysis frequency factor [s^{-1}]
Char heat of formation [J/K]	Char oxidation specific heat [J/kg]

As a simple example to highlight the consequences of these divergences, let's look at the "*Comp. ratio*" in SARA model which is supposedly standing for composite ratio, and set with a baseline value of "0.62", a value extremely similar to typical volumetric fiber fraction for high-performance structural CFRP. But as it was found, this input parameter is the polymeric resin weight fraction, which then translates into a CF volumetric fraction of 28.1%, an extremely low fiber content. So, in addition to possibly wrongly assuming the real parameter meaning, it could cause severe results variations as the resin is typically the composite element that demises completely in comparison to the carbon fibers. Consequently, this baseline value may result in a substantially reduced ground-impacting fragments' mass compared to the actual final mass. This result could then inappropriately lead to greater casualty risk from critical S/C End-of-Life management selection, such as an uncontrolled re-entry instead of a controlled re-entry. A simple naming error with the potential of provoking extensive re-entry damage.

6.2 Composite demise models comparison

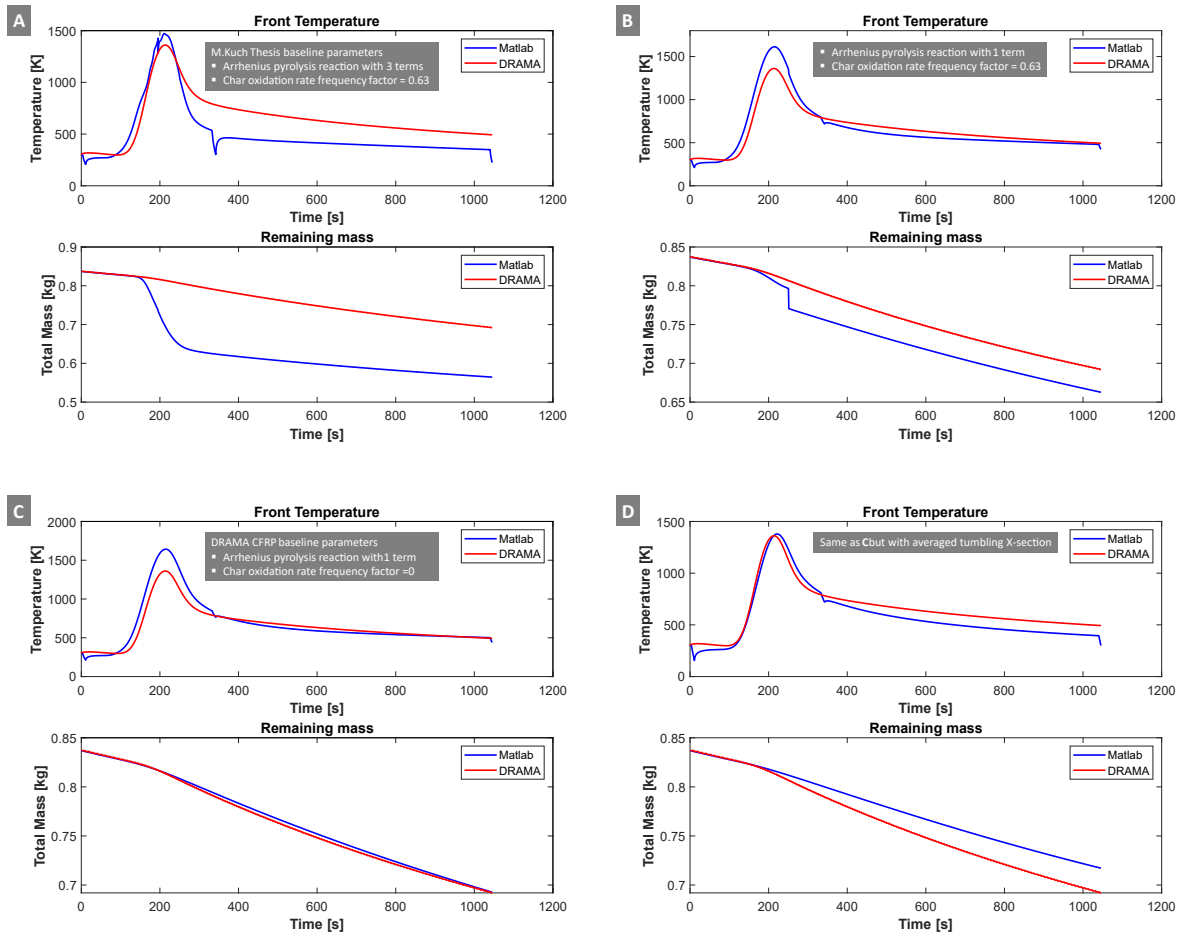


Figure 6.3: Comparison of DRAMA and recovered and updated Matlab code from Kuch [20]. The evaluated parameters are the Arrhenius pyrolysis reaction terms' number and the char reaction rate/char oxidation reaction frequency factor.

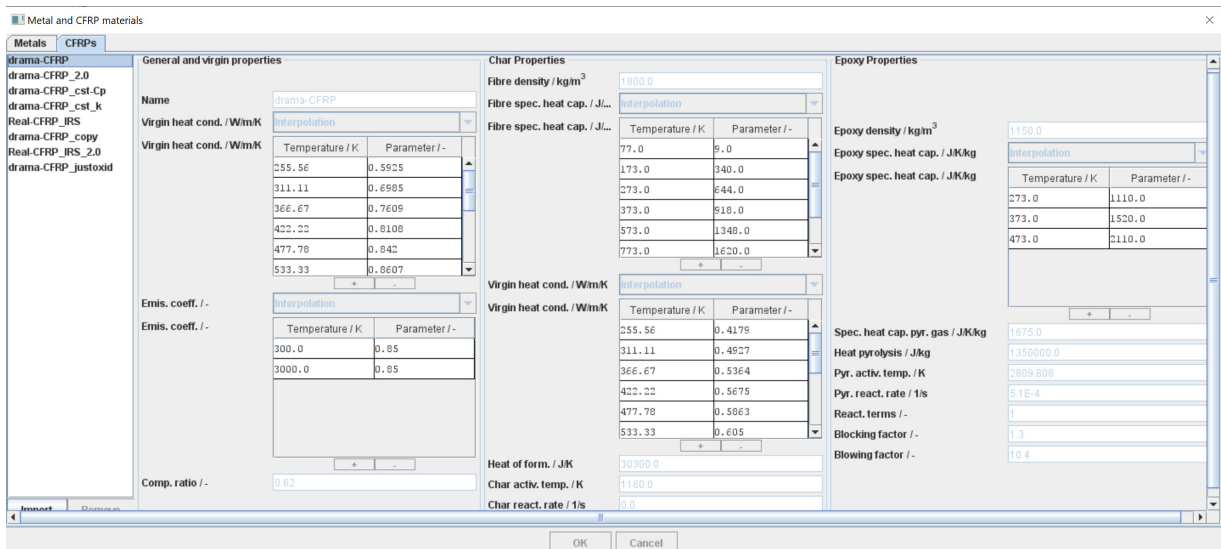


Figure 6.4: SARA module composite material parameter input window with current CFRP baseline material data displayed. The "0" char reaction rate can be observed at the bottom of the central column.

In summary, the current DRAMA version 3.1.0 CFRP-like material model is critically obscure and uses wrongly defined material properties which can lead to high uncertainties and results in misinterpretations and unsafe mission design selection. So until a complete update and clarifications of the user interface parameters and manual, I would not recommend implementing new material or using this composite model to perform a re-entry assessment analysis without prior warning.

6.3 Evaluation of extracted composite material parameters implementation

Now that the composite ablation model concordance was validated between SARA and the recovered one, a process to correlate experimental data obtained in the thesis work to this model was developed.

6.3.1 Composite material parameters compatibility process

The first step consisted of gathering the thermo-physical experimental data relevant to this demise model for the composite system of interest, either from literature, previous work or dedicated test campaigns. The table 6.3 presents examples of testing techniques linked to the specific outcome parameters required for this demise model. After implementing these data in the Matlab code, a parametric sensitivity analysis was performed on the dataset. This step allows for the identification of the optimal tuning parameters with respect to their capabilities to fit the PWT test front and back surface temperatures, in addition to the sample's final mass.

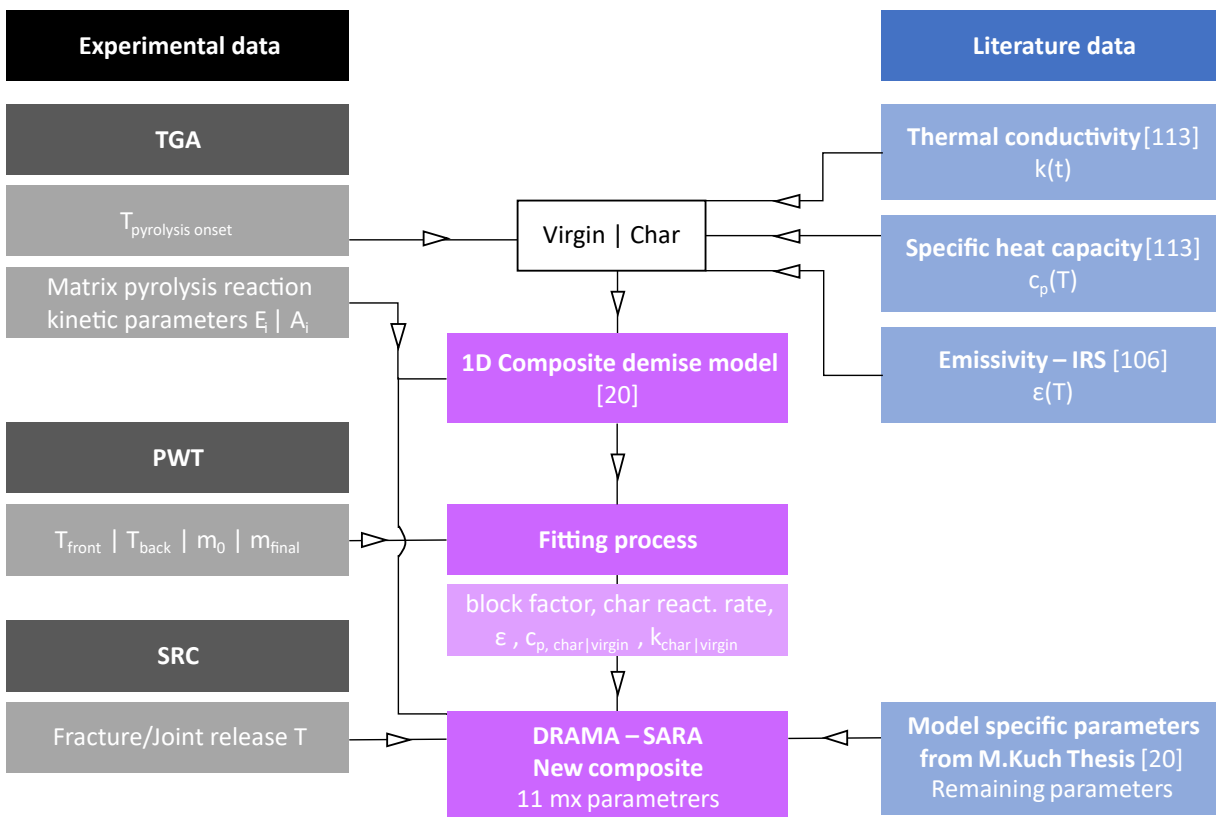


Figure 6.5: Experimental-to-model method flow chart

6.3 Evaluation of extracted composite material parameters implementation

The four best tuning parameters identified are the blocking factor, char oxidation reaction rate, virgin and charred state thermal conductivity. This means that their values are artificially tuned to fit the experimental data. However, for the thermal conductivities, their evolution with respect to temperature are kept based on the work of Tranchard et al. [113].

The next phase involves fitting the PWT data sequentially, one re-entry condition at a time. A trade-off game with the tuning parameters is then required to achieve the best fit with a single parameter set. Finally, the new specific composite material parameters were extracted and incorporated into a new SARA CFRP-like material. It is important to note that the thermal conductivity values are not obtained from high heating rate testing methods. However, this approach can still be justified by adopting a conservative approach, as much higher heating rates are expected to provide lower values, as exposed by Aspinall et al. [114], where such effect is identified as the thermal lag [115]. To mitigate this uncertainty, specific high heating rate thermal conductivity and emissivity measurements on the different materials can be performed. This mitigation step was not conducted for this project due to equipment and time limitations.

Table 6.3: List of 1D ablation demise model input parameters related their respective experimental evaluation techniques.

Testing technique	Outcome parameters for demise model
Thermogravimetric Analysis (TGA)	Matrix pyrolysis onset temperature Pyrolysis reaction terms (Ea_i, A_i, n) Demise reactions identification
Temperature Modulated DSC	Specific heat capacity (T)
Laser Flash Analysis (LFA), Hot disc	Thermal conductivity (T)
Calorimetric analysis, EMF (IRS)	Emissivity coefficient (T)
Static Re-entry Chamber (SRC)	Demise onset temperature
Plasma Wind Tunnel (PWT)	Front and Back temperature profile Mass loss

6.3.2 New composite materials' demise parameters extraction

CF/epoxy, FF/epoxy and CF-FFpbp/epoxy composite systems were evaluated with the detailed above procedure. The following figures 6.6, 6.7 and 6.8, show the datasets implemented in DRAMA, and the resulting overlays graphs between experimental data from the PWT (red) and our matlab model (blue). These graphs present the front and back sample temperatures, as well as total mass as a function of time for these three materials, each with the same set of material parameters. For the composite virgin-to-char transformation temperature threshold implemented through the temperature-dependent properties, it was set at 400°C (673K) for the FFRP/CF-FFpbp and 445°C (718K) for the CFRP. This was identified from TGA tests.

Critical evaluation of DRAMA and improved composite demise modelling

CFRP – HTS45/VTC-401

General and virgin properties		Char Properties		Epoxy Properties																															
Name	CFRP HTS45-VTC401	Fibre density / kg/m ³	1800.0	Epoxy density / kg/m ³	1210.0																														
Virgin heat cond. / W/mK	Interpolation	Fibre spec. heat cap. / J/K...	Interpolation	Epoxy spec. heat cap. / J/K/kg	Interpolation																														
Virgin heat cond. / W/mK	<table border="1"> <thead> <tr> <th>Temperature / K</th> <th>Parameter / -</th> </tr> </thead> <tbody> <tr><td>273.0</td><td>0.1</td></tr> <tr><td>2500.0</td><td>0.15</td></tr> </tbody> </table>	Temperature / K	Parameter / -	273.0	0.1	2500.0	0.15	Fibre spec. heat cap. / J/K...	<table border="1"> <thead> <tr> <th>Temperature / K</th> <th>Parameter / -</th> </tr> </thead> <tbody> <tr><td>200.0</td><td>650.2</td></tr> <tr><td>708.0</td><td>1570.8</td></tr> <tr><td>718.0</td><td>1422.5</td></tr> <tr><td>728.0</td><td>1433.1</td></tr> <tr><td>2500.0</td><td>1577.3</td></tr> </tbody> </table>	Temperature / K	Parameter / -	200.0	650.2	708.0	1570.8	718.0	1422.5	728.0	1433.1	2500.0	1577.3	Epoxy spec. heat cap. / J/K/kg	<table border="1"> <thead> <tr> <th>Temperature / K</th> <th>Parameter / -</th> </tr> </thead> <tbody> <tr><td>200.0</td><td>422.27</td></tr> <tr><td>708.0</td><td>1832.15</td></tr> <tr><td>718.0</td><td>1422.45</td></tr> <tr><td>728.0</td><td>1433.06</td></tr> <tr><td>2500.0</td><td>1577.25</td></tr> </tbody> </table>	Temperature / K	Parameter / -	200.0	422.27	708.0	1832.15	718.0	1422.45	728.0	1433.06	2500.0	1577.25
Temperature / K	Parameter / -																																		
273.0	0.1																																		
2500.0	0.15																																		
Temperature / K	Parameter / -																																		
200.0	650.2																																		
708.0	1570.8																																		
718.0	1422.5																																		
728.0	1433.1																																		
2500.0	1577.3																																		
Temperature / K	Parameter / -																																		
200.0	422.27																																		
708.0	1832.15																																		
718.0	1422.45																																		
728.0	1433.06																																		
2500.0	1577.25																																		
Emis. coeff. / -	Interpolation	Virgin heat cond. / W/mK	Interpolation	Spec. heat cap. pyr. gas / J/K/kg	1675.0																														
Emis. coeff. / -	<table border="1"> <thead> <tr> <th>Temperature / K</th> <th>Parameter / -</th> </tr> </thead> <tbody> <tr><td>200.0</td><td>0.997</td></tr> <tr><td>600.0</td><td>0.99</td></tr> <tr><td>800.0</td><td>0.977</td></tr> <tr><td>1000.0</td><td>0.957</td></tr> <tr><td>1500.0</td><td>0.879</td></tr> <tr><td>2000.0</td><td>0.759</td></tr> </tbody> </table>	Temperature / K	Parameter / -	200.0	0.997	600.0	0.99	800.0	0.977	1000.0	0.957	1500.0	0.879	2000.0	0.759	Virgin heat cond. / W/mK	<table border="1"> <thead> <tr> <th>Temperature / K</th> <th>Parameter / -</th> </tr> </thead> <tbody> <tr><td>200.0</td><td>0.0481</td></tr> <tr><td>2000.0</td><td>0.0527</td></tr> </tbody> </table>	Temperature / K	Parameter / -	200.0	0.0481	2000.0	0.0527	Heat pyrolysis / J/kg	152000.0										
Temperature / K	Parameter / -																																		
200.0	0.997																																		
600.0	0.99																																		
800.0	0.977																																		
1000.0	0.957																																		
1500.0	0.879																																		
2000.0	0.759																																		
Temperature / K	Parameter / -																																		
200.0	0.0481																																		
2000.0	0.0527																																		
Comp. ratio / -	0.367	Heat of form. / J/K	30300.0	Pyr. activ. temp. / K	150500.0																														
		Char activ. temp. / K	1160.0	Pyr. react. rate / 1/s	3.26000005E10																														
		Char react. rate / 1/s	1.65	React. terms / -	1																														
				Blocking factor / -	2.1																														
				Blowing factor / -	10.4																														

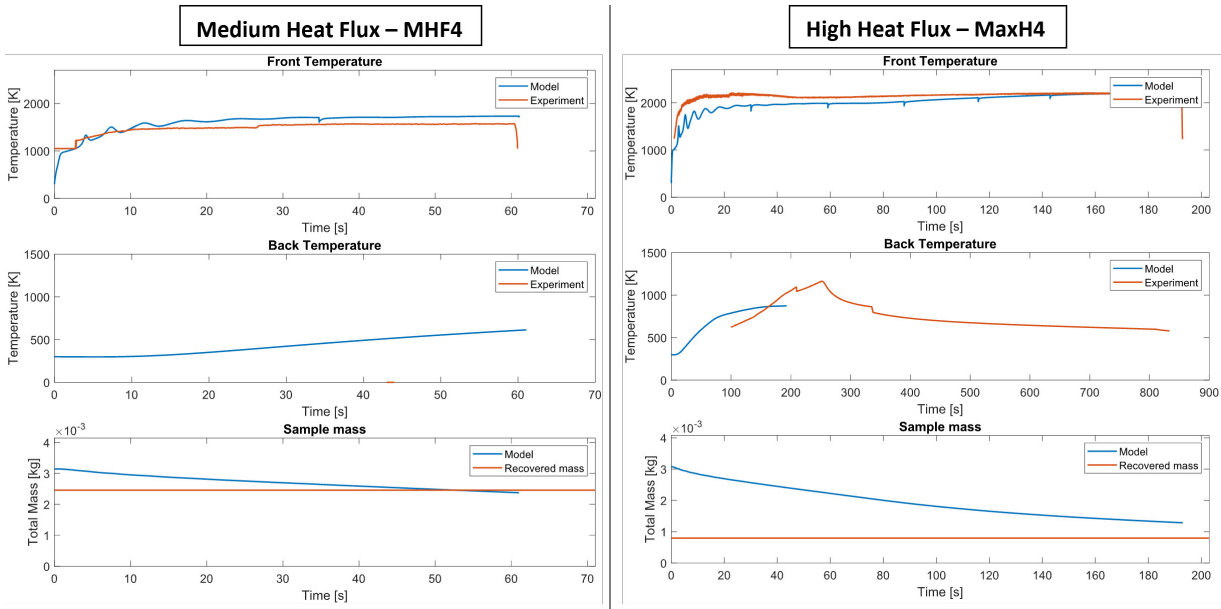


Figure 6.6: SARA material input window with the experimentally extracted parameter for the HTS45/VTC-401 CFRP. Bottom graphs: fitting results of these parameters with PWT Data from our test campaign with 2 test conditions

6.3 Evaluation of extracted composite material parameters implementation

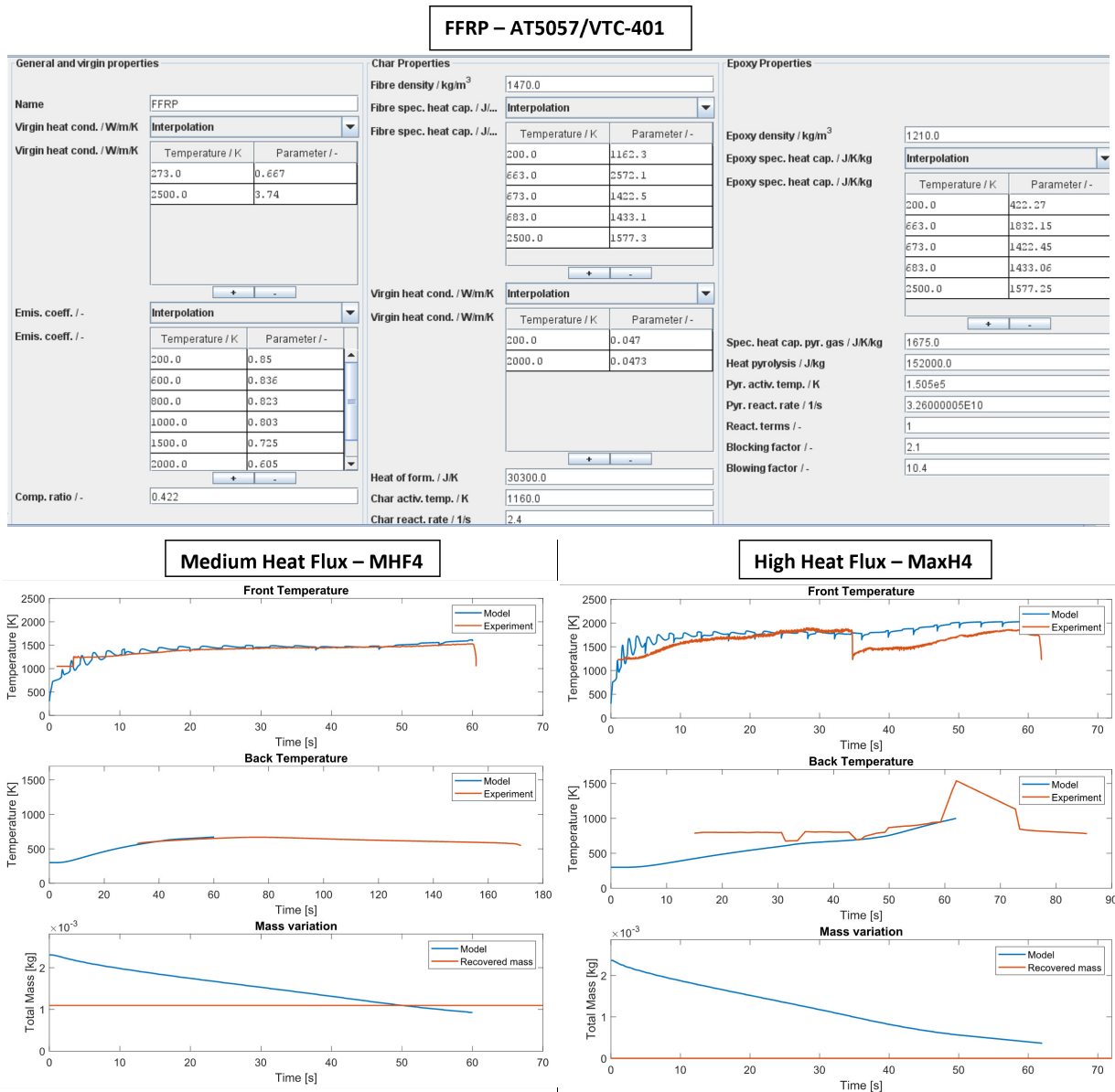


Figure 6.7: SARA material input window with the experimentally extracted parameter for the AT5057/VTC-401 FFRP. Bottom graphs: fitting results of these parameters with PWT Data from our test campaign with 2 test conditions.

Critical evaluation of DRAMA and improved composite demise modelling

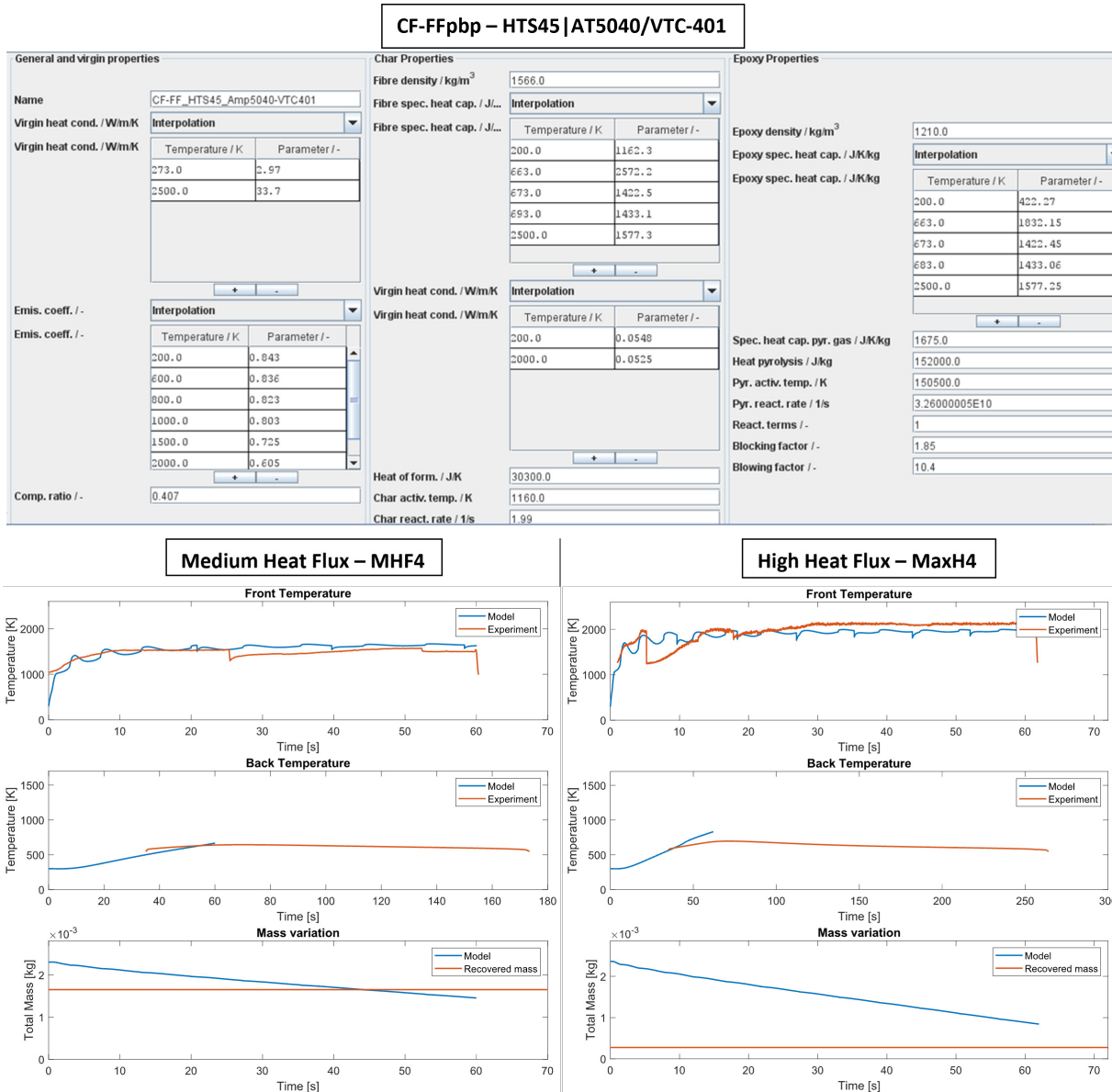


Figure 6.8: SARA material input window with the experimentally extracted parameter for the CF-FF ply-by-ply hybrid composed of HTS45|AT5040/VTC-401 with PWT data from IRS with 2 test conditions.

These results demonstrate an overall good fit between the model and the PWT data. The differences that can be noticed for example for the CF-FFpbp material final mass (figure 6.8), are to be attributed to the final selection of the tuning parameters, as only one set of parameters can be attributed to the material whatever the test conditions. This final selection is based on the average and a conservative approach in terms of re-entry risk. The small spikes noticeable on the front temperature of HTS45/VTC-401 and the FFRP, respectively figures 6.6 and 6.7, originate from the combination of plies' separation and the large difference between virgin and char thermal conductivities. Larger is the difference larger are the spikes. The accuracy and potential implementation of these new composite materials in the material database of the upcoming DRAMA version update are currently under discussion with ESA.

Re-entry surviving mass with new versus built-in CFRP in SARA

This chapter proposes a comparison, using SARA, between the built-in CFRP and the experimentally validated HTS45/VTC-401 material, named here *new CFRP*.

This comparative analysis evaluates the surviving mass of a single-element object. It was performed for three different hollow geometries with monolithic walls, a box, a sphere and a cylinder. Then through the use of the integrated Monte-Carlo (MC) tool from DRAMA, a parametric sweep analysis was conducted with the initial object's mass (wall thickness) as a sensitivity parameter, ranging from 10-500 kg. Such a method allows the assessment of these two materials' parameters' effects on the final mass with respect to the geometry.

The respective parametric sweep results are displayed in the following figures 6.9, 6.10 and 6.11. For all the geometries, the variation between the two materials is small and the new CFRP becomes more conservative already from a low initial mass, around 40kg.

Table 6.4 presents the derived wall thicknesses based on the identified initial mass limits. These values represent the maximum composite thickness, indicating that the new CFRP is more conservative in terms of casualty risk. In other words, a larger surviving mass is expected for an object made from this material with a thickness lower than these reported values.

The disparities in results between these two CFRP models are not entirely understood, and further investigation is required to assess multiple factors. As initial insights, the substantial difference in resin weight content, 0.62 (baseline) versus 0.367 (newCFRP), might seriously weight the pyrolysis reaction term balance. Similarly for the oxidation term balance, where the "Char reaction rate" parameters are set to 0 for the baseline and 2.4 for the newCFRP.

Table 6.4: SARA built-in versus experimental CFRP sensitivity analysis results.

Geometry	Box	Sphere	Cylinder
New CFRP conservative wall thickness limit [mm]	4.0	6.7	4.8

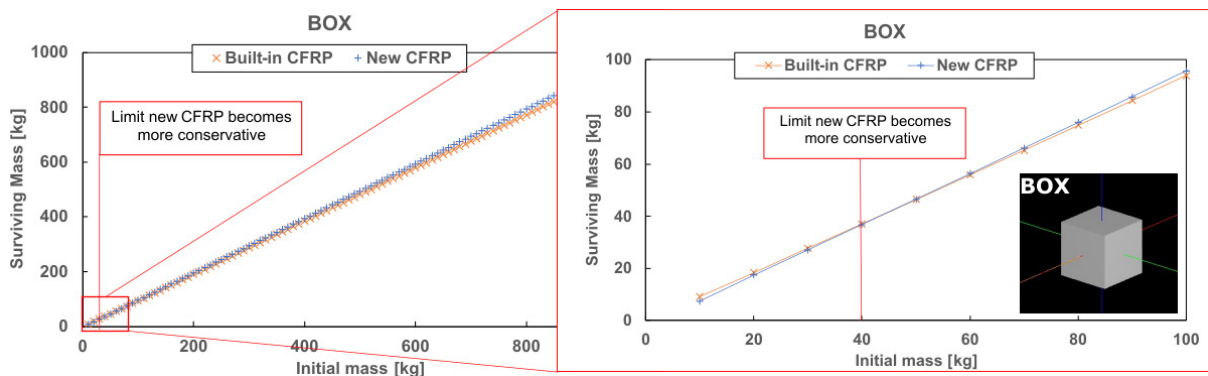


Figure 6.9: Comparison of the box's surviving mass made with the 2 CFRP versions.

Critical evaluation of DRAMA and improved composite demise modelling

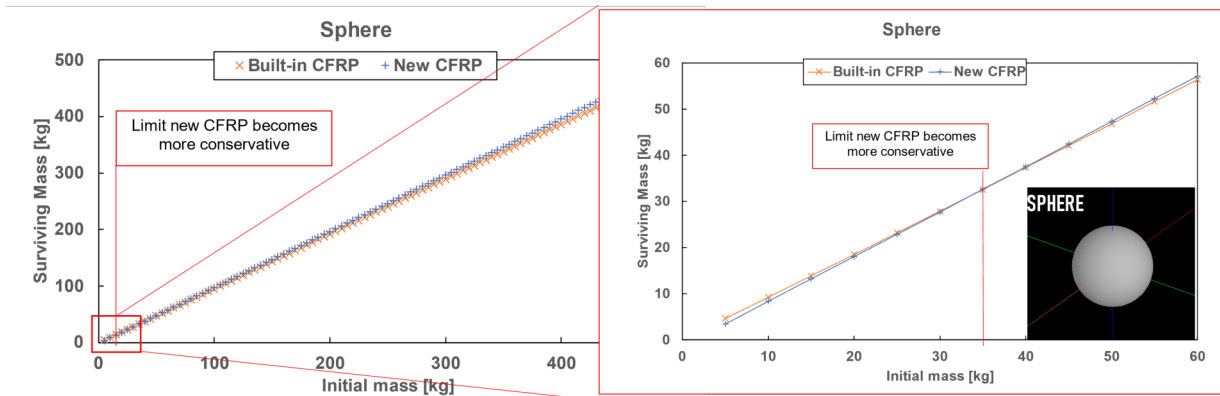


Figure 6.10: Comparison of the sphere's surviving mass made with the 2 CFRP versions.

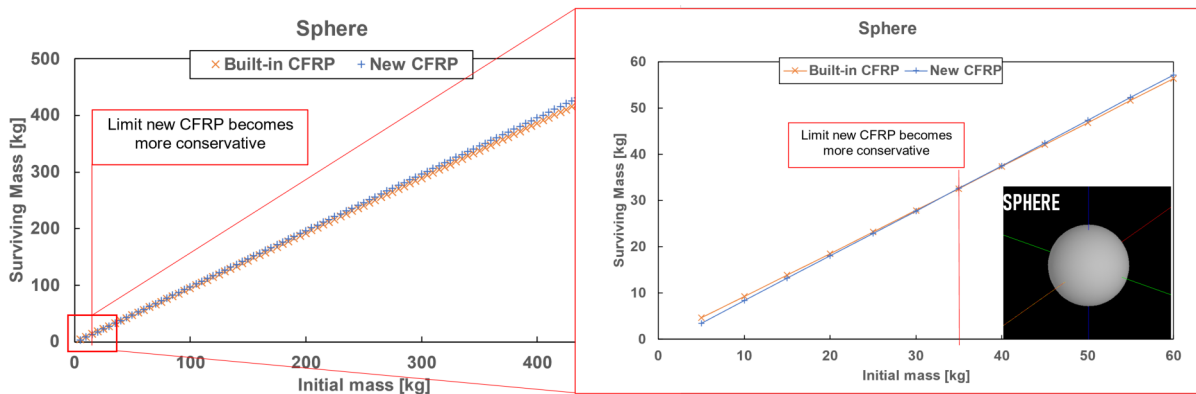


Figure 6.11: Comparison of the cylinder's surviving mass made with the 2 CFRP versions.

6.4 ClearSpace-One end-of-life analysis study case

This section presents an assessment of the novel composite materials structural integration effect on CS-1 (inspired from ClearSpace-One) re-entry analysis with SARA module. Four D4D specific criteria were selected allowing a comparative analysis of the various technology combinations:

Break-up altitude | Surviving mass | Number of fragments | Casualty risk.

This approach combines the two key indexes highlighted by Trisolini et al. [15] in their study towards efficient S/C demise improvement. Figure 6.12 presents a simplified model of the CS-1 spacecraft without the solar panels or robotic arms, incorporating 90 geometric elements, which was implemented within SARA module. Each element is associated with realistic mass budgets and materials. It includes several critical elements with respect to demisability, including cameras for navigation and capture, as well as optical sensors such as star trackers, which incorporate critical ceramic material. Critical as well, the propulsion system (thrusters) is entirely made of re-entry resistant titanium. On the same side but capable of partial/complete demise if released early enough and designed with appropriate thickness, are the attitude control elements which are mainly composed of stainless steel and iron (magnetorquer, reaction wheel), along with batteries and electronics. These latter feature multiple casings, designed with steel and glass fiber composites. On the demisable equipment front, an aluminum-lithium alloy (Al-Li) tank has been incorporated (alloy selected based on current demisable tank research), along with internal sandwich panels comprised of aluminum skins and honeycomb (HC-AA7075). The decision to opt for an Al-Li tank instead of titanium allows the evaluation of the demise state of a large element.

The external structure of interest consists of six external side panels (ExtPan 1|2|3|4|5|6) and a trigger box (Int) encapsulating the entire spacecraft, as depicted by the central box in figure 6.12 (this hierarchical design is a software necessity). They were designed to have a thickness ranging from 1.5-2mm, which was a requirement in order to implement the material in DRAMA.

Two categories of evaluation parameters were selected, the external structure material and its fastening system material. For the first, five facesheet materials were tested: aluminium (DRAMA AA-7075), CFRP-realistic, CFRP-new, FFRP, CF-FFpbb. For the CFRP, two versions were considered: a modified version of the built-in CFRP material (named CFRP-realistic) was created, incorporating four realistic (but not verified) parameters from Kuch's thesis [20]. The other called CFRP-new is based on the HTS-45/VTC-401 composite material tested along this research, similarly to the FFRP and CF-FFpbb. Their model specific parameters are displayed in figures 6.6, 6.7 and 6.8.

With regards to the fastening system, three fasteners materials were integrated, a titanium alloy (Ti6Al4V), a stainless steel (306L) and the novel short-CF/PEEK. Their integration in the software was simply their trigger temperature parameter set within the trigger box element (Int).

The evaluation procedure was to sequentially assign one facesheet material to these seven structural elements in combination with one fastener type. A breakup temperature trigger (child release trigger)

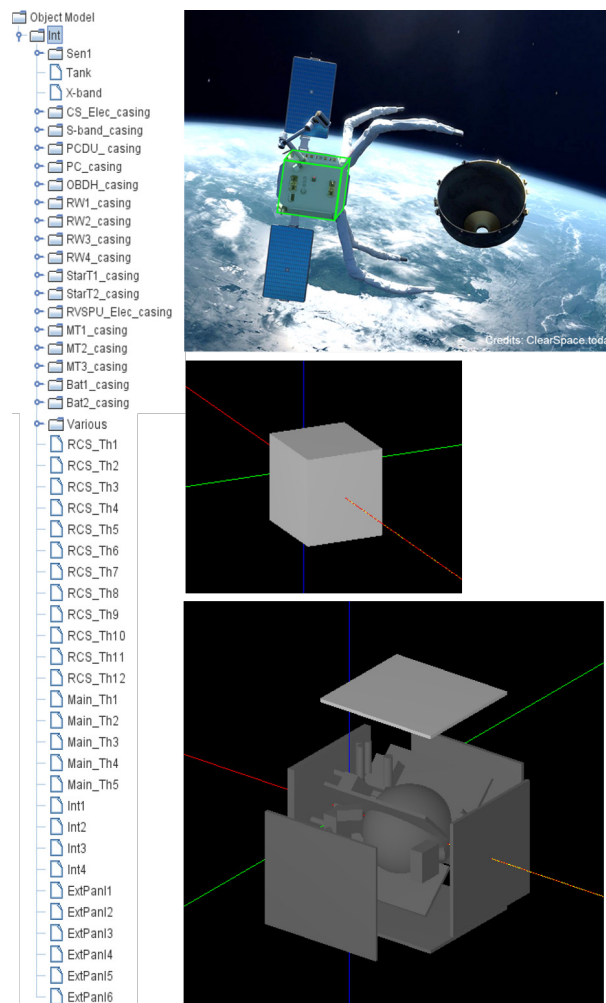


Figure 6.12: DRAMA model of CS-1 core structural element and internal components. The green box represent the external structure and is modelled as a simple box (named Int in the list of object). And at the bottom, an illustration of the 90 elements assembly, initially modelled within the previous box element.

Critical evaluation of DRAMA and improved composite demise modelling

was exclusively set for the Int box element. This trigger temperature is determined based on the fracture temperature extracted from the SRC test results obtained in this work, or on the melting temperature of the structural elements for the metallic parts. The respective material's trigger temperatures are summarized in Table 6.5.

Table 6.5: Combination evaluation matrix and the selected trigger temperature, based on the lowest of the two combination.

			Facesheets			
			Aluminium	CFRP	FFRP	CF-FFpbp
		$T_{trigger}$ [K]	933	1223	658	863
Fasteners	Ti6Al4V	1880	933	1223	658	863
	SS	1076	933	1076	658	863
	short-CF/PEEK	560	560	560	560	560

Figure 6.13 illustrates two cases of altitude versus ground distance during re-entry, the top one is for a metallic fastener, and the bottom graph is for a CF-PEEK fastener. A different behaviour is clearly observed, with a narrow disintegration range observed in the first case, whereas a high-altitude opening in the second case distinctly leads to the complete disintegration of most onboard components, leaving only critical ones to impact the Earth's surface at various locations. These critical components typically consist of ceramics (optical elements) or high-melting-point metals (propulsion system, solar array drive mechanisms, or magnetorquers).

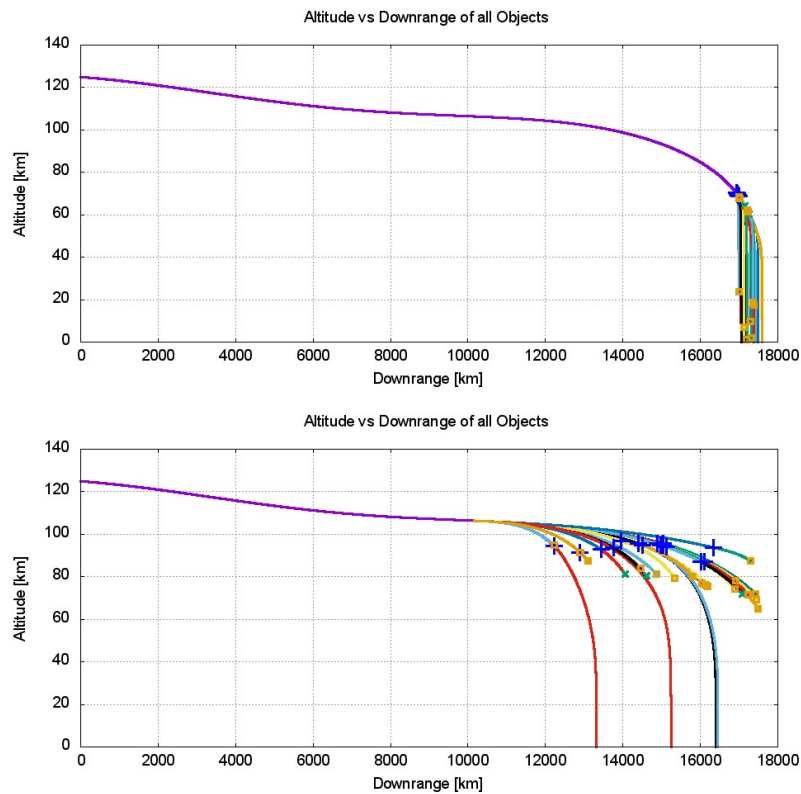


Figure 6.13: Representations of the S/C and derived fragments re-entry trajectories (altitude versus ground distance/downrange). Top graph illustrates the integration of metallic fasteners, and where the bottom one either short-CF/PEEK fasteners or aluminium external facesheets.

Figure 6.14 presents the value obtained for the four criteria (Break up altitude, Surviving mass, number of fragments and casualty risk, for the sandwich panel facesheets types, and the three fastener variants. The parameter window is illustrated in figure A.12 of Appendix A. Note that the results of the built-in CFRP which is by default in DRAMA are presented in figure A.2 of appendix A. This material was excluded from the comparative graphs presented here due to their unrealistic and incomplete parameter settings, rendering the derived values irrelevant.

From the break-up altitude comparative graph, the best option are, as expected, aluminum panels whatever the fastener, and short-CF/PEEK fasteners, whatever the panel type. They allow the break-up to take place 12-35 km higher than for the other configurations, and therefore significantly reduce the surviving mass exposed in the right graph. The importance of a low temperature break-up system is thus clearly highlighted from these simulations. SS and titanium fasteners lead to similar break-up altitudes, although they have 800°C trigger temperature difference, but this shows that the SS break up temperature is still too high to ensure an early opening, whereas CF-PEEK, 560K, falls in the right temperature range experienced during this early trajectory path.

Surprisingly, the integration of FFRP or CF-FFpbp facesheet panels did not induce an earlier breakup. In fact, FFRP demonstrated only slightly better overall demisability than CFRP. This outcome could possibly be attributed to the significantly higher specific heat of flax fibers, coupled with their earlier virgin-to-char transformation. In reality, PWT and SRC test results indicate that FFRP completely demises within minutes, while CFRP maintains structural integrity. Therefore, further testing under varied conditions and correlation with experimental models are necessary to evaluate the reliability of these parameters and potentially obtain more realistic ones compatible for this limited model.

Overall, full CFRP panels exhibit the highest resistance to re-entry, as expected. The difference in demise kinetics between the two CFRP materials can be observed by comparing their similar breakup altitudes and resulting differences in surviving mass. The new CFRP results are expected to have a higher confidence,

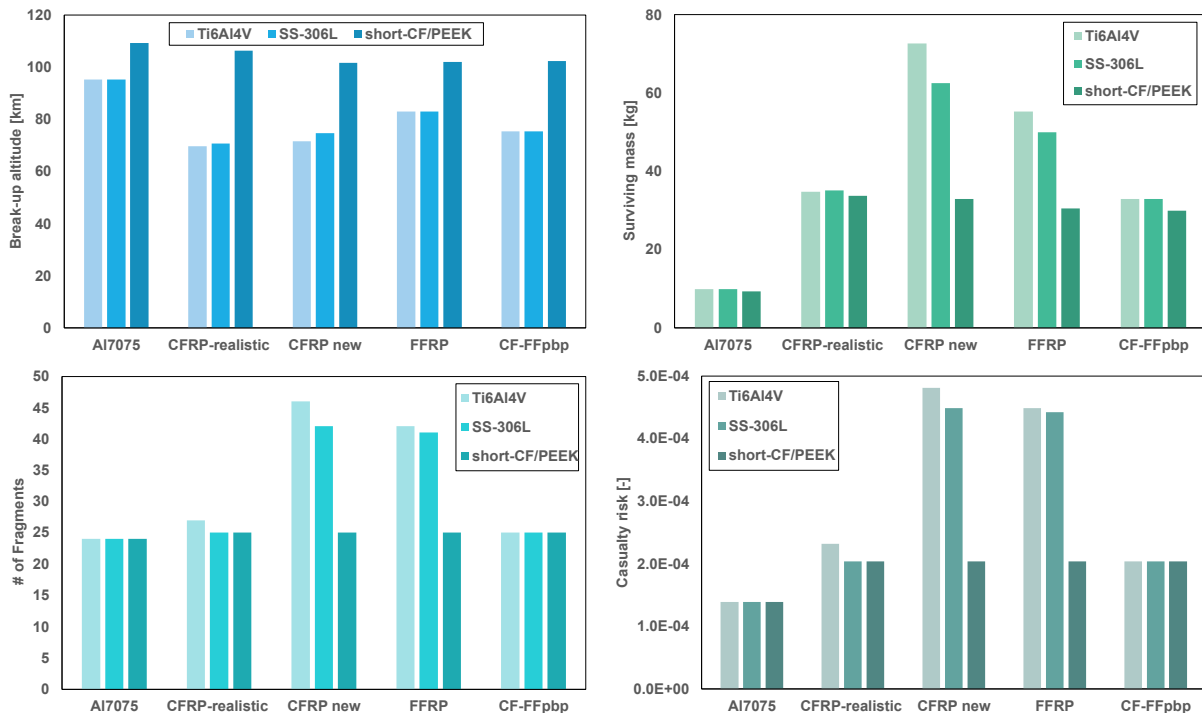


Figure 6.14: Comparative overview of the D4D specific criteria resulting from the combination of four sandwich facesheets with three fasteners versions.

as their parameters are all derived from the same materials and experimental data measured in this thesis. In contrast, CFRP-realistic parameters are based on various experimental data and old studies employing materials that are not exactly found in structural panels (ablators).

Integrating CF/PEEK fasteners allows for the highest breakup altitude, resulting in a re-entry scenario similar to a configuration integrating aluminum sandwich panels in terms of fragment numbers and casualty risk. This behavior is depicted in figure 6.13.

However, the Al-Li tank, set as a demise state sensor, did not completely disintegrate with the four combinations involving metallic fasteners and the two CFRP panels. This result underscores the critical nature of these materials and the impact of their assembly.

The expected direct relationship between fragment numbers and casualty risk is evident when comparing the two bottom graphs. Interestingly, none of the evaluated configurations allow for an uncontrolled re-entry mission option based on the casualty risk threshold of 10^{-4} . This underscores the necessity for additional efforts in designing the surviving fragments if such a mission-ending strategy is required. Notably, this need arises despite the absence of some typical or potentially critical parts in this simplified model. These include the bulky solar array drive mechanisms, harnessing elements (such as cabling and tubing systems), and even the thin external thermal protection cover (MLI).

6.5 Summary

A complete composite material implementation method within DRAMA is presented in this chapter. This approach facilitates the integration of newly tested composite materials into the SARA database, relying on specific thermo-physical parameters. However, trade-offs and assumptions, such as adopting the conservative scenario as a safety factor, must be made when selecting tuning parameters to replicate the best possible experimental characteristics under various testing conditions. The critical step of such a process is the fitting phase, due to the multiple tuning parameters. Further work can be done to limit or reduce their numbers.

One significant challenge in achieving concordant trends arises from the model input design, which currently does not account for the heating rate. The heating rate plays a crucial role in the thermophysical properties and, consequently, the ablation (pyrolysis and oxidation reactions) of materials. As a result, a comprehensive remodelling effort may be necessary for the entire demise model to incorporate this aspect [54].

When undertaking such a remodeling effort, potential simplifications of input parameters could be introduced, utilizing predefined composite material classes based on reinforcement configurations, such as weave type or ply thickness. Such modifications should extensively enhance the user interface and overall ease of use.

The experimentally extracted CFRP material reveals a linked geometry and wall thickness sensitivity difference compared to the built-in version. Objects with higher BC (rounder) exhibit a higher thickness limit, as reported in Table 6.4. This suggests that such material configurations tend to provide increased protection, allowing for a larger surviving mass in re-entry scenarios when compared to objects with lower BC (less round). This correlation between material geometry and conservative thickness limit emphasizes the importance of considering both factors in assessing casualty risk during re-entry events.

The comparative assessment of our novel D4D technologies combinations through DRAMA certainly shows the promising aspects toward reduced casualty risk by the implementation of a high altitude break-up structural element, allowing to choose materials such as composites for the panels, which have higher specific properties than the well demisable aluminum.

7 Conclusion

Conclusion

With the increasing threat imposed by the growing number of space debris in strategic Earth orbit regions, the motivation for research and development of solutions to this worldwide problem is on a path to create a key sector of interest in the space industry.

Among the various space debris mitigation measures, design for demise (D4D), with the goal to produce parts that fulfill their mission in space to then disintegrate effectively upon reentry, is closely related to materials science and engineering, as part of a multiscale approach. The materials and structures' response to the high heat flux and other complex physical phenomena behind the re-entry conditions form an integral part of the D4D solutions .

This thesis thus focused on the identification, evaluation and development of a high demisability structural external panel and its assembly fasteners with innovative composite materials. The goal was to maximize the overall spacecraft disintegration during the re-entry. Such system aims for the release of the external protective panels earlier in the re-entry flight, thus exposing the internal components to the high enthalpy airflow.

To answer to such innovative technology development, the research methodology was approached by the two typical and complementary design processes, experimental testing on one side and the validation of theoretical models and simulations on the other. In order to better screen the materials demisability within a laboratory environment, a new Static reentry chamber creep test was proposed and evaluated, as a cheaper and complementary alternative to the plasma wind tunnel test usually employed to assess demisability. In addition, it allows evaluating the thermomechanical behaviour following re-entry temperature profiles.

Carbon fibre reinforced CF/PEEK bolts have been evaluated regarding their demise and thermo-structural properties. The results showed that in order to reach sufficient demisability under moderate load, the use of short carbon fibers bolts enables to liberate the joint through the matrix melting and degradation, while preserving sufficient mechanical properties during use.

The second approach focused on the development of novel materials combinations for the sandwich panel skins. Three approaches were evaluated: the first one made use of highly demisable flax plies combined to carbon plies, with the goal to reach a compromise between the skin stiffness and weight to remain equivalent to an aluminum panel, while ensuring that plies can detach thanks to the rapid degradation of the flax fibers. The ply-by-ply carbon/flax fibre hybrid configuration showed best results, and forms a promising solution, with the caveat linked to the relatively high sensitivity to humidity of the panels. A second approach investigated the incorporation of a reactive aluminium-magnesium micro-powder filler. This helps to simultaneously improve the demise through melting and/or reaction of the metal, and through an increase of the through-thickness thermal conductivity of the composite. Finally, based on the simple observation from the bolts that a discontinuous carbon fibre ply might provide the most efficient compromise between stiffness and demisability, discontinuous CFRP prepregs developed by Composite Busch SA were evaluated in the Static reentry chamber experiment.

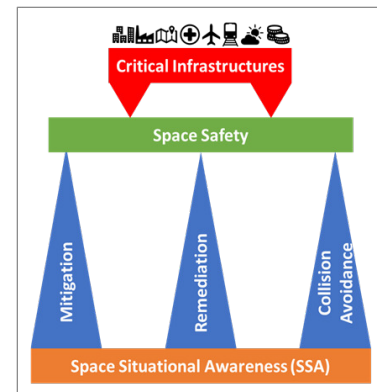


Figure 7.1: Illustration of the space safety and space situational awareness importance on our critical infrastructures.

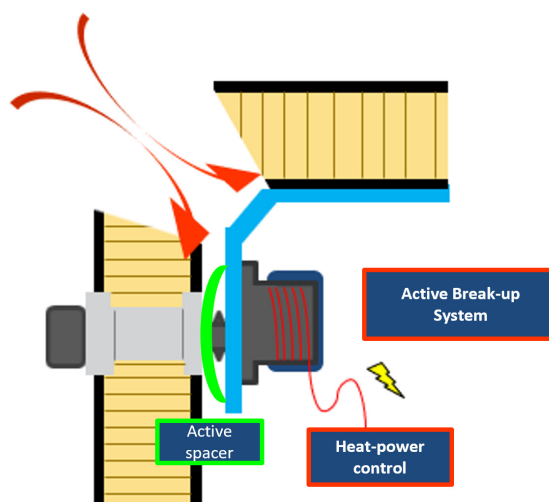


Figure 7.2: Illustration of a dual assisted break-up concept implementing the low-temperature demise CF/PEEK bolts releasing a potentially demisable sandwich panel.

The conducted thermo-mechanical tests on cut-CF technology validate its potential for creating a demisable and high-performance composite system, as compared to standard continuous-CF designs. The key advantage lies in its seamless integration into existing space-qualified composite materials, with minimal impact on mechanical properties and added prepreg manufacturing steps. This innovation holds promise for enhancing the sustainability and performance of space structures at a relatively low time scale and cost. The combination of these two approaches, joint and panel, can be illustrated in figure 7.2. The bolt could be locally heated to ensure an active break-up system at the right time during re-entry, thus liberating the panels which will then desintegrate separately, while exposing the inner part of the whole structure.

Finally, a complete composite material implementation method within DRAMA was developed. This approach facilitates the integration of newly tested composite materials into the SARA module, relying on 11 specific thermochemical/-physical parameters. Significant challenges were identified in the model input design, in addition to a built-in model physics which currently does not account for the heating rate. The heating rate plays a crucial role in the thermophysical properties and, consequently, the ablation (pyrolysis and oxidation reactions) of materials. Nonetheless, solutions were found to integrate some of the new materials in the model, with satisfactory agreement, and the strong need to significantly improve the DRAMA tool for better consideration of composites demise was highlighted.

7.1 Perspectives

The core motivation behind this project stemmed from the growing interest among space industry stakeholders in this particular technology. The spacecraft design processes are continually being driven towards more stringent sustainability requirements. Thus there are many perspectives to this work, in the search for the best demisable structures. The proposed materials solutions show great promise and open the path towards novel design methods for composite structures, taking into account their end of life. This was however not pushed to high TRL yet, and only demonstrated at the laboratory level. Therefore, potential collaborations with flight demonstrators, such as the Deimos team working on the DRACO mission with a launch planned for 2027, could help recognize the full potential of the presented technologies. This, in turn, might pave the way for their integration into ClearSpace's next-generation satellites.

In order to optimise the materials configurations, further tests on hybrid flax/carbon or cut-CF prepreps

Conclusion

should be conducted, with a specific set of requirements in mind, to ensure that all the mission related needs are fulfilled (mechanical, vibration, outgassing, etc..) and the demisability is fostered. In particular for the cut-CF plies, this may entail to further optimize the width and length of the tows, to reach the best compromise in function of the part construction.



Figure 7.3: Credit: Mike Keefe, Denver Post, 2009

A Appendix

A.1 Facesheet material details

Table A.1: Datasheet sandwich panel facesheet material characteristics, with composite versions integrating the VTC-401 epoxy. The equivalent mechanical properties were computed with ESAcomp. $L|T|z$ respectively stands for longitudinal, transversal and through-thickness directions. Values indicated with * are not available for confidentiality purposes.

Base material name	Aluminium	CFRP	FFRP [116]			CF-FFtbt hybrid
Reinforcement/grade	2024-T81 [101]	Tenax TM HTS45 [117]	AT TM 5040	AT TM 5043	AT TM 5057	AT TM 5027
Reinforcement type	Bulk metal	UD	Twill 2x2	Twill 2x2	UD	UD
Composite systems ply properties						
Density [kg/m³]	2785	1550	1350	1350	1350	1375
Fiber gsm/ply [g/m²]	-	50	300	200	200	160
V_{fibre} [%]	-	60	55	55	55	55
Cured ply thickness [mm]	-	0.055	0.48	0.43	0.24	0.32
CTE_L [$\mu \cdot K^{-1}$]	23	0.2	0.62	0.62	0.62	0.43
Thermal cond., k_{L T z} [W/m k]	151.0	6.5 0.65 0.27	*	*	*	*
E₁ [GPa]	72.4	140	*	*	*	*
E₂ [GPa]	72.4	9	*	*	*	*
G₁₂ [GPa]	27.7	4.5	*	*	*	*
ν [-]	0.33	0.32	*	*	*	*
E₃ [GPa] 72.4	9	*	*	*	*	*
σ_{UTS} [MPa]	485	2372.4	*	*	*	*

A.2 Cut-CF (SMC-HP) and continuous-CF (Nappe) samples details

		Sample#	Length [mm]	Width [mm]	Thickness [mm]	m_0 [g]	m_ aft [g]	Mass loss [%]
UD/Nappe	0° dir	1		11.75		3.22	3.196	-0.75%
		2	60.1	12.2	2.85	3.32	3.296	-0.72%
		3		12.21		3.36	3.337	-0.68%
Cut-CF / SMC-HP	90° dir	1		12.18		3.31	3.286	-0.73%
		2	60.5	11.76	2.84	3.22	3.191	-0.90%
		3		11.69		3.24	3.211	-0.90%
	0° dir	1		10.8		-	-	-
		2	60	10.88	2.89	2.975	2.945	-1.01%
		3		10.68		2.903	2.873	-1.03%

Figure A.1: Cut-CF (SMC-HP) and continuous-CF (Nappe) DMA samples dimensions and masses before and after test.

		#sample	Length [mm]	width [mm]	thickness [mm]	mass [g]	m_ aft [g]	Mass loss [%]
UD/Nappe	LowHR	1		24.95		15.74	12.91	-17.98%
		2	140	24.79	2.88	15.73	13.24	-15.83%
	HighHR	3		24.83		15.81	13.04	-17.52%
		4		24.82		15.77	13.01	-17.50%
Cut-CF / SMC-HP	LowHR	1				24.98		15.79
		2	140	25.03	2.87	15.51	14.13	-8.90%
	HighHR	3		24.82		15.69	13.99	-10.83%
		4		24.94		15.63	14.03	-10.24%

Figure A.2: Cut-CF (SMC-HP) and continuous-CF (Nappe) . SRC samples dimensions and masses before and after test. The low mass loss of the cut-CF samples comes from the earlier test termination in comparison to the continuous UD ones, which required a longer test duration to fail.

A.3 SEM analysis of the aluminium oxide formation from hygro-aging of aluminium sandwich panels

The aluminum sandwich panel manufactured by APCO Technologies, integrates facesheets with external surfaces coated with Alodine S1200 (Chromatation), which is validated through EDX results where the chromium atoms clearly stands out on such samples' surface. The typically 0.2-0.3 m corrosion resistant oxide coating of $Al_2O_3 + Cr_2O_3$, as found on ambient samples in figure A.4, can be observed to have grown by 2.5 to 3 times under a high humidity exposure for 18 days. The oxide formation kinetic analysis require further investigation.

Appendix A. Appendix

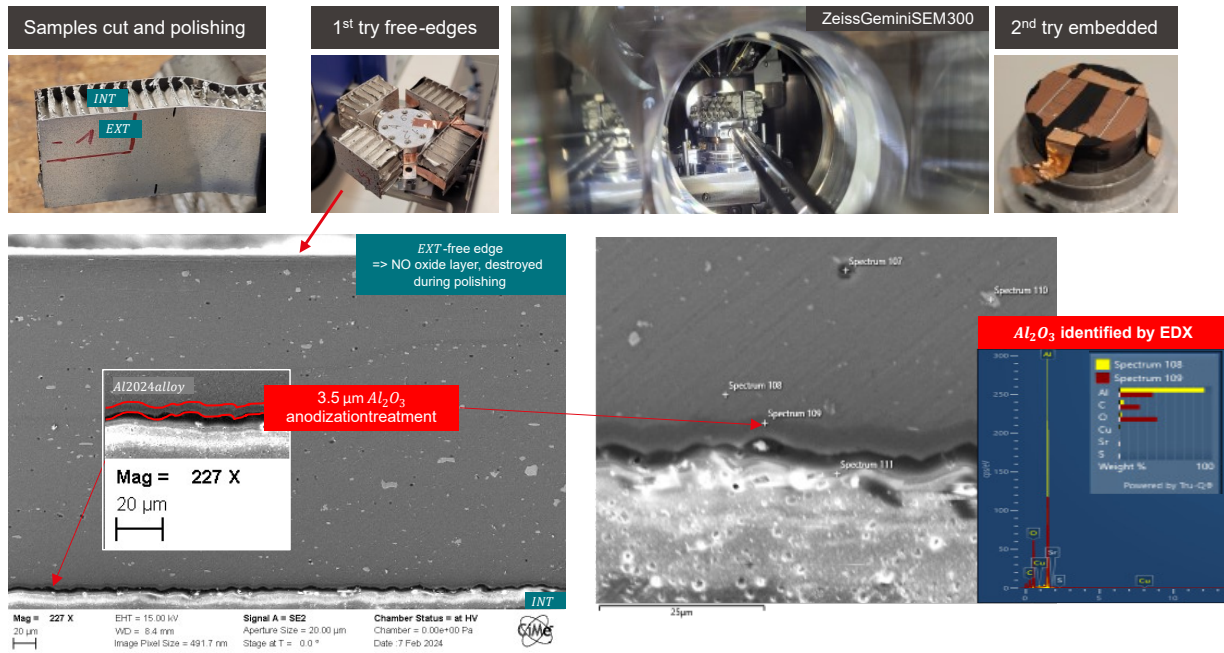


Figure A.3: Top, aluminum sandwich panels samples and Zeiss microscope chamber pictures. Bottom, sample cross-section views in a free-edge and an embedded configurations, using the secondary electron detector.

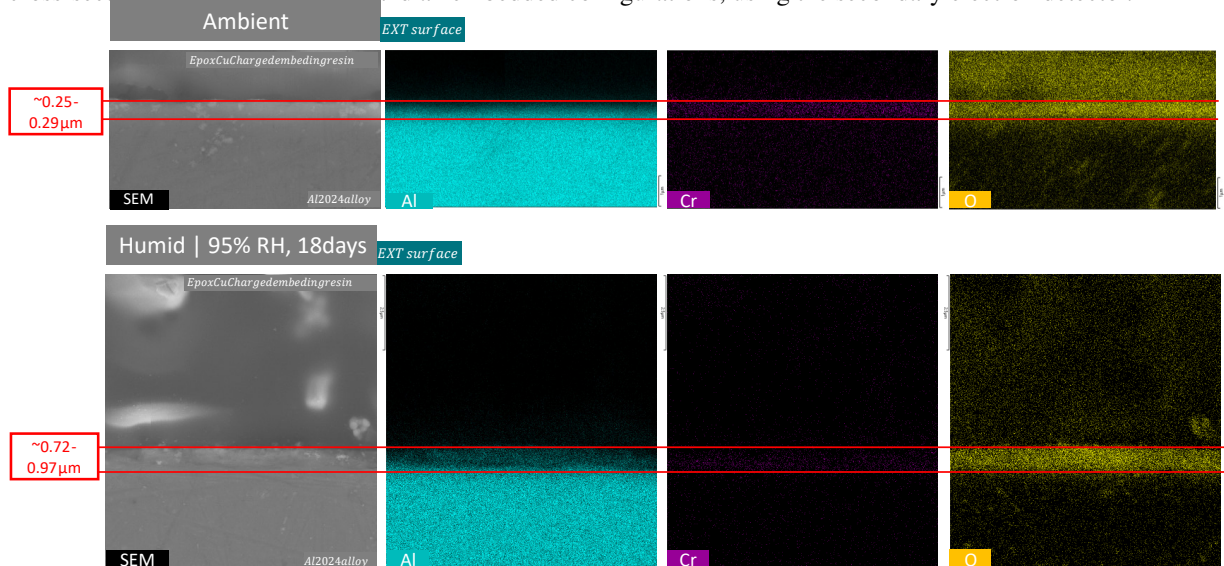


Figure A.4: Aluminum facesheet samples cross-section views from the secondary electron detector, complemented by the EDX results highlighting the carbon, chromium and oxygen atoms. With respectively on top, an ambient stored sample and on the bottom, a hygro-aged sample.

A.4 Static reentry chamber video link and temperature profiles reference

Link for the test videos: <https://drive.switch.ch/index.php/s/OPnVa9T8K1LaHjn>

Images of the fully assembled SRC setup.

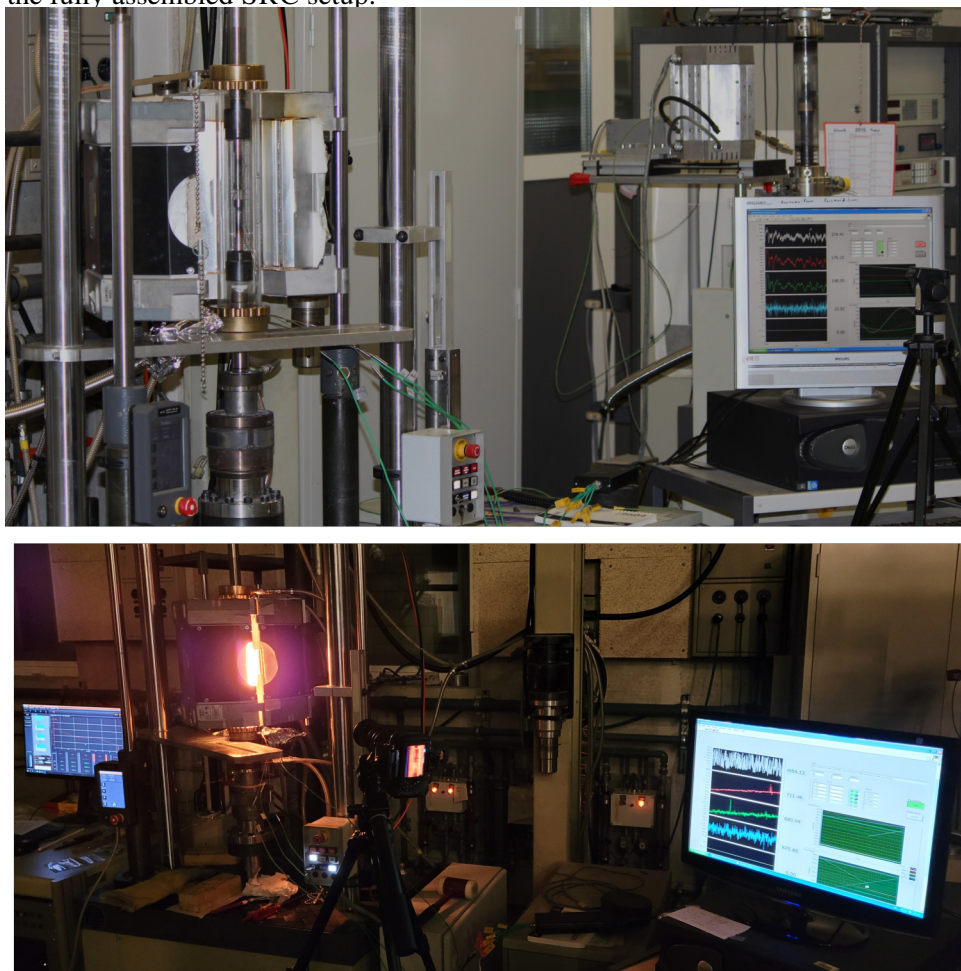


Figure A.5: Pictures of the Static Re-entry Chamber (SRC) fully assembled setup before and during a test.

A.5 Plasma wind tunnel additional data

Link for the test videos: <https://drive.switch.ch/index.php/s/OPnVa9T8K1LaHjn>

A.5.1 Front temperatures with LP3 pyrometer

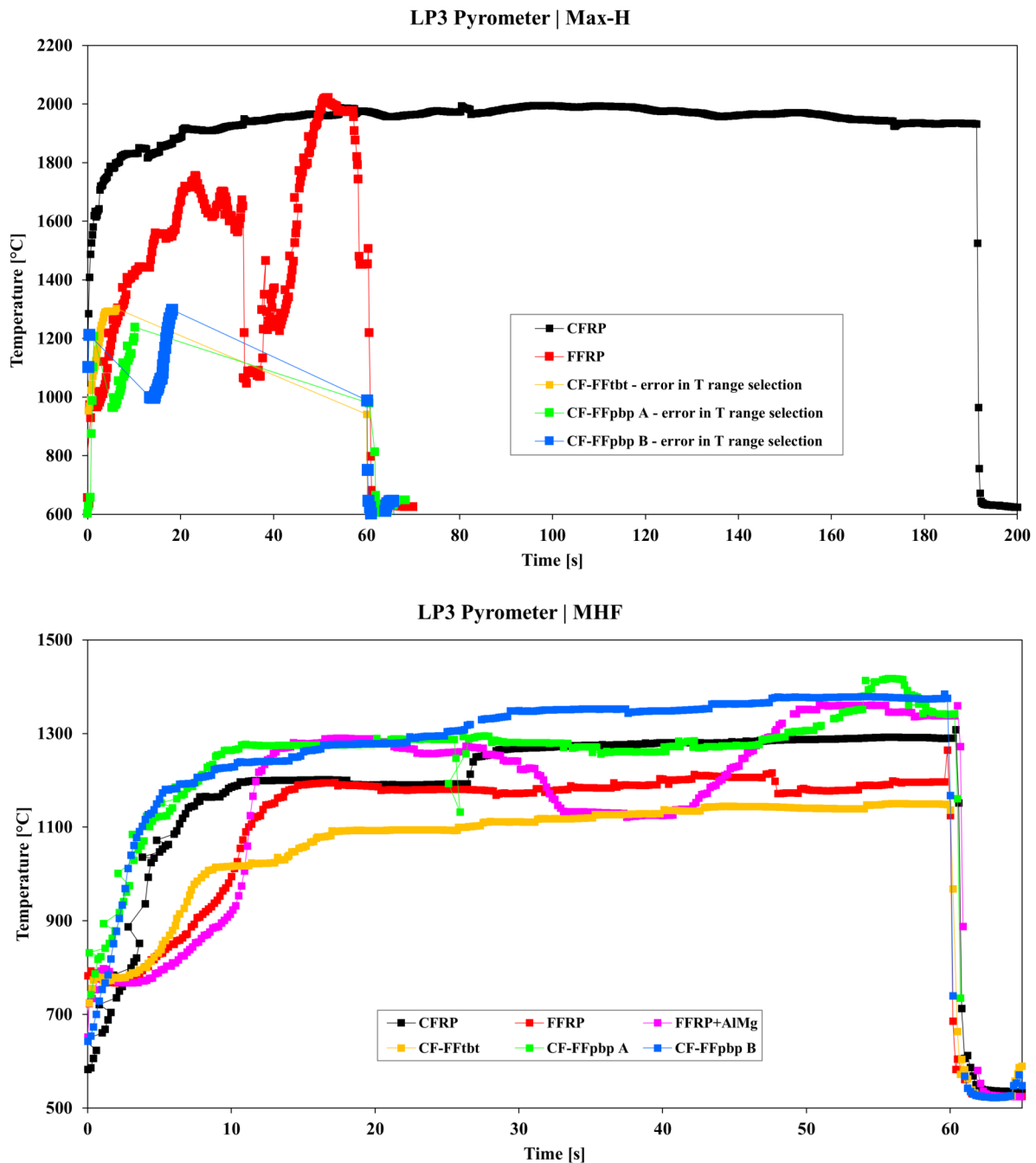


Figure A.6: Complete data overlay of the front temperatures data recorded from the LP3 pyrometer under Max-H (top) and MHF (bottom) conditions.

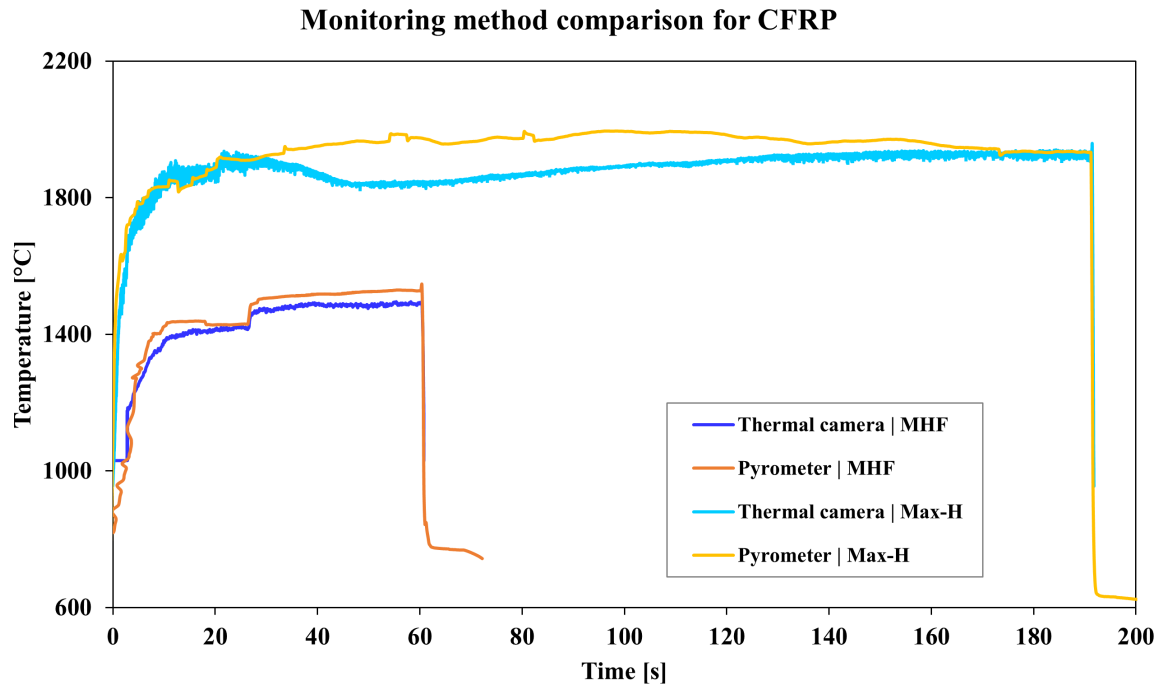
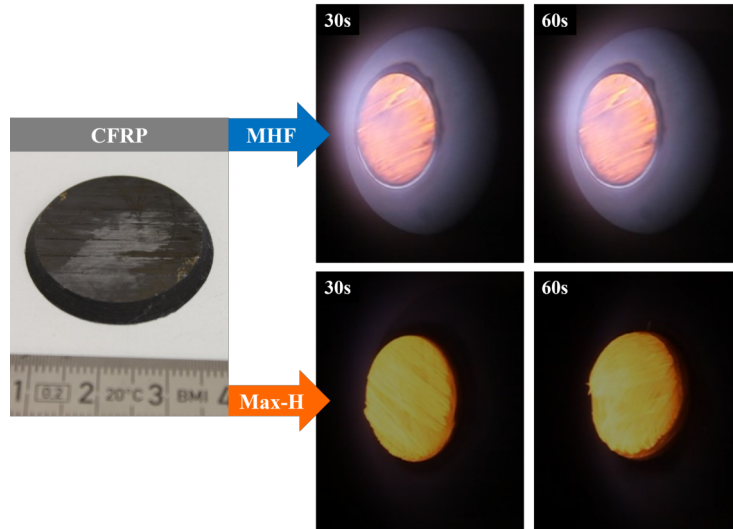
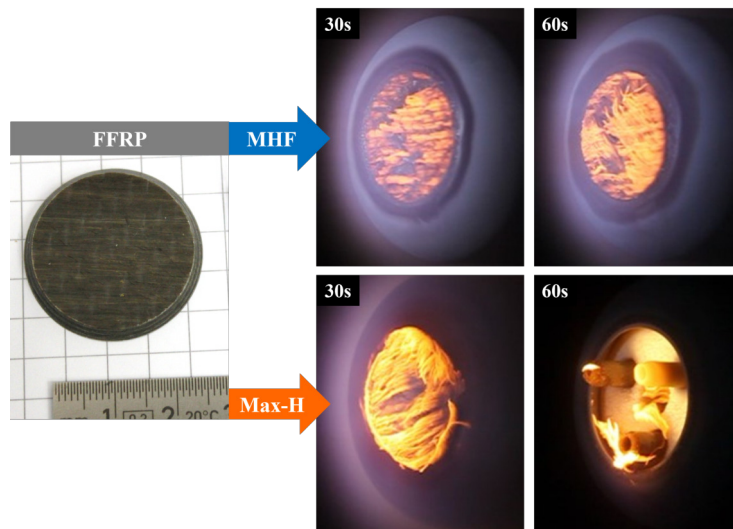


Figure A.7: Comparative overlay of all front temperature data for CFRP sample type under both MHF and Max-H.

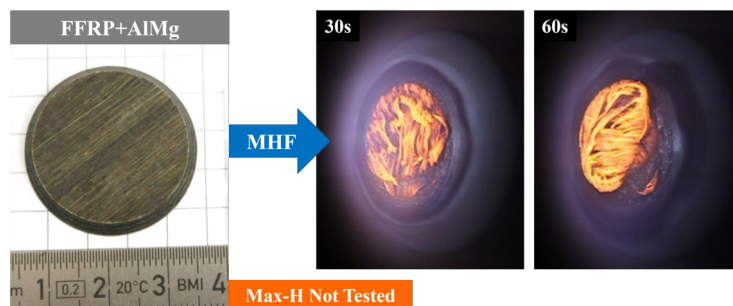
A.5.2 Front surface temperature monitoring technique comparison



CFRP



FFRP



FFRP+AlMg

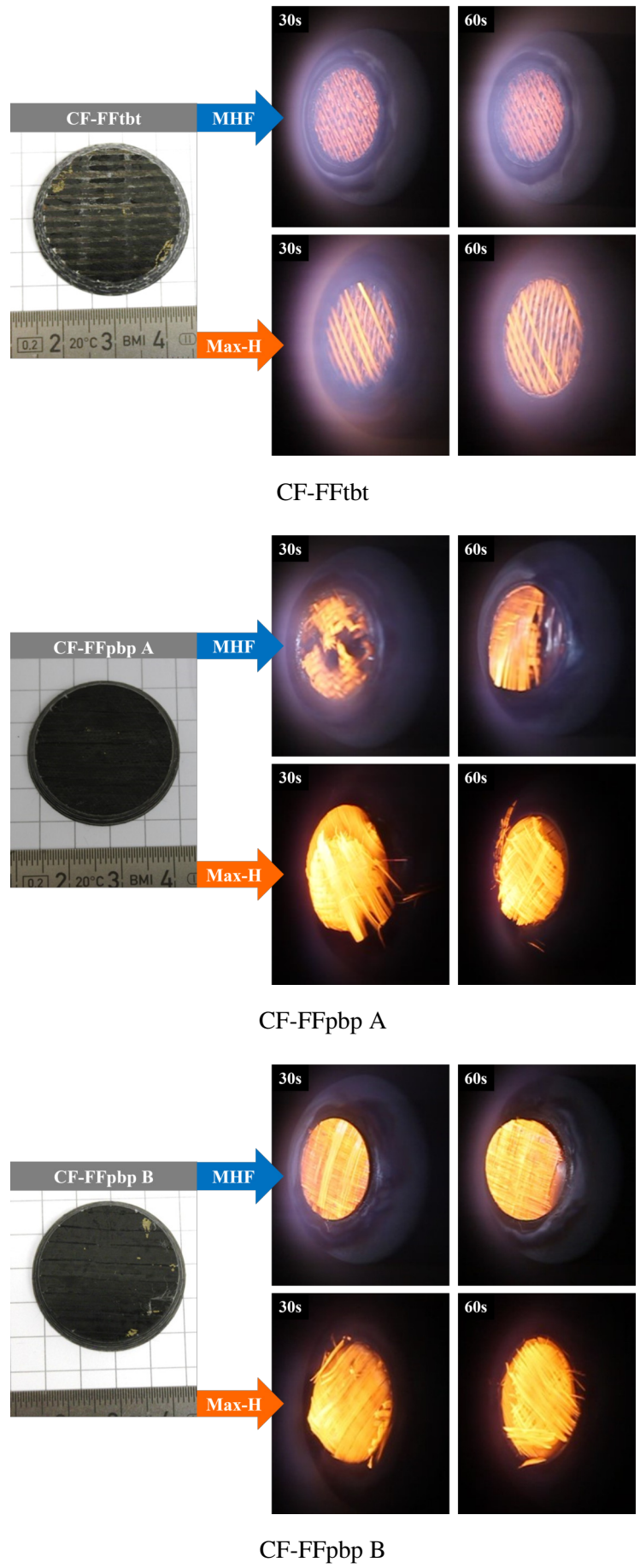


Figure A.8: Optical video snapshots of the all the PWT tested samples.

A.6 Novel technology assessment and market potential

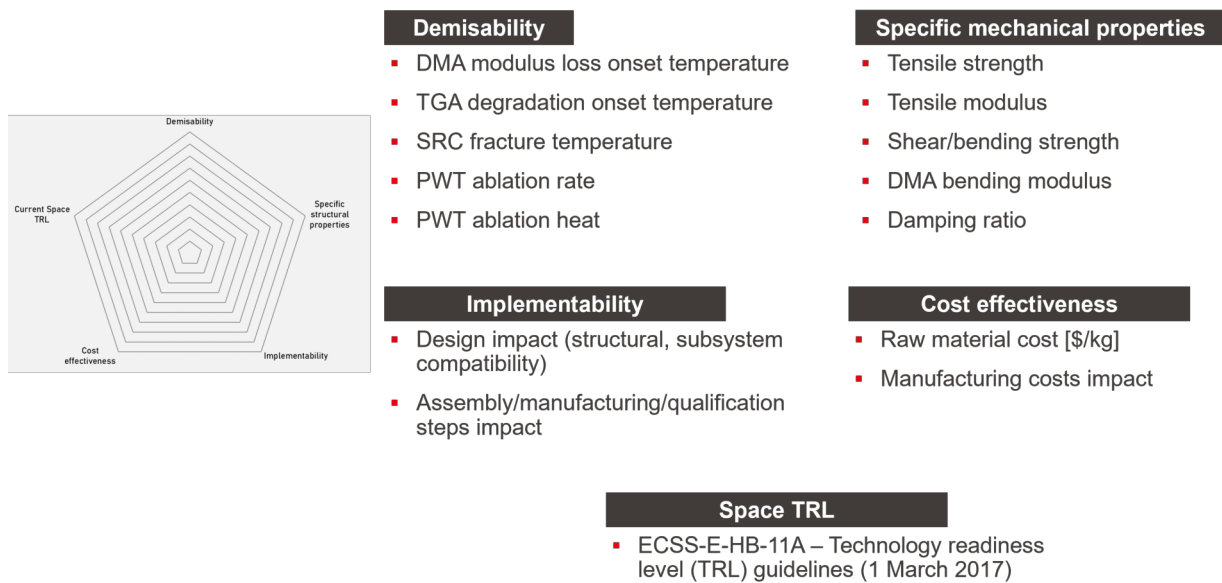


Figure A.9: Radar plot manual: listing of the integrated parameters within the 5 indexes of the plots.



Figure A.10: Radar plot of the SS and short-CF/PEEK fasteners as function of 5 D4D dedicated indexes.

The cut-CF "predictions" version integrate evaluated mechanical properties from the CFRP versions in addition to the demise properties of the CF-FFpbp, as closely similar demise behaviour is expected.



Figure A.11: Radar plot of the 4 skins (+ an extended version of cut-CF) as function of five D4D dedicated indexes.

A.7 Modelling spare parts

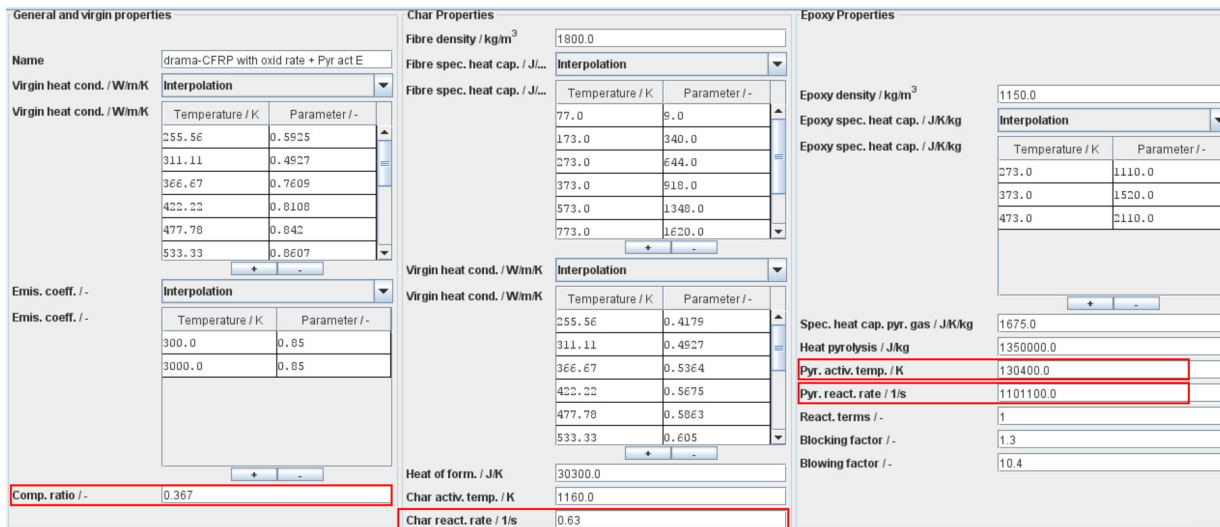


Figure A.12: Corrected version of the SARA built-in CFRP material, with highlighted in red parameters from Kuch [20] work, and realistic values such as a adequate structural resin weight fraction corresponding to a $V_f=55\%$.

Appendix A. Appendix

Table A.2: Overview of the D4D specific criteria resulting from the combination of four sandwich facesheets with three fasteners versions. The built-in CFRP is in orange to highlight the danger of using such material resulting in non-conservative criteria as it is poorly described, with unrealistic and missing parameters.

Fasteners Type	Criteria	Facesheet versions					
		Monolithic material - metal model Al7075	CFRP built-in	CFRP-realistic	CFRP new	FFRP	CF-FFpbb
Ti6Al4V	Break-up alt [km]	95.4	78.2	69.8	71.6	83.0	75.5
	Landing mass [kg]	9.9	34.8	72.7	55.242	32.9	40.1
	# of fragments	24	27	46	42	25	32
	Casualty risk [-]	1.39E-04	2.32E-04	4.81E-04	4.49E-04	2.04E-04	3.51E-04
SS-306L	Break-up alt [km]	95.40	84.0	70.8	74.7	83.00	75.50
	Landing mass [kg]	9.9	35.1	62.5	50.0	32.9	40.1
	# of fragments	24	25	42	41	25	32
	Casualty risk [-]	1.39E-04	2.04E-04	4.49E-04	4.42E-04	2.04E-04	3.51E-04
short-CF/PEEK	Break-up alt [km]	109.4	99.6	106.4	101.7	102.1	102.4
	Landing mass [kg]	9.28	33.7	32.9	30.45	29.9	29.2
	# of fragments	24	25	25	25	25	25
	Casualty risk [-]	1.39E-04	2.04E-04	2.04E-04	2.04E-04	2.04E-04	2.04E-04

Bibliography

- [1] ESOC ESA. ESA's re-entry predictions. URL <https://reentry.esoc.esa.int/reentry>.
- [2] Amy Thompson published. SpaceX launches a record 143 satellites on one rocket, aces landing, January 2021. URL <https://www.space.com/spacex-launches-143-satellites-transporter-1-rocket-landing>.
- [3] Debris from Musk's spacecraft crashes on to Aussie farm, July 2023. URL <https://www.nzherald.co.nz/world/debris-from-elon-musks-spacex-craft-crashes-on-to-australian-property/6J3NYQD3VOKUC6FFZHAPSCAA4E/>. Section: World, The Country.
- [4] SpaceX, . URL <http://www.spacex.com>.
- [5] Clean Space, . URL <https://technology.esa.int/program/clean-space>.
- [6] ESTEC ESA. DIVE - Guidelines for Analysing and Testing the Demise of Man Made Space Objects During Re-entry, 2021.
- [7] ClearSpace One - A Mission to make space sustainable, October 2020. URL <https://clearspace.today/>.
- [8] Steven C. Wofsy. Atmospheric Chemistry and Global Change. *Eos, Transactions American Geophysical Union*, 80(40):468–468, 1999. ISSN 2324-9250. doi: 10.1029/EO080i040p00468-02. URL <https://onlinelibrary.wiley.com/doi/abs/10.1029/EO080i040p00468-02>. eprint: <https://onlinelibrary.wiley.com/doi/pdf/10.1029/EO080i040p00468-02>.
- [9] James C. Beck, Ian Holbrough, Thorn Schleutker, and Ali Guelhan. Improved representation of destructive spacecraft re-entry from analysis of high enthalpy wind tunnel tests of spacecraft and equipment. *Acta Astronautica*, 164:287–296, November 2019. ISSN 00945765. doi: 10.1016/j.actaastro.2019.07.033. URL <https://linkinghub.elsevier.com/retrieve/pii/S0094576519312056>.
- [10] NASA SETI. The Cygnus OA6 Shallow Reentry Observing Campaign mission website. URL <https://atv5.seti.org/cygnus/>.
- [11] NASA. Cygnus Cargo Craft Released From Space Station - NASA, . URL <https://www.nasa.gov/image-article/cygnus-cargo-craft-released-from-space-station/>.
- [12] Andrew S Feistel, Michael A Weaver, and William H Ailor. COMPARISON OF REENTRY BREAKUP MEASUREMENTS FOR THREE ATMOSPHERIC REENTRIES. In *Sixth IAASS Conference*, September 2013.
- [13] Gary L Steckel and Paul M Adams. Evaluation of Reentry Effects of Delta II Second Stage Propellant Tanks. Technical Report TOR-2018-00670, 2018.
- [14] Thorn Schleutker, Sebastian Willems, and Ali Gülhan. Dynamic Experimental Simulation of the Demise during Re-Entry Flight, September 2021. URL https://indico.esa.int/event/321/contributions/6324/attachments/4346/6560/2021_CSID_DLR_Schleutker.pdf.
- [15] Mirko Trisolini, Hugh G. Lewis, and Camilla Colombo. Demisability and survivability sensitivity to design-for-demise techniques. *Acta Astronautica*, 145:357–384, April 2018. ISSN 0094-5765. doi: 10.1016/j.actaastro.2018.01.050. URL <https://www.sciencedirect.com/science/article/pii/S0094576517314248>.
- [16] Lucia Suriani, Antonio Caiazzo, Britta Ganzer, Tobias Lips, Patrice Laurenti, Bradley Lockett, Thorn Schleutker, Tiago Soares, and James Beck. Re-entry safety: Analysis and plasma wind tunnel testing of spacecraft design solutions to reduce on-ground casualty risk. *Journal of Space Safety Engineering*, December 2023. ISSN 2468-8967. doi: 10.1016/j.jsse.2023.11.014. URL <https://www.sciencedirect.com/science/article/pii/S2468896723001398>.
- [17] bcomp_admin. Natural fibre reinforced satellite panel, May 2020. URL <https://www.bcomp.ch/news/natural-fibre-reinforced-satellite-panel-for-cleaner-space-exploration-finalist-for-jec-innovation-award/>.

Bibliography

- [18] Adam Pagan, Régis Voillat, Georg Herdrich, Julien Rion, Lucie Bricout, Tiziana Cardone, and Benoit Bonvoisin. Demisability of novel Bio-Composite Material under Experimentally simulated Uncontrolled Re-entry Conditions. September 2019.
- [19] Adam S. Pagan. *Experimental Investigation of the Demise of Aerospace Materials in Uncontrolled Atmospheric Entries (Provided from personal communication)*. Doctoral Thesis, University of Stuttgart, Stuttgart, 2024. URL <https://www.researchgate.net/profile/Adam-Pagan>.
- [20] Maurice Kuch. Entwicklung eines Modells für die ablative Zerstörung von Kohlefaser-Epoxy Komposites beim Wiedereintritt. Master's thesis, TU Braunschweig, Braunschweig, 2011.
- [21] Adam S. Pagan and Georg Herdrich. Key parameters governing the ground risk from reentering pressure vessel debris. *Journal of Space Safety Engineering*, 9(2):189–200, June 2022. ISSN 2468-8967. doi: 10.1016/j.jsse.2022.04.002. URL <https://www.sciencedirect.com/science/article/pii/S2468896722000362>.
- [22] ESA - European Space maTerIal deMisability dATabasE (ESTIMATE), . URL <https://estimate.sdo.esoc.esa.int/>.
- [23] LeoLabs - LEO catalog, System metrics, . URL https://platform.leolabs.space/system_metrics.
- [24] Chronology of Space Launches - Gunter's Space Page, . URL <https://space.skyrocket.de/directories/chronology.htm>.
- [25] Space Environment Statistics · Space Debris User Portal, . URL <https://sdup.esoc.esa.int/discosweb/statistics/>.
- [26] ESA's re-entry predictions, . URL <https://reentry.esoc.esa.int/home/recovereddebris>.
- [27] IRGC - Space debris, . URL <https://www.epfl.ch/research/domains/irgc/specific-risk-domains/space-debris/>.
- [28] Intensifying space activity calls for increased scrutiny of risks, 2021. URL <https://www.epfl.ch/research/domains/irgc/spotlight-on-risk-series/intensifying-space-activity-calls-for-increased-scrutiny-of-risks/>.
- [29] Space debris conference I, . URL <https://space-debris-conference.sdo.esoc.esa.int/>.
- [30] NASA. TSecond International Orbital Debris Conference (IOC II), . URL <https://orbitaldebris.jsc.nasa.gov/navigation.html>.
- [31] T. Maclay and D. McKnight. Space environment management: Framing the objective and setting priorities for controlling orbital debris risk. *Journal of Space Safety Engineering*, 8(1):93–97, March 2021. ISSN 2468-8967. doi: 10.1016/j.jsse.2020.11.002. URL <https://www.sciencedirect.com/science/article/pii/S2468896720301415>.
- [32] ESA and ESA Director General's Office. ESA Space Debris Mitigation Policy 2023, March 2023. URL <https://technology.esa.int/upload/media/ESA-ADMIN-IPOL-2023-1-Space-Debris-Mitigation-Policy-Final.pdf>.
- [33] ESA Space Debris Mitigation Working Group. ESA Space Debris Mitigation Requirements, October 2023. URL https://technology.esa.int/upload/media/DGHKMZ_6542582e18e33.pdf.
- [34] ESA Space Debris Office. ESA'S ANNUAL SPACE ENVIRONMENT REPORT- 2023. Technical Report GEN-DB-LOG-00288-OPS-SD, European Space Agency, December 2023. URL https://www.sdo.esoc.esa.int/environment_report/Space_Environment_Report_latest.pdf.
- [35] ESA-Space debris mitigation, . URL <https://technology.esa.int/page/space-debris-mitigation>.
- [36] Paul D. Wilde and William Ailor. Chapter 9 - Re-Entry Operations Safety. In Firooz A. Allahdadi, Isabelle Rongier, and Paul D. Wilde, editors, *Safety Design for Space Operations*, pages 603–775. Butterworth-Heinemann, Oxford, January 2013. ISBN 978-0-08-096921-3. doi: 10.1016/B978-0-08-096921-3.00009-X. URL <https://www.sciencedirect.com/science/article/pii/B978008096921300009X>.
- [37] Tommaso Sgobba and Isabelle Rongier, editors. *Space Safety is No Accident*. Springer International Publishing, Cham, 2015. ISBN 978-3-319-15981-2 978-3-319-15982-9. doi: 10.1007/978-3-319-15982-9. URL <http://link.springer.com/10.1007/978-3-319-15982-9>.
- [38] The ESA/NASA Automated Transfer Vehicle - 5 (ATV-5) Shallow Reentry Observing Campaign., . URL <https://atv5.seti.org/>.
- [39] Amandine Denis, Ertan Umit, Damien LE Quang, Thierry Magin, and Olivier Chazot. QARMAN: POST-FLIGHT MISSION OVERVIEW, DATA ANALYSIS, AND LESSONS LEARNED FROM VKI RE-ENTRY CUBESAT. 2022.
- [40] Paolo Minacapilli, Flor Criado Zurita, Saúl Campo Pérez, Gabriele De Zaiacomo, Irene Pontijas, Andrea Fabrizi, Andrea Pizzetti, Andrés Caparrós Quero, Beatriz Delmas, Angel Naranjo Valiente, Carlos Menor, Santiago Molina, Mercedes Pavía, Benjamin Bastida Virgili, Stijn Lemmens, Beatriz Jilete, and Martin Spel. Addressing DRACO mission phase A design challenges, 2022. URL <https://indico.esa.int/event/416/contributions/7450/attachments/4815/7597/DRACO%20-%20CSID2022%20conference%20-%20presentation.pdf>.
- [41] G Koppenwallner, B Fritsche, T Lips, T Martin, L Francillout, and E De Pasquale. ANALYSIS OF ATV DESTRUCTIVE RE-ENTRY INCLUDING EXPLOSION EVENTS.

- [42] R. Blanchard, Richard Wilmoth, Christopher Glass, N. Merski, Scott Berry, Timothy Bozung, Alan Tietjen, Jodean Wendt, and Don Dawson. Infrared Sensing Aeroheating Flight Experiment: STS-96 Flight Results. *Journal of Spacecraft and Rockets*, 38, March 2001. doi: 10.2514/2.3713.
- [43] Chen Zhou, Zhijin Wang, Jiaoyang Zhi, and Anatolii Kretov. Aerothermodynamic Optimization of Aerospace Plane Airfoil Leading Edge. *Journal of Aerospace Technology and Management*, 9(4):503–509, October 2017. ISSN 2175-9146. URL <https://jatm.com.br/jatm/article/view/820>. Number: 4.
- [44] Craig A. Kluever. Spaceflight Mechanics. In Robert A. Meyers, editor, *Encyclopedia of Physical Science and Technology (Third Edition)*, pages 507–520. Academic Press, New York, January 2003. ISBN 978-0-12-227410-7. doi: 10.1016/B0-12-227410-5/00892-9. URL <https://www.sciencedirect.com/science/article/pii/B0122274105008929>.
- [45] Pasquale M. Sforza. Chapter 6 - Atmospheric Entry Mechanics. In Pasquale M. Sforza, editor, *Manned Spacecraft Design Principles*, pages 117–198. Butterworth-Heinemann, Boston, January 2016. ISBN 978-0-12-804425-4. doi: 10.1016/B978-0-12-804425-4.00006-4. URL <https://www.sciencedirect.com/science/article/pii/B9780128044254000064>.
- [46] William Ailor, W. Hallman, G. Steckel, and M. Weaver. Analysis of Reentered Debris and Implications for Survivability Modeling. 587: 539, July 2005.
- [47] Guiding Aeolus' safe reentry, . URL https://www.esa.int/Applications/Observing_the_Earth/FutureEO/Aeolus/Guiding_Aeolus_safe_reentry.
- [48] Rosa Jesse. Aeolus reentry: live – Rocket Science. URL <https://blogs.esa.int/rocketscience/2023/07/24/aeolus-reentry-live/>.
- [49] Adam S Pagan, Bartomeu Massuti-Ballester, Georg Herdrich, James A Merrifield, James C Beck, and Volker Liedtke. DEVELOPING AN EXPERIMENTAL PROCEDURE TOWARDS A STANDARDISED TESTING OF AEROSPACE MATERIAL DEMISABILITY. 2016.
- [50] Keiichiro FUJIMOTO, Takayuki ITOH, Hideyo NEGISHI, Ryoh NAKAMURA, Yasuhide WATANABE, and Kota TANABE. Computational Aerothermodynamics for HTV Small Re-entry Capsule Project. page 20 pages, 2019. doi: 10.13009/EUCASS2019-755. URL <https://www.eucass.eu/doi/EUCASS2019-0755.pdf>. Artwork Size: 20 pages Medium: PDF Publisher: Proceedings of the 8th European Conference for Aeronautics and Space Sciences. Madrid, Spain, 1-4 July 2019.
- [51] Adam Pagan, Bartomeu Massuti-Ballester, Georg Herdrich, Jim Merrifield, James Beck, Volker Liedtke, Nils Stelzer, and Benoit Bonvoisin. Characterisation of Demisable Materials through Plasma Wind Tunnel Testing. March 2015.
- [52] Aerospace & Advanced Composites GmbH. AAC - WRK-Facility-Description-I2R0.pdf, April 2020. URL <https://www.aac-research.at/wp-content/uploads/2023/01/WRK-Facility-Description-I2R0.pdf>.
- [53] Adam Pagan, Bartomeu Massuti-Ballester, Georg Herdrich, James Merrifield, James Beck, Volker Liedtke, and Benoit Bonvoisin. Experimental Investigation of Material Demisability in Uncontrolled Earth Re-entries. June 2017.
- [54] Thorn Schleutker. Development of Demisable Fiber Reinforced Plastic Composites, October 2022. URL <https://indico.esa.int/event/416/contributions/7452/attachments/4829/7375/Development%20of%20Demisable%20Fiber%20Reinforced%20Plastic%20Composites.pdf>.
- [55] Jacob R. Gissinger, Scott R. Zavada, Joseph G. Smith, Josh Kempainen, Ivan Gallegos, Gregory M. Odegard, Emilie J. Siochi, and Kristopher E. Wise. Predicting char yield of high-temperature resins. *Carbon*, 202:336–347, January 2023. ISSN 0008-6223. doi: 10.1016/j.carbon.2022.11.002. URL <https://www.sciencedirect.com/science/article/pii/S0008622322009150>.
- [56] M. B. Peter (Peter Moses Bweya) Waswa. *Spacecraft design-for-demise strategy, analysis and impact on low earth orbit space missions*. Thesis, Massachusetts Institute of Technology, 2008. URL <https://dspace.mit.edu/handle/1721.1/46797>. Accepted: 2009-09-24T20:47:32Z.
- [57] Philippe Reynier. Survey of convective blockage for planetary entries. *Acta Astronautica*, 83:175–195, February 2013. ISSN 0094-5765. doi: 10.1016/j.actaastro.2012.06.016. URL <https://www.sciencedirect.com/science/article/pii/S0094576512002548>.
- [58] Eunbi Lee, Chi Hyeong Cho, Sae Hoon Hwang, Min-Geun Kim, Jeong Woo Han, Hanmin Lee, and Jun Hyup Lee. Improving the Vertical Thermal Conductivity of Carbon Fiber-Reinforced Epoxy Composites by Forming Layer-by-Layer Contact of Inorganic Crystals. *Materials*, 12(19):3092, September 2019. ISSN 1996-1944. doi: 10.3390/ma12193092. URL <https://www.ncbi.nlm.nih.gov/pmc/articles/PMC6804115/>.
- [59] Luigi T. De Luca. Chapter 6 - Nanoenergetic Ingredients to Augment Solid Rocket Propulsion. In Qi-Long Yan, Guo-Qiang He, Pei-Jin Liu, and Michael Gozin, editors, *Nanomaterials in Rocket Propulsion Systems*, Micro and Nano Technologies, pages 177–261. Elsevier, January 2019. ISBN 978-0-12-813908-0. doi: 10.1016/B978-0-12-813908-0.00006-X. URL <http://www.sciencedirect.com/science/article/pii/B978012813908000006X>.

Bibliography

- [60] Alessandro Finazzi, FILIPPO MAGGI, CHRISTIAN PARAVAN, DENNIS DAUB, STEFANO DOSSI, ALESSANDRO MURGIA, TOBIAS LIPS, GEERT SMET, and KOBAYE BODJONA. Thermite-for-Demise (T4D): Preliminary assessment on the effects of a thermite charge in plasma wind tunnel experiments. page 12 pages, 2023. doi: 10.13009/EUCASS2023-499. URL <https://www.eucass.eu/doi/EUCASS2023-499.pdf>. Artwork Size: 12 pages Medium: PDF Publisher: Proceedings of the Aerospace Europe Conference - EUCASS - CEAS - 2023.
- [61] Geert Smet, René Seiler, and Nico Reichenbach. Exothermic reaction aided spacecraft demise, October 2018. URL https://indico.esa.int/event/234/contributions/4039/attachments/3086/3792/2018CSID_GSmet_ExothermicReactionAidedSpacecraftDemise.pdf.
- [62] Mark Fittock and D4DBB team. OHB - D4D Breadboarding TN11 Final Report - Joining technologies for demisability. Test report D4DBB-OHB-FR-001, January 2019.
- [63] Lilith Grassi. ThalesAlenia Space - DEMISABLE JOINT Final Report. Technical Report TASI-SD-DJ-ORP-0140, December 2020.
- [64] Isil Sakraker-Ozmen, Simon Hümbert, Sabina Hadzic, Marc Brodbeck, and Joel Patzwald. ADDITIVE MANUFACTURING FOR D4D: THERMOPLASTIC DEMISABLE JOINTS FOR HIGH ALTITUDE BREAK-UP. Heilbronn, Germany, June 2022. URL <https://elib.dlr.de/189688/>.
- [65] Joel Patzwald. DESIGN-FOR-DEMISE CONCEPTS WITH ADDITIVELY MANUFACTURED SATELLITE PARTS. Master's thesis, RWTH Aachen University, Aachen, 2021. URL <https://elib.dlr.de/144527/>.
- [66] WISA WOODSAT - The first wooden satellite in the world!, . URL <https://www.wisaplywood.com/wisawoodsat/>.
- [67] Space: the wooden frontier, August 2021. URL <https://www.kyoto-u.ac.jp/en/research-news/2021-08-31>.
- [68] Josh Dinner published. Japan has a wild idea to launch a satellite made of wood in 2024, May 2023. URL <https://www.space.com/wooden-satellite-lignosat-japan-2024>.
- [69] Stephane Galera, Julien Annaloro, and Valentin Ledermann. THE TOPOLOGY OPTIMIZATION APPROACH, A PROMISING TECHNOLOGY TO ADOPT AS A DESIGN FOR DEMISE SOLUTION, October 2023.
- [70] Sonja Caldwell. NASA-6.0 Structures, Materials, and Mechanisms, October 2021. URL <http://www.nasa.gov/smallsat-institute/sst-soa/structures-materials-and-mechanisms>.
- [71] Seong-Hyeon Park, Javier Navarro Laboulais, Pénélope Leyland, and Stefano Mischler. Re-entry survival analysis and ground risk assessment of space debris considering by-products generation. *Acta Astronautica*, 179:604–618, February 2021. ISSN 0094-5765. doi: 10.1016/j.actaastro.2020.09.034. URL <https://www.sciencedirect.com/science/article/pii/S0094576520305737>.
- [72] Jean Lachaud, Thierry Magin, Ioana Cozmuta, and Nagi Mansour. A Short Review of Ablative-Material Response Models and Simulation Tools. page 90, August 2011.
- [73] Online Materials Information Resource - MatWeb, . URL <https://www.matweb.com/>.
- [74] Takashi Nakamura, Hiroshi Nakamura, Osamu Fujita, Toru Noguchi, and Kichiro Imagawa. The Space Exposure Experiment of PEEK Sheets under Tensile Stress. *JSM International Journal Series A*, 47(3):365–370, 2004. ISSN 1344-7912, 1347-5363. doi: 10.1299/jsmea.47.365. URL http://www.jstage.jst.go.jp/article/jsmea/47/3/47_3_365/_article.
- [75] In-operando dynamic visualization of flow through porous preforms based on X-ray phase contrast imaging. *Composites Part A: Applied Science and Manufacturing*, 2021. doi: 10.1016/j.compositesa.2021.106560.
- [76] Haoyue Xin, Kun Wang, Hui Ren, and Qingjie Jiao. Comparative Study on Combustion Behavior of Aluminum-Based Alloy Fuels and Aluminum Powder in Solid Propellants. *Metals*, 13(8):1492, August 2023. ISSN 2075-4701. doi: 10.3390/met13081492. URL <https://www.mdpi.com/2075-4701/13/8/1492>. Number: 8 Publisher: Multidisciplinary Digital Publishing Institute.
- [77] Alexios Argyropoulos. *Process development of pre-impregnated hybrid thin-ply composites*. PhD thesis, EPFL, Lausanne, 2023.
- [78] Joel Galos. Thin-ply composite laminates: a review. *Composite Structures*, 236:111920, March 2020. ISSN 0263-8223. doi: 10.1016/j.compstruct.2020.111920. URL <https://www.sciencedirect.com/science/article/pii/S0263822319336943>.
- [79] S. Ryan, F. Schäfer, R. Destefanis, and M. Lambert. A ballistic limit equation for hypervelocity impacts on CFRP Al H/C satellite structures. 36:1908, January 2006. URL <https://ui.adsabs.harvard.edu/abs/2006cosp...36.1908R>. Conference Name: 36th COSPAR Scientific Assembly ADS Bibcode: 2006cosp...36.1908R.
- [80] Mohammed Iqbal C, Santhosh Kumar L, S R Chakravarthy, R Jayaganthan, R Sarathi, and Srinivasan A. Study of burning rate characteristics of propellants containing Al–Mg alloy nanopowder. *Nano Express*, 1(2):020007, September 2020. ISSN 2632-959X. doi: 10.1088/2632-959X/aba22f. URL <https://iopscience.iop.org/article/10.1088/2632-959X/aba22f>.
- [81] Julien Le Chapelain. MSDS_po-Mg_anglais_130411. 2010.

- [82] Junjie Chen and Jiecheng Han. A combination of graphene and graphene nanoplatelets: An effective way to improve thermal conductivity for polymers. *Results in Physics*, 15:102803, December 2019. ISSN 2211-3797. doi: 10.1016/j.rinp.2019.102803. URL <https://www.sciencedirect.com/science/article/pii/S2211379719330530>.
- [83] C Li, Navid Zobeiry, K Keil, S Chatterjee, and A. Poursartip. *ADVANCES IN THE CHARACTERIZATION OF RESIDUAL STRESS IN COMPOSITE STRUCTURES*. May 2014.
- [84] Aditi S. Joshi. Study of aluminum honeycomb sandwich composite structure for increased specific damping. Master's thesis, Purdue University, 2014. URL https://docs.lib.purdue.edu/cgi/viewcontent.cgi?article=1761&context=open_access_theses.
- [85] Bowen Xu, Rijk Blok, and Patrick Teuffel. An investigation of the effect of relative humidity on viscoelastic properties of flax fiber reinforced polymer by fractional-order viscoelastic model. *Composites Communications*, 37:101406, January 2023. ISSN 24522139. doi: 10.1016/j.coco.2022.101406. URL <https://linkinghub.elsevier.com/retrieve/pii/S2452213922003485>.
- [86] Laurens Beelen. Effect of moisture absorption on the performance of flax fibre reinforced composites. Master's thesis, KU Leuven, 2022. URL <https://osf.io/9ufb6/download>.
- [87] Optimal design of a novel graded auxetic honeycomb core for sandwich beams under bending using digital image correlation (DIC) - ScienceDirect, . URL <https://www.sciencedirect.com/science/article/pii/S0263822322001179>.
- [88] Adam S. Pagan, Bartomeu Massuti-Ballester, and Georg H. Herdrich. Experimental Thermal Response and Demisability Investigations on five Aerospace Structure Materials under Simulated Destructive Re-Entry Conditions. In *46th AIAA Thermophysics Conference, AIAA AVIATION Forum*. American Institute of Aeronautics and Astronautics, June 2016. doi: 10.2514/6.2016-4154. URL <https://arc.aiaa.org/doi/10.2514/6.2016-4154>.
- [89] Alexandre A. Looten, Albert Vodermayr, Antonio Caiazzo, Ralf Usinger, Muriel Richard, and Véronique Michaud. Advancing spacecraft demisability through a novel composite bolt joint system: a step toward sustainable and safe space environments. *CEAS Space Journal*, December 2023. ISSN 1868-2510. doi: 10.1007/s12567-023-00531-x. URL <https://doi.org/10.1007/s12567-023-00531-x>.
- [90] Stéphane Heinrich, Joel Martin, and Julien Pouzin. Satellite design for demise thermal characterisation in early re-entry for dismantlement mechanisms. *Acta Astronautica*, 158:161–171, May 2019. ISSN 0094-5765. doi: 10.1016/j.actaastro.2018.03.021. URL <http://www.sciencedirect.com/science/article/pii/S009457651731278X>.
- [91] Joel Patzwald. High Altitude Break-up Concepts with Additively Manufactured CF-PEEK, September 2021. URL <https://indico.esa.int/event/321/contributions/6386/attachments/4354/6570/Presentation%2520Patzwald%2520-%2520ESA%2520Clean%2520Space%2520Days.pdf>. <https://elib.dlr.de/144526/>.
- [92] Aditya Ramgobin, Gaëlle Fontaine, and Serge Bourbigot. A Case Study of Polyetheretherketone (II): Playing with Oxygen Concentration and Modeling Thermal Decomposition of a High-Performance Material. *Polymers*, 12(7):1577, July 2020. ISSN 2073-4360. doi: 10.3390/polym12071577. URL <https://www.ncbi.nlm.nih.gov/pmc/articles/PMC7408228/>.
- [93] Parina Patel, T. Richard Hull, Richard E. Lyon, Stanislav I. Stoliarov, Richard N. Walters, Sean Crowley, and Natallia Safronava. Investigation of the thermal decomposition and flammability of PEEK and its carbon and glass-fibre composites. *Polymer Degradation and Stability*, 96(1):12–22, January 2011. ISSN 01413910. doi: 10.1016/j.polymdegradstab.2010.11.009. URL <https://linkinghub.elsevier.com/retrieve/pii/S0141391010004167>.
- [94] P. Fontaine, E. Weiss-Hortala, V. Botaro, J. M. F. Paiva, and Y. Soudais. Impact of Atmosphere on Recovered Carbon Fibers From Poly Ether Ether Ketone (PEEK) Based Composites During Thermoconversion. *Waste and Biomass Valorization*, 12(12):6389–6402, December 2021. ISSN 1877-2641, 1877-265X. doi: 10.1007/s12649-021-01445-7. URL <https://link.springer.com/10.1007/s12649-021-01445-7>.
- [95] Mathieu Udriot, Karin Treyer, Emmanuelle David, Orell Bühler, Laszlo Etesi, and Valère Girardin. Rapid Life Cycle Assessment Software for Future Space Transportation Vehicles' Design - The Assessment and Comparison Tool. page 15, EPFL, Lausanne, June 2023. doi: 10.13009/EUCASS2023-015. URL <https://www.eucass.eu/component/docindexer/?task=download&id=6710>.
- [96] Stephan Hellmich, Mathieu Udriot, Xiao-Shan Yap, Emmanuelle David, and Alexandre Achille Looten. Sustainable Space Hub at EPFL: a review of ongoing research projects. page 15, June 2023. doi: 10.13009/EUCASS2023-016. URL <https://www.eucass.eu/component/docindexer/?task=download&id=6711>.
- [97] Jessica Delaval. On the atmospheric Impact of Spacecraft Demise upon Reentry – The Clean Space blog, November 2022. URL <https://blogs.esa.int/cleanspace/2022/08/11/on-the-atmospheric-impact-of-spacecraft-demise-upon-reentry/>.
- [98] Anithambigai Permal, Mutharasu Devarajan, Huong Ling Hung, Thomas Zahner, David Lacey, and Kamarulazizi Ibrahim. Thermal and mechanical properties of epoxy composite filled with binary particle system of polygonal aluminum oxide and boron nitride platelets. *Journal of Materials Science*, 51(16):7415–7426, August 2016. ISSN 1573-4803. doi: 10.1007/s10853-016-0016-3. URL <https://doi.org/10.1007/s10853-016-0016-3>.

Bibliography

- [99] Abdollah Omrani and Abbas A. Rostami. Understanding the effect of nano-Al₂O₃ addition upon the properties of epoxy-based hybrid composites. *Materials Science and Engineering: A*, 517(1):185–190, August 2009. ISSN 0921-5093. doi: 10.1016/j.msea.2009.03.076. URL <https://www.sciencedirect.com/science/article/pii/S0921509309004195>.
- [100] Mustapha Assarar, Wajdi Zouari, Hamid Sabhi, Rezak Ayad, and Jean-Marie Berthelot. Evaluation of the damping of hybrid carbon–flax reinforced composites. *Composite Structures*, 132:148–154, November 2015. ISSN 0263-8223. doi: 10.1016/j.compstruct.2015.05.016. URL <https://www.sciencedirect.com/science/article/pii/S0263822315003815>.
- [101] ASM Material Data Sheet, . URL <https://asm.matweb.com/search/SpecificMaterial.asp?bassnum=MA2024T81>.
- [102] Julien Rion. Natural fiber composites for space applications.
- [103] Saeid Hosseinpour Dashatan, Moumita Sit, Zhongyi Zhang, Erwan Grossmann, Jérémy Millot, Ya Huang, and Hom Nath Dhakal. Enhanced vibration damping and viscoelastic properties of flax/epoxy composites and their carbon fibre hybrid laminates. *Composites Part A: Applied Science and Manufacturing*, 175:107819, December 2023. ISSN 1359-835X. doi: 10.1016/j.compositesa.2023.107819. URL <https://www.sciencedirect.com/science/article/pii/S1359835X23003950>.
- [104] Na Deng, Yu-feng Zhang, and Yan Wang. Thermogravimetric analysis and kinetic study on pyrolysis of representative medical waste composition. *Waste Management (New York, N.y.)*, 28(9):1572–1580, 2008. ISSN 0956-053X. doi: 10.1016/j.wasman.2007.05.024. URL <https://www.ncbi.nlm.nih.gov/pmc/articles/PMC7126006/>.
- [105] Kalpana Patidar, Ajit Singathia, Manish Vashishtha, Vikas Kumar Sangal, and Sushant Upadhyaya. Investigation of kinetic and thermodynamic parameters approaches to non-isothermal pyrolysis of mustard stalk using model-free and master plots methods. *Materials Science for Energy Technologies*, 5:6–14, January 2022. ISSN 2589-2991. doi: 10.1016/j.mset.2021.11.001. URL <https://www.sciencedirect.com/science/article/pii/S2589299121000616>.
- [106] Adam S. Pagan. Applying Ground Experiment Findings to the Simulation of Destructive Pressure Vessel Re-entry, February 2021. URL https://indico.esa.int/event/389/contributions/6622/attachments/4424/6677/ATD3_2021_Presentation_PAGAN_Adam.pdf.
- [107] Thorn Schleutker. On Demisable Fiber Reinforced Plastic Composites, October 2023. URL <https://indico.esa.int/event/450/contributions/8944/attachments/5715/9471/2023%20-%20CSID,%20Schleutker,%20On%20Demisable%20Fiber%20Reinforced%20Plastic%20Composites.pdf>.
- [108] A. Pagan and G. Herdrich. A simple but universal systematic ranking of quantitative material demisability from experimental findings. 2020. URL <https://conference.sdo.esoc.esa.int/proceedings/isdrw05/paper/3>.
- [109] Sanghoon Lee, Yosheph Yang, and Seong-Hyeon Park. Aerothermal effects of ablation on carbon-based space objects. *International Journal of Heat and Mass Transfer*, 202:123731, March 2023. ISSN 0017-9310. doi: 10.1016/j.ijheatmasstransfer.2022.123731. URL <https://www.sciencedirect.com/science/article/pii/S0017931022011991>.
- [110] Thorn Schleutker, Ali Gülhan, Erhard Kaschnitz, Patrik Kärräng, Tobias Lips, and Felix Hermann. Influence of the Alloy and Dynamic Loads on Demisability of Aluminium, October 2023. URL <https://indico.esa.int/event/450/contributions/8947/attachments/5723/9633/2023%20-%20CSID,%20Schleutker,%20Influence%20of%20the%20Alloy%20and%20Dynamic%20Loads%20on%20Demisability%20of%20Aluminium.pdf>.
- [111] B Fritsche. MODELLING THE THERMAL DECOMPOSITION OF CARBON FIBRE MATERIALS DURING RE-ENTRY. In *6th European Conference on Space Debris*, Darmstadt, Germany, August 2013.
- [112] NRLMSIS 00, . URL <https://ccmc.gsfc.nasa.gov/models/NRLMSIS-00/>.
- [113] Pauline Tranchard, Fabienne Samyn, Sophie Duquesne, Bruno Estèbe, and Serge Bourbigot. Modelling Behaviour of a Carbon Epoxy Composite Exposed to Fire: Part I—Characterisation of Thermophysical Properties. *Materials*, 10(5):494, May 2017. ISSN 1996-1944. doi: 10.3390/ma10050494. URL <https://www.ncbi.nlm.nih.gov/pmc/articles/PMC5459023/>.
- [114] Tim J. Aspinall, Emmajane L. Erskine, Derek C. Taylor, and Rory M. Hadden. Influence of heating rate and atmospheric conditions on the thermal response of CFRP and its constituents. *Results in Materials*, 19:100406, September 2023. ISSN 2590-048X. doi: 10.1016/j.rinma.2023.100406. URL <https://www.sciencedirect.com/science/article/pii/S2590048X23000444>.
- [115] Ana X. H. Yong, Graham D. Sims, Samuel J. P. Gnaniyah, Stephen L. Ogin, and Paul A. Smith. Heating rate effects on thermal analysis measurement of T_g in composite materials. *Advanced Manufacturing: Polymer & Composites Science*, 3(2):43–51, April 2017. ISSN 2055-0340. doi: 10.1080/20550340.2017.1315908. URL <https://doi.org/10.1080/20550340.2017.1315908>. Publisher: Taylor & Francis _eprint: <https://doi.org/10.1080/20550340.2017.1315908>.
- [116] bcomp_admin. ampliTex™, March 2020. URL <https://www.bcomp.ch/products/amplitex/>.
- [117] TEIJIN CARBON. Tenax Filament Yarn Product Data Sheet, January 2023. URL https://www.tejjincarbon.com/fileadmin/user_upload/Datenbl%C3%A4tter/Filament_Yarn/Product_Data_Sheet_TSG01en_EU_Filament_.pdf.



PhD. student in materials science and space engineering

EDUCATION

2020-2024	PhD candidate – EPFL/ESA Network Partnering Initiative Laboratory for Processing of Advanced Composites and ESA Clean Space Office Design for demise applied to spacecraft structural panels and experiment for ClearSpace-one platform
2018-2019	Master Thesis at Composite Research Network group, Materials Engineering department, UBC Vancouver (CA)
2016-2018	Master in Materials Science and Engineering Minor in Space Technology, EPFL
2012-2016	Bachelor in Materials Science and Engineering, EPFL

EXPERIENCE

May-Oct 2023	Visiting Doctoral Researcher ESTEC European Space Agency, Noordwijk (NL)
Nov-Dec 2019	Primary/secondary school substitute class teacher ESVJ, Le Sentier
June 2018-Now	Helicopter attendant and loadmaster, Military service Inspection and preparation of helicopters, Swiss Air Force
Mar-May 2018	Student Internship, CERN EN-MME Engineering Design and Simulation office
2017-2018	Propulsion team leader, EPFL Rocket Team association Participation to IREC 2018, New Mexico (USA)
Aug 2017	International Space Workshop SDTP, BMSTU Moscow
July-Aug 2015	Internship in clean room, CHEOPS project Almatech, Lausanne

PUBLICATIONS

2023	<i>Advancing spacecraft demisability through a novel composite bolt joint system: a step toward sustainable and safe space environments.</i> Alexandre A. Looten, Albert Vodermayr, Antonio Caiazzo, Ralf Usinger, Muriel Richard & Véronique Michaud CEAS Space Journal
2021	<i>Aluminium core design comparison for spacecraft sandwich structural panels</i> Alexandre A. Looten Technical report, EDAM-EPFL

CONFERENCES & WORKSHOPS

April 2023	Material Research Society (MRS) Spring Meeting & Exhibit Oral presentation, San Francisco (USA)
Oct 2022 & 2023	Clean Space Industry days (CSID) Oral Presentation, ESA (NL)
Dec 2021	Aerothermodynamics and Design for Demise (ATD3) Workshop, online
June 2022	ESA - FAR 2nd International Conference on Flight Vehicles, Aerothermodynamics and Re-entry Missions Engineering Oral Presentation, Heilbronn (GER)
April 2021	ESA 8th Space Debris conference Oral Presentation, online
Dec 2020	ESA 5th Space Debris Re-entry Workshop, online

ALEXANDRE A. LOOTEN

04/07/1993 Geneva
Swiss/French

CONTACT

Route de la Maladière 30
Chavannes-près-Renens
Switzerland

+33 6 22 18 07 29
alexandre.looten@epfl.ch

LANGUAGES

French - Mother tongue
English - Fluent (C1)
German - Advanced (B2)
Norwegian - Notions (A1)

SPORTS

Gymnastic agrès, biking,
sailing, back/cross-
country skiing, kitesurfing